Characterization and Optimization of the Two-Way Effect in Melt-spun NiTi-based Shape Memory Alloys

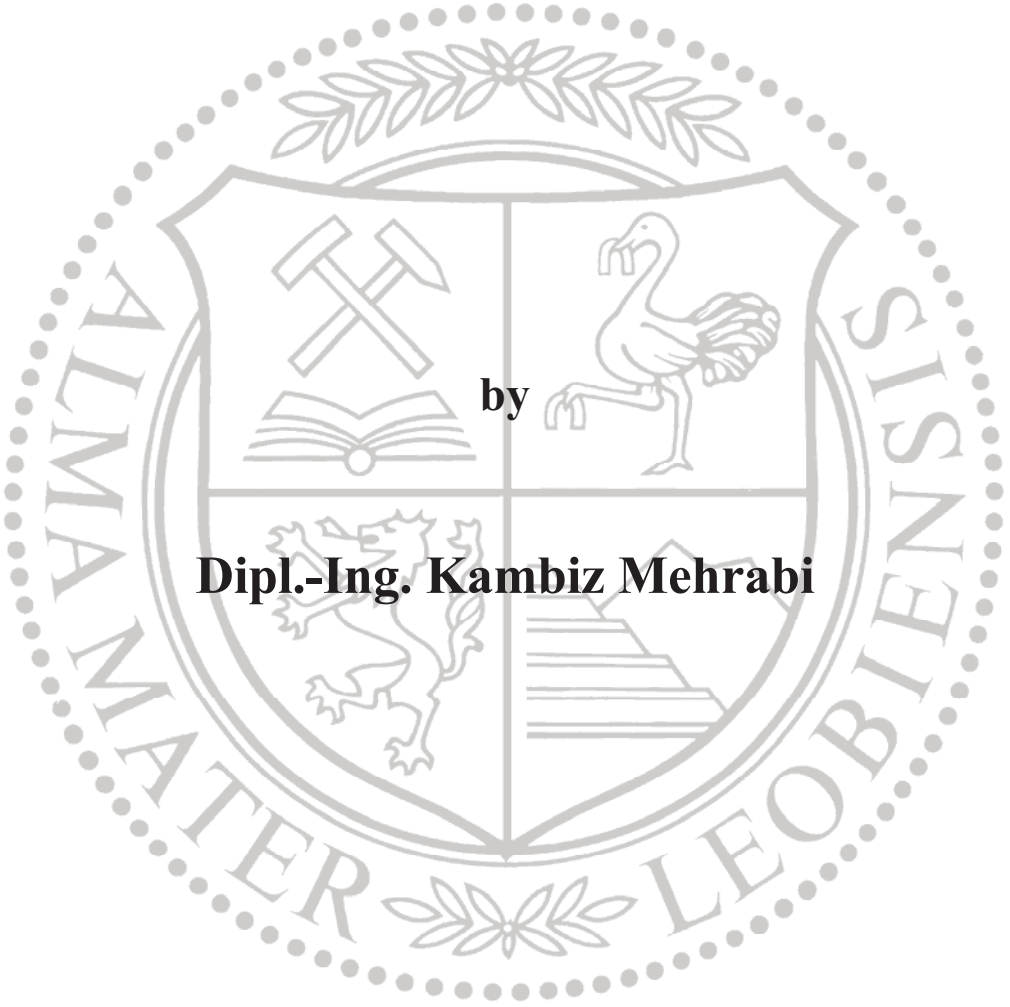

by

Dipl.-Ing. Kambiz Mehrabi

Dissertation submitted in partial fulfillment of the requirements for the degree of a

Doctor of Montanistic Sciences (Dr. mont.)

at the Montanuniversitaet Leoben, Austria.

March 2011

Affidavit

I declare in lieu of oath, that I wrote the PhD thesis and performed the associated research myself, using only literature cited in this volume.

Leoben, March 2011

Kambiz Mehrabi

To Shima, my wife, best friend and greatest supporter

Abstract

Shape memory alloys have been successfully introduced into a variety of technical areas over the past few years. A very promising field for their application in the near future is the microsensor and microactuator technology, since with a shape memory element a pre-determined response can be obtained very easily by thermal or electric stimulus. For long-term applications, however, it is very important to investigate and optimize the stability of the shape memory effect especially with respect to size and transformation temperatures, since the switching-temperatures should stay constant during the life-time of a shape memory element. From the several modes of using the shape memory effect, the intrinsic two-way shape memory effect (TWSME) is the most suitable to apply in actuators since no resetting force has to be considered in design.

In order to get small-dimensioned shape memory alloys (SMAs) with good functional and mechanical properties, a rapid solidification technique was employed. NiTi-based alloy samples have been fabricated by melt-spinning and splat-cooling. The application of rapid solidification can change the microstructure drastically, improve the ductility and shape memory characteristics, and lead to small-dimensioned samples. As an initial step, different parameters of melt-spinning, such as ejection temperature and pressure, wheel speeds and various crucible materials, were investigated in order to obtain ductile ribbons showing shape memory effect. Cooling rates during melt-spinning are directly proportional to the wheel speed and inversely proportional to the square of the ribbon thickness. The influence of different solidification rates and crucibles on microstructure, properties and transformation temperatures was studied and compared with results of splat-cooled disks.

The second step was to investigate the influence of copper (5-25 at.% Cu) and tungsten (2 at.% W) on the microstructure and the functional and mechanical behavior of NiTi thin ribbons. All samples show a shape memory effect immediately after processing without further heat treatment. The stress-strain, strain-temperature, stress-temperature and cyclic properties of various ribbons were obtained, giving a better understanding of the behavior of SMA under different test conditions.

The third step was aimed to study the influence of different thermomechanical training methods on the two-way shape memory effect of ribbons (magnitude and stability) and to examine its correlation with a stress-assisted two-way memory effect (SATWME), which is

of particular interest for applications. The results displayed that the different training methods used in this work were effective in developing a useable two-way shape memory effect.

Finally, when dealing with the weak intrinsic two-way shape memory effect, it is essential to elaborate the stability behavior thoroughly and to know how changes within the substructure affect the magnitude of the TWSME. Several thousand thermal cycles were performed on the trained shape memory elements, continuously observing the changes in the TWSME, substructures, mechanical properties and actuating temperatures. It was found that a good stability of the TWSME can be achieved by proper training process. Therefore, the trained material has the potential for interesting applications, e.g. as microsensors and microactuators.

Acknowledgements

First and foremost, I would like to express my sincere appreciation to my thesis advisor, Professor Dr. Albert C. Kneissl, whose creative vision inspired the work of this dissertation and for constructive comments and criticism. His experience and guidance have been invaluable and really helped to teach me how to think like a scientist. It is truly a pleasure working with him and having him as an advisor.

I would also like to specially thank Professor Dr. Ivan Anžel for giving me the opportunity to use the facilities in Slovenia to conduct some of the experiments. This encouragement and collaboration throughout this thesis is greatly valued and appreciated. I am also grateful to Dr. Mihael Brunčko, who has provided not only technical and scientific advice but also his friendship.

I am most indebted to my parents, who supported and encouraged me throughout my life in all ways they could. I wish to make both of them proud. Also special thanks go to my mother-in-law for concern and sacrifice so much to move to Leoben with us to make this all possible.

Above all, my loving thanks go to my beloved wife, Shima, who has shown great understanding and patience towards this work as well as everything else I do. I could not have asked for more.

Finally, I owe my warmest thanks to the staff of the institute, all the people and my friends who have been supportive of my endeavor towards my PhD study and to Him, who knows every thing.

Table of Contents

CHAPTER 1

Scope of the thesis

1.1 Introduction

The technical importance of most engineering materials is based on their mechanical, electrical or magnetic properties, which should, normally, be as independent as possible from environmental influences. Beside these conventional materials there is another group of materials, which are not interesting so much for their properties under certain conditions, but much more for how they react on changes of these conditions. This group of materials is known as functional materials. Beside others, shape memory materials belong to this group.

Characteristic for shape memory materials is an unconventional, unique correlation of strain, stress and temperature, which is based on crystallographic reversible thermoelastic martensitic transformation. The low-temperature and the high-temperature phases are, analogous to steel technology, named martensite and austenite (also parent phase). The transformation start and finish temperatures are A_s (austenite start) and A_f (austenite finish) and M_s (martensite start) and M_f (martensite finish) during heating and cooling, respectively. The temperature triggered transformation can be accompanied by unusually large strain; if external forces constrain the deformation, the stress can strongly increase (capability to perform mechanical work). At temperatures above A_f the reversible martensitic transformation can be triggered by an increase of stress level. In this case an unusually large strain accompanied by a very small additional stress increase can be observed. Upon unloading, transformation and shape change take place in reverse direction and order (the crystal, which transformed to martensite as the last one, will transform back to austenite as the first one upon unloading, and the one, which became martensite as the first one, will transform back to austenite as the last one). In martensitic state the shape memory alloys (SMAs) are capable of large inelastic shape changes, which do not base on dislocation glide, joined with relatively small increase of stress. The following phenomena can be distinguished: 1.) pseudoplasticity (PP) and one-way shape memory effect (SME), 2.) two-way shape memory effect (TWSME) and 3.) pseudoelasticity (PE) or superelasticity (SE).

The scientific fundamentals of the shape memory effect have been elaborated over the past years to a large extent, setting the frame for a successful development of shape memory components as functional parts integrated in various devices. Shape memory elements can sense thermal, mechanical, magnetic or electric stimuli and exhibit actuation or some pre-determined response, making it possible to tune some technical parameters such as shape, position, strain, stiffness, natural frequency, damping, friction and other static and dynamic characteristics of material systems in response to environmental changes.

Due to the fact that shape memory elements can function as sensors as well as actuators, they have attracted also keen attention as promising candidates for smart materials. Their performances such as sensoring (heat, stress), large-stroke actuation, high damping, adaptive responses, shape memory and pseudoelastic capability can be utilized very advantageous to design intelligent (smart) composites [1.1].

Simple design and compact size may be the main advantages of a shape memory actuator. Consisting solely of one piece of SMA, the actuator can convert heat directly into mechanical

work. Strokes of complicated shapes can be realized using simple elements, free of mechanical joints, without requiring lubrication, without motors, valves etc., thus facilitating essentially the miniaturization and improving reliability. Only heating and cooling devices are necessary to use the shape memory effect of the alloy. All this makes shape memory elements superior to a variety of conventional work producing elements. The most important advantages of the shape memory actuation mechanism compared to competing technologies may be summarized as follows:

- simple, compact and safe mechanism
- high force or large motion
- high power/weight (or power/volume) ratio
- creation of clean, silent, spark-free and zero-gravity working conditions
- few mechanical parts
- non-linear characteristic allowing a higher work output in case of narrow switching intervals.

An actuating element represents a multiple-cycle application of the shape memory effect. At present, cyclical shape changes based on the shape memory effect are mainly realized by the extrinsic TWSME. In this case the temperature controlled change between two pre-set shapes is obtained by constructive means. This solution has the disadvantage that for designing the element, the external force - usually a steel spring – has always to be taken into consideration, thus restricting the choice of the shape change and impeding the miniaturization of the element. Consequently, for the design of microactuators, it would be more reasonable to apply the intrinsic two-way shape memory effect. The smaller the size, the more important the advantage of the intrinsic two-way shape memory effect will become.

In order to keep the overall system working properly, the shape change has usually to be executed within small tolerances. Although mechanical fatigue (crack growth) may have a limiting impact on life cycles in certain cases, in most applications the element will become inoperative earlier due to fading of the functional parameters (functional fatigue, i.e. shift of transformation temperatures, decreasing of SME or TWSME size). Consequently, functional fatigue during cycling is of major importance and must be a dominating parameter determining the quality of a shape memory element.

In this thesis NiTi-based SMAs will attract our attention. This comes from the fact that NiTi-based alloys have relatively large size of shape memory effect and pseudoelasticity, and especially because of biocompatibility, which makes them indispensable for applications in human medicine. And precisely the medical device industry with its low volume but high value products is dominating the market for NiTi-based SMAs. The main goals of this work are described in the next chapter.

1.2 Aims of this work

This thesis has been carried out within the research group "Shape Memory Alloys" at the Chair for Metallography at the University of Leoben. Based on the results of previous research of the working group e.g. [1.2, 1.3] on the interrelationship of microstructure and functional stability in wire specimens of NiTi and NiTiW shape memory alloys, it is presently tried to make a step to smaller dimensions and transfer the experience concerning functional stability of SMAs to sensors and actuators of microsize dimensions with NiTi-based shape memory materials. Also in the past, it was made an effort to fabricate thin films by magnetron sputtering but this method was not very appropriate for the demand because the samples were very difficult to handle, concerning the measurement of mechanical properties and training [1.4-1.7]. Therefore, it was decided to work with melt-spinning process.

The scope of this work will focus on: (i) optimized melt-spinning of NiTi-based alloys , (ii) the influence of training parameters on the size of the intrinsic TWSME and degradation characteristics, (iii) improvement of the TWSME with respect to size and stability of NiTi-based ribbons.

The detailed aims of the thesis are:

- To produce NiTi-based ribbons by an optimized melt-spinning process.
- To assess the microstructures of ribbons and to optimize the parameters with respect to intrinsic TWSME.
- To perform training on a newly developed device and optimize the training conditions with respect to the size of the TWSME.
- To evaluate the long-term stability of the TWSME of rapidly solidified thin ribbons.
- To examine the influence of Cu and W on binary NiTi for comparison reasons and for determining the hopefully beneficial influence, concerning the size and stability of the TWSME.
- To gain new knowledge on the mutual dependence of the chemical composition, parameters of rapid solidification, microstructure, mechanical treatments, training and thermal cycling parameters, mechanical and functional properties.

In context of the present work functional properties denote:

- Properties connected to the shape memory effect: size of the SME, the long-term stability of the TWSME and the shift of transformation temperatures due to thermal cycling (repeated thermal induced transformation).
- Properties connected to the pseudoelastic behavior: stress level and size of pseudoelastic deformation, dependence on temperature in NiTi-based ribbons.

The results of this work should enhance considerably our fundamental knowledge on shape memory alloys in general and enable the construction of improved shape memory elements with high stability of the two-way shape memory effect for microactuators and microsensors. Thereby there will hopefully be beneficial implications for some industrial branches, e.g. biomedical and automotive industry.

CHAPTER 2

Overview of shape memory alloys

2.1 History of shape memory alloys

The shape memory effect was discovered first in 1932 by a Swedish physicist, Arne Ölander [2.1], namely, the pseudoplastic behavior of the Au-Cd alloy. The alloy was plastically deformed when it was cooled and returned to its original shape when it was heated. Later in 1938, Greninger and Mooradian [2.2] observed the same effect also in CuZn and CuAl. The basic phenomenon of the memory effect governed by the thermoelastic behavior of the martensite phase was reported a decade later by Kurdjumov and Khandros [2.3] and later, Chang and Read [2.4] observed shape memory effect in AuCd alloy. In 1961, Muldaver and Feder used an AuAgCd alloy in a thermally actuated electrical switch and took the first patent for a shape memory alloy [2.5].

In 1962 William J. Buehler and his co–workers at the Naval Ordnance Laboratory discovered shape memory effect in an alloy of nickel and titanium, which can be considered the major breakthrough in the field of shape memory materials. This metal later became known as Nitinol, an acronym for Nickel-Titanium Naval Ordnance Laboratory [2.6, 2.7].

Buehler's original task was finding a metal with a high melting point and high impact resistant properties for the nose cone of the Navy's missile SUBROC. From among sixty compounds, Buehler selected twelve candidates to measure their impact resistance by hitting them with hammer. He noted that a nearly equiatomic nickel–titanium alloy (50 at.% Ni - 50 at.% Ti) seemed to exhibit the greatest resistance to impact in addition to satisfactory properties of elasticity, ductility and fatigue. One day he took some Nitinol bars from melting furnace and laid them out on a table to cool. He intentionally dropped one on the floor out of curiosity. The bar produced a bell–like quality sound. Than he ran to the fountain with cold water and chilled the warm bar. The bar was once again dropped on the floor. On his amazement it exhibited the anechoic acoustic response. Buehler knew that acoustic damping signaled a change in atomic structure that can be turned off and on by simple heating and cooling near room temperature, but he did not yet know that this rearrangement in the atomic structure would lead to shape memory effect [2.7, 2.8]. It was in 1960 when Raymond Wiley joined Buehler's research group. He worked on failure analysis of various metals. He demonstrated to his management the fatigue resistance of a Nitinol wire by flexing it. The directors who were present at this meeting passed the strip around the table, repeatedly flexing and unflexing it and were impressed with how well it held up. One of them, David Muzzey, decided to see how it would behave under heat. He was a pipe smoker, so he held the compressed Nitinol strip in the flame of his lighter. To the great amazement of all, it stretched out completely. When Buehler heard about that, he realized that it had to be related to the acoustic behavior he had noted earlier [2.7, 2.8].

After this moment, an extensive study began to reveal the shape memory characteristics of NiTi and the first efforts to exploit the potential of NiTi as an implant material were made by Johnson and Alicandri in 1968 [2.9]. The use of NiTi for medical applications was first reported in the 1970s [2.10]. In the early 1980s the idea attained more support, and some orthodontic and mainly experimental orthopedic applications were released. After the confirmation of biocompatibility of NiTi, the application field of NiTi has been tremendously enlarged.

Emerging applications of NiTi shape memory alloys include microelectro-mechanical systems (MEMS), biomedical devices and implants such as stents for opening up arteries, and deployable aerospace applications like actuators for maneuvering the wings of an aircraft. Applications of shape memory alloys are summarized well by [2.11, 2.12].

2.2 Definition of the shape memory alloys

2.2.1 Introduction

The term Shape Memory Alloys (SMA) is applied to that group of metallic materials that demonstrate the ability to return to some previously defined shape or size when subjected to the appropriate thermal procedure. Generally, these materials can be plastically deformed at some relatively low temperature, and upon exposure to some higher temperature will return to their shape prior to the deformation. A material that shows shape memory only upon heating is referred to as having a one-way shape memory. Some materials also undergo a shape change upon cooling. This is called two-way shape memory.

Shape Memory Alloys are novel materials that have the ability to return to a predetermined shape by the material composition and processing history, when heated above their transformation temperature. When a SMA is cold, or below its transformation temperature, it has a very low yield strength and can be deformed quite easily into any new shape and will remain in that shape at that low temperature [2.13]. However, when that material is heated to above its transformation temperature, it undergoes a change in crystalline structure, which causes it to return to its original undeformed shape. If the SMA encounters any resistance during this transformation, it will apply a force on the resisting member. This phenomenon can be used as a remote actuation mechanism.

SMAs with transformation temperatures above their operating temperature (often room temperature) exhibit the SME described above. SMAs with transformation temperatures below operating temperature exhibit what is known as pseudoelasticity, or sometimes called superelasticity, and are referred to as superelastic. SMAs in the superelastic state are capable of recovering their previous shape after the removal of even relatively high applied strains. In this effect, the deformation from an applied load is not plastic and shape recovery is achieved isothermally on unloading.

2.2.2 Crystallographic aspects of SMAs

The crystalline structure of a material, in part, dictates the material's overall behavior. For this reason, it is important to have a basic understanding of the crystallographic and microscopic aspects of shape memory alloys (SMAs). This is true even for those looking to use them in large scale applications. The SME is typically made possible by a SMA's ability to exist in two distinct crystallographic structures: the high-temperature phase, called austenite (named after the English metallurgist William Chandler Austen [2.14]) and the low-temperature phase, called martensite (named after the German metallographer Adolf Martens [2.14]). Particularly, it is the transition from the less-symmetric martensite to the more-symmetric austenite that allows the material to return to its original shape. The less-symmetric twinned microstructure of the martensite phase allows the SMA to form with several rhombus variants, thus accommodating various macroscopic geometries generated by applied stresses. However, there are no variants in the austenite phase and, therefore, when returned to austenite the material must return to its original microstructure, eliminating the geometry accommodated by the rhombus variants of the martensite. In general, the martensite is a relatively soft and easily deformed phase, stable at low temperatures and under high stresses while the austenite is the stronger phase, stable at high temperatures and low stresses. Conversely, the austenitic phase only takes on a single form and tends to be harder and stronger [2.15].

The unique ability of SMAs to recover their shape is in part due to the ordered crystalline structure between the austenitic and martensitic phases and involves rearrangement of atoms within the crystal lattice. The martensitic transformation is associated with an inelastic deformation of the crystal lattice with no diffusive process involved. The phase transformation results from a cooperative and collective motion of atoms on distances smaller than the lattice parameters. Martensite plates can grow at speeds which approach that of sound in the metal (up to 1100 m/s). The martensitic transformation can occur at low temperatures where atomic mobility may be very small and this fact results in the absence of diffusion in the martensitic transformation within the time scale of transformation. The absence of diffusion makes the martensitic phase transformation almost instantaneous (a first-order transition). When a shape memory alloy undergoes a martensitic phase transformation, it transforms from its high–symmetry (usually cubic) austenitic phase to a low symmetry martensitic phase (highly twinned monoclinic structure). Nitinol's high temperature phase has B2 crystal structure and its low temperature phase has B19' crystal structure. If one ignores the difference between Ni and Ti atoms, B2 crystal structure is simply body-centered cubic and B19 has the same symmetry as hexagonal-close packed, except that the two species of atoms break hexagonal symmetry changing the structure to tetragonal. B19' is a small distortion from B19 [2.16, 2.17]. See Figure 2-1.

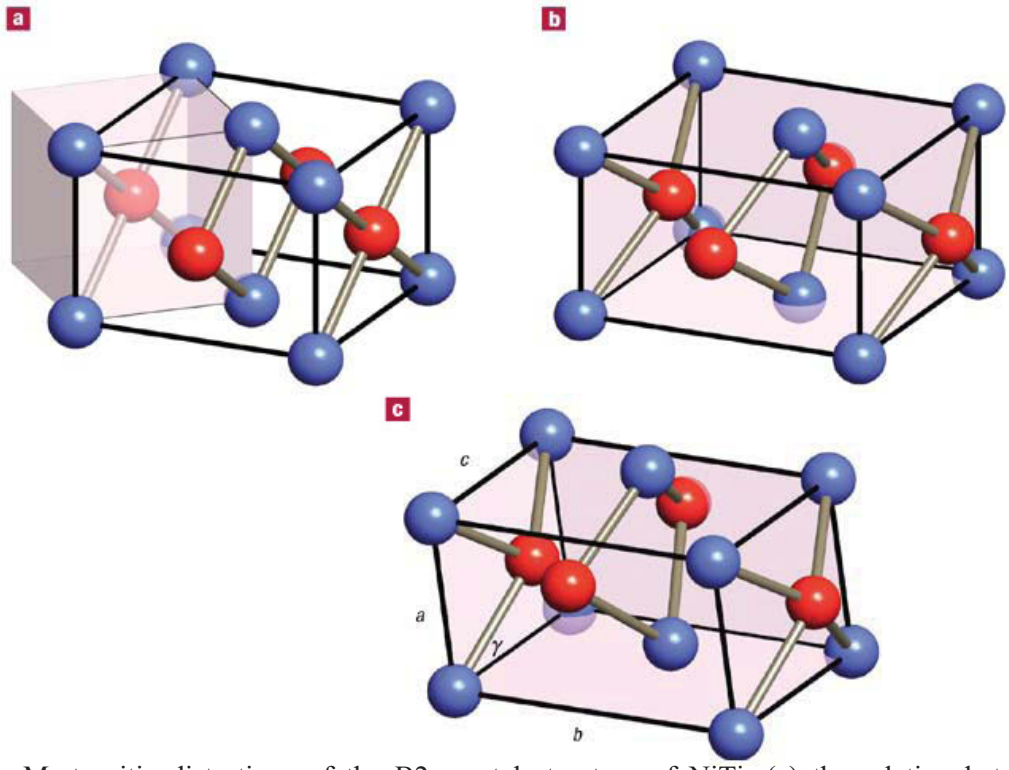

Fig. 2-1: Martensitic distortions of the B2 crystal structure of NiTi; (a) the relation between the cubic B2 cell (shaded box) and the undistorted tetragonal, (b) the orthorhombic B19 structure, (c) the monoclinic B19' structure. Ni and Ti atoms are represented by red balls and blue balls, respectively [2.17, 2.18].

This ordering allows the material to undergo a displacive (diffusionless) martensitic phase transformation either through a temperature change (thermal-induced martensite) or the application of stress (stress-induced martensite) rather than the diffusional transformation associated with solid-state transformations of typical metals. This fact means that the energy necessary for the martensitic transformation can be provided not only by a thermal input but also by a mechanical input [2.15].

Figure 2-2 shows the NiTi in austenitic and martensitic forms in a two-dimensional view. As shown in the figure, the austenite is symmetric and thus has one layout for the atoms, while the martensite could be found in two different alignments based on the level of stress applied to the alloy. Based on the stress direction, the martensite could be detwinned either to the left or to the right direction. Thus from a two-dimensional point of view there are two possible variants for martensite [2.19].

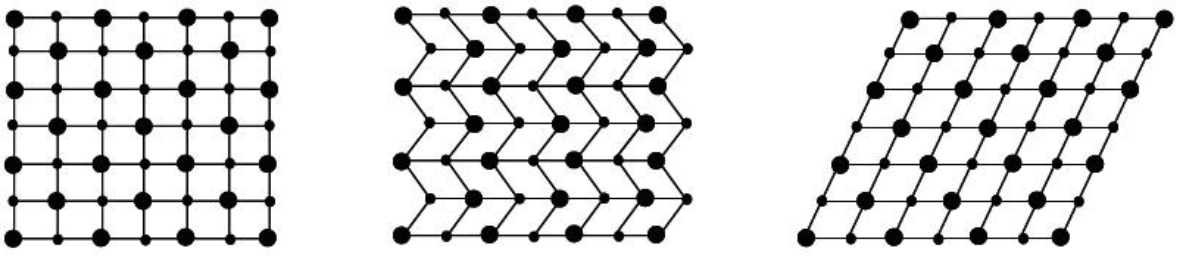

Fig. 2-2: Schematic view of a typical SMA microstructure in a two-dimensional plane: (a) austenite, (b) multi-variant twinned martensite, (c) single variant detwinned martensite [2.19].

The shape memory recovery is a result of the need of the crystal lattice structure to accommodate to the minimum energy state for a given temperature. In SMAs, the relative symmetries between the two phases lead to a highly ordered transformation, where the displacements of individual atoms can be accurately predicted and eventually lead to a shape change on a macroscopic scale. However, when the martensitic transformation starts during cooling, in order to minimize the volume change, the self-accommodation of martensite variants takes place. Martensite variants mutually reduce the transformation strain accompanying the formation of the individual variants. Thus the specimen as a whole will not experience significant shape change. The transformation start and finish temperatures from austenite to martensite are called M_s and M_f respectively, and transformation start and finish temperatures from martensite to austenite are called A_s and A_f where the former transformation is named as forward transformation and the latter one as back transformation.

The crystal structure of martensite is less symmetric compared to that of the parent phase. If a single crystal of parent phase is cooled below M_f, then martensite variants with a total of 24 crystallographically equivalent habit planes are generally created. There is however, only one possible parent phase (austenite) orientation, and all martensitic configurations revert to that single defined structure and shape upon heating above A_f. The mechanism by which single martensite variants deform is called twinning, and it can be described as a mirror symmetry displacement of atoms across a particular atom plane, the twinning plane. Most metals deform by slip or dislocation, however, shape memory alloys respond to stress by simply changing the orientation of the crystal structure through the movement of twin boundaries. However, deformation beyond this will result in classical plastic deformation by slip, which is irrecoverable and therefore has no memory effect.

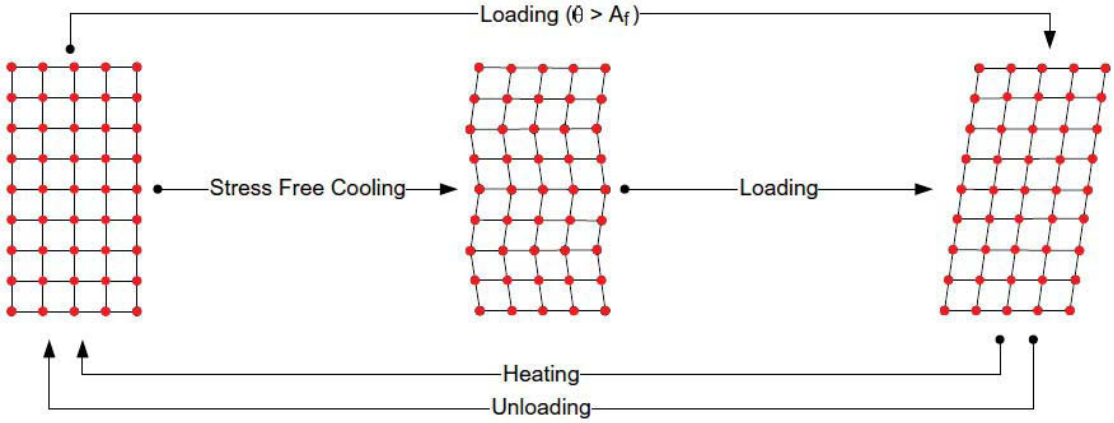

Fig. 2-3: Schematic of austenite-martensite phase transformation [2.20].

Figure 2-3 gives an overview of the martensitic phase transformation in shape-memory alloys. During the deformation from austenite phase to martensite phase at temperature below the martensitic finish temperature (M_f), the alloy starts in the twinned martensite condition, during loading detwinning occurs and the structure becomes one of deformed martensite resulting in a net macroscopic shape change. When the alloy is unloaded the deformed martensite structure remains resulting in the apparent plastic strain. If the alloy is reheated to a

temperature above A_f then the original parent phase structure and orientation is restored via a thermoelastic type of transformation. No matter what the distribution of the martensite variants, there is only one possible orientation in the reverted parent structure. When the alloy is cooled back down to below M_f the twinned martensite structure is restored. It should be noted that the transformation between parent phase and self-accommodating martensite results in no macroscopic shape change. Thus a one-way shape memory is achieved.

Figure 2-3 can also explain the origin of the superelastic effect. In this case, the alloy is deformed at a temperature above A_f and the martensite transformation is entirely stress-induced. The symmetrical parent phase is changed into the lower symmetry, deformed martensite phase directly. Upon unloading, the decreasing stress and surrounding elasticity of the matrix results in the martensite plates shrinking back and the original parent phase structure being restored. The driving force for phase transformation in shape memory alloys is the chemical free energy between the phases. When the difference in chemical free energies is enough to overcome the energy to nucleate the other phase, transformation will start and continue as the energy for growth is supplied by further increase in chemical energy difference.

Ordinary metals cannot reverse the deformation once deformation occurs by dislocation motion and atomic planes sliding over one another, taking on a new crystal position and resulting in permanent change of the crystalline order. Unlike regular metals, SMAs deform by detwinning which changes the tilt orientation of twins and does not cause any dislocation movement. Detwinning allows the martensite phase to absorb dislocations to a given extent. Shape recovery only occurs after detwinning, but not after a deformation process involving slip [2.21].

2.2.3 Macroscopic aspects of SMAs

It have been explained that the SME is caused by the temperature-stress-phase relationship at the atomistic scale, however, for the purposes of design we are more interested in the macroscopic behavior of the material. Therefore it is necessary to characterize the performance of SMAs by analyzing their stress-strain-temperature relationship. The stress, strain and temperature of SMAs have a complex interdependent relationship. This differs from most metallic materials for which it is assumed that stress and strain have linear elasticity.

The elastic modulus is a measure of the stiffness of a material, with stiffer materials having a higher modulus. However, this relationship is insufficient to describe the macroscopic behavior of SMAs which are non-linear. Therefore, the Young's modulus of shape memory alloys becomes difficult to define especially between the M_s and the A_s transformation temperatures. At these temperatures, the alloys exhibit nonlinear elasticity, and the modulus is both temperature and strain-dependent [2.22]. This inherent nonlinearity is due to differences in the physical properties of austenite and martensite. The modulus is dependent on the relative phase fraction of martensite and austenite present in the material. Therefore, the modulus is dependent on temperature and stress and the above equation is no longer valid.

Figure 2-4 illustrates the mechanical behavior of a NiTi alloy as a function of temperature. In order to relate the behavior of the alloy which occurs on the macro level with the phase transformations that occur on the atomistic level, the crystal structure of the alloy is shown in the figure at the various stress-strain-temperature levels. In this Figure the specimen is first subjected to a displacement-controlled load/unload cycle at a relatively low temperature (0→2 in the Figure), leaving a 5% seemingly plastic strain. The material starts in a twinned martensite (M) state and becomes detwinned upon loading. The specimen is then subjected to a temperature increase while holding the load at a small positive value (2→5). The shape memory effect is seen as the strain is recovered between points 3 and 4 when the material transforms to austenite (A). The temperature is then held at a relatively high value and the specimen is again subjected to a load/unload cycle under displacement control (5→10). The material undergoes an increase in strain from about 1% to 7% at constant load (6→7) during stretching which is reversed at a lower constant load (8→9) during subsequent unloading (pseudoelastic behavior). In this case the material transforms from austenite to detwinned martensite during loading and then back to austenite during unloading [2.23].

One of many mechanical properties that change during the phase transformation is the yield strength. The martensitic structure deforms by moving twin boundaries. These twin boundaries are quite mobile. Martensite therefore has low yield strength. Austenite, on the other hand, deforms by dislocation generation and movement. Only a certain amount of martensite can deform based on this twin movement process and once this limit is exceeded, the material will again deform elastically and eventually yield the second time by an irreversible process (movement of dislocations).

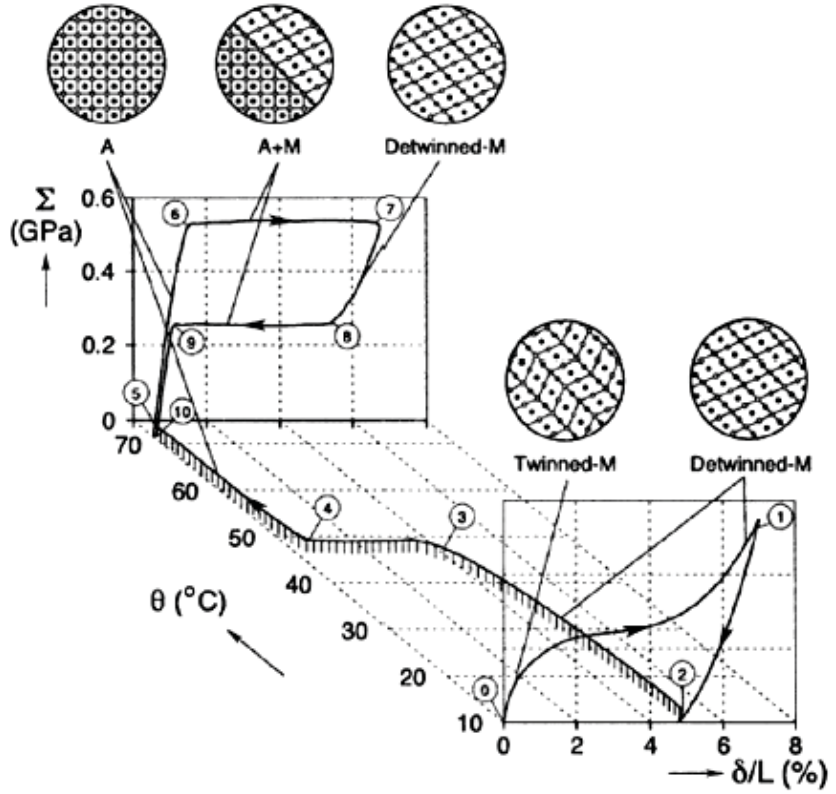

Fig. 2-4: Stress (Σ) - strain (δ/L) - temperature (θ) relationship in SMA characteristic curve: shape memory effect 0 → 4; pseudoelastic response 5 → 10 [2.23].

Figure 2-5 again demonstrates the schematic of stress-strain response of a shape memory alloy. In this Figure, the plateau refers to the thermal hysteresis, which means that both martensite and austenite are controlled by the frictional stress of the twin boundaries. It is the yield strength ratio between the Martensite and Austenite that controls the ratio of resistances to reversible and irreversible deformations (twin movement to slip). In shape memory alloys, it is important to have this ratio as high as possible in order to recover the most amount of the deformation [2.12].

There are three possible deformation mechanisms which are explained below and represented in the Figure. 1st Case: If the material is in the austenitic phase, in Stage I, elastic deformation of austenite occurs, in Stage II, stress-induced martensite forms and in Stage III, slip deformation occurs. 2nd Case: If the material is in the martensitic phase, in Stage I, elastic deformation of martensite occurs, in Stage II, detwinning of martensite proceeds with the growing of some favored variants at the expense of others, in Stage III, slip deformation of martensite occurs. 3rd Case: If the initial material is a mixture of austenite and martensite phases, a mixture of the 1st and 2nd mechanisms take place. Upon unloading, the martensite phase unloads elastically in all mechanisms and pseudoelastic strain would follow the elastic strain (transformation from martensite to austenite) in Case I and III. Further strain can be recovered by heating above A_f, and this behavior is called shape memory effect. The remaining permanent strain is inelastic strain as a result of dislocations formed during loading. The recoverable strain decreases with increased plastic deformation which mainly corresponds to the second plateau region in NiTi. This is because of the fact that slip formation inhibits reverse transformation due to the relaxation of stored elastic energy [2.24].

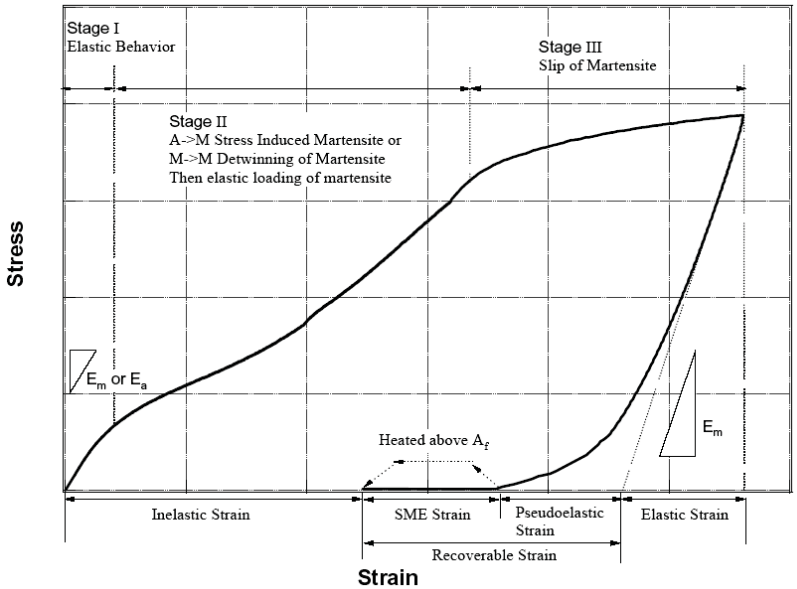

Figure 2-5: Schematic stress-strain behavior of shape memory alloys [2.12].

Additional insights can be obtained from the stress-strain curves shown in Figure 2-6. When the material is in the purely martensitic phase, the yield stress to induce martensite detwinning and produce appreciable strains is quite small. If loading were continued, the martensite would

eventually become completely detwinned and would deform elastically until plastic slip is induced. Obviously, the amount of reversible strain is limited by the onset of plastic slip in the martensitic phase. Rather complex behavior is involved at intermediate temperatures Mf<T<Af depending upon the state of the alloy. The stress required to yield the material in the austenitic phase is much higher than that for martensite. At temperatures in the vicinity of Af , yielding is due to the production of SIM. The stress required to induce SIM continues to increase with increasing temperature above Af until a critical temperature is reached, at which point plastic slip will be induced in lieu of SIM [2.25].

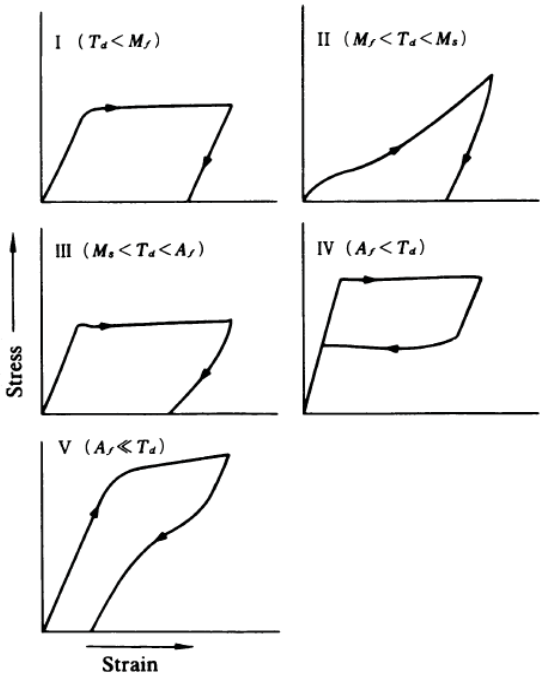

Fig. 2-6: Stress-strain curves for a shape memory alloy at various temperatures [2.25].

2.2.4 Hysteresis curves

The physical properties of austenite and martensite are different. Therefore as the phase transformation progresses and the transformation point is passed, a variety of property changes will occur. Any of these property changes can be used to follow the progression of the phase transformation. Temperature plays the key role and for any given SMA, as mentioned earlier, there are four significant temperatures that characterize the transformation from martensite to austenite and vice versa. Transformation temperatures (M_s, M_f, A_s, A_f) can be determined by measuring some physical properties as a function of temperature. There is an inherent hysteresis associated with this phase transformation; stated alternatively, the transformation temperatures differ upon heating and cooling during the phase transformation.

Hysteresis is generally defined as the difference between the temperatures at which the material is 50 % transformed to austenite upon heating and 50 % transformed to martensite upon cooling. The overall hysteresis between forward and reverse transformation in shape memory alloys is small, typically between 10 and 50 °C. This hysteresis loop is due to the

behavior of the free energies during the phase transformations and can be attributed to friction associated with the movement of twin-related martensite boundaries [2.20, 2.26].

Figure 2-7 demonstrates the relationship between temperature and phase in the absence of an applied stress. As can been seen, the temperature phase relationship exhibits a hysteretic behavior. The no-load transformation temperatures for a particular alloy vary over a range of temperatures depending upon the material constituents and processing history. For example in NiTi-based SMAs the temperature range for the martensite start temperature is from approximately -150 °C to 150 °C and is strongly dependent on the composition. In order to accurately characterize the SMA behavior it is necessary to account for the effect of applied stress on the transformation temperature. An increase in applied stress shifts the transformation temperatures higher, thus shifting the entire hysteresis curves as shown in Figure 2-8 [2.27].

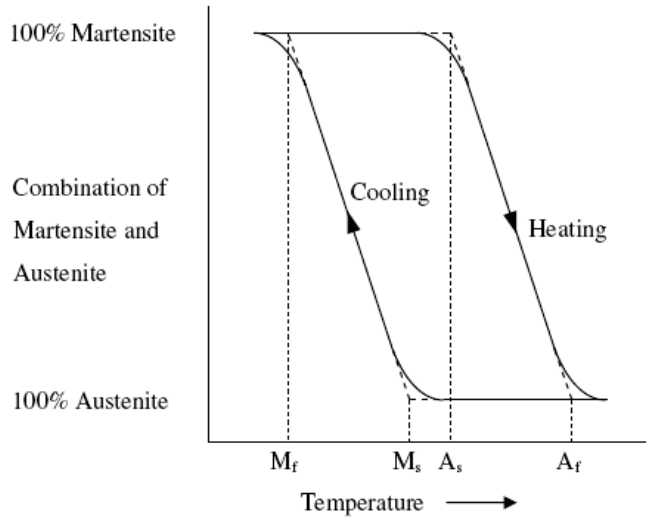

Fig. 2-7: Temperature-phase relationship and hysteresis curve for a thermoelastic martensitic transformation [2.27].

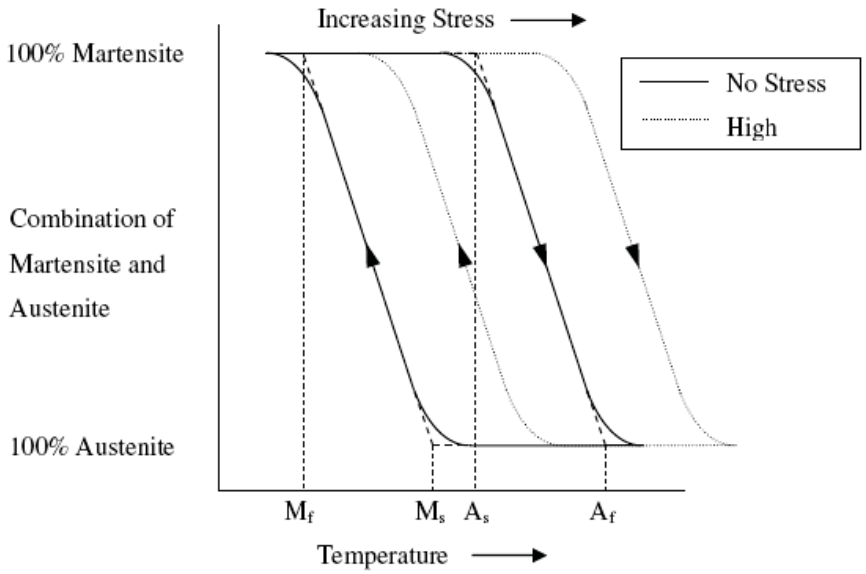

Fig. 2-8: Stress effect on transformation temperatures and hysteresis [2.27].

2.2.5 Martensitic transformations

Shape memory results from a particular type of phase transformation that produces the structure known as martensite. Martensite results from the solid state process of displacive transformation. Solid state transformations are usually of two types: diffusional and displacive. Diffusional transformations are those in which the new phase can only be formed by moving atoms randomly over relatively long distances. This requires long range diffusion as the new phase that is formed is of a different chemical composition than the matrix from which it is formed. Since this type of a transformation requires atomic migration, the diffusional transformation is dependent upon both time and temperature [2.28].

Displacive transformations, on the other hand, do not require large atomic migration; in this case the atoms are rearranged into a new, more stable atomic structure in a cooperative fashion. This rearranging is done without changing the chemical nature of the matrix. Since no atomic migration is involved, these displacive transformations progress in a time independent fashion, with the motion of the surface between the two phases being limited by only the speed of sound. These transformations are also referred to as athermal transformations. Martensitic transformations are of the displacive type. Martensite forms through a highly ordered crystallographic shear transformation and upon cooling from a higher temperature phase called the parent phase or austenite. The martensite phase in SMA is not the typical martensite phase found in steel. The martensite phase here is a relatively ductile and soft phase, but this term was used to refer to steels [2.28]. In steels this parent phase is known as austenite and this is the term also often used to describe the parent phase in shape memory alloys although, technically speaking, this is incorrect.

When the SMA is above the austenite transition temperature it has a crystalline structure that takes on a high elastic modulus and this is due to the symmetry in the crystalline structure, referred to as the parent phase. But when the SMA is below the Martensite transformation temperature a martensitic crystalline structure will be more thermodynamically stable. Typically the parent phase is a high temperature cubic phase and the martensite is a lower temperature and lower symmetry phase. The parent and martensite phases are shown in Figure 2-9.

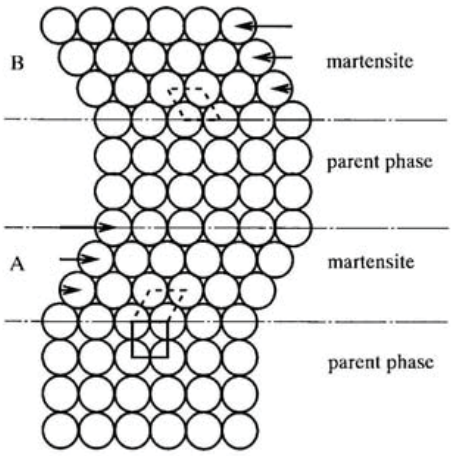

Fig. 2-9: Parent and martensitic phases [2.26].

Although in his early work Cohen [2.29] describes the formation of martensite as being free from nucleation and growth, it is now accepted that the fundamental characteristics of martensite transformations are in fact consistent with the nucleation-growth concept. The martensite is normally metastable and it will only form through very rapid cooling. In fact the rate of growth is so high in these reactions that the volume change associated with the reaction is controlled almost entirely by the nucleation rate. In many martensitic transformations however, the low temperature phase is itself an equilibrium phase rather than a metastable one. In these cases the phase transformation occurs by the fast growth martensitic mode even with very slow cooling rates. The transformations in these systems occur martensitically but there is no need for a rapid quench to secure the fast growth mode as there is in steel. This is the case with shape memory alloys and many pure elements.

Martensitic transformations are first order transformations. This means that heat is liberated when Martensite is formed. It proceeds by nucleation and growth, and a large strain arises around the martensite when it is formed in the parent phase. There is a hysteresis associated with the transformation and there is a temperature range over which Martensite and Austenite coexist. Therefore it is possible to state that Martensite is formed upon cooling with the volume fraction of Martensite increasing as the temperature is reduced. It is important to note that the volume fraction is independent of time and is dependent solely on temperature.

In a crystallographic context, the phase transformation from Austenite to Martensite is thought of to occur in two parts: the *Bain strain* and the *lattice invariant shear (LIS)* or lattice accommodation. The Bain strain, referred to as lattice deformation, consists of all atomic movements that are needed to form the new structure (i.e., phase) from the old (Figure 2-10a). It is important to note that the interface progresses through each atomic layer and each atom is required to move by only a very small amount. The movements that are required to produce the new structure are called Bain strain. In real materials, Bain strain generally consists of several atomic shuffles in addition to the movement illustrated in Figure 2-10b. The Bain strain is attributed to the shape change inherent in martensite transformation. The strain, which must be reduced in order for nucleation and growth to occur, is relieved in the lattice invariant shear.

It is called LIS because the structure of the martensite will not be changed. Martensitic transformation is defined simply as a lattice deformation involving shearing deformation and resulting cooperative atomic movement. There is a one to one correspondence called *lattice correspondence* between the lattice points of parent and martensitic phases. In order to reduce the strain during nucleation and growth two types of LIS mechanisms could take place; *dislocation slip* (Figure 2-10c) or *twinning* (Fig. 2-10d) [2.28]. In both cases, each individual cell, or parallelogram, has the new martensitic structure, but the overall shape is that of the original austenite. The kind of alloy elements determines whether slip, which is a permanent process and common accommodation mechanism in many martensites, or twinning will occur. But typically twinning is the mechanism found in SMAs, including the NiTi-based alloys. The twinning process of accommodation plays a key role in the shape memory effect and should be reviewed in more detail. Some key properties of twin boundaries are that they are of a very low energy and they are quite mobile; thus the relative stability of a martensitic phase is not strongly affected by the number or location of these boundaries [2.27]. By comparing edges of the

structures shown in the Figures 2-10c and 2-10d, one can see that slip accommodation requires that atomic bonds be broken, while all bonds remain intact in the twinned structure.

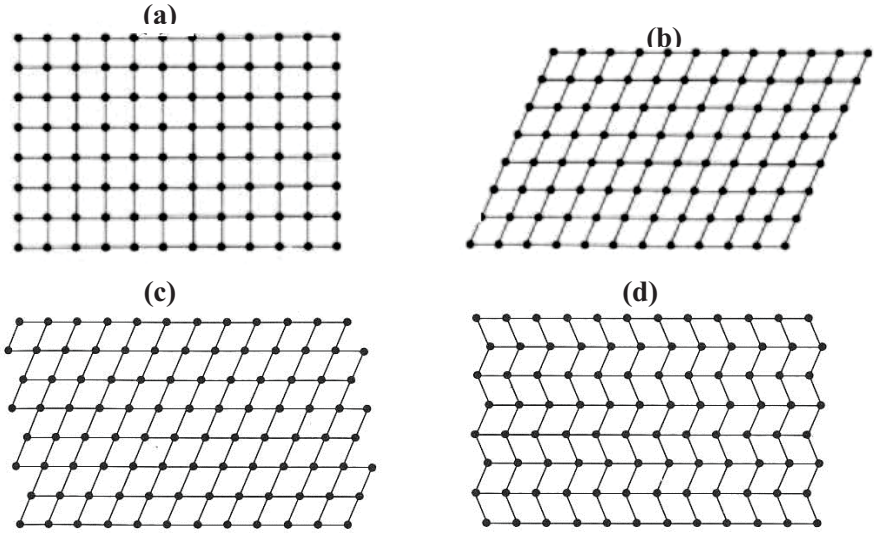

Fig. 2-10: Transformation from austenite to martensite in two-dimensions; (a) being completely austenitic, (b) Bain strain, (c) LIS, accommodation by slip and (d) LIS, accommodation by twinning [2.25].

While the twinning of martensite relieves the strain induced by the martensite transformation, there is still the issue of the shear that is created. To alleviate this, the different bands of martensite will self-accommodate. This is where many different favorable two or four habit plane variants combine in such a way that there is no bulk strain. This can be seen in Figure 2-11, below. The habit plane is a specific plane between the parent and martensitic phase along which the shear occurs during transformation. Since there is no strain and rotation in the habit plane through out the entire transformation, this type of shape deformation is called lattice invariant shear strain. Martensites with different habit planes are called variants. When the Martensite transformation starts during cooling in order to minimize the strain a second step takes place in addition to LIS which is *self-accommodation* of martensite variants.

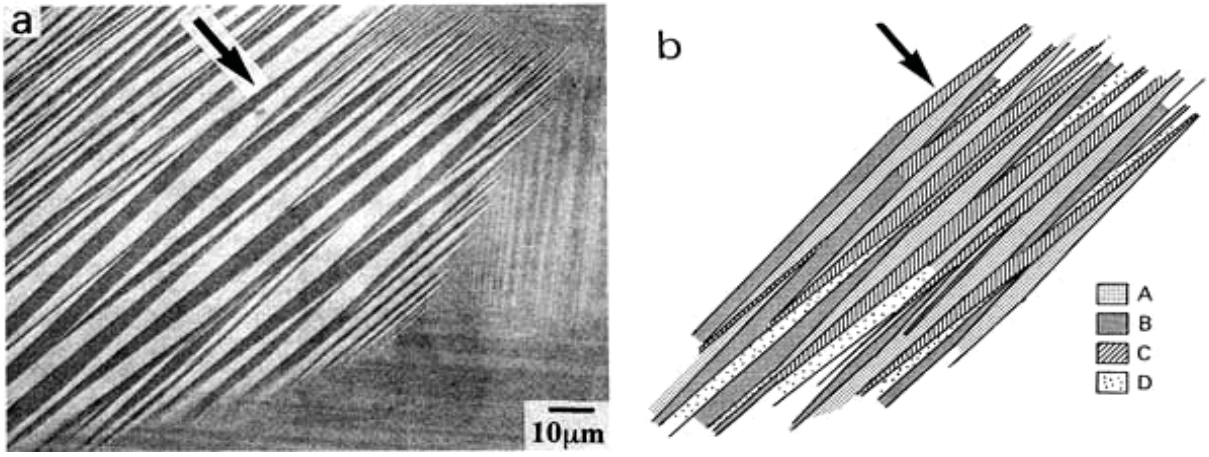

Fig. 2-11: Self-accommodation of martensite; (a) a typical SEM micrograph; (b) four habit plane variants (A, B, C, D) [2.27].

Figure 2-12 schematically represents the crystal transformations associated with the SME. Figure 2-12a is the parent phase of the material when above A_f. Figure 2-12b is self-accommodated martensite below M_f and as a result, little macroscopic strain is generated. Upon heating and cooling, and in the absence of external forces, the crystal structures will cycle between Figure 2-12a and Figure 2-12b, respectively. The positions of the martensite interfaces change under the influence of stress, creating a balance of variants whose shears best accommodate the direction of applied strain (Figure 2-12c) and if the stress is high enough, it will become a single variant of martensite under stress. This process of condensation of many twin variants into a single favored variant is called detwinning. When the specimen is heated above A_f, the reverse transformation occurs, and the original shape is regained as in Figure 2-12a. The example above assumes that the deformation proceeds solely by the movement of twin boundaries and that the transformation is crystallographically reversible. If any of these conditions are not satisfied the complete SME is not obtained [2.17, 2.28-2.30].

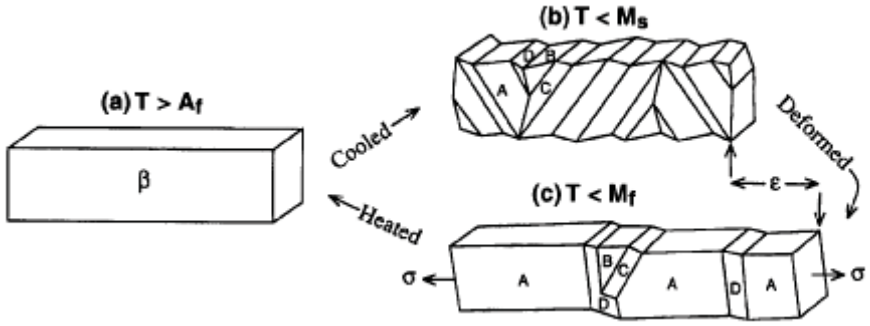

Fig. 2-12: Mechanism of SME; (a) original parent phase of a crystal, (b) self-accommodated martensite, (c) variant A becomes dominant when stress is applied [2.28].

The detwinned martensite could be found in two different alignments based on the level of stress applied to the alloy. Based on the stress direction, the martensite could be detwinned either to the left or to the right direction. For example, under uniaxial loading conditions, three different phases can be observed for a shape memory alloy in Figure 2-13, the austenite phase A and two martensitic twin variants M±. From crystallographic observations it is known that a macroscopic body under uniaxial loading forms a layered structure, each layer being in one of the three above phases. Motivated by this observation, the SMA shape transformation process can be described as in Figure 2-14. The far left is a martensite phase at low temperature with M+ and M-twined next to each layer. When a uniaxial force is applied, the twined structure will change to a single direction, either M+ or M- in Figure 2-13. In the heating process, Nitinol material can generate high force and strain recovery. In the cooling process, A is simply turned to M+ and M- and does not produce any force. Once martensitic crystals have nucleated, they grow at a rate proportional to the cooling rate or the rate of increase of the applied stress. Similarly, these crystals shrink upon heating and it has been found that in thermally induced transformations, the martensitic crystals that were formed first are the last to undergo the reverse transformation [2.31].

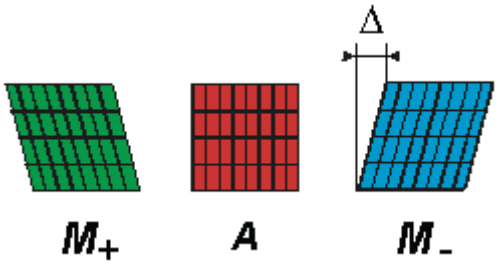

Fig. 2-13: Martensite and Austenite [2.32].

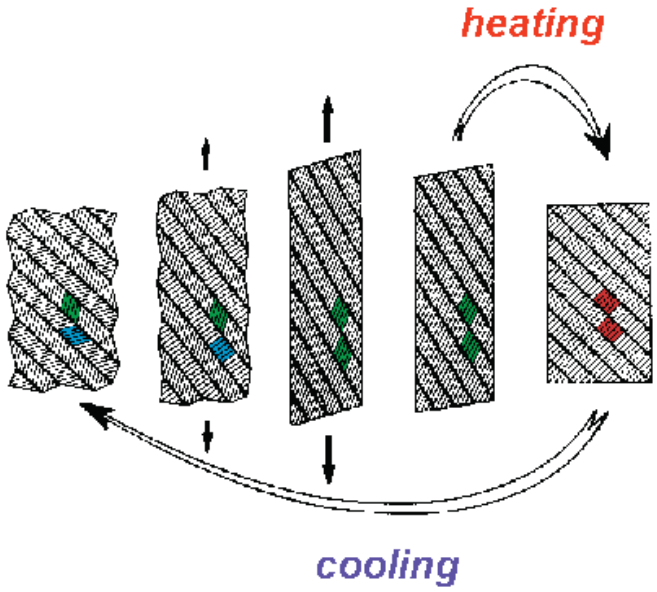

Fig. 2-14: The shape transformation process [2.32].

Martensite transformations can be also classified in two categories: thermoelastic and non-thermoelastic. The thermoelastic nature means that a decrease in the SMAs temperature equivalently acts as an increase in stress due to growth of martensitic plates causing an increase in internal stresses [2.15]. What distinguishes shape memory alloys from conventional materials is none other than their ability to form thermoelastic martensite. For thermoelastic martensite transformations, the transformation temperature hysteresis is small, the interface between parent and martensite is mobile and the transformation is crystallographically reversible due to a much smaller driving force. For non-thermoelastic martensite transformations, the transformation temperature hysteresis is large, the interface between the martensite and parent phase is immobile, and once the martensite grows to some critical size, the reverse transformation takes place by renucleation of parent phase.

In non-thermoelastic transformations lowering the temperature below M_s causes the martensite to grow to its limiting size and upon further cooling, additional transformation only occurs by the nucleation of new plates. Old plates will not grow even at lower temperatures. During thermoelastic transformation, again the plate grows to a limiting size for a specific temperature below M_s. Further cooling however, causes additional transformation by the growth of old plates as well as by the nucleation of new plates. The continued growth of thermoelastic

martensite occurs in a jerky motion. The growth rate remains high but occurs over very small distances as more free energy becomes available with the decreasing temperature. In thermoelastic transformations growth stops when the free energy available to drive the reaction is counter balanced by the strain energy generated in the parent matrix. Because of the very small volume change, plastic flow does not occur and a balance is achieved between the elastic strain energy made available by the lower free energy state of the martensite phase [2.33].

It is obvious that greater free energy is required for non-thermoelastic transformations as ΔT is much larger. This is probably a result of the larger shear that is required to form these martensites. Most of the thermoelastic shape memory alloys are intermetallic alloys since they have ordered structure, which means that lattice sides are occupied by particular species of atoms. Since martensite transformation is a diffusionless process the product martensite is also ordered and the process is crystallographically reversible. Also ordering promotes a higher flow stress in the parent phase which prevents the damage of martensite/parent interphase during growth of martensite [2.12].

2.2.6 Commercial Shape Memory Alloys

The basis of shape memory behavior is now accepted to be a thermoelastic martensitic transformation. Compared with other metallic materials showing a martensitic transformation, the hysteresis between the forward and reverse martensitic transformation temperature in SMAs is rather small. For instance, the martensitic transformation temperature hysteresis in an AuCd SMA is around 15 °C, whereas the hysteresis in a FeNi alloy is 420 °C [2.34], and in normal steels around 200 °C. Many alloys have been found to show this small temperature hysteresis and thus show SME [2.35].

The thermoelastic alloys that display the memory effect all have an ordered structure. An ordered structure results in good reversibility and avoidance of slip. Ordered alloys can only have one transformation pathway for retransformation into the parent phase without destroying the original ordered structure. The wrong path of transformation actually increases the energy of the system and changes the structure of the alloy. Reversibility is therefore guaranteed in an ordered alloy. Furthermore, some certain disordered alloys do demonstrate a memory effect, i.e. Fe based alloys such as FeMnSi and FeMnSiCoNi. The actual mechanism is different from that described and will not be discussed further in this dissertation. Over the last years, a large number of binary and ternary ordered alloys have been found that demonstrate the shape memory effect. These include AgCd, AuCd, CuAlNi, CuAuZn, CuSn, CuZn, CuZnAl, CuZnGa, CuZnSi, CuSnSn, InTl, NiAl, MnCu and NiTi-based alloys. Although a relatively wide variety of alloys are known to exhibit the shape memory effect, only those that can recover substantial amounts of strain or that generate significant force upon changing shape have been exploited for commercial purposes. Therefore, the only ones that have met with any commercial success are: CuZnAl, CuAlNi and NiTi-based alloys. However, NiTi-based alloys are by far the most widely used [2.36].

The response behavior of these alloys can be altered and controlled through particular processing and alloying procedures. Varying composition allows control of many properties such as actuation temperatures (phase transformation temperatures), strength and work output during transformation. Cold work and heat treatment can also be employed to control these properties. The properties of the two alloy systems are quite different. NiTi alloys have higher recovery strains and stresses, longer cyclic life, tend to be more thermally stable, have excellent corrosion resistance, susceptibility to stress-corrosion cracking and have much better ductility [2.37] than Cu-based alloys [2.34, 2.38, 2.39]. Therefore as shown in Table 2-1, the performance characteristics of NiTi SMAs are superior to those of Cu-based alloys. However, the copper-base alloys are much less expensive, can be melted and extruded in air with ease. If high performance is not required and cost considerations are important, for instance, in safety devices, temperatures fuses and fire alarms, the use of Cu-based SMAs can be recommended.

Another advantage these alloys have over the copper based systems is their comparatively poor electrical conductivity. This presents the interesting possibility of using the alloys in solid state actuator applications where the alloy is heated by electrical current. For this reason the recent growth of research and commercial interest in smart structures incorporating solid state actuators, has also resulted in concurrent research into NiTi alloys. Additionally, despite its nickel content, NiTi is a biocompatible material exhibiting good corrosion properties and low cytotoxicity, thereby lending its actuation capabilities for applications within the medical field [2.40]. By appropriate alloying and processing the NiTi alloys can be tuned to have Ms temperatures of –200 °C to +110 °C again, presenting many interesting medical opportunities.

In NiTi alloys, the addition of a third element is effective in improving transformation behavior, shape memory characteristics and mechanical properties. For instance, when Ni is partially replaced by Co or Fe [2.41] or Ti is replaced by V, Cr or Mn [2.42], the transformation temperatures are shifted significantly to lower temperatures. The addition of Zr, Hf [2.43-2.45], Pd, Pt or Au [2.46-2.48] can raise transformation temperatures. Substitution of Ni by Cu has the unique effect of reducing the composition sensitivity of the martensitic transformation start temperature [2.49, 2.50] to narrow the hysteresis, to reduce the flow stress level in the martensite state, to suppress the R-phase transformation and to prevent X-phase (Ti_3Ni_4) precipitation.

Commercial copper-base shape memory alloys are available in ternary CuZnAl and CuAlNi alloys, or in their quaternary modifications containing manganese. Elements such as boron, cerium, cobalt, iron, titanium, vanadium and zirconium are also added for grain refinement. The thermal stability of copper-base alloys is ultimately limited by the decomposition kinetics. For this reason, prolonged exposure of CuZnAl and CuAlNi alloys at temperatures above 150 °C and 200 °C, respectively, should be avoided. Aging at lower temperature may also shift the transformation temperatures. In the case of aging the beta phase, the results from the change is in long-range order [2.39]. When aged in the martensitic state, the alloys exhibit an aging induced martensite stabilization effect [2.38]. Table 2.2 presents a summary of the advantages and disadvantages of the different SMAs.

Table 2-1: Properties of typical shape memory alloys [2.33, 2.51].

Properties		**NiTi**	**CuZnAl**	**CuAlNi**
Specific Heat Capacity (J/Kg°C)		450-620	390-400	373-574
Thermal conductivity (20 °C) (W/mK)		8.6-18	84-120	30-75
Density (Kg/m^3)		6400-6500	7540-8000	7100-7200
Latent heat or Enthalpy (J/Kg)		19000-32000	7000-9000	7000-9000
Electrical resistivity (10^6Ωm)	martensite	0.5-0.6	0.12	0.14
	parent phase	0.82-1.1	0.07	0.1
Thermal expansion coefficient (10^{-6}/K)		6.6-11	17	17
Melting Point (°C)		1250-1300	950-1000	1000-1050
Maximum overheating temperature (°C)		400	150	300
Normal working stress (MPa)		100-130	40	70
Normal number of thermal cycles		$>10^5$	$>10^4$	$>5\times10^3$
Fatigue strength (N=10^6)(MPa)		350	270	350
Transformation strain max.	N = 1	6-8%	4-6%	5-6%
	N < 10^2	6-8%	4%	4%
	N < 10^5	2-4%	-	-
	N < 10^7	0.5%	-	-
Young's Modulus (GPa)	martensite	28-41	70	70
	parent phase	70-97	70-100	80-100
Recovery stress max (MPa)		500-900	400-700	300-600
One-way memory max.		8%	5%	6%
Two-way memory max.		3-5%	1%	1.2%
Superelastic strain		8-10%	2%	2%
Transformation temperature (°C)		-200 to 100	-200 to 150	-200 to 200
Hysteresis (°C)		2-50	5-20	20-40
Damping capacity (SDC%)		15-20	30-85	10-20
Grain size (μm)		1-100	50-150	25-100

Table 2-2: Advantages and disadvantages of different SMAs [2.52]

Alloy Type	Advantages	Disadvantages
Ni-based		
NiTi (Nitinol)	Large recoverable strain capabilities, corrosion resistance, biocompatibility, large hysteresis.	High manufacturing cost, difficult to manufacture and machine.
NiTiCu	Increased workability, stable transformation temperatures, reduced ageing effect, narrower stress hysteresis (good for recentering).	Decreased Young's modulus (E).
NiTiAl	Prevents growth of precipitants during ageing, reduced permanent deformation strains.	Shape memory effect decreases gradually in over-aged specimens.
NiTiCoV	Superelastic at room temperature, good workability, lower transformation temperature.	—
NiTiZr	Improved mechanical and shape memory properties with Zr content between 1 – 2 at %.	Too brittle for hot-forging and hot-rolling processing.
NiTiNb	Increased peak to peak transformation hysteresis.	—
NiTiFe	Increased shape memory strain, recovery rate, and slip strength. Reduced transformation temperature.	Reduced ductility.
Cu-based		
CuZnAl	Low cost, can be fabricated using conventional metallurgical methods, good rigidity, high damping capacity.	Maximum recoverable strain up to approximately 5%, martensite stabilization possible, difficult to cold work if it has high Al content.
CuAlNi	Wide range of transformation temperatures, stability at higher temperatures, high damping capacity, low cost.	Difficult to process, can only be hot-worked, brittle.

2.2.6.1 Low-temperature shape memory alloys

A low temperature SMA is defined as a material with a transformation temperature below 100 °C. Although many SMA materials fit into this category (AgCd, CuSn and InTi), NiTi and some copper based alloys are the only low temperature shape memory alloys to experience commercial success [2.51]. Two commercially available copper-base shape memory alloys are ternary CuZnAl and CuAlNi. As with other SMAs, the martensitic transformation temperatures can be adjusted by varying chemical composition. However, unlike the more common NiTi, copper-base shape memory alloys are metastable in nature [2.53]. Solution heat treatment in the parent Beta-phase region and subsequent controlled cooling are necessary to retain the Beta-phase for shape memory effects. The as-quenched transformation temperature is usually unstable. Post-quench aging at temperatures above the normal A_f temperature is generally needed to establish stable transformation temperatures. Prolonged exposure of CuZnAl and CuAlNi alloys at temperatures above 150 °C or 200 °C respectively causes decomposition of chemical phases.

Recent focus has been placed on CuZnAl due to its low cost of production, ease of fabrication, and excellent heat and electrical conductivities. Like NiTi, CuZnAl can be trained to produce two-way shape memory behavior. However, copper based alloys have lower strain recovery (approximately 5%), and are less corrosive resistant than NiTi. Additionally, the need for extensive thermal processing and instability when exposed to high temperatures for extended periods of time makes NiTi better suited for many applications [2.51].

Since its discovery in 1963, a considerable amount of research has been focused on the characterization and commercialization of NiTi and its alloys. In recent years, NiTi has experienced commercial success due to its beneficial material characteristics such as:

- Large strain memory (up to 8%)
- Excellent corrosion resistance
- Relative thermal stability
- Good fatigue properties
- Biocompatibility

2.2.6.1.1 NiTi-based shape memory alloys

The NiTi alloys are the most important practical shape memory alloys (SMA) with excellent mechanical properties such as high strength and ductility. To reduce the cost of NiTi and improve its properties, a third metal is often added to the binary alloy. Some of these metals include copper, aluminum, cobalt, vanadium, zirconium, niobium, chromium, and iron. The alloying of NiTi with heavy elements is an alternative solution to improve inherent radiopacity (appearance in radiographic imaging) of NiTi. Possible ternary elements include iridium, platinum, gold, rhenium, tungsten, palladium, rhodium, tantalum, silver, ruthenium, or hafnium. This addition of alloying elements provides a way to control transformation temperatures, control the hysteresis width, and affect the martensitic and austenitic strength. [2.54]

Addition of third elements opens even more possibilities for adapting binary NiTi alloys toward more specific needs of applications. Adding a third element implies a relative replacement of Ni and /or Ti. Therefore it must be always very well indicated which atom Ni or Ti or both is replaced by the third element. Alloying third elements will influence not only the transformation temperatures but will also have an effect on hysteresis, strength, ductility, shape memory characteristics and also on the B2→R→B19' sequence. More application oriented, one can distinguish four purposes to add third elements [2.55, 2.56]:

- to decrease (Cu) or increase (Nb) the hysteresis,
- to lower the transformation temperatures (Fe, Cr, Co, Al),
- to increase the transformation temperatures (Hf, Zr, Pd, Pt, Au),
- to strengthen the matrix (Mo, W, O, C).

Typically, addition of Fe, Al, Cr, Co, Cu, Pd, Pt, Au, Mo and W are as a substitution for Ni, and Nb, Zr and Hf for Ti. Furthermore, the addition of a third or fourth element to NiTi can be a powerful tool for controlling its properties, and can be used to:

- control transformation temperatures,
- increase the stability of Ms with respect to thermal history,
- control the hysteresis width,
- increase austenitic strength,
- reduce or increase the martensitic strength,
- improve corrosion resistance,
- suppress the R-phase.

Substituting Cu for Ni in binary Ni-Ti increases the workability of the alloy, makes a marked increase in the damping capacity of the material and its internal friction, decreases the Young's modulus (E), lowers the martensite phase yield strength, reduces the aging effect, narrows the stress hysteresis and temperature hysteresis, makes lower flow stress level in the martensite state and lower sensitivity of the transformation temperatures to small variations in the Ni content, stabilizes the transformation temperature, and no large-scale shift in M_s is observed [2.57, 2.58]. Because of the aforementioned advantages, ribbons of NiTiCu SMAs would be a good candidate for applications that require short response time at thermal cycle, such as actuators and sensors. The smaller temperature hysteresis provides faster actuation times or cycle rates, it can also make the actuator more suitable for thermal actuation. Also they suppress resistively anomalies, thus allowing for better actuator control [2.59]. Most important, they improve geometrical and thermal actuator stability, because of a better crystallographic compatibility between the parent and the product phase. There is a good correlation between the width of the thermal hysteresis and the intensity of irrecoverable deformation associated with thermomechanical cycling.

In order to see the relations among the three phases, B2, B19 and B19′ in Ni-Ti-Cu alloys, the martensitic transformations are plotted against the Cu content in Figure 2-15. As shown in the Figure, initially with increasing Cu content, M'_s (for B19 martensite) increases slightly, and the M_s (for B19′ martensite) decreases largely. Therefore, the temperature range over which the B19 martensite is stable becomes wider with increasing Cu content. [2.60]. In the range 5-15

at.% Cu the transformation sequence is B2 (cubic)→ B19(orthorhombic)→ B19'(monoclinic). With increasing Cu content, the transformation start temperature of the B2→B19 does not change, but the second transformation is shifted to lower temperatures, and for Cu content higher than 15 at.% it does not occur even at liquid nitrogen temperature, therefore only the B2→B19 transformation is observed. This is important since the B2→B19 transformation hysteresis is much smaller than that of the B2→B19' occurring in binary Ni-Ti alloys. It is known to be very suitable for actuators because of its large transformation elongation and small hysteresis.

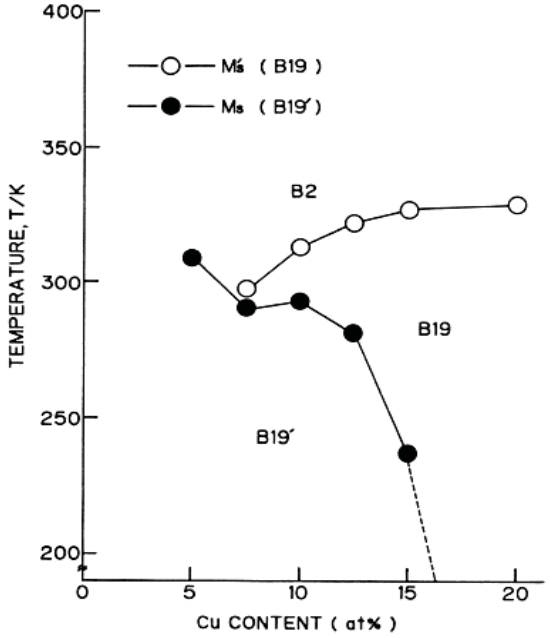

Fig. 2-15: Cu content dependence on the martensitic transformations of Ti-$Ni_{(50-x)}$-Cu_x alloys [2.60].

Figure 2-16 is the equilibrium Ni-Ti-Cu phase diagram at 870 °C [2.61]. It is seen in the diagram that in Ni-Ti-Cu alloys in which Cu is substituted for Ni, the parent phase remains as a single B2 phase up to 30 at.% and these alloys show shape memory effect.

This transformation has been also observed in NiTiPd and NiTiAu alloys, but from these additions Cu is the most attractive from an economic point of view. Transformation hysteresis accompanied by the B2→B19 transformation in NiTiCu alloys decreases with increasing Cu content due to a decrease in lattice deformation. Therefore, NiTiCu alloys with high Cu content are desirable for actuators that operate sensitively according to a temperature change.

However, NiTiCu alloys with Cu content higher than 10 at.% are brittle due to the TiCu phase formed near the grain boundaries, and therefore cannot be deformed into a wire or plate by both hot and cold working, which is necessary for fabricating actuators. In order to overcome the brittleness of the alloys, many metallurgical processing technologies have been examined, including powder metallurgy and rapid solidification [2.62]. The melt-spinning process could be one of the best alternatives for fabricating NiTiCu alloys with high Cu content because it enables ribbons to be obtained directly from the molten metal, and the high solidification rate suppresses the formation of TiCu particles. A summary of the martensitic transitions is reported in Figure 2-17 according to [2.63]. Additionally, in Figure 2-18 the Cu-NiTi section of the

phase diagram is presented according to [2.64] with minor corrections in order to make them coherent with the accepted equilibriums.

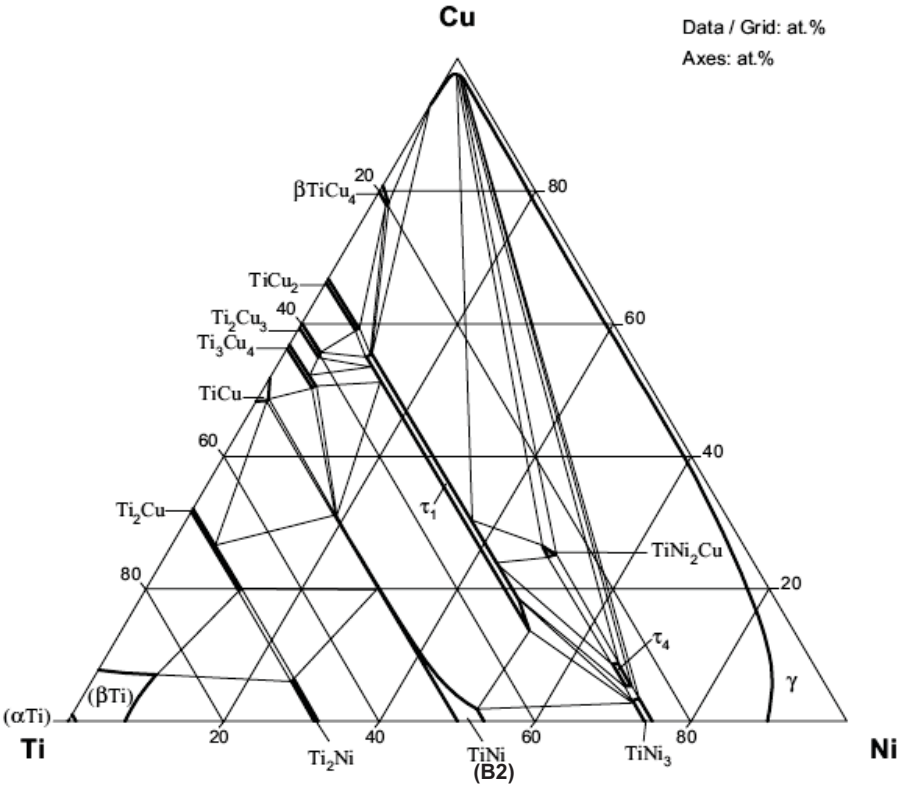

Fig. 2-16: Cu-Ni-Ti. Isothermal section at 870 °C [2.58]

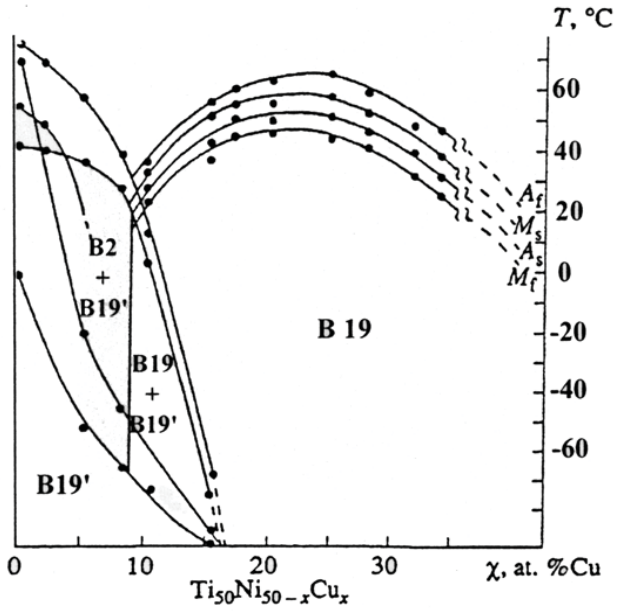

Fig. 2-17: Cu-Ni-Ti Martensitic transformations in the alloys of the pseudobinary NiTi-TiCu section obtained by rapid solidification at 10^5 K.s^{-1} [2.63]

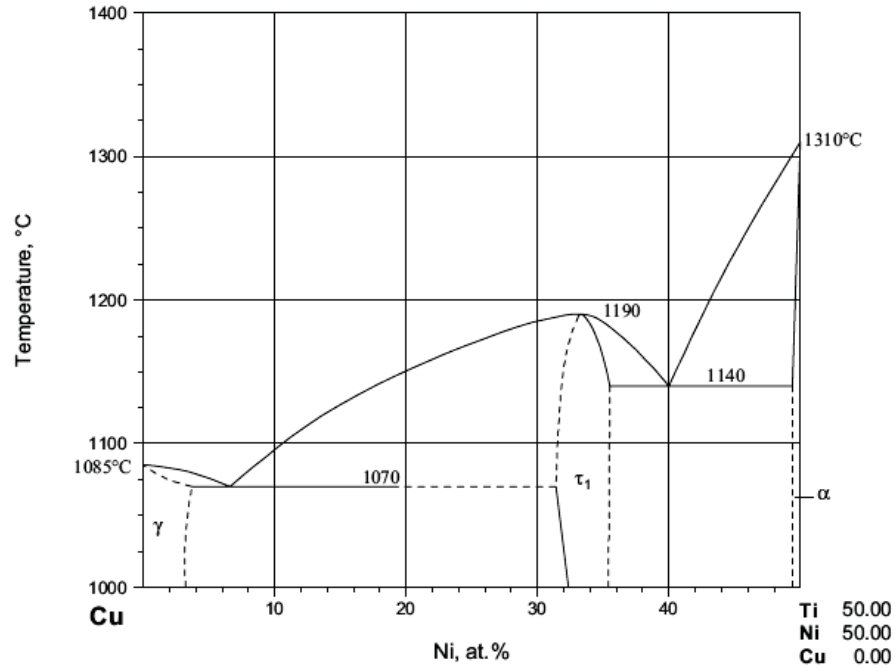

Fig. 2-18: Cu-Ni-Ti. Polythermal section Cu-NiTi [2.64]

NiTi-based ternary alloys with the addition of one of Pd, Pt, Zr, and Hf have been the most studied high temperature SMAs up-to-date. Although the transformation temperatures of NiTiAu are higher than NiTiPd for a given composition, there is not much work performed on this alloy [2.65]. These two alloys have transformation temperatures higher than 450 °C [2.66, 2.67]. The other alloy system which has received little attention like the NiTiAu alloys is NiTiPt since they are very expensive materials.

NiTiHf systems have been investigated due to the relatively low cost of addition and high transformation temperatures. However, the amount of Hf addition is limited since there is no continuous solid solution between NiTi and NiHf. The transformation temperatures of the alloy do not increase much up to 10at% Hf but at concentrations higher than 10 at%, transformation temperatures increase linearly up to 525 °C at 30at%Hf [2.68, 2.69].

Second phases such as $(Ti,Hf)_2Ni$ and $(Ti+Hf)_4Ni_2O_x$ were identified in NiTiHf alloys [2.70, 2.71]. Although the former may be desirable for improving the shape memory properties, the latter is not desirable as it may influence the workability and shape memory properties by premature dislocation slip during martensite variant orientation or stress-induced martensitic transformation. [2.72]. The disadvantages of NiTiHf alloys are the large hysteresis and poor shape memory behavior. It was reported that the hysteresis is of the order of 40-50 °C and sometimes even larger. It was observed that shape recovery is 80% when the Ni50Ti38Hf12 is deformed at room temperature to a strain of 2.5% which is attributed to the high stress for the reorientation of martensite and detwinning but the low critical stress for slip [2.71]. Meng et al. [2.70, 2.73] examined the tensile properties of Ni49Ti36Hf15 at room temperature and above A_f temperature and observed significant strain hardening which means martensite reorientation is not easy. To increase the critical shear stress for slip, Karaman's group [2.74] studied severe plastic deformation of NiTiHf alloys and they observed an increase in the recoverable

transformation strain (recoverable strain) and a decrease in the irrecoverable strain levels under constant stress experiments. They also investigated the thermal cyclic behavior of the Ni49.8Ti42.2Hf8 alloy after severe plastic deformation via equal channel extrusion and found that cyclic stability is improved and thermal hysteresis is decreased.

Zr is added to NiTi alloys at the expense of Ti as well, which has opposite effects to Au and Pt additions for Ni. Mulder et al. [2.75] determined that M_s temperature of NiTiZr alloys increases with a rate of 18 °C per at.%. Addition of Zr up to 30 at.% significantly increases phase transformation temperatures and has similar microstructure and shape memory properties as NiTiHf alloys. It was also observed that the transformation temperatures decrease during thermal cycling which was attributed to the precipitation of the alloy. Basically, NiTiZr alloys are the least potential ones in high temperature shape memory alloys because they exhibit poor ductility and unstable shape memory response.

Alloying element additions of Zr, Hf, Au, Pt, and Pd also can embrittle the alloy [2.76-2.78]. Increased transformation temperature and decreased ductility are undesirable for medical devices taking advantage of the pseudoelastic properties of NiTi. Transformation temperatures of NiTi alloy decrease slightly with increasing Pt or Pd additions; for instance, M_s is about 26 °C lower in NiTi alloy with 10 at.% Pd. [2.79]. In contrast, above 10%, the transformation temperatures increase linearly up to 1040 °C with Pt addition and reach 510-563 °C for Ti50Pd50 binary alloy [2.79, 2.80]. The slight decrease in transformation temperatures with Pt addition is desirable from the standpoint of maintaining pseudoelasticity at body temperature. Moreover, the Pt and Pd doped alloys exhibited reasonable strain recovery when deformed below M_f and heated to room temperature, with little dependence on the percentage of alloying element [2.37, 2.81].

Otsuka et al. [2.82] reported that the shape memory behavior of NiTiPd alloys is fairly good at room temperature however becomes poor with increasing temperature due to the decrease in critical shear stress for slip. Lindquist and Wayman [2.79] reported 6% unconstrained shape recovery. Otsuka and his co-workers [2.83] studied the shape memory effect in Ti50Pd50 alloys and reported poor shape memory behavior which can be attributed to the low critical stress for slip such that high density of slip is introduced in addition to twinning in martensite. NiTi alloys with 40-50at%Pd show 0.5% shape recovery when loaded in tension.

As explained above NiTiPd alloys also suffer from low critical stress for slip especially at high temperatures which causes plastic deformation during phase transformation and thus, poor shape memory behavior. Thus, to improve the shape memory response of the NiTiPd alloys different approaches have been used such as alloying with a fourth element, precipitation hardening or thermomechanical treatments [2.65].

2.2.6.1.2 Cu-based shape memory alloys

The most common copper based SMAs include CuZnAl, CuAlNi and CuAlMn. When compared to NiTi, the main advantage of these alloys is that they are relatively inexpensive, and that they can be fabricated using conventional metallurgical methods [2.84].

Copper based SMAs are suitable for use in actuators, safety valves, and pipe couplings. The good rigidity and high damping capacity of copper-based SMAs make them suitable for passive vibration control [2.85]. Properties of copper based SMAs have not been widely reported, but the Young's modulus and the yield strength increase for the high temperature phase of the alloy [2.84]. Among Cu-based SMAs, CuZn based have actually been used and Cu-Al based SMAs have shown promise. Many Cu-based SMAs possess martensitic transformation from body centered cubic ordered parent phase to a mixture of monoclinic β' and orthorhombic γ' martensitic phases [2.86].

The martensitic transformation start temperature of Cu-40at%Zn alloy is far below room temperature [2.87]. Thus, to increase the Ms temperature and to stabilize the parent phase, ternary elements such as Al, Ga, Si and Sn are added. CuZnAl ternary alloys exhibit the most excellent properties as compared to other Cu-based SMAs due to their higher ductility and resistance to grain boundary fracture properties. However, the shape memory properties only allow for a maximum recoverable strain up to approximately 5% [2.57]. Alloys with lower aluminum content can be cold-worked using interpass annealing. With increased aluminum content, the cold working process becomes more difficult. Also, this alloy can suffer from stabilization of the martensite if it is quenched rapidly in the martensite phase, therefore negating the shape memory effect [2.84].

Ms temperature of CuAl alloy is a little above room temperature when the Al content is 14wt%. The alloys with Al content higher that 14 wt% are susceptible to precipitation of a second phase γ2 which does not undergo phase transformation. When Ni is added as a ternary element, precipitation of γ2 is suppressed. However, as the Ni content increases the alloy becomes brittle [2.88]. Excellent SME is observed in CuAlNi alloys with Al content close to 14wt% and with 4.5wt%Ni content. Some advantages of CuAlNi SMAs include a wide range of useful transformation temperatures, stability at higher temperatures, small hysteresis, and low cost [2.57, 2.84]. CuAlMn is difficult to process, and can only be hot-worked.

Due to the large grain size, CuZnAl and CuAlNi tend to be brittle. Adding small quantities of other metals like boron, cesium, and cobalt can control this problem. They have no real effect on the shape memory characteristics. But they cause an increase in the ductility of the alloy at room temperature because of grain refinement. However, caution must be exercised because this addition can compromise the shape memory characteristics [2.84].

The mechanical properties of Cu-based shape memory alloys highly depend on the resistance to grain boundary fracture since it occurs very easily. For instance, the fracture stress of single crystal CuAlNi alloys is about 600MPa while that in the polycrystals is 280MPa [2.89]. Therefore, above A_f, no superelasticity is observed in polycrystalline CuAlNi alloys since grain boundary fracture occurs before the martensite is stress-induced, however, they exhibit superelasticity as large as 18% in the single crystalline state [2.90]. The intergranular cracking

occurs not because of the impurities at the grain boundaries such as Bi, Sb, S, P, O and Pb which are known to cause intergranular embrittlement of Cu [2.88], but instead takes place due to elastic and plastic incompatibilities between grains, a consequence of high elastic anisotropy [2.91].

The detailed studies on CuAlNi alloys have shown that the formation of stress-induced martensite along grain boundaries upon quenching is the main reason for intergranular cracking. If the stress due to the displacement associated with the formation of stress-induced martensite is not accommodated by a deformation mode, to maintain compatibility at a grain boundary, the displacement causes a crack of a width which depends on the orientation mismatch between two adjacent grains. Small grain size, small orientation dependence of transformation strain and ease of plastic deformation might be the conditions to reduce the crack size. CuZnAl alloys are rather ductile in polycrystalline state due small orientation dependence of transformation strain, thus, they exhibit pseudoelasticity (superelasticity) at stresses as high as 300 MPa [2.92].

2.2.6.2 High-temperature shape memory alloys

Many industries, such as the military, automotive industry and some actuating valves (with automatic control) require alloys with transformation temperatures above 100 °C. Alloys that fit this criterion are considered high temperature SMA. The existing high temperature SMAs can be classified in three regimes in terms of their transformation temperature ranges: 100 °C to 400 °C, 400 °C to 700 °C, and 700 °C and over. Such classification is a result of different issues and operative microstructural mechanisms associated with each temperature range and available alloy systems. Some of the known HTSMAs are NiTi with Pd, Pt, Zr, and Hf additions, Ti-Pd, Ti-Pt, Ni-Al, Ni-Mn, TaRu, NbRu, TiIrPt and ZrCu-based binary and ternary systems. In addition, there are few new alloy systems with transformation temperatures lower than 100 °C but demonstrating superelasticity at high temperatures. These high temperature superelastic alloys are CoNiGa, CoNiAl, NiFeGa [2.51].

NiTi based alloys, Pt Zr and Hf and Zr-based intermetallics are the most common high temperature SMAs in the first temperature regime. Firstov and his coworkers studied the Zr-based quasi-binary intermetallics [2.93, 2.94]. They reported that these alloys suffer from transformation-induced plasticity and are significantly more brittle than the NiTi based ternary alloys. Thin films, on the other hand, have demonstrated improved high temperature shape recovery as compared to their bulk counterparts [2.94].

The martensite transformation temperature of NiTi can be increased by the substitution of aluminum, platinum, or palladium for nickel, as well as, zirconium or hafnium for titanium. The addition of Zr or Hf to NiTi has been shown to have brittle phases dependant on the composition, while the addition of Pd does not [2.53]. Initial research into high temperature SMA began with the complete substitution of elements such as Au, Pd and Pt for Ni [2.95]. It was found that although TiPd had a high transformation temperature, the high temperature transformation properties were not good due to low critical stress for slip.

It was suggested that the critical stress for slip could be increased three ways:

1) addition of a ternary element,
2) strengthen the parent phase by age hardening,
3) strengthen the parent phase by thermomechanical treatment.

As a result, Pd was added to equiatomic NiTi in varying compositions [2.96]. It was shown that the substitution of 20-50at% Pd for Ni increased the martensite start temperature with a maximum martensite start temperature of 527 °C [2.97]. The most commonly studied composition is Ti50Pd30Ni20 due to the transformation temperature above 200 °C. Slight variations in the composition are also studied ($Ti_{50+x}Pd_{30}Ni_{20-x}$ [2.98] and $Ti_{50}Pd_{50-x}Ni_x$ [2.99]) due to the lack of precipitation in Ti50Pd30Ni20. In bulk materials, hot rolling followed by cold rolling and annealing was found to produce superelasticity in TiPdNi. This is a result of a large number of dislocations being introduced during rolling that subsequently experience thermal rearrangement during annealing [2.97]. Precipitation can be used as an alternative to cold rolling or extruding to increase recovery strain at high temperatures due to the increased density of dislocations [2.99]. Ion beam assisted deposition also has the ability to increase the density of dislocations and may be another alternative to thermomechanical treatments for thin film SMA [2.100].

The challenge on the high temperature superelastic alloy systems such as CoNiGa, CoNiAl and NiFeGa is poor workability because these alloys suffer from poor ductility, thus the practical use of these new alloys depends highly on the solution to this problem. It was reported that introduction of γ second phase improves the workability of the alloys both at high temperatures and at room temperature as well [2.101, 2.102].

The number of high temperature SMA systems with transformation temperatures higher than 400 °C is quite limited. The martensitic transformation in binary and ternary Au-Ti and Ti-Pd alloys occurs in the second temperature regime and has been extensively studied by Donkersloot and Van Vucht [2.95]. They have also explored the phase transformation characteristics of equiatomic binary Ti-Pt system for which the transformation temperature is around 1000 °C, in the third temperature regime. The main issue with the alloys in the second regime is dynamic recrystallization and martensite aging effect in the course of forward and reverse phase transformation. Otsuka and his co-workers [2.103, 2.104] have focused on the recrystallization process in TiPd alloys which appears to be directly affecting the high temperature shape memory response and transformation stability.

The binary Ta-Ru and Nb-Ru intermetallics which have transformation temperatures higher than 700 °C demonstrate multistage phase transformations and undergo B2 to tetragonal to monoclinic martensitic transformations [2.105, 2.106]. The equiatomic compositions result in the best shape recovery with low thermal hysteresis [2.105]. TaRu and NbRu exhibit low strain recovery, 2% under compression and around 5% and 4% under tension, respectively [2.106]. They are based on equilibrium phases and transitions as opposed to metastable phases in conventional SMAs, thus, they do not show over-aging effects caused by decomposition and precipitation at elevated temperatures [2.51].

2.3 Nickel-titanium shape memory alloys

2.3.1 Metallurgical properties of NiTi alloy

Several different types of materials have shown shape memory properties, but in the past decades an alloy of nickel and titanium called Nitinol, attracted most attention because it combines excellent functional properties with good mechanical strength, ductility and long fatigue life. Moreover it exhibits good corrosion resistance and high special electric resistance (which allows the material to be easily heated using an electric current). The maximum strain that can be obtained from this kind of alloy reaches 8%. This is a high number under SMA standards since most of the other alloys only achieve between 2 to 4% strain. In fact NiTi is the only shape memory alloy that has found wide application in actuators, couplings, and medical uses [2.107-2.109].

The Naval Ordnance Laboratory that discovered the shape memory effect in this alloy was initially researching its corrosion resistance. In the galvanic series of metals, NiTi alloys are slightly nobler than 316 stainless steel. This better resistance is provided by a naturally formed very thin titanium oxide (TiO_2) coating known as a passive film. The formation of this film is exactly the same as that for pure titanium. It is very stable and therefore the NiTi alloys are resistant to many forms of corrosive attacks. However in some aggressive conditions, such as highly acidified chloride solutions, breakdown of this passive film can occur. Such corrosive environments are very severe for most engineering materials; nevertheless if NiTi is to be used in these conditions, some form of protective coating is advisable [2.30].

Electrochemical measurements show that NiTi based alloys have a good resistance to pitting in a chloride environment [2.110, 2.111]. However data obtained from a scratch test indicated that the healing of the passive film may be a difficult and relatively slow process [2.112, 2.113]. Comparing with other commercially available SMAs, NiTi is by far the most corrosion resistant. For applications such as actuators, electrical connectors and fasteners, NiTi has a superior corrosion behavior and therefore is a better candidate in such applications. In the case of coupling applications, corrosion resistance is more than adequate except in very severe operating conditions, where protection is advisable. As a general rule, if no corrosion protection is deemed necessary for the pipes and tubes, then none is required for the NiTi used to join them. The corrosion resistant behavior has led to studies on the biocompatibility of NiTi and a number of medical applications. It has been found through clinical tests that the biocompatibility is excellent with no metallic contamination of the organs. The titanium rich oxide surface prevents the nickel content of the alloy reaching the tissue. This has resulted in great activity in the medical market and has been one of the catalysts driving shape memory research [2.30].

As an actuator, it is capable of up to 5% strain recovery and 350 MPa restoration stress throughout many cycles. For example, a NiTi wire 0.5 mm in diameter can lift as much as 7 kg. Nitinol also has resistance properties, which are suitable for actuation by resistive heating. When an electric current is passed directly through the wire, it can generate enough heat to

cause the phase transformation. In most cases, the transition temperature of the SMA is chosen such that room temperature is well below the transformation point of the material. Only with the intentional addition of heat, the SMA can exhibit actuation [2.114]. In essence, Nitinol is an actuator, sensor, and heater all in one. Unfortunately, high cost and poor workability is often a factor in determining whether an application has commercial potential.

2.3.2 Phase diagram of NiTi

Many researches studied the phase diagram of Ni-Ti system since thermal treatments are important to improve the shape memory properties of NiTi alloys. Laves et al. [2.115] first reported the single phase NiTi at near equiatomic composition. Poole and Hume-Rothery [2.116] confirmed the decomposition of NiTi into Ti_2Ni and Ni_3Ti which was first reported by Duwez and Taylor [2.117]. It was found that NiTi phase extends to lower temperatures, however, the solubility range decreases with lowering temperature on Ni-rich side [2.116, 2.118]. Purdy et al. [2.118] first described that the martensitic transformation proceeds with a diffusionless process at low temperatures although they did not use the term "martensitic transformation". After the discovery of martensitic transformation in NiTi alloys in 1963, Wasilewski et al. [2.119] found a new phase, Ti_2Ni_3, and noticed that there is a vertical boundary on the Ti-rich side, and solubility range of NiTi phase is very narrow at 500 °C and below.

Up to this point, although some of the basics of the phase diagram were established, there were some difficulties in understanding all the phase transformations and the presence of some of the phases like Ti_2Ni_3. Nishida and his co-workers [2.120] studied extensively the transformations at high temperatures in the Ti-52at%Ni alloy. They found that at lower aging temperatures and shorter aging times Ti_3Ni_4 phase appears, at higher aging temperatures and longer aging times Ni_3Ti phase forms and at intermediate aging temperatures and times Ti_2Ni_3 phase nucleates.

The solubility limit on the Ti-rich side of the binary NiTi alloy is almost vertical and precipitation of Ti_2Ni phase preferentially appears at grain boundaries in bulk NiTi alloys. These precipitates decrease the fracture strength and degrade the shape memory behavior of the NiTi alloys. The possible solution to this problem is producing the Ti-rich NiTi alloy as thin films and heat treating the thin films at high temperatures like 700 °C for 1 hour or about 10 hours at 500 °C for a homogeneous distribution of Ti_2Ni precipitates in the grains [2.121]. Since the amorphous thin film supersaturates Ti atoms at high temperatures or during longer heating times excess Ti can precipitate upon crystallization [2.122].

Fully annealed near-equiatomic NiTi alloys transform from B2 to monoclinic B19' phase upon cooling. If near equiatomic NiTi alloys are thermally cycled or thermo-mechanically treated, the martensitic transformation occurs in two steps, i.e., B2 to R-phase and then to monoclinic B19' phase [2.123]. The R-phase was first reported as tetragonal phase, however, rhombohedral distortion was recognized later [2.124, 2.125]. Ni-rich NiTi alloys which are aged at an appropriate temperature also show two-step phase transition [2.126-2.128].

Certain heat treatments can actually produce precipitates as a second phase from the supersaturated solid solution obtained by quenching. In Ni-rich SMA, the Ti would bond with the excess Ni and make nickel rich precipitates, and vice versa in Ti-rich alloys. Note that no precipitates are formed with alloys of Ni composition between 50 and 50.5 percent; the diffusion will not take place due to the lack of excess Ni. A schematic version of a generally accepted phase diagram is shown in Figure 2-19 [2.129]. The amount of precipitates in this material is very important, since these precipitates ultimately change the mechanical and functional properties substantially. Therefore, having a sufficient understanding of the different precipitates that are created during a particular heat treatment is necessary.

The central part of Figure 2-19 where NiTi transforms to B19' martensitic phase is important. Because of the narrow range however, the alloys may often contain precipitates of a second intermetallic phase. On the nickel rich side Ti_3Ni_4, Ti_2Ni_3 and Ni_3Ti precipitation formation has been reported and resulted in confusion for a while, whether there is a eutectoid reaction or not. But it is understood that the Ti_3Ni_4 and Ti_2Ni_3 phases are intermediate phases and they transform to equilibrium Ni_3Ti phase with longer aging time. For Ti-rich side the equilibrium phase is Ti_2Ni but Ti is so active that it easily combines with oxygen and carbon at high temperatures. The order-disorder transition temperature is at 1090 °C as indicated by dotted line on the phase diagram. As it can be deduced from the phase diagram, the composition range for the order-disorder transition from B2 to bcc phases are from 49 to 57 at% Ni at 1090 °C. The composition range should be kept close to equiatomic composition since precipitations do not exhibit shape memory behavior [2.122].

In the molten state, Titanium is very reactive and this results in some oxygen being present in the matrix. This fact is often overlooked. From the Ni-Ti-O phase diagram [2.130], oxygen decreases the stoichiometric range of the NiTi compound and can unexpectedly result in compositions within a three phase field. This Ni_3Ti can be present for example in a Titanium rich alloy. Furthermore, the oxide Ti_4Ni_2O is isostructural with the intermetallic Ti_2Ni, which can make phase identification difficult. If the composition of the alloy deviates from stoichiometry, then larger precipitates are present, as seen for Ti-rich alloy. These larger second phase particles can have a marked effect on the hot workability of NiTi, particularly on the Titanium rich side where they are brittle and often result in cracking [2.30].

The behavior of SMAs is very sensitive to the temperature and duration of the aging, because their composition may change. TTT diagram in Figure 2-20 shows that in general the precipitation starts as fine $Ti_{11}Ni_{14}$, gradually changes to Ti_2Ni_3 and finally ends as Ni_3Ti ($NiTi \rightarrow Ti_{11}Ni_{14} \rightarrow Ti_2Ni_3 \rightarrow Ni_3Ti$ as the heat treatment temperature is increased or as time at a constant temperature is increased) in equilibrium with the NiTi matrix. All the while, the NiTi ratio in the matrix is being shifted towards higher Ti content and higher transformation temperature.

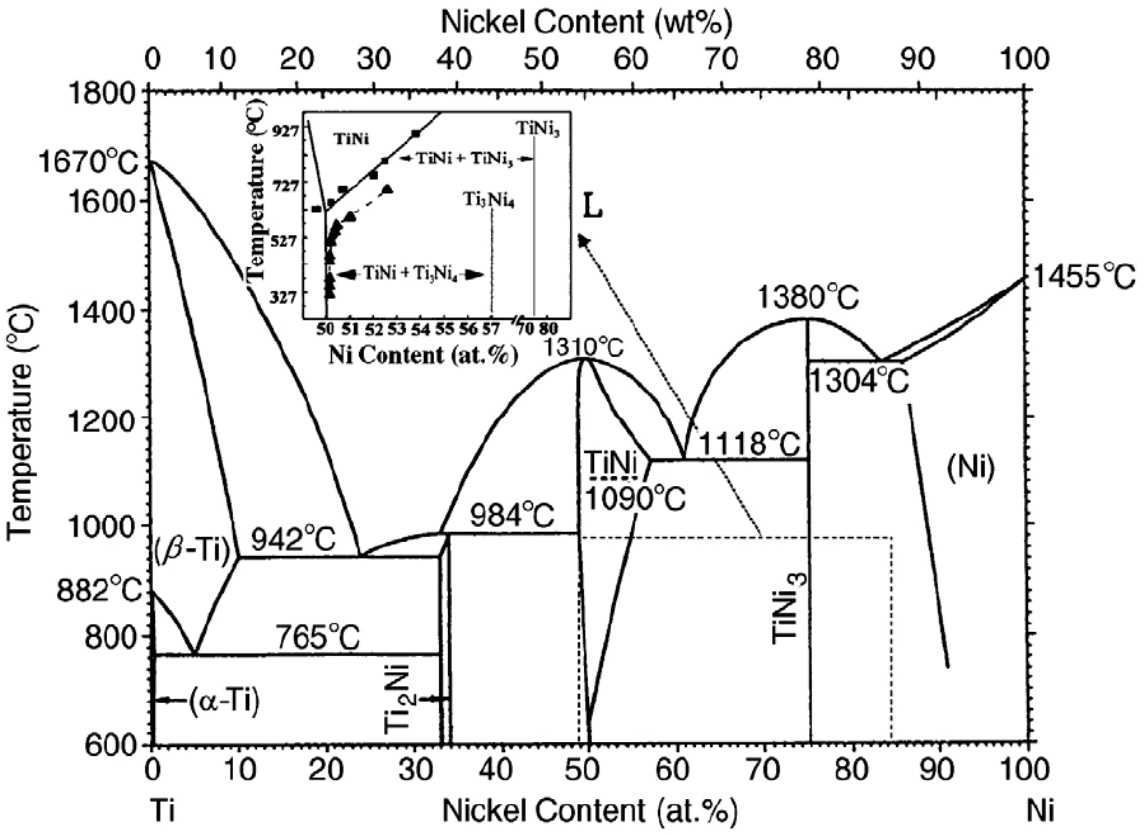

Figure 2-19 Phase diagram of the binary NiTi system [2.129].

When the precipitates form, two fundamental things happen in the crystallographic matrix. First the balance of Ti and Ni is changed. For example, in a Ni-rich NiTi alloy if a precipitate is formed then the Ni concentration in the equiatomic matrix will be reduced. This will change the transition temperatures as previously described in other sections. Secondly, coherency stress fields are produced. These stresses can affect the alloy by changing the transition temperatures, inhibiting grain growth along grain boundaries, affecting the way in which the martensitic transformation takes place, supporting the formation of an R-phase, etc. How much of an effect the precipitate has depends on the composition of the alloy, the type of the precipitate, the thermo-mechanical treatment to produce the precipitate, as well as where the precipitate nucleates in the microstructure [2.131].

Another important factor in determining the transformation temperatures of a SMA is the grain size. During a laser heat treatment, the grain size of the material can be altered to effectively change the forward and reverse transformation temperatures. A relationship between the elastic energy of the material and grain size can obtained, and a thermodynamic analysis shows that the elastic energy will decrease with increase in grain size [2.57]. Small crystals possess larger internal stresses due to anisotropy, which is produced by the different orientations of the grains, and that in turn aids the martensitic transformation. Therefore when grain size is small M_s is higher, conversely the M_s is lower when the grain size is large [2.131].

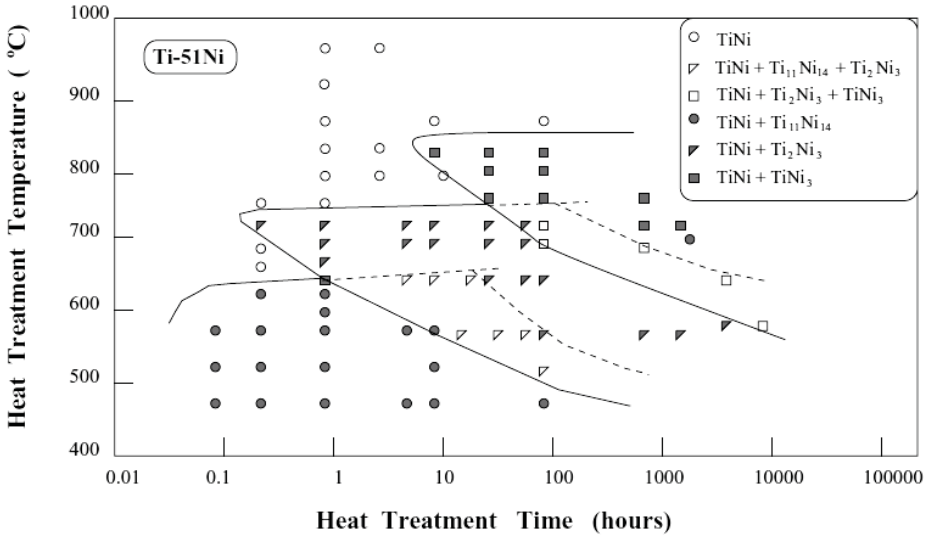

Fig. 2-20: Temperature-time-transformation (TTT) diagram [2.132].

2.3.3 Crystallographic characteristics

The SME is made possible by a SMA's ability to exist in three distinct crystallographic structures: martensite, austenite, and R-phase. Which phase exists at any given time is determined by the material temperature, stress, and temperature-stress history.

Nitinol's first-order phase transformation progresses from the parent austenite, a simple cubic B2 (i.e. CsCl) structure, to the daughter martensite phase (monoclinic B19') via an athermal transformation [2.37, 2.133]. This transformation is instantaneous once enough energy, in the form of temperature flux or stress, has been introduced to the system. The crystal structures of the austenite and martensite phases in NiTi alloys are shown in Figure 2-21. The primary crystalline structure associated with the martensitic phase is that of a B19' monoclinic geometry and its lattice structure consists of a rhombus alignment with an atom at each of the rhombus corners. Variants are associated with the twinned form as can be seen in Figure 2-21(a). The highly symmetric austenite phase has a B2 (ordered bcc) or CsCl structure with an orthorhombic geometry where the nickel atom resides at the center of the crystallographic cube and the titanium atoms at each of the cube's eight corners as seen in Figure 2-21(b).

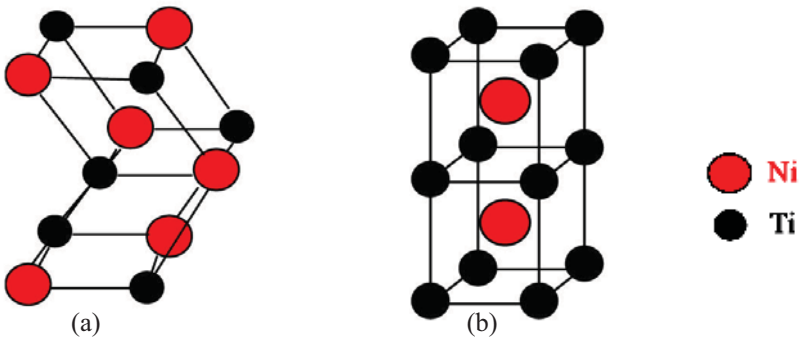

Fig. 2-21: Three dimensional crystalline structure of NiTi SMAs: (a) monoclinic B19' twinned martensite structure with a= 0.2889 nm, b = 0.4120 nm, c = 0.4622 nm and β□= 96.8°, (b) cubic B2 austenite lattice structure with a_o = 0.3015 nm [2.19, 2.134].

The phase transformation can also result in other martensitic phases, such as the rhombohedral (R) phase. The R-phase is often called a *pre-martensitic* transformation because of its occurrence before the onset of the primary martensitic phase transformation. B2→B19' transformation occurs in quenched NiTi alloys, while in aged Ti–Ni (with Ti_3Ni_4 precipitation) or cold-worked NiTi and in ternary Ti–Ni–Fe (Al) alloys, B2→R→B19' transformation occurs.

A schematic crystallographic description of the relationship between these structures is shown in Figure 2-22, which shows the structure relationship among B2, B19, and B19'. By comparing Figures 2-22a and 2-22b, it is clear that shear of the basal plane (close-packed plane) is necessary to create B19 structure from B2 parent structure. However, for the structural change from B2 to monoclinic B19', this shear is not enough. Instead a non-basal shear is also necessary to produce a monoclinic β angle, as seen from Figure 2-22c. For a long time there had been no explanation for the origin of the non-basal shear in forming the B19' structure, but very recently important results from elastic constant measurement enabled a simple understanding of the monoclinicity of the B19' martensite [2.122, 2.135].

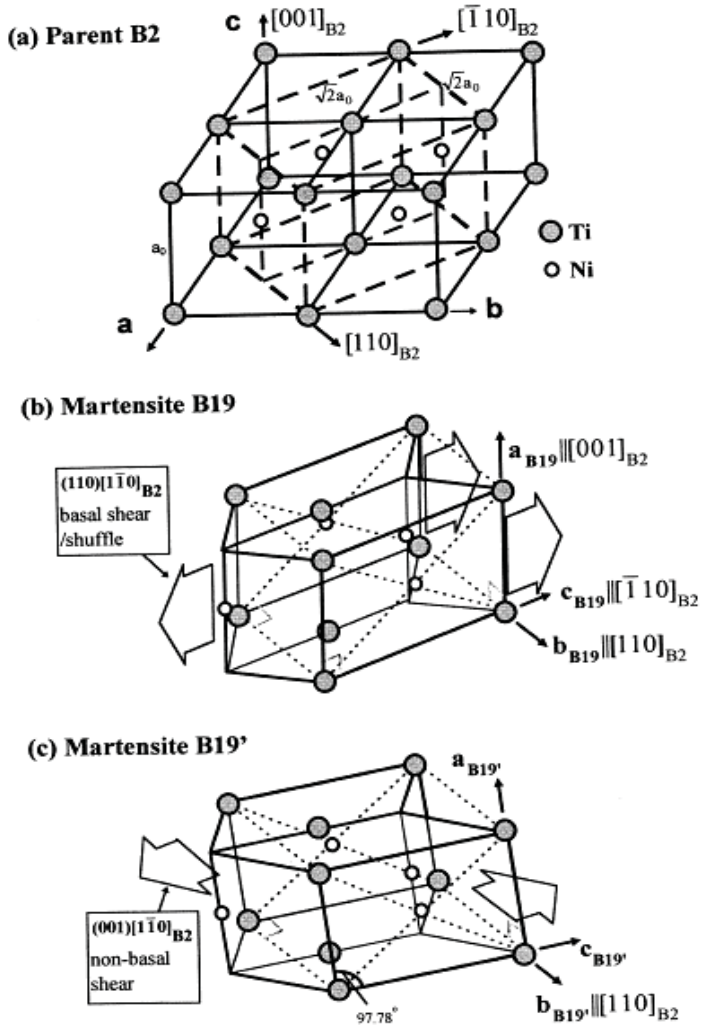

Fig. 2-22: Structural relationship among cubic parent phase (B2) and two kinds of martensites B19 and B19'. (a) the parent phase B2, (b) orthorhombic martensite B19, (c) monoclinic B19' martensite of NiTi [2.122].

2.3.3.1 Austenite phase

The austenite phase of NiTi is often referred to as having a body-centered cubic (bcc) structure; however, technically it is not bcc and instead has what is known as a B2 structure with body centered symmetry which is ordered like CsCl type with lattice constants of about a=0.301nm. The B2 austenite structure of NiTi consists of Ti atoms situated at the vertices of the cube with a single Ni atom in the centre. Figure 2-23 provides a two-dimensional representation of the NiTi austenite phase with the Ti atoms represented as dark circles, and the Ni as light circles. An important property of the B2 austenite structure is that its highly symmetric lattice is inherently univariant, meaning it can only exist in one distinct crystallographic structure [2.27, 2.136].

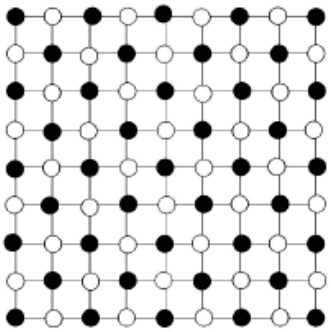

Fig. 2-23: Two-dimensional representation of B2 structure in austenite NiTi [2.27].

In an alloy, however, there exist several species of atoms. It is therefore important to identify the lattice site locations of these atoms. In steel, for example, these atoms are disordered, meaning that different elements are randomly distributed on the lattice sites. In Nitinol, however, the atoms are ordered, meaning that the Ni and Ti atoms are found on very specific sites (Figure 2-24). During the course of a martensitic transformation, the martensite takes on the same ordering as the austenite. This is referred to as inherited ordering. Shape memory alloys are generally based on a bcc symmetry, some with the bcc structure, more often with the B2 structure, and some with an even more complex ordering called DO3, still based on the bcc symmetry [2.28, 2.137].

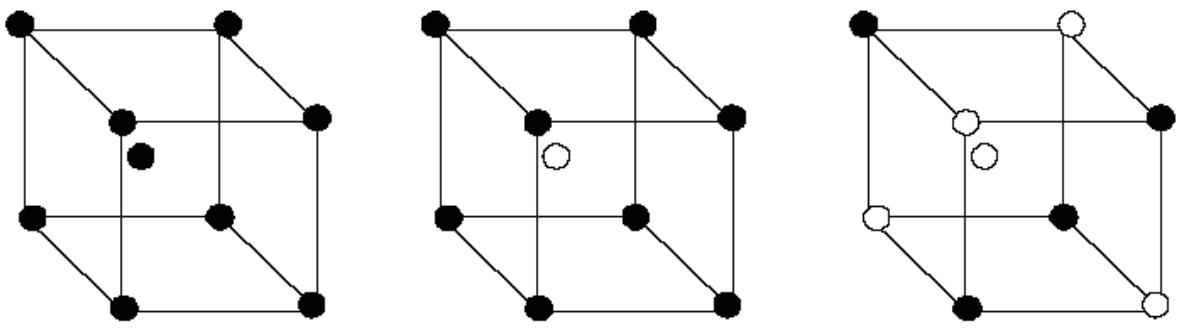

Fig. 2-24: Ordered and disordered structures commonly found in shape memory alloys: (a) bcc structure, (b) B2 structure in Nitinol, (c) DO3 structure found, for example, in Cu-Al-Ni alloys [2.28].

2.3.3.2 Martensite phase

Shape memory alloys at low temperatures exist in the martensite phase which has a monoclinic lattice structure. Martensite is formed by a displacive athermal transformation upon cooling from the higher temperature austenite phase under low or no stress. The displacive athermal transformation refers to one in which atoms are cooperatively rearranged into a new more stable structure, without a change in the chemical nature of the material, and progresses in a time-independent fashion [2.137]. So far three martensitic phases are determined for NiTi and NiTiX alloy systems. B19' is the most common phase observed in NiTi and its alloys.

The first determination of the crystal structure of the martensitic phase was in a polycrystalline Ti-49.75 Ni (at.%) alloy by Otsuka et al [2.138]. Their results, obtained from both X-ray diffraction measurements (XRD) and transmission electron microscopy (TEM), show that the unit cell of the martensite phase is monoclinic. The crystal structure was also further confirmed in a single crystal Ti-49.2 Ni (at.%) by Kudoh et al [2.139] using a 4-circle diffractometer, in a polycrystalline equiatomic NiTi alloy by Michal et al [2.133] using TEM techniques, by Bührer et al [2.140] using neutron diffraction measurements and by Knowles [2.141] using high resolution electron microscopy. The lattice parameters and atomic positions in the monoclinic martensitic crystal structure determined by different authors are shown in Table 2-3. Although slight differences exist, the lattice parameters reported by Otsuka et al have been widely recognized as the standard structure [2.134].

Table 2-3 Monoclinic martensite lattice parameters a, b, c, β and atomic positions in the crystal structure measured by different authors.

	Ostuka *et al*[51]	Kudoh *et al*[52]	Michal and Sinclair[53]
a	0.2889 nm	0.2898 nm	0.2885 nm
b	0.4120 nm	0.4108 nm	0.4622 nm
c	0.4662 nm	0.4646 nm	0.4120 nm
β	96.8°	97.78°	
γ			96.8°
Ti	0, 0, 0 0, 1/3, 1/2	0, 0, 0 0.1648, 0.5672, 1/2	0, 0, 0 0.055, 1/2, 0.558
Ni	1/2, 1/2, 0 1/2, 5/6, 1/2	0.6196, 0, 0.4588 0.5452, 0.1084, 1/2	0.580, 0, 0.472 0.475, 1/2, 0.086

When the new phase is formed an accommodation method must exist that allows the preservation of the external macroscopic dimensions of the material. In SMAs this accommodation is achieved by a mechanism known as twinning, which is capable of accommodating shape changes in a reversible way [2.137].

Bricknell et al [2.142] investigated the influence of Cu additions (up to 25 at.% Cu) on the lattice parameters in NiTi alloys by XRD and TEM. The morphology as well as the crystal structures of both the austenitic and martensitic phases of the alloys are remarkably similar in these alloys, although there are slight changes in lattice parameters. For the alloy with 5 at.%

Cu, the lattice parameters are a_o = 0.3025 nm for the austenitic phase, and a = 0.293 nm, b = 0.421 nm, c = 0.458 nm and β□= 97.3° for the martensite phase.

Figure 2-25 schematically shows one of the lattice transformations from B2 to B19' via the orthorhombic B19 base (X_{B19}, Y_{B19} and Z_{B19}). Since the martensitic transformation is diffusionless, a given vector in the parent phase transforms into a specific vector in martensite through so called lattice correspondence. From the difference of symmetry between the B2 and B19' crystal structures in NiTi alloys [2.143], there are, in total, twelve martensite lattices which can be formed from the B2 lattice, that is, the a, b, c axes in the B19 lattice can originate from twelve different crystal directions in the B2 lattice. Each correspondence is called a correspondence variant [2.134].

Chernov et al [2.144] measured the transformation kinetics in ternary Ti-Ni-Cu alloys with up to 4 at.% Cu by XRD. The direct B2→B19' transformation was found when Cu substitutes for nickel, and the two-stage B2→R→B19' transformation was measured when Cu substitutes for both nickel and titanium. Fukuda et al [153] investigated the transformation mechanism in Ti-44.5Ni-5.0Cu alloys and Ti-44.0Ni-5.0Cu-1.0Al (at.%) alloys by means of in situ TEM observation, electrical resistivity measurements and X-ray diffraction analysis.

A two-stage transformation B2→B19→B19' upon cooling was observed by TEM, but not by the electric resistivity measurement. It was explained that upon cooling, B19' starts to replace B19 before the B2→B19 transformation finishes. Only a small amount of B19 exists throughout the transformation. Therefore, the B2→B19 transformation can not be differentiated from the B19→B19' transformation in the XRD analysis and the electrical resistivity measurements [2.134]. The amount of transformation strain of B19 is less than B19' phase and much more than R-phase. Stability of mechanical and thermal properties under thermomechanical treatments, lower hysteresis due to small transformation strain and lower cost due to Cu addition make NiTiCu suitable for industrial applications [2.12].

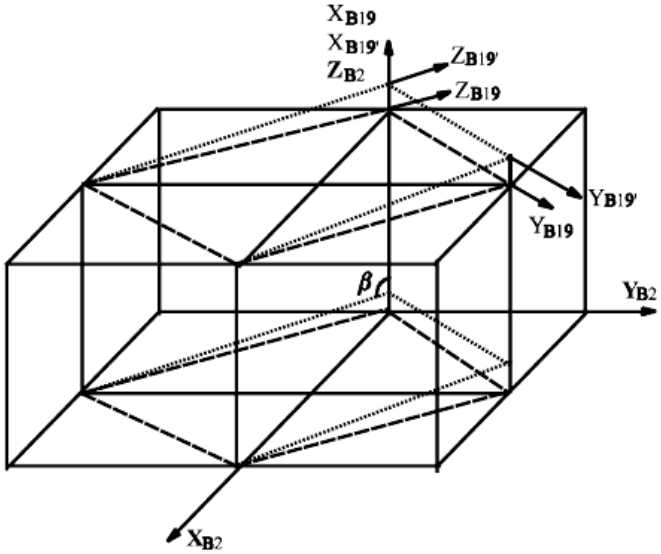

Fig. 2-25: Schematic representation of the correspondence of the lattices B2 and B19' via the B19 base X_{B19}, Y_{B19} and Z_{B19} [2.134].

2.3.3.3 R-Phase

The third phase, so called pre-martensitic phase, is a rhombohedral phase (R-phase). The R-phase appears upon cooling due to annealing, chemical alloying elements, or microstructural defects in the material, prior to the martensitic transformation. It forms as a rhombohedral distortion of the B2 structure along $<111>_p$ directions, which is the reason for the name R-phase transformation [2.145, 2.146]. The lattice parameters of the R-phase are well accepted as a = 0.3015 nm and β□= 89.46° at the R-phase transformation temperature T_R = 35 °C for NiTi alloys [2.147]. The R-phase is elongated 0.94% along the parent $[111]_{B2}$ orientation which is one order smaller than B19' [2.20]. Aging, cold working and annealing, thermal cycling, increasing Ni content and alloying of NiTi (e.g. NiTiFe and NiTiAl) could promote R-phase transformation by suppressing M_s temperature [2.20, 2.148].

Essentially the R-phase is in competition with the martensite reaction. Methods of suppressing the M_s will thus allow the R-phase to form. These include:

- Lattice dislocations [2.123, 2.126]
- The formation of precipitates in Ni-rich alloys [2.149, 2.150]
- Ternary elements [2.125, 2.128]

In Ti-rich NiTi phases the M_s temperature may be high enough to suppress the R-phase even if dislocations are introduced into the lattice [2.33].

Unlike the austenite-martensite phase transformation that has a temperature hysteresis in excess of 20 °C, the austenite to R-phase transformation is associated with a temperature hysteresis as small as 1.5 °C [2.151]. B2 to R-phase transformation results in only small shape change (~0.5%) which results in very small temperature hysteresis. Also this small transformation strain is responsible for the stability of transformation temperatures after thermomechanical treatments.

The R-phase is a martensitic-like phase and exhibits both the shape memory and superelastic effect; this makes it suitable for actuation devices that demand a small thermal hysteresis [2.151]. It has been proved that these kinds of actuators suffer less from fatigue and can yield millions of cycles before failing or degrading. Several researchers have described this effect in more detail including Otsuka [2.151] and Suzuki and Tamura [2.152], who describe the fatigue properties. However, the maximum recoverable strain is much lower than a typical martensitic transformation, with strains reaching only 0.5 % [2.151]. There is also an increase in the electrical resistivity, internal friction peaks and thermal activity. The austenite to R-phase transformation is fully reversible and the size of the hysteresis is dependent on the interfacial energies of the phase boundaries.

The R-phase will nucleate from the dislocations in the structure, join and continue to grow. Upon further cooling the plates will continue to form and finally the entire region changes to the R-phase. Subsequently, upon heating the R-phase will shrink and disappear in the same manner as they grew. The appearance and disappearance of the R-phase repeats in the same manner upon repeated cooling and heating, and it is well known that the rhombohedral phase transformation has superior cyclic deformation properties when compared to the martensite

phase transformation [2.153]. To obtain an R-phase transformation several conditions can be used. Dislocations can be introduced into the system via cold working and annealing, precipitates can be introduced by solution treating and aging the alloys or introduction of a third element which suppresses the martensitic transformation can also be used [2.123]. Due to the properties of the R-phase transformation, these alloys can be used for such devices as thermal actuators, where a small temperature hysteresis and reliability are required.

A differential scanning calorimetry thermogram for NiTi showing the various phases upon heating and cooling, including the R-phase, is presented in Figure 2-26. Differential scanning calorimetry is a thermoanalytical technique in which the difference in the amount of heat required to increase the temperature of a sample and reference is measured as a function of temperature. When a sample undergoes a physical transformation such as a phase transition, more (or less) heat will need to flow to it than the reference to maintain both at the same temperature. Whether more or less heat must flow to the sample depends on whether the process is exothermic or endothermic [2.27].

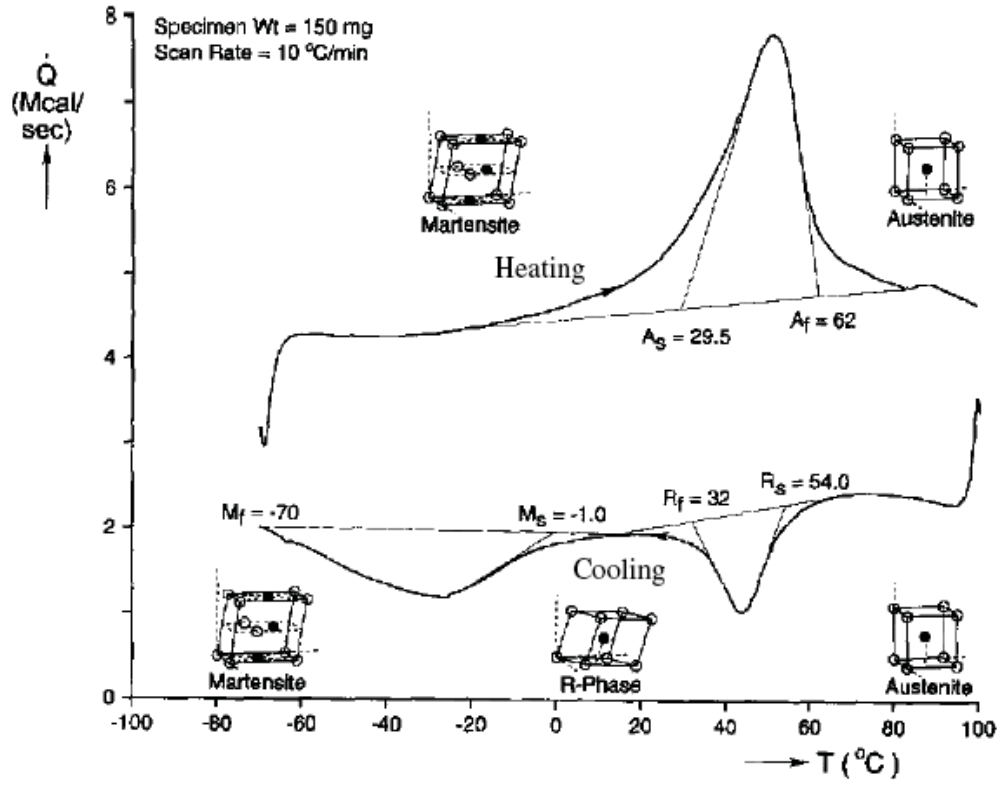

Fig. 2-26: Differential scanning calorimetry thermogram of NiTi [2.136].

2.3.4 Mechanical properties of NiTi alloy

A relatively large number of researchers have been interested in exploring the mechanical characteristics of NiTi in its two important phases. Like most SMAs, NiTi alloys show marked differences in mechanical behavior in the martensitic and austenitic state. Several experimental studies have been conducted to specify the mechanical properties of SMAs [2.122, 2.154-2.156]. The outcomes of experimental research in the past two decades assisted in developing a range for the mechanical parameters that would be expected from NiTi in its austenite and martensite phases.

While most metals deform by slip or dislocation, NiTi responds to stress by simply changing the orientation of its crystal structure through the movement of twin boundaries (detwinning). This orientation is evident in the stress-strain behavior by the stress plateau that occurs both in martensitic and in austenitic NiTi, until the material consists only of the correspondence variant which produces maximum strain. However, deformation beyond this will result first in elastic deformation of the oriented structure and then in classical plastic deformation by slip and dislocation.

The ambient temperature deformation behavior of NiTi alloys is very dependant upon the phase of the alloy and its transformation temperatures. This is shown below in Figure 2-27 [2.33]. Labelling of the different deformation regions is in accordance with that used by Liu et al [2.157] and other authors. Curve 1 represents an alloy in the parent phase where the M_d temperature (i.e. the temperature above which martensite cannot be stress-induced) is below ambient. The curve shows a conventional elastic limit followed by plastic deformation.

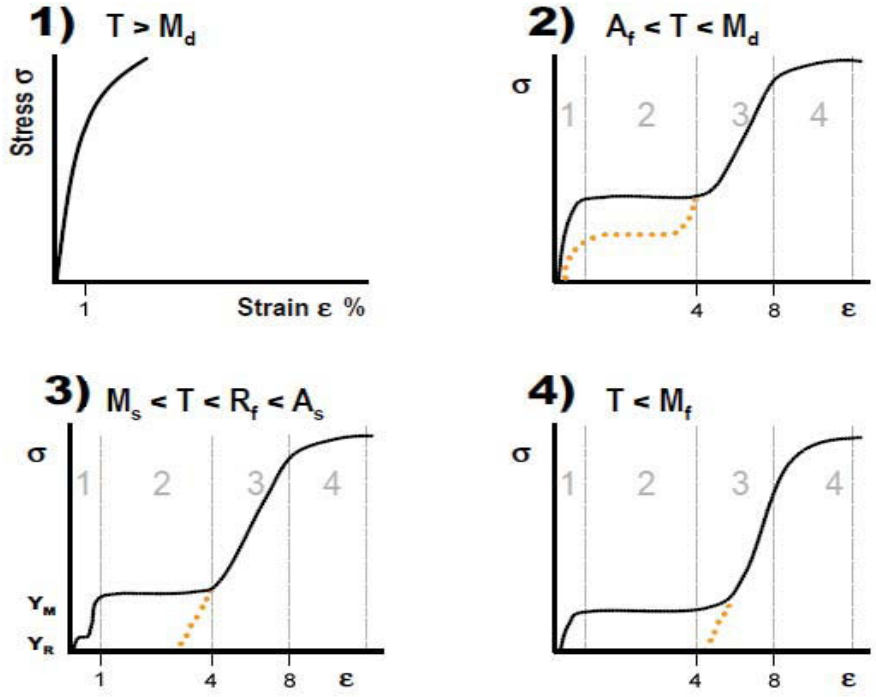

Figure 2-27 Stress Strain Behavior of NiTi (after Morgan [2.33]).

Curve 2 shows an alloy tested above A_f but below M_d. Stage 1 shows some initial elastic loading of the parent phase. At a particular stress, martensite is induced and further strain results in the stress orientated variant growth plateau represented by stage 2. If the alloy is unloaded at this point then superelastic shape recovery will take place and the curve will follow the path represented by the broken line. If the alloy is not unloaded however, the further strain results in elastic deformation of the stress-induced martensite (detwinned), stage 3, until eventually the yield stress is exceeded and plastic deformation takes place, stage 4. Ultimately ductile fracture takes place via void coalescence around second phase particles.
Curve 3 shows an alloy that has been cooled from the parent phase and the ambient testing temperature is between A_S and M_S but below R_f. During stage 1 deformation an initial yielding takes place at Y_R due to the rearrangement of the R-phase variants over a strain range of approximately 0.8%. A stress-induced martensite plateau (stage 2) is formed at Y_M. This is a lower stress than the equivalent in Curve 2 and is complete after a total strain of approximately 4%. If the alloy is unloaded after re-orientation of the martensite variants is complete, then the strain formed by the elongation is left in the alloy, this is represented by the broken line. This strain can be recovered via the one-way memory effect by heating above A_f. If the stress is not released after stage 2 then subsequent loading results in elastic deformation of the re-orientated martensite variants (stage 3). Eventually the stress required for slip to take place is exceeded and permanent deformation takes place (stage 4) leading to eventual ductile failure. If the same alloy was tested below A_s but above R_s then Y_R would not occur during stage 1.

Curve 4 is an alloy tested below its M_f temperature in the fully self-accommodating, martensitic condition. As the multivariant martensitic phase is deformed at a very low stress, an elastic deformation of the martensite and detwinning process takes place after the stage 1, as well as growth of certain favorably oriented martensitic variants at the expense of other variants. The plate variants begin to realign at a constant stress until reorientation is complete (stage 2) and results in a large plastic strain, which is not recovered upon unloading. Then subsequent loading results in elastic deformation of the martensite variants (stage 3) and eventual plastic deformation (stage 4) and failure. The yield point due to reorientation of the R-phase is absent from stage 1 in this alloy as the structure is fully martensitic before the test, therefore no R-phase can exist [2.33].

At the end of the deformation in stage 2, and after unloading, it is possible that only one martensitic variant remains if the end of the stress plateau is reached; otherwise, if the deformation is halted midway, the material will contain several different correspondence variants. This mode of deformation dominates at temperatures lower than M_f and results in the stress plateau [2.122, 2.158]. It is obvious that the maximum recoverable strain depends heavily upon the stage 2 plateau strain. This can vary greatly with alloy composition, testing orientation, deformation mode and prior thermomechanical testing [2.159]. Therefore the 8% recoverable strain in the Figure should be considered an ideal rather than a norm. The length of the martensitic plateau in the stress-strain curve extends typically to around 4%-5%. Also the plateau can vary from a continuous curve with an inflection point to a clear horizontal plateau with a sharp yield point [2.15]. Figure 2-28 also shows the mechanical behavior of shape memory alloys as three dimensional stress-strain-temperature relationship.

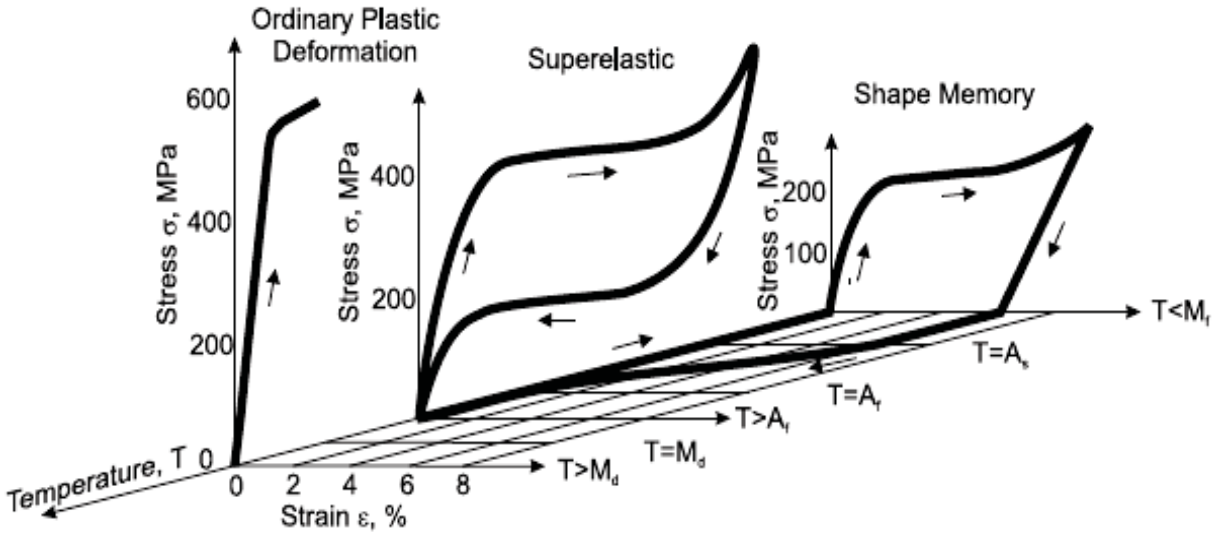

Fig. 2-28: Three dimensional stress-strain-temperature relationship for the mechanical behavior of SMAs [2.160].

2.4 The shape memory effects

2.4.1 Introduction

The shape memory effect (SME) is a property which covers two basic requirements: thermoelastic martensitic transformation and twinning as a deformation mode. The deformation processes that are mainly responsible for shape memory effect are deformation of martensite or stress-induced martensitic transformation. As discussed earlier, the deformation of martensite should occur by twinning to realize the shape memory effect, because slip is an irreversible process. The martensitic transformation occurs in self-accommodating manner to keep the same shape upon cooling (upon transformation) and to minimize the energy change. Further deformation proceeds with twin boundary motion which is the reorientation process of one martensite variant to another. Saburi et al. [2.161] demonstrated that the most favorable correspondence variant grows at the expense of the others and gives the largest strain under the applied stress. Martensite transforms back to austenite upon heating above A_f. When the temperature is below M_f the specimen is in complete martensitic state, thus the deformation is the deformation of martensite, however at temperature above M_f, a part or whole of the deformation is by stress-induced martensitic transformation. The superelasticity or transformation pseudoelasticity concept arises from the stress-induced martensitic transformations. Superelasticity occurs by the stress-induced transformation upon loading and transforms back to austenite upon unloading [2.65]. Pseudoelasticity is a more general term than superelasticity. It encompasses also rubber-like behavior which is observed in some SMAs when the specimens in martensite phase are bent and heated to recover their original shape.

Deformations at temperatures higher than M_d do not lead to stress-induced transformation because dislocation slip is the only deformation mechanism. M_d is the highest temperature at which pseudoelasticity is observed. At a temperature above M_d, the stress to induce the martensitic transformation lies above the critical slip stress of the SMA resulting in permanent plastic deformation due to the thermoelastic nature of the material, and the shape memory alloy is deformed like ordinary materials by slipping.

In shape memory effect, the shape of parent phase is remembered. Remembering the shape of both parent and martensite phases under certain conditions is known as two-way shape memory effect (TWSME). TWSME occurs if internal stress fields due to microstructure promote certain martensite variants to lower the energy of the system.

2.4.2 Superelastic Effect and stress-induced martensite

The superelastic effect, also known as pseudoelastic effect (PE), is an isothermal martensitic transformation that takes place due to application of stress at a temperature above A_s. The superelastic effect of memory alloys is characterized by the impressive amount of possible elastic strain, which is more than 20 times higher compared to conventional materials, it is beyond elasticity, therefore called superelasticity. The martensite formed in this way is known as stress-induced martensite (SIM).

The effect is based on an internal transformation of the crystal structure, which is called austenite in the initial condition and which transforms to the martensite if external stresses affect the material. Upon loading, the austenite undergoes typical elastic deformation until the critical or yield stress is reached. At this point, the martensitic phase transformation initiates. Detwinning then occurs along the stress plateau until the alloy is in its fully detwinned martensite phase, which is unstable at high temperatures, thus when the load is removed the SMA transforms back into austenite and the original shape of the alloy is fully recovered. Figure 2-29 provides a schematic of the stress-strain curve and related microstructures associated with the superelastic effect.

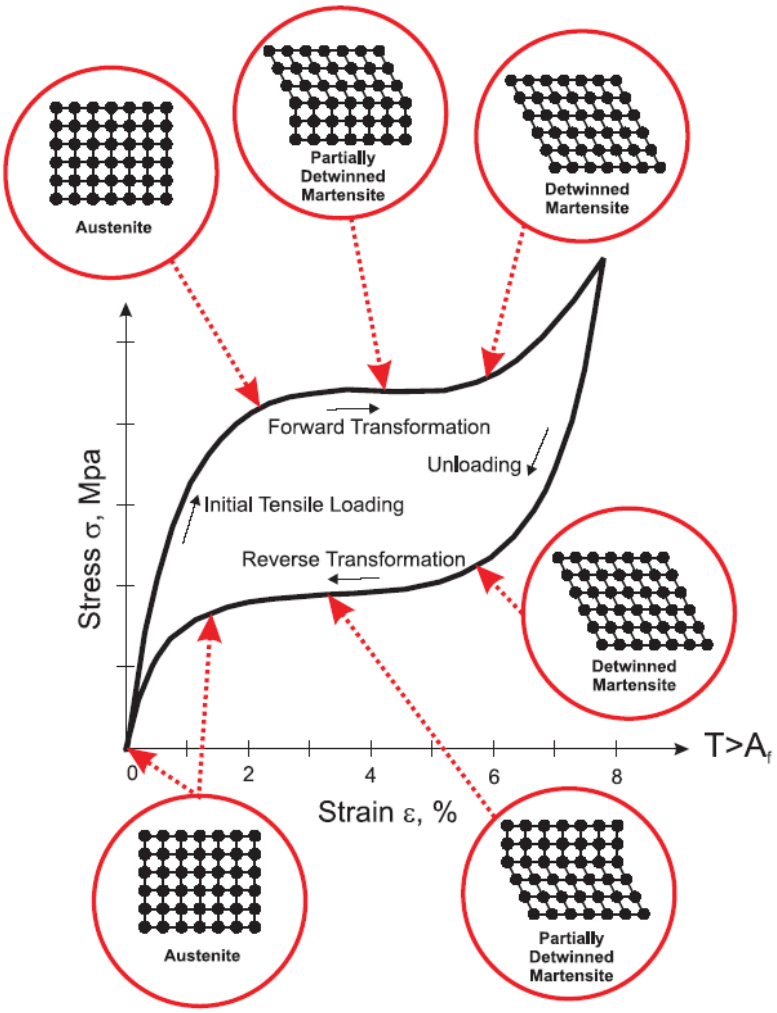

Fig. 2-29: Typical stress-strain curve for an SMA undergoing the superelastic effect [2.162].

The loading and unloading paths during this loading cycle do not coincide, with the unloading path being a lower stress plateau compared to the loading plateau. The energy driving this reverse transformation is the chemical free energy between the austenite phase and martensite phase [2.163]. In order for the superelastic effect to occur, the critical slip stress must be above the critical stress to cause stress-induced martensite.

The stress-strain behavior can be approximated as piece-wise continuous, starting with a linear elastic region as shown in Figure 2-30 (segment 1). In this case, the stress eventually reaches a level at which stress-induced martensite (SIM) is formed. Increasing stress effectively increases the transformation temperatures high enough that the martensite start temperature (M_s) is greater than the operating temperature, thus initiating the formation of martensite. This can also be thought of as increasing the temperature required to stabilize austenite over martensite. As the austenite is converted into SIM there is a reduction in the elastic modulus and a plateau develops (segment 2). Once the SMA is completely converted into stress-induced martensite, there is an increase in the elastic modulus as elastic deformation of the detwinned rhombic crystalline structure occurs (segment 3).

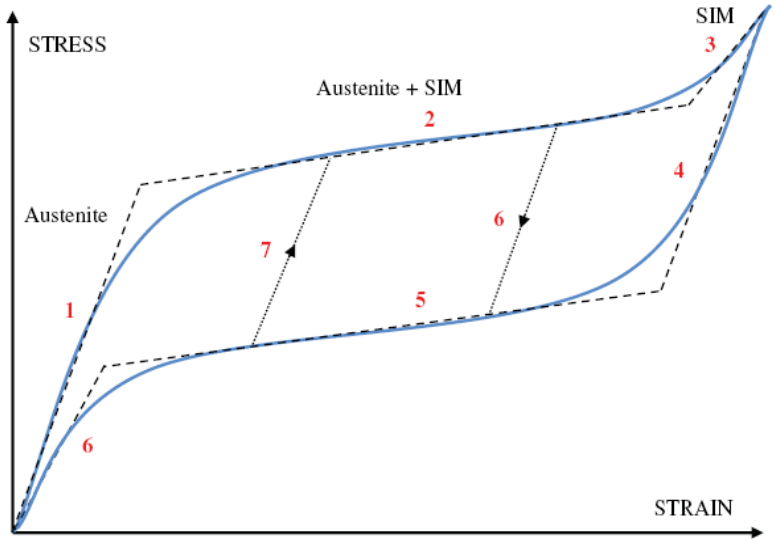

Fig. 2-30: Loading, unloading, and reloading behavior of austenite [2.27].

As with martensite, the unloading behavior of austenite is dependent upon which piece-wise continuous segment the material is in when unloading occurs. When the material is within the first linear elastic region (segment 1), unloading is elastic and follows the same curve as loading. When the material is unloaded after being loaded beyond the first critical stress (segments 2 and 3), the material exhibits what is known as the superelastic (or pseudoelastic) effect. If the material is unloaded from fully stress-induced martensite (SIM) (within segment 3), segments 4, 5, and 6 follow. This pathway exhibits three distinct piece-wise continuous segments similar to that observed in loading. If unloading occurs when the material is partially SIM (segment 2), unloading follows segment 6 until it intersects with the unloading plateau of segment 5. At this point unloading follows the path as described for unloading of fully SIM. The modulus of this unloading line (segment 6) is proportional to the fraction of SIM present at

the time of unloading. The reloading behavior of austenite shares some similarities with that of martensite. If the material was reloaded within the initial linear elastic region (segment 1), it acts as a linear elastic material and follows the same path as loading and unloading. If the material is reloaded when it is on some portion of the superelastic unloading loop (segments 4, 5, and 6), including both unloading from fully SIM and partially SIM (segments 2 and 3), then the reloading follows a new path, segment 7, until it intersects with the loading curve (segment 2 or 3) where it then continues along the loading curve. This reloading path (segment 7) has a modulus that is proportional to the fraction of SIM present in the material at the point of reloading [2.27].

It is worth noting that the transformation temperatures are affected by an applied stress in the same way as the isothermal stress-induced transformations. In superelastic transformations the temperature is held constant while the stress is varied. In the case of memory transformations the stress or applied load is held constant while the temperature is varied. The Clausius-Clapeyron equation applies to both cases and the $d\sigma/dM_s$ slopes are equal.

All the transformation temperatures are affected in a similar way during shape memory transformation and the Clausius-Clapeyron relationship can be written in the more generalized form:

$$\frac{d\sigma}{dT} = -\frac{\Delta H}{T\varepsilon_o} = -\frac{\Delta S}{\varepsilon_o} \qquad (2\text{-}1)$$

The left side of Equation 2-1 refers to the change in stress with respect to a change in the martensite start temperature, while ΔH, ΔS, T, and ε_o represent the latent heat, entropy, temperature and strain of the transformation, respectively. This relationship shows an increase in the difficulty to induce the martensitic phase transformation with an increase in temperature, which subsequently leads to an increase in the forward transformation stress, an increase in the reverse transformation stress, and deformation by permanent slip above a temperature M_d [2.15]. This is very important when considering shape memory alloys for actuator applications. If the alloy is to operate against an applied load then $d\sigma/dT$ for that alloy is fundamental to its operating parameters. The value of $d\sigma/dT$ is often referred to as the stress rate.

It is possible to plot the temperature-stress conditions for superelasticity and memory effect on one diagram for the same alloy as shown in Figure 2-31. Depending upon the temperature and stress coordinates, the alloy will either display the mechanical superelastic effect or the thermal memory effect. The Clausius-Clapeyron relationship is shown as a line with positive gradient, which represents the critical stress to induce martensitic transformation, being intersected by the negative gradient of the critical stress for slip. The hatched region is the region that if the stress is applied above A_f, the stress-induced martensite transformation occurs at a stress above the critical stress for inducing martensite. Upon unloading the martensite transforms back to austenite since martensite is unstable above A_f in the absence of stress.

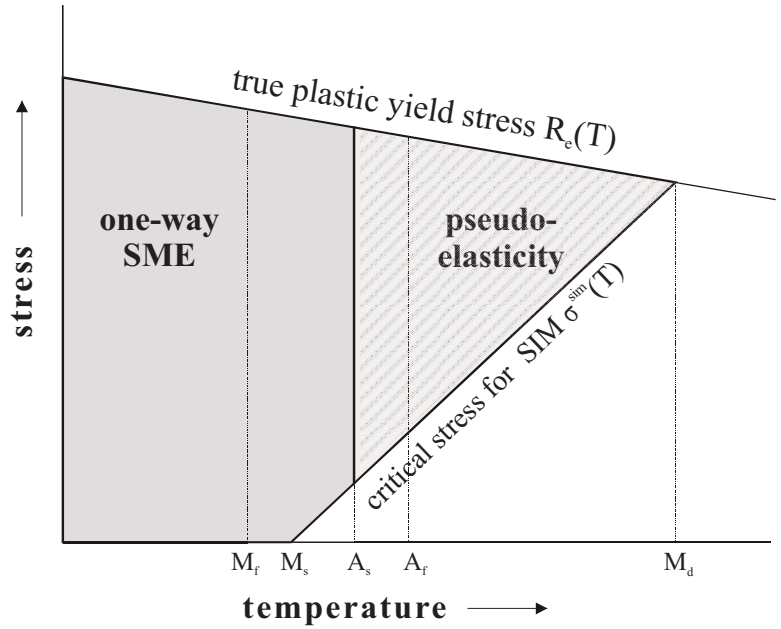

Fig. 2-31: Schematic representation for shape memory effect and superelasticity as a function of stress and temperature coordinates [2.164].

2.4.3 One-way shape memory effect

In one-way shape memory effect, also known as pseudoplasticity, the material undergoes permanent deformation at a temperature below M_f and then regains its undeformed shape when the SMA specimen is heated above the A_f temperature and it does not change again after cooling below M_f temperature, as shown in Figure 2-32. As explained earlier, the transition temperature depends on the stress level of the martensitic phase and hence increases in almost all SMAs with corresponding increase in stress.

Typically plastic strains up to 8%, or even 11%, can be recovered in one-way SME. There is however a critical stress above which permanent damage is caused to the SME. This critical stress is lower than the true yield stress of the SMA and defines the upper limit to which the SMA can be safely loaded without causing damage to the SME [2.165]. One-way SME is a one-time phenomenon and hence proper thermomechanical treatment is needed in order to obtain a complete cycle. Care, however, has to be taken neither to overload nor overheat the SMA specimen, which will lead to degradation in the shape memory effect. Figure 2-33 provides the stress-strain curve associated with the shape memory effect [2.162].

The martensite stress-strain relationship can be approximated by several piece-wise continuous segments, illustrated in Figure 2-34. Within the first continuous segment the material undergoes linear elastic deformation with a constant elastic modulus (segment 1). The stress eventually reaches a level capable of detwinning the martensite's twinned microstructure into a variant that better accommodates the applied stress, resulting in the second continuous segment. This segment has a much lower elastic modulus due to the relative ease with which twin boundaries move, and appears as a plateau (segment 2). Finally, once the material is fully

detwinned it is entered the last continuous segment (segment 3), where there is elastic deformation of the detwinned rhombic crystalline structure and then plastic deformation.

The unloading behavior of martensite is dependent upon which piece-wise continuous segment the material is in when unloading occurs. When the material is fully twinned (segment 1), the unloading is elastic and follows the loading curve. When the material is fully detwinned (segment 3), the unloading follows segment 4. This curve may have an elastic modulus that differs from that of detwinned elastic loading (segment 3). Finally, if the material is a combination of twinned and detwinned martensite (segment 2), unloading follows a curve with a modulus proportional to the fraction of twinned and detwinned martensite at the point of unloading (segment 5). As seen in Figure 2-34, unloading from segments 2 and 3 results in a residual strain or deformation in the material. However, this residual strain can be removed by raising the material temperature above that of the austenite finish temperature (A_f) [2.27].

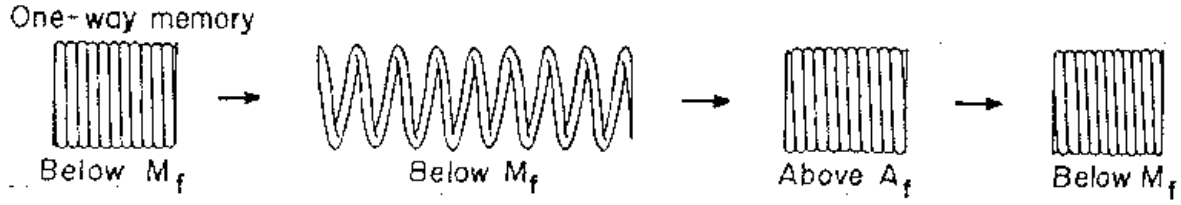

Fig. 2-32: Coil spring example showing the one-way memory effect [2.166].

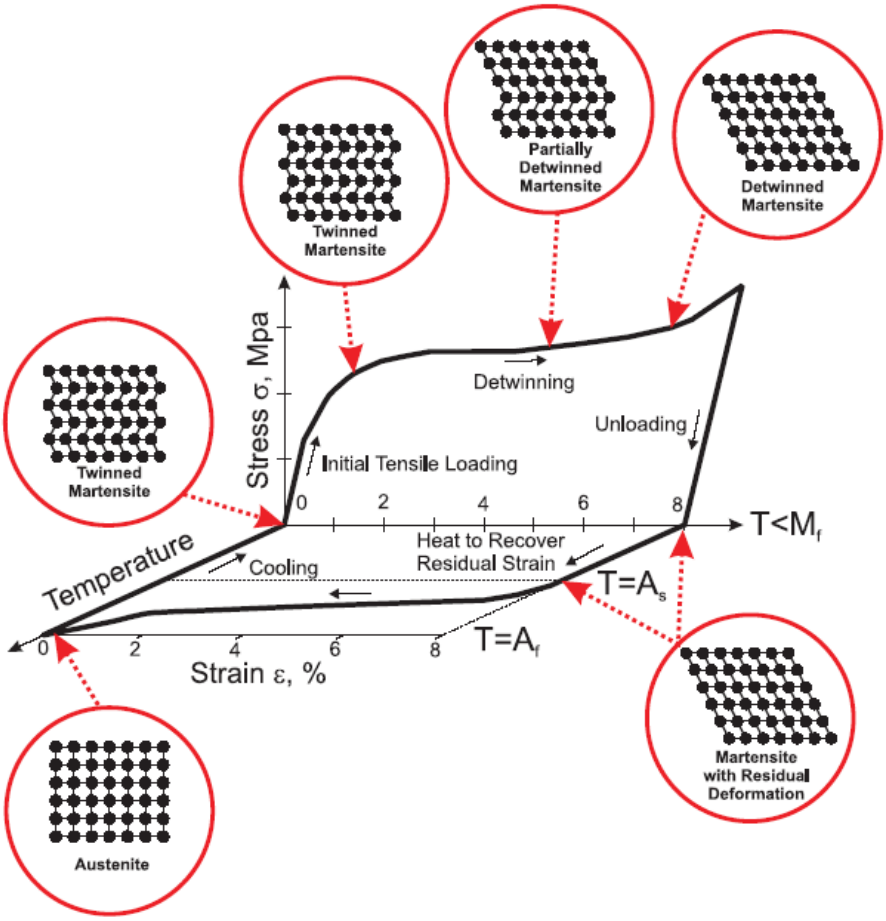

Figure 2-33: Typical stress-strain curve for an SMA undergoing the shape memory effect [2.162].

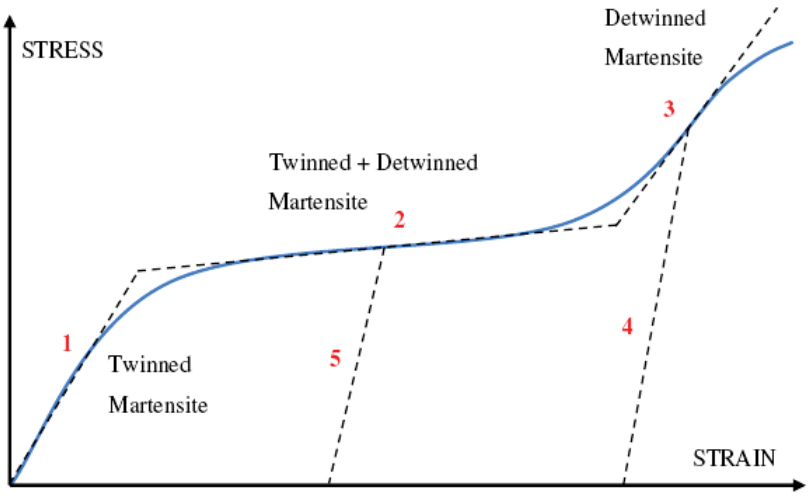

Fig. 2-34: Loading, unloading, and reloading behavior of martensite [2.27].

2.4.4 Two-way shape memory effect (TWSME)

In the one-way memory effect discussed in the preceding section, only one shape is remembered by the alloy, i.e. the hot parent phase shape. But it is possible in some of the shape memory alloys to demonstrate two-way shape memory ability in which the shape change occurs upon both heating and cooling. TWSME depends solely on temperature, which means that change in temperature will cause changes in shape. The amount of this shape change is always significantly less than the change obtained with one-way shape memory, and very little stress can exerted by the alloy as it tries to assume its low-temperature shape. The heating shape change can still exert very high forces, as with the one-way memory. This effect was first called the reversible shape memory effect [2.167, 2.168], but now it is called two-way shape memory effect (TWSME). Whereas the SME and SE are inherent in the material, the TWSME can be observed only after proper thermomechanical procedure called training.

The principle involved in all training techniques is that sites of internal stress are created by some mechanism inside the high-temperature phase. The sites are either irreversible defects such as dislocations caused by the deformation, or they consist of stable stress-induced martensite, which does not undergo a reverse transformation when heated, or second phase particles and precipitates created through stress aging [2.169]. Dislocations are introduced and when the SMA is heated, the martensite transforms but the dislocations remain. When the SMA is cooled again, the martensite re-forms in such a way that the stress fields of the dislocations are accommodated. In this case the self-accommodation of the martensite variants will be lost on cooling and predominant variants form resulting in a memorized shape change. There are only a limited number of particular variants; the other variants do not appear. Since the martensitic transformation strongly interacts with stress, the stress selects certain variants of martensite in the nucleation process in order to lower the energy of the system and contributes to create a certain shape of martensite.

When these existing variants grow on cooling, a macroscopic shape strain is observed. Based on free energy calculations, the energy of the complex dislocation arrays generated during training depends on the martensite variants formed. Therefore, the crystallographically equivalent variants are not thermodynamically equivalent. The TWSME was explained as being caused by this so-called thermodynamic anisotropy, which is due to the microstructural anisotropy induced by transformation cycling [2.134].

As with superelasticity, the martensite transformation takes place under the influence of stress, though in this case the stresses are internal rather than external. However, the TWSME has several disadvantages in comparison to the one-way shape memory effect, such as a limited reversible strain in the range of 2%, and lower transformation forces on cooling, since the TWSME is due to the selective nucleation of certain martensite variants, while the one-way shape memory effect is due to the strong reversibility and unique lattice correspondence upon reverse transformation. Also as mentioned before, thermomechanical treatment is quite necessary for the completion of the training of the SMA. It can have undesirable effects like elevation of the transformation temperatures, widening of the hysteresis loop, and an increase in the levels of residual strains as well. A schematic representation of the observed behavior is reported in Figure 2-35 [2.19]. Also Figure 2-36 shows the TWSME in a coil spring. It differs from the one-way memory effect in two respects: a) a shape change during cooling, b) indefinite repeatability of the shape memory effect by thermal cycling (heating and cooling).

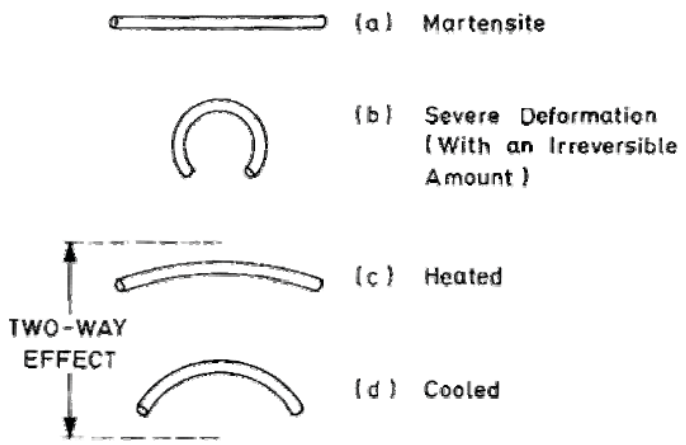

Fig. 2-35: Schematic representation of Two-way shape memory effect [2.19].

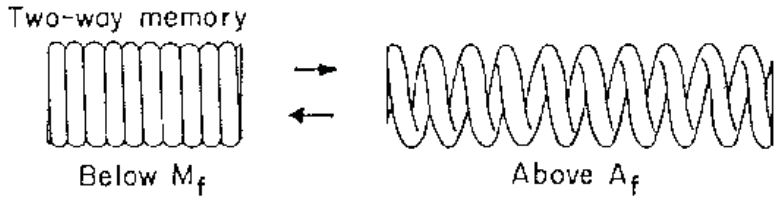

Fig. 2-36: Coil spring example showing the two-way memory effect [2.166].

2.4.5 Training processes

It is important to note that the two-way shape memory effect (TWSME) is not an inherent property and special thermomechanical treatment is required to train a SMA. Till now, hundreds of papers have been published and more than 20 different training methods have been developed, which generally involve repeated cycles combining temperature, stress and strain variations to produce oriented internal stresses in austenite and induce preferential martensite variants during cooling. They have in common that they are diffusionless processes.

There are some training methods with applying of severe load and building up of dislocations, but in addition to dislocations being the source of the nuclei there are other methods such as constrained aging quenching, laser or ion irradiation, sputter-deposited thin film or external magnetic field. The most common of these is aging the alloy under constant constraint. The effect differs from system to system and can result in either the stabilization of martensite from the deformation, or the decomposition during aging producing orientated second phases within associated strain fields. The presence of these nuclei results in stress/strain fields, causes the growth of non self-accommodating variants during stress-free thermal cycling. The following TWSME training methods are most commonly used and are explained in Sections 2.4.5.1 through 2.4.5.6 [2.30].

2.4.5.1. Thermal cycling after over-deformation below M_f

The alloy is cooled below M_f and severely bent (deformed) to a strain above its critical value for producing true plastic deformation, and dislocations are formed which in turn produce the characteristic stress field. The specimen is then unloaded and when reheated to the parent phase (Austenite), the SMA will not completely recover its deformed shape due to the excessive deformation of the Martensite. The alloy is cycled through this process a number of times. As the number of cycles increases the re-orientation of the martensite variants becomes easier. After some cycles, if the SMA is cooled again to the martensitic state, the alloy will, in a spontaneous manner, revert back toward the over-deformed shape. It is noted that some permanent plastic deformation is essential for the two-way shape memory effect and that complete shape recovery does not occur either by heating or cooling of the alloy. In this respect it may be argued that shape recovery does not fully occur [2.170].

2.4.5.2. Mechanical cycling above A_f – pseudoelastic cycling

This method consists of repeatedly stress-inducing Martensite by loading and unloading the parent phase (Austenite) above the A_f temperature, but below the M_d where pseudoelastic (or superelastic) behavior is expected. This cycling builds up dislocation debris within the alloy and after training the martensite variants are re-orientated as a result of the applied stress selecting a predominant variant [2.171].

2.4.5.3. Thermal cycling with deformation below M_f – shape memory cycling

This procedure consists of repeatedly carrying out shape memory cycles until the two-way behavior begins. A typical first shape memory cycle consists of the component being cooled to below M_f, deformed to a level below the shape memory strain limit, and then load free heated to recover the original high temperature undeformed shape. After a number of such cycles (10-15 in number) have been carried out, the component will begin to spontaneously change shape upon cooling, moving in the direction in which the component was consistently deformed during the training cycles. The amount of spontaneous shape change during cooling will be significantly less than that which was being induced in the shape memory deformation. The spontaneous shape change will usually be 1/5 to1/4 of the training strain.

2.4.5.4. Thermal cycling with deformation above A_f – Combined SME/PE cycling

The component is first deformed in the parent phase condition (Austenite) to stress induce a certain amount of stress biased Martensite, then cooled to below M_f while holding the induced strain in the component, then heating up to recover the original undeformed shape. When this routine is repeated a number of times, TWSME behavior will be obtained on subsequent heating and cooling. This particular method for training a SMA to perform in the TWSME mode is more frequently applied than the ones described in the preceding sections.

2.4.5.5. Thermal cycling with constant stress/strain – constrained cycling

This is probably the most commonly used training method at present. In this method the sample is deformed below M_f under constant stress or strain, thus producing a stress-biased martensitic microstructure. The sample is then constrained in the deformed condition and heated to above A_f. The sample is typically cycled from below M_f to above A_f a number of times ($N>10$ to stabilize the hysteresis loop), with the sample constrained in the original deformed shape, to complete the training routine. This training method proves to be particularly effective and is relatively straightforward to carry out.

2.4.5.6. Limitations on the use of two-way shape memory

The four foremost limitations on the application of TWSME are [2.30]:
1. The strain limit: There is a limit to the amount of reversible strain which can be recovered. Typically this is in the neighborhood of 2%.

2. Hysteresis: The inherent temperature hysteresis between the heating and cooling transformations is present.
3. Low transformation forces on cooling: This means that one can push much better with the SMA on heating than on cooling.
4. Upper temperature limit: If too high temperature is used during training then the memory may be lost due to annealing.

2.4.6. Rubber-like behavior

In conventional alloys elasticity is reversible and results from applied stress. Elastic strain may be either independent of or dependent on time and also may be linear or non-linear. On removal of the stress, the atoms return to a position of minimum free energy. Numerous elastic anomalies are known to exist. In monophase alloys these anomalies are related to the movement of zero to three-dimensional defects [2.165]. Diffusional hops of atoms into new positions under tension result in additional strains and are seen in interstitial alloys.

Shape memory alloys also show elastic anomalies caused by reversible stress-induced phase transformations and have been described in iron, nickel, and copper based alloys. Rubber-like behavior occurs during loading and unloading in aging martensitic state associated with twinning and detwinning of the martensite variants by reversible movement of twin boundaries. It is accompanied with large deformations with no considerable increase in stress. It is, therefore, very non-linear in comparison with the one-way and TWSM effects. Another distinguishing nature of rubber-like behavior is that it is entirely isothermal [2.30].

2.4.7. All-round shape memory effect

The all-round shape memory effect (ARSME) behavior was discovered and named by Honma et al. [2.172] in Japan. This effect is obtained in off-stoichiometric Ni-rich NiTi SMAs trained by constrained aging. It is essentially TWSME with the high and low temperature shapes being exact inverses of each other. Stated alternately, the SMA sample deflects one way when heated and the other way when cooled. The One-Way SME, Superelastic behavior and Rubber-like behavior are inherent properties of SMAs; however, TWSME and ARSME are not inherent properties, but can be obtained by training procedures. The metallurgical criteria driving ARSME are different than for TWSME which are diffusionless training processes. Also the training method for ARSME is quite different than for TWSME with some diffusion process and can be attained only in certain Ni-Ti alloy systems (those with greater than 50.5 atomic % of Ni). This phenomenon was attributed to the effect of the $Ti_{11}Ni_{14}$ precipitates (coherent Ti3Ni4) which introduce internal stress fields that make the transformations of R-phase and martensite proceed in certain ways [2.30, 2.172, 2.173].

Aging may take place in one or more steps. As a result of aging treatments precipitates form from the supersaturated matrix. In Ni-rich NiTi the precipitates are mainly Ti_3Ni_4. Figure 2-37 summarizes the training process and resulting behavior: the first step is heating the sample (a straight ribbon) at a high temperature (800 °C) and then quenching it; this is called a solution treatment, probably executed to maintain the high ordering which is present at high temperatures. After this the sample is constrained in a stainless steel tube and heated at moderate temperature (400-500°C). During this thermomechanical treatment, some precipitation of the Ti_3Ni_4 phase occurs. As has been seen, in NiTi with high nickel content, two transformations occur, the first one being austenite→R-phase and starting at M'_s. The third step of the training process is cooling the sample at $T > M'_s$ after which it is released; it is partially curved in the way imposed by the tube. On further cooling, between 30 °C and -70 °C a spontaneous shape change, opposite to the one imposed during the aging, is observed during the R-phase and martensitic transformations, i.e. the ribbon curls to the other side. On heating above 30 °C, the after aging shape is recovered and the ARSME cycle can be repeated. The precipitation reaction results in particles that create a back stress and this stress causes a deflection away from the constrained shape when the applied stress is released and cooled [2.174].

The ARSME is just a TWSME in which the shape changes are greater than in a normal TWSME, and the shapes at high and low temperatures are inversely curved. The reversible strain is limited to ± 2 %. Another problem common to diffusion controlled processes is the fact that the high and low temperature shapes seem to be very hard to define in advance. The ARSME is explained as follows: when the sample is constrained in the tube, tensile stresses will occur in the outside part of the sample and compressive stresses in the inside part (with reference to the neutral axis) because of the bending. The precipitation occurs in such a way that the normal to the plate shape precipitates is perpendicular to the tension axis, as shown in Figure 2-38, which could be a detail of the outside part. As a result of the plate the lattice is locally distorted, yielding tensile stresses perpendicular to the external stress. These local stresses still exist after the external stress has been removed, and on cooling they make those martensite variants form, which extend in the direction of the internal stresses, i.e. a contraction in the direction of the initial imposed stress occurs, causing the sample to curl to the other side [2.175].

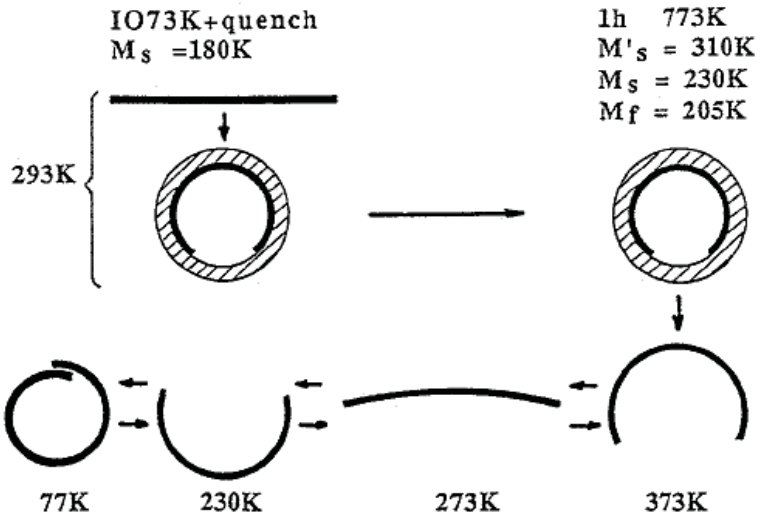

Fig. 2-37: Thermomechanical treatment leading to the all-round SME [2.174].

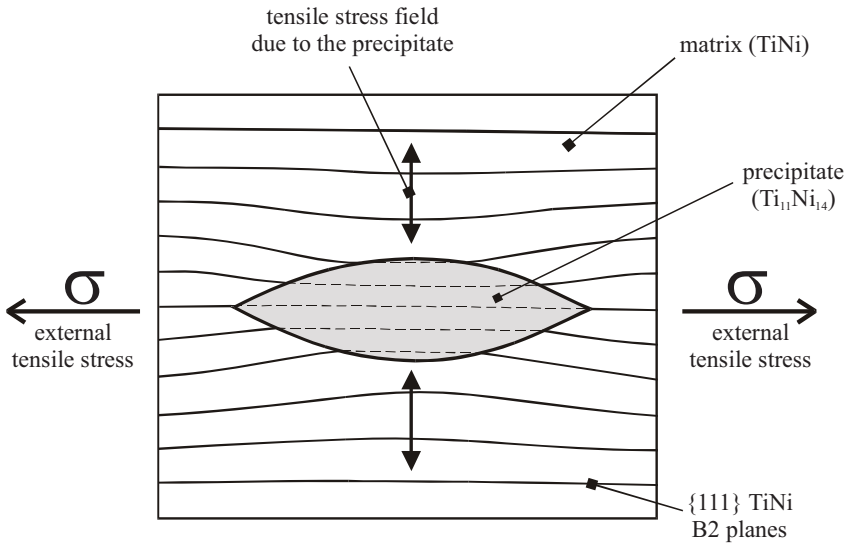

Fig. 2-38: Schematic illustration of the precipitation of Ti_3Ni_4 orientated b y the external tensile stress and providing an internal perpendicular tensile stress field [2.162].

2.5. Applications of shape memory alloys

Shape memory alloys present unique properties in comparison with other structural materials that make them good candidates in various engineering and medical applications. At present, about ten basic SMA systems are in use for industrial and engineering applications. With addition of alloying elements and by various permutations of the basic systems, the number of useable SMA systems can be increased drastically.

In the early growth of shape memory alloy technology the most important applications were for fasteners and couplings, mainly in the military sector. With the maturing of the technology, and the broader availability of alloys, industrial applications appear in a wide spectrum of commerce. Eyeglass frames were an early example of a new use of superelasticity which has grown to be a world wide product. Cellular phone antennas consume millions of feet of superelastic wire, and the development of underwire for women's brassieres, formerly limited to Asian market, is now expanding into a worldwide fashion. In the automotive sector, European car manufacturers have long been using SMA actuators for transmission fluid control. SMA actuators continue to achieve steady growth in safety valves for both consumer and industrial applications. Research and development activities continue in vibration and damping principles. Employing either passive or active means are well proven but the commercialization has been slow to develop. Active tuning of resonance frequency and seismic vibration controls may find their niches in the near future. Micro-electromechanical (MEM) devices fabricated using thin film NiTi actuators will also be briefly discussed. Typical other examples are electrical switches, sensors, safety devices, temperature switches, fire alarms, artificial limbs, catheters, and many others [2.176].

While most attention has been focused on the medical devices due to the attractive value of the business, the consumption of shape memory alloy materials in the consumer and industrial sections however far exceeds the usage in the medical field, and the list of commercial applications is growing at a rapid pace. NiTi SMAs are used in orthodontic treatments for misalignments of teeth, impact canines and other problems where the superelastic characteristics of NiTi are exploited. NiTi is used for artificial joints for femoral heads and sockets. The SMAs are used as blood vena cava filters that when inserted into the body, open up at body temperature to arrest clots. They are used for bendable surgical tools and in implants such as stents, joints, clamps etc. SMAs are being used in arterial stents, which are at a lower temperature when inserted into the artery and expand due to body heat. The stents are used to support and enlarge blocked arteries. They are also being used as orthodontic wire because they provide a constant corrective force on teeth [2.177]. Figure 2-39 illustrates an application of NiTi as arterial stents.

There are five documented functions that a SMA can deliver: 1) Free recovery, 2) Constrained recovery, 3) Actuation recovery, 4) Superelastic recovery, 5) High Vibration damping [2.178].

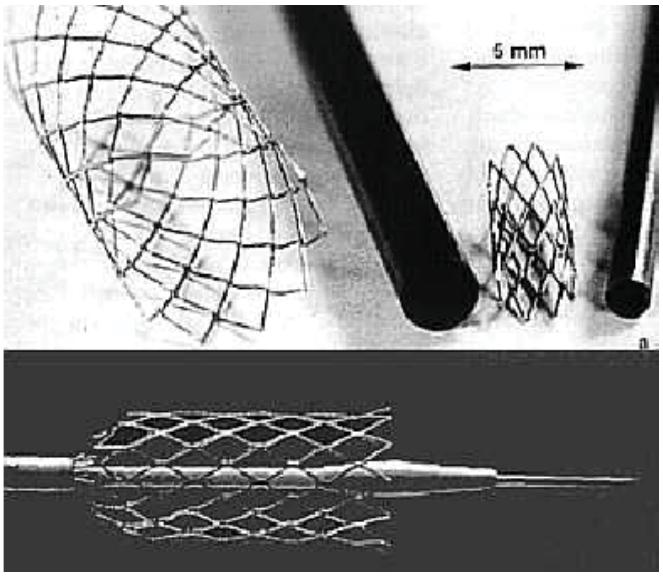

Fig. 2-39: SMAs used in arterial stents [2.52].

2.5.1 Free recovery

This category of shape memory alloys is deformed while in a martensitic phase. The only function required is that they return to previous (parent) shape upon heating. For free recovery applications minimal work is required for a material to return to the original shape and this kind of application is mostly used in control devices and relay mechanisms.

A prime application is a blood–clot filter (Figure 40). The filters are constructed from NiTi wires and are used in one of the outer heart chambers to trap blood clots, which potentially could cause serious health problems if travelling around the blood circulation system. The blood–clot filter is introduced in a compact cylindrical form about 2.0-2.5 mm in diameter. The body heat causes transformation to its functional shape. The wire is shaped to anchor itself in a vein and catch passing clots [2.179, 2.180].

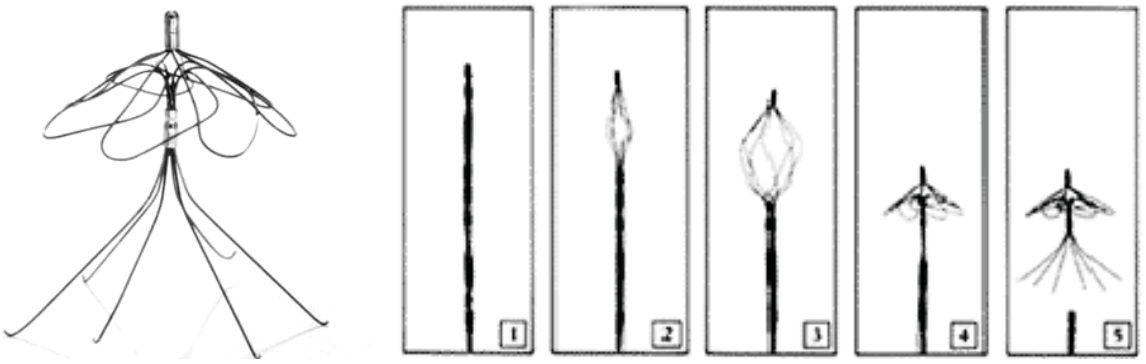

Fig. 2-40: Nitinol blood–clot filter a) filter in the recovery form, b) filter release [2.181].

2.5.2 Constrained recovery

The alloy is prevented from full shape recovery. This means that the alloy generates large amount of stresses on the constraining element by restricting the material's ability to return to the original shape upon heating. This type of function is being used increasingly in fittings, couplings and connectors for machinery. The most successful example of this type of product is hydraulic–tube couplings.

2.5.2.1 Pipe Couplings

This kind of couplings was made first for the F–14 jet fighter. It was made initially from NiTi alloy, now is usually made from Cu-Zn-Al alloy [2.182]. The couplings are established at room temperature and are in the austenite phase. The coupling is machined at normal temperature to have an inner diameter 4 % less than the outer diameter of the tubes to be joined. After cooling the coupling below the M_f temperature in liquid nitrogen, the diameters are expanded to have greater diameter than the tubes (see Figure 2-41 top). When the coupling is warmed to austenite phase, it shrinks in diameter and strongly holds the tube end together (see Figure 2-41 bottom). The tubes prevent the coupling to recover its original shape. This creates stresses powerful enough to create a joint, which is better than a weld. These couplings are used in the plumbing of atomic submarines and warships as well as maintenance and repair of pipes (with diameters as large as 150 mm) laid on the ocean floor to transport oil inland from oil fields.

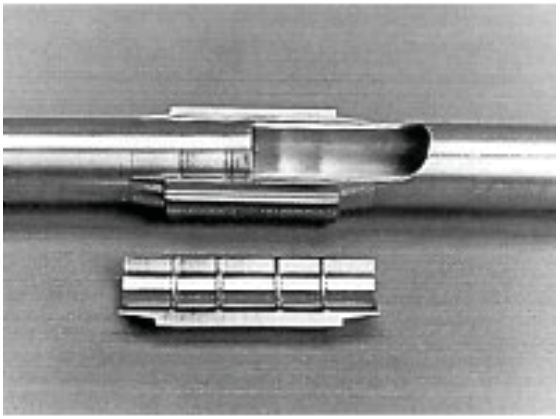

Fig. 2-41: Hydraulic–tube couplings [2.183].

2.5.2.2 Fasteners and Connectors

Fasteners and connectors are used in place of rivets and bolts when the far side of the fastened objects cannot be accessed, like in mid-air structures. Here, the original fastener is in the austenite state. It is dipped in liquid nitrogen to straighten. It is then inserted into the hole and actuates as it gets back to room temperature and is installed tightly. Connectors in electrical appliances also follow the same principle.

2.5.3 Actuation recovery

Shape memory actuators sense a change in temperature and undergo a phase change at a particular temperature to deliver a corrective force and displacement [2.26]. The alloy is able to recover its shape but operates against applied stress, resulting in work production. A vast majority of applications employ SMA in this mode. Actuation is the controlled production of work output or energy release. It is likely that the main use of shape memory alloys within smart structures will be as actuators operating through the conversion of thermal energy into kinetic energy and work output. It is perhaps the large strains and high work output that offer most opportunities for innovative design with SMAs.

The use of these alloys as solid state actuators offers many benefits:

- High recovery forces
- Large recoverable output strains
- Different actuation modes (linear, bending, torsion)
- High work output per unit volume or mass

One application of this group is a temperature-actuated switch. The switch can be designed so that it opens or closes above a particular temperature. Those switches are usually applied in instruments for safety purposes. One such example is a fire safety switch, which is designed to shut off the electricity or flammable gas flow when fire occurs [2.179, 2.182].

Thermal actuators are used to protect filters, which are used for water filtration as they can get damaged if they are exposed to hot water. When hot water flows, the SMA spring is heated, overcoming the bias spring force and closing the valve for filter protection. The cooling system in diesel engines employs an electrically driven fan, which is turned off and on as required to maintain a specified system temperature. Thermally operated electrical switches must operate reliably while subjected to strong vibrations. The bimetal-operated switches used for this application suffer from chatter due to their low contact force and short stroke. These conditions have been completely corrected by the use of high contact force SMA switches. NiTi shape memory actuators has had great success for space applications. Actually due to their unique properties, SMAs have become an attractive solution for applications where conventional actuators cannot provide the desired operation characteristics. They are lightweight, powerful, scalable, and offer smooth, silent, clean operation. These unique properties make SMA actuators ideal for motion generation at the meso- and micro-scales.

Conventional actuator technologies are unable to match the high power to weight ratio offered by SMAs. A comparison of various actuator technologies is provided schematically in Figure 2-42. The inherently high power vs. weight ratio that exists in shape memory alloys makes them ideally suitable for work producing devices. These actuators can be categorized in two major groups: linear and rotational. Subsequently each one of these groups can operate as a differential or non-differential actuator. SMA actuators can also be categorized as high stroke or strain actuators, high force actuators, or both. The bulk of the work though has been in overcoming the maximum displacement possible for any shape memory alloy configuration. Since shape memory alloys are by nature powerful the main limitation has been the useful

stroke that can be derived from them. The following sections will show different kinds of SMA actuators that have been developed [2.184].

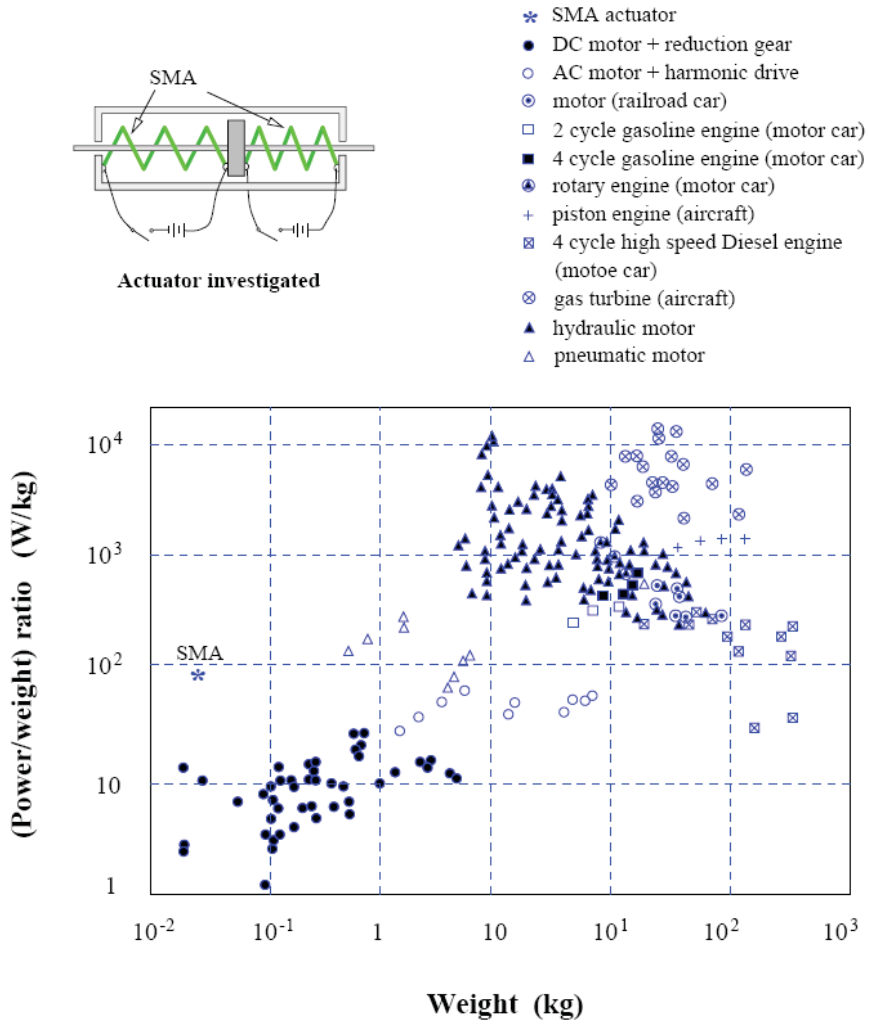

Fig. 2-42: Power/weight ratio versus weight diagram of several actuators [2.184].

The actuator properties of SMAs originate from the diffusionless solid-state phase transformation that can occur in these materials [2.34, 2.26]. In diffusionless transformations, no atomic bonds are broken or formed, so this transformation merely consists of a distortion of the atomic lattice. A transformation strain is associated with this distortion, which can be used for actuation. The transformation is triggered by changes in temperature, stress state and in some alloys magnetic field.

The difference or hysteresis depends on the alloy and its composition, but typical values are 30–50 K. This hysteresis complicates the use of SMAs as continuously controlled actuators, and they are therefore most often used as discrete (on/off) actuators. However, in Ni-rich NiTi alloys, next to the austenite and martensite states, also a third rhombohedral phase occurs, which is called the R-phase. The phase transformation between austenite and this R-phase is known to have a very small hysteresis of approximately 2 K and an excellent resistance to fatigue [2.26, 2.153]. These properties make this transformation very attractive for actuation applications.

Both one-way SMA and two-way SMA may be used for deployable structures. Although two-way SMA can perform in two directions due to its two-way shape memory mechanism, transformation strain associated with it is normally only half of that in one-way SMA. An alternative solution is to put two one-way SMA based actuators one against another to generate mechanical two-way performance, i.e. heating SMA in one actuator to get forward motion, and heating SMA in another actuator to reverse. The advantage of mechanical two-way actuator is higher motion and higher force than that in material two-way actuator, while the advantage of material two-way actuator is simpler, compacter and much less elements involved.

Figure 2-43 shows three basic types of SMA actuators using one-way SMAs. Figure 2-43a shows a one-way actuator. The SMA element is elongated initially, at low temperature, and is then heated to move element P in the direction of the arrow. Figure 2-43b shows a Biased Actuator, which is capable of moving the element P back and forth. The SMA element is deformed at low temperature, before being connected to the spring. When it is heated, the recovery force which is generated pulls the spring, thus storing energy in it. When the SMA element is cooled, the energy stored in the spring is released and the SMA element deforms back, thus completing the cycle. Figure 2-43c shows a two-way actuator which includes two SMA elements. Two opposing SMA elements are used, instead of the SMA element and bias spring of the biased actuator. Any motion can be obtained by appropriately cooling or heating the two SMA elements [2.184].

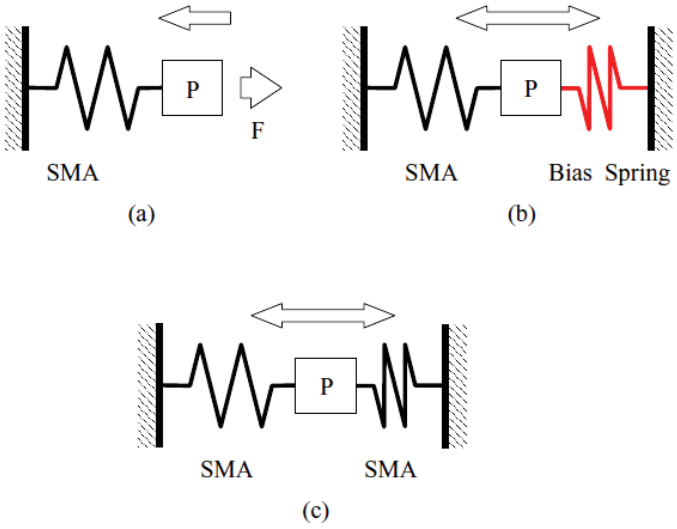

Fig. 2-43: Basic types of SMA actuators using one-way SMAs, (a) one-way actuator; (b) biased actuator; (c) two-way actuator [2.184].

To deploy a structure, it is necessary that a relative movement, i.e. a rotation or a linear motion, occurs between different parts of that structure. Such movement can be generated either by a specially designed actuator or simply by a part of the structure changing its shape. In the 1960's, Nitinol sheets and rods had been considered to unfurl satellite antennas upon exposure to solar heating (Figure 2-44) [2.34]. Figure 2-45 shows another simple SMA satellite antenna made of Nitinol wire.

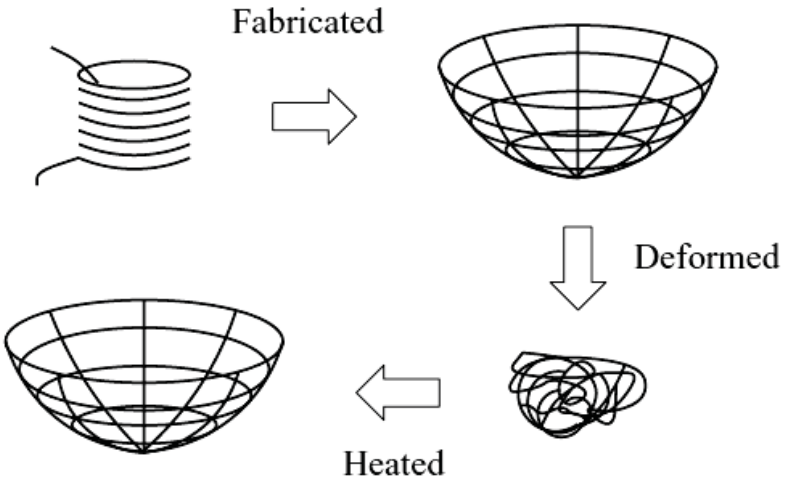

Fig. 2-44: SMA satellite antenna [2.184].

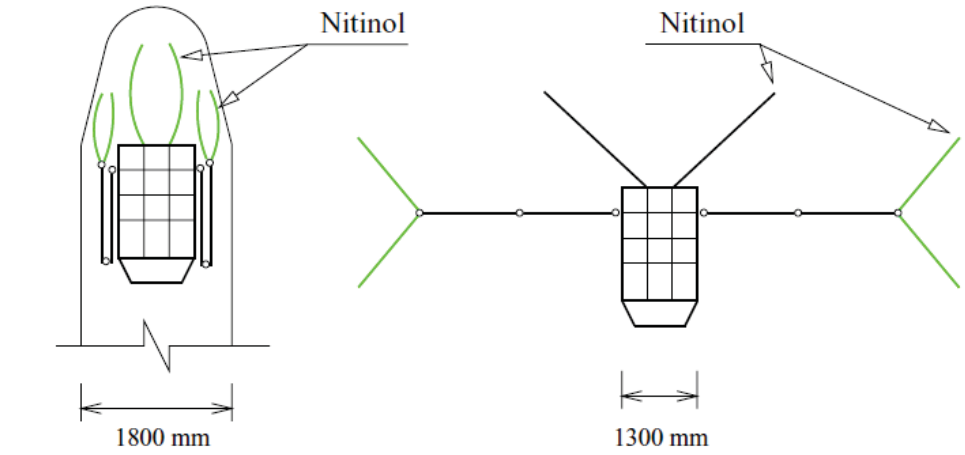

Fig. 2-45: SMA satellite antenna [2.184].

2.5.4 Superelastic recovery

The only isothermal application of the memory effect, superelastic recovery involves the storage of potential energy through comparatively large but recoverable strains. In the commercial industry, the superelastic properties of SMAs have made them excellent materials to use in eyeglass frames, cell phone antennas and golf clubs that can be subject to a large deformation and when released they will return to the original shape [2.177, 2.185, 2.186]. These industrial parts, formerly of stainless steel, are now universally manufactured from superelastic NiTi alloy due to great resistance to permanent set on bending and accidental damage. Utilizing the same principle for manufacturing superelastic NiTi eyeglass frame, significant cold work is often used to enhance the low temperature superelasticity. Ni-rich chemistry or ternary addition is also used to achieve this desired property. A photograph of typical eyeglass frames and cellular phone antennas are shown in Figure 2-46.

Women's brassieres have both esthetic as well as structural requirements. The application of superelastic NiTi alloy to the wire re-enforcement, called the underwire, was first developed in Japan and is now a significant global market for SMA. NiTi underwires offer improved comfort due to the much lower elastic modulus than the conventional steel wires. An additional advantage is the fact that the superelastic NiTi wires are resistant to permanent deformation which can be the result of washing and drying cycles. Various sizes and shapes are now available offering a wide range of stiffness and design options. A photo of NiTi underwires is shown in Figure 2-47 [2.52].

Superelasticity is also commercially used in orthodontic applications, especially in correcting misaligned teeth as shown in Figure 2-48. Superelastic NiTi wires are used for making continuous, gentle, corrective force to give large rapid movement of teeth. Based on clinical observations the optimal forces for tooth movement are 0.5−1.25 N. The forces at the lower end of the range correspond to the smaller rooted teeth and the forces at the upper end of range are optimal for the larger rooted teeth. Optimal wires are from NiTi alloy with diameter from 0.4 mm to 0.6 mm [2.187].

Similar shape memory alloy devices are used for healing broken bones (Figure 2-49). Staples of the shape memory materials are attached to each part of broken bone. These staples apply a constant, well-defined force to pull the two pieces together. This force helps to heal up the two pieces of bone together [2.188, 2.189]. The aerospace industry has used SMAs in helicopter blades and aircraft wings to reduce noise and vibrations [2.190, 2.191]. Figure 2-50 illustrates these applications.

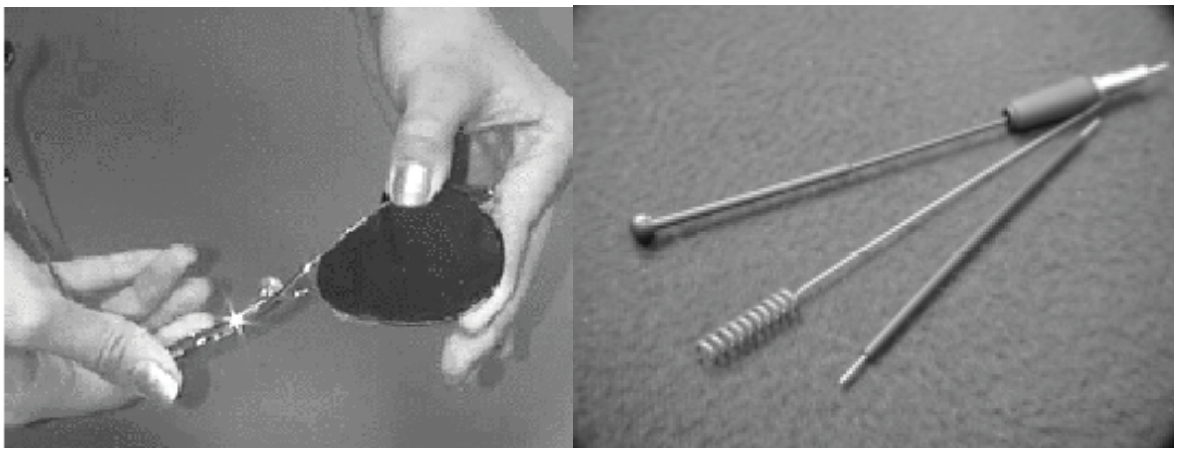

Fig. 2-46: Applications of SMAs: Superelastic eyeglass frames, cell phone antennas [2.52].

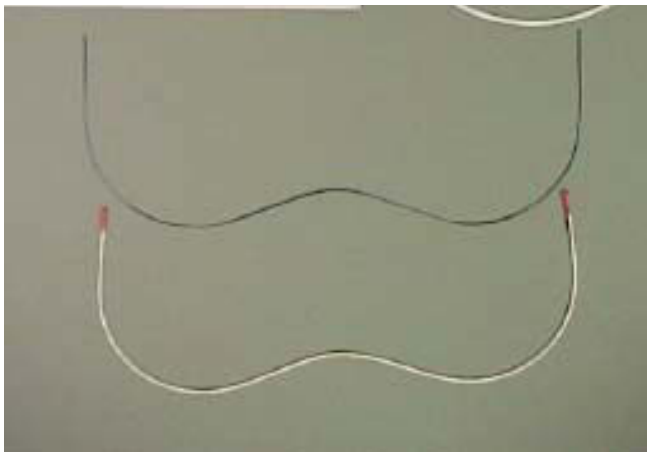

Fig. 2-47: Photographs of various designs of superelastic NiTi underwires [2.176].

Fig. 2-48: SMAs used in orthodontic braces [2.52].

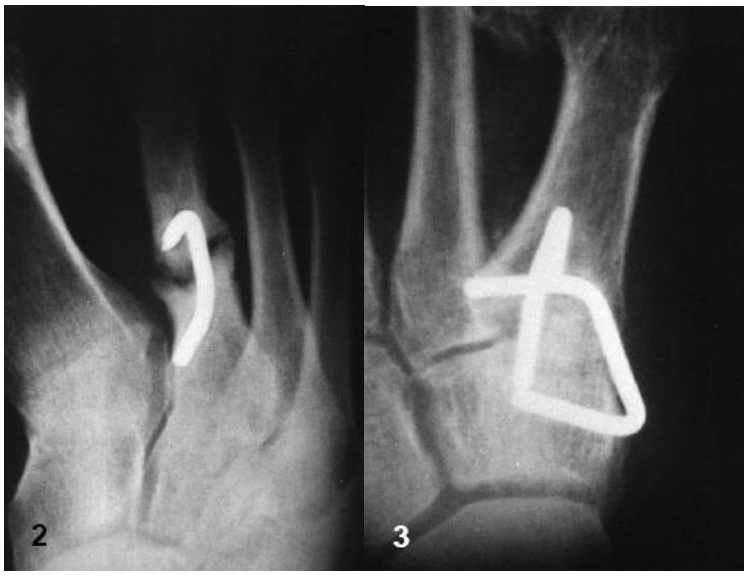

Fig. 2-49: NiTi shape memory clamps for healing broken bones [2.189].

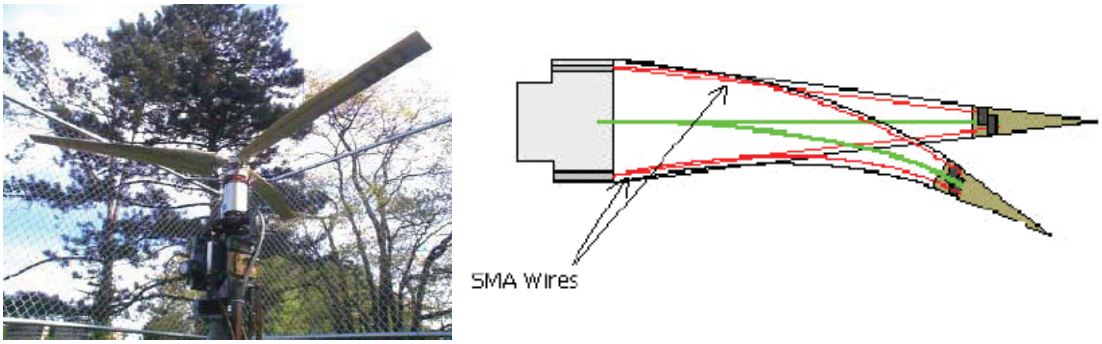

Fig. 2-50: SMAs in aerospace industry: helicopter blades and smart aircraft wing [2.52].

2.5.5 High vibration damping

Because of their excellent energy dissipation capabilities and their recentering properties (returning ability to original undeformed shape), SMAs show promise for use in seismic isolation. A study by [2.192] identified the key characteristics that a damping material used in seismic isolation should exhibit: increased stiffness at large levels of strain, a significant energy-absorbing effect at low strains, and optimal damping properties for increased levels of strain and strain rate which are consistent with SMA properties. In the martensitic form, the shape memory effect produces a high damping capacity. In the austenitic form, the superelastic response provides an energy-absorbing effect with zero residual strain upon unloading (recentering capability). Although the strain rates applied in this experiment are lower than those experienced during an earthquake, SMAs like NiTi can endure deformation to large strain levels without experiencing damage from plastic deformation. This results in an optimal recentering capability. Many current studies are investigating the application of the damping

properties and recentering potential of SMAs to seismic resistant design and retrofit. Dolce and Marnetto [2.193] have developed a device where the SMA wire is always in tension. The NiTi wires provide recentering capabilities and the steel elements provide the energy dissipation effect [2.194]

Recently, Memry Corp. developed a new type of shape memory alloy named Zeemet with high damping properties for use as inserts in golf wedges and putters (Figure 2-51). The benefits to the golfer when using a SMA club include an increased spin on the ball, greater control and solid feel. High vibration damping capacity in the martensite state takes advantage of the hysteresis behavior of shape memory materials [2.195].

Fig. 2-51: Shape memory alloy golf clubs.

CHAPTER 3

Experimental Procedures and Methods

3.1 Production Techniques

3.1.1 Materials

The precursors for the melt-spinning were prepared by vacuum arc-melting on a water-cooled groove crucible in a reduced Ar atmosphere using pure metal pieces from Ti-granules containing 99.99 wt.% titanium and Ni-chips containing 99.98 wt.% nickel and Cu-wire containing 99.99 wt.% copper, in such ratios that the final alloy compositions were Ni-50.3Ti, Ni-50.3Ti-5Cu and Ni-50.3Ti-25Cu (in at.%). Moreover, some of the NiTi-based alloys investigated in the present study were delivered from the company Fibra, Ostrava, Czech Republic. The Ni-50.3Ti and Ni-50.3Ti-2W (in at.%) alloys were provided in the form of coiled wire with a diameter of 3 mm. The wires were produced by vacuum induction melting, hot extrusion, stepwise cold-drawing and intermediate annealing. All arc-melted samples and wires had a martensite transformation finish temperature (M_f) of above 30 °C. Accordingly all samples were fully martensitic at room temperature.

3.1.2 Arc-melting

Shape memory alloys used for melt-spinning and splat-cooling were prepared from the elements with the Edmund Bühler arc-melter type AM with powerful generators for melting quantities of up to approximately 200 g. A schematic and photograph of the arc-melter used are shown in Figure 3-1. The apparatus consists of a water-cooled copper base-plate containing several groove crucibles (Figure 3-2a), a water cooled chamber, a Ti getter, and a W electrode which can move relatively freely by a pressure compensating mechanism. A 20 V DC voltage is applied between the Cu base-plate (positive pole) and the W electrode (negative pole) which results in a discharge of current (up to 400 A) and the formation of an arc. This enables temperatures of up to approximately 3500 °C to be reached in the plasma discharge [3.1]. However, the high temperatures may result in evaporation.

Ni-50.3Ti, Ni-50.3Ti-5Cu and Ni-50.3Ti-25Cu (in at. %) ingots, 7 g by mass, were produced by arc-melting, under a static inert He atmosphere (200 mbar). The Ni was cut into small pieces with the possibility of contamination reduced by treating in a $HF:HNO_3:H_2O$ = 1:4:5 solution for 5 minutes before washing with acetone and ethanol, respectively. The surface of the Cu-wire was subsequently ground on 2400 grade SiC grinding paper.

Before striking the arc, the chamber was evacuated to 1×10^{-5} mbar using a combination of rotary and diffusion pumps. The chamber was then flushed three times with argon overpressure of 200 mbar and evacuated each time to 1×10^{-5} mbar. Prior arc-melting, the Ti-getter was melted under an argon overpressure of 800 mbar to remove O_2 from the atmosphere and thereby to reduce the possibility of oxidation during melting of the samples. All ingots produced were sectioned into three parts, rotated and repositioned in the arc-melter with the ends now placed in

the centre and the centers at the ends. They were remelted and the process repeated twice to minimize macro-segregation and ensure homogeneity in the as-cast ingot (Figure 3-2b). Samples were weighed before and after arc-melting, they were used only as reliable samples if the weight loss was less than 0.2 wt.%.

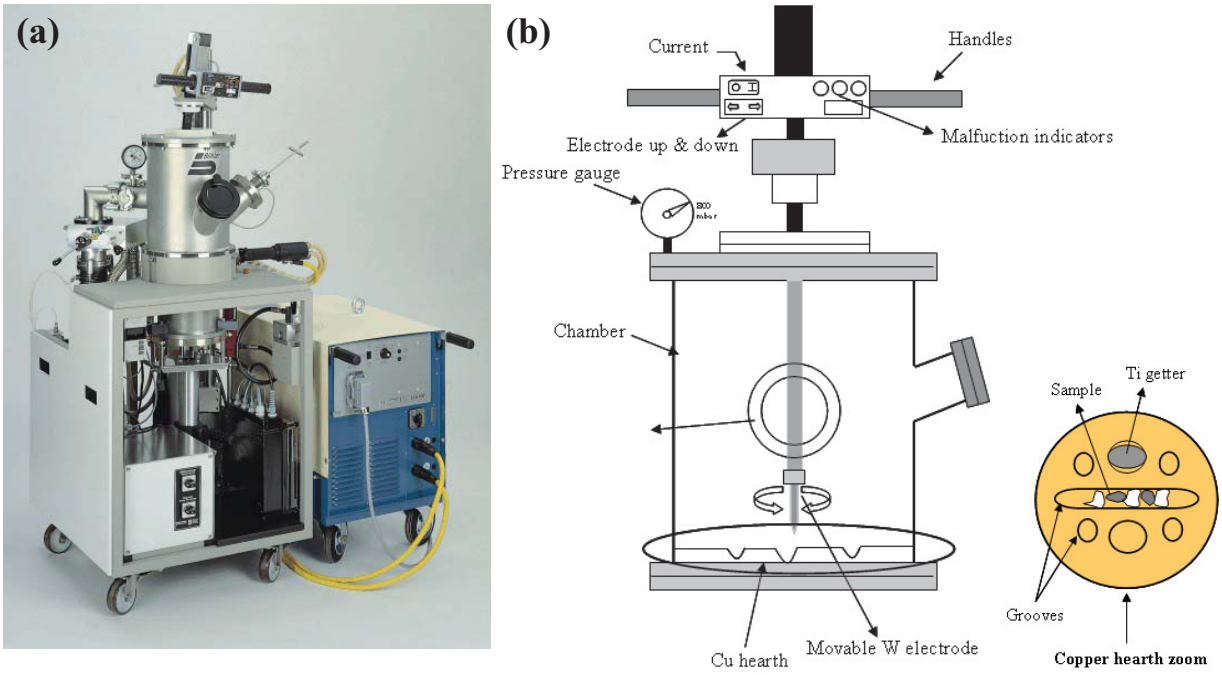

Fig. 3-1: Arc-melter type AM; (a) photograph of the apparatus, (b) schematic illustration.

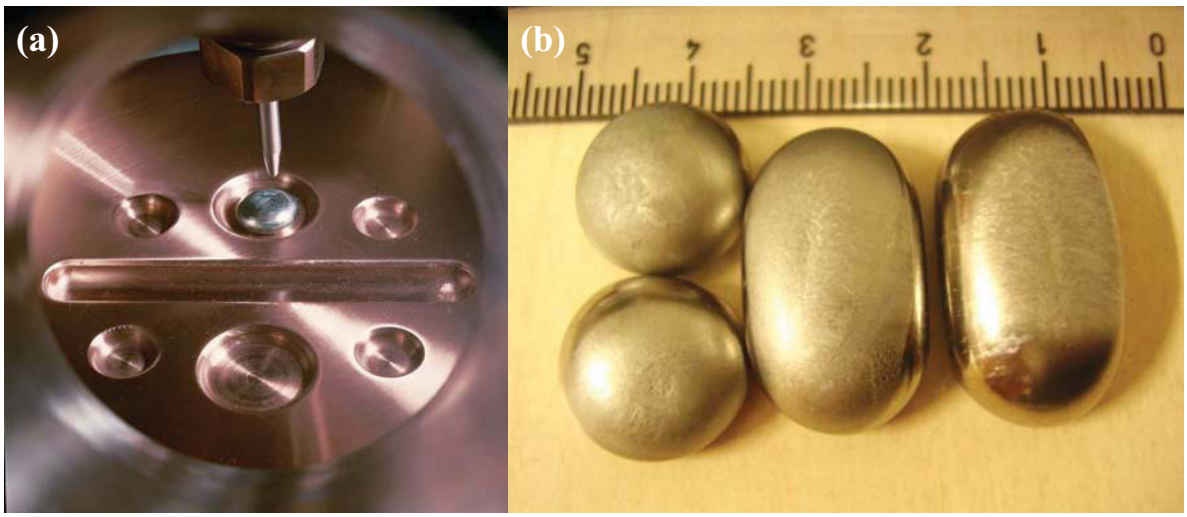

Fig. 3.2: (a) Multi-purpose button and groove crucibles in a copper base plate and the Ti getter, (b) arc-melted ingots.

3.1.3 Rapid solidification methods

The term of rapid solidification is rather vague but it is considered arbitrarily that a phenomenon is rapid solidification when the cooling rate to values higher than 10^2 K/s. Although rapid solidification techniques date back almost 40 years, application to shape memory alloys only goes back to about one decade. Duwez [3.2] used a *gun-quenching* technique for quenching the Au–Si system, where cooling rates of 10^6 to 10^8 K/s were achieved. In this process, a small liquid globule was propelled into small droplets by means of a shock wave and the droplets were sprayed on a cold copper substrate to form thin foils. These samples were irregular in shape with varying thickness from about 1 μm to 50 μm. The edges of some individual droplets were very thin (~ 100 nm) and were directly used for transmission electron microscopy. A schematic of the gun-quenching setup is shown in Figure 3-3a. The gun quenching system consists of an induction coil melting a small amount of material and a high-pressure inert-gas shockwave that splits the melt into smaller droplets and propels them against a cooling copper strip.

The piston-anvil technique or, more commonly, *splat-quenching* was developed to produce larger specimens. This technique, pictured in Figure 3-3b, reaches cooling rates of up to 10^7 K/s. Pietrokowski [3.3] designed a piston and anvil technique in which the liquid globule is squeezed between a fast moving piston and a fixed anvil. Ohring and Haldipur [3.4] modified the piston and anvil technique by arc-melting a droplet on a water-cooled substrate and quenching to a foil between a hammer and the supporting substrate, thus avoiding crucible problems encountered in handling the alloys with high melting point. The foils produced in this way were about 15–30 mm in diameter, depending on the sample volume, and relatively uniform in thickness, thus making them more suitable for structural, electrical and magnetic property measurements than the foils prepared by the gun technique. This technique is still used today for basic alloy development where a large number of different compositions are probed, as it introduces very little contamination and requires little material.

The next logical step in increasing sample size is to move from splats to ribbons. For technical applications, techniques which allow the fabrication of metals in the shape of ribbons are of great interest. The earliest potentially continuous process applied to metallic glasses was reported by Chen and Miller in 1970 [3.5]. In this two-roller or roll quenching process a molten metal is put into the gap between a pair of rapidly rotating rollers. A commonly used process is the well known *melt-spinning* technique patented by Strange and Pim [3.6], in which the molten stream is cast on the outside of a rotating wheel. The process was developed for fabricating crystalline filaments and later adopted for continuous production of metallic glass and microcrystalline ribbons [3.7]. As shown in Figure 3-3c, in melt-spinning, the molten material is extruded through the crucible nozzle onto the rotating copper wheel by applying a top pressure of gas and a long thin ribbon is produced. The alloy is melted by high frequency induction by a solenoid which surrounds a non-reactive crucible. Also it is possible to produce rapid-solidified bulk samples via traditional casting into copper molds. Copper has been used throughout due to its excellent heat conduction and relatively cheap cost compared to silver. The general

schematic for a *casting-box* is depicted in Figure 3-3d, illustrating (1) the induction coil to heat the sample; (2) the quartz tube to hold the sample; and (3) a copper mold to quickly cool the sample. Copper molds are not usually water-cooled, but instead made oversized so that the thermal mass of the mold is sufficient to cool the sample [3.8].

Some common demands for quenching method are: reproducibility, sufficient quench rate, a significant extension of solid solubility, grain refinement and the consequent decrease in transformation temperatures, reduced micro-segregation and allowance of grain refiner and other ternary alloys to be introduced into the melt.

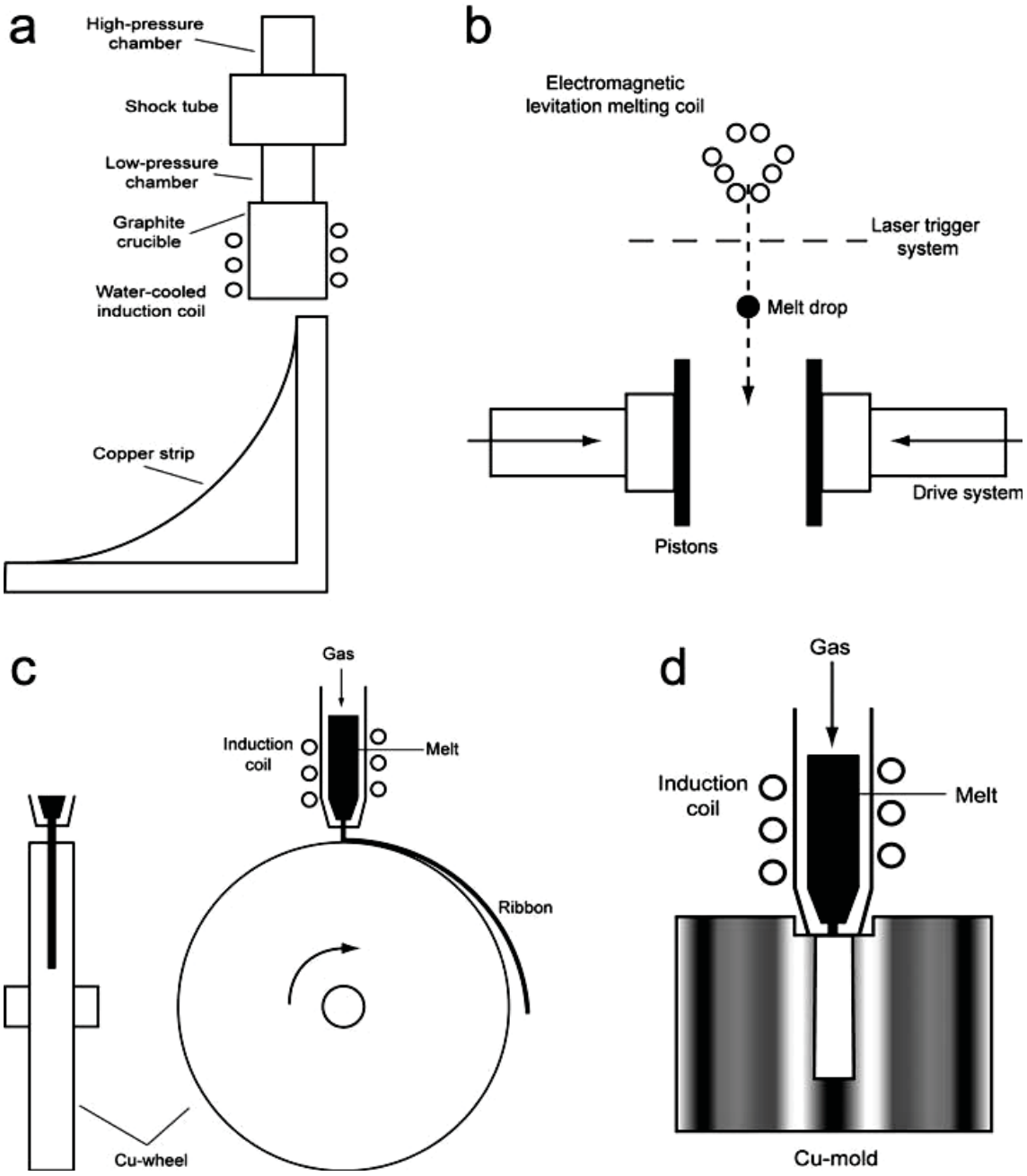

Figure 3-3: (a) Gun-quenching system, (b) splat-quenching system, (c) melt-spinning technique, (d) casting-box concept for laboratory production [3.8, 3.9].

3.1.3.1 Melt-spinning

Melt spinning systems are designed to produce amorphous, metastable and microcrystalline metallic ribbons under varying atmospheric conditions. Two forms of melt spinning have evolved; one for the formation of wire and the other for ribbon:

- Free Jet Melt Extrusion (wire)
- Chill Block, Free Flow Casting, Planar Flow Casting (ribbon)

Of its two forms, chill-block is commonly found in research laboratories whereas planar flow is predominantly used in industry due to the large tonnages that it can produce. In chill-block melt-spinning, the sample is inductively melted in a non-reactive crucible (quartz, graphite, or boron nitride) with a nozzle in the bottom and then ejected via inert-gas pressure onto a rotating copper wheel. A long thin ribbon is continuously produced, and by varying casting pressure and wheel speed, samples of 10 to 200 μm thickness can be fabricated. This technique has been commercialized and ribbons several centimeters wide and several meters long are possible. The nozzle in the bottom of the crucible traditionally has a circular shape that produces a melt stream with a diameter ~1 mm. Ribbons can be produced by slotted shape nozzles or a series of circular or slotted nozzles with overlapping melt puddles. Sheet widths up to 300 mm have been made with such configurations [3.10]. The amount of heat that has to be removed from the casting, decreases with decreasing ribbon thickness. Hence, the wheel speed can control the cooling rate of the ribbon in chill-block melt-spinning. The cooling rates obtained in melt-spinning are usually in the range of 10^5-10^6 K/s [3.11].

The mass of alloy must not stand much over the position of the RF coil. This mass being processed affects the outcome of the melt-spinning operation, in that due to the nature of the heating via an RF coil, there exists a temperature profile within the melt. Since the temperature is measured from the top surface of the molten mass, variance in the alloy mass can translate into significant temperature differences between the top surface and the bulk of the alloy. This difference is important because the temperature of the melt before ejection is one of the most important control parameters of the process. The temperature affects the viscosity of the melt, which determines how the material will flow from the crucible and the formation of the melt puddle (Figure 3-4). If the temperature of the melt were too high, pellets and brittle small flakes would be the result. If the temperature were too low, the result would be very brittle sections of ribbons with a very uneven surface that would crumble upon handling [3.12].

Generally, the solidification process of the ribbons can be extremely sensitive to small changes in any of the numerous existing parameters for the development. Factors such as wheel speed, the temperature of molten metal, the size of the nozzle or overpressure affect the ejection viscosity of the fluid and the thickness of the ribbon. Other variables such as material of the wheel and the distance between it and the outlet influence adherence and quality of the ribbon. Some of the parameters [3.13] which are important in the melt-spinning method of quenching the melt are discussed below:

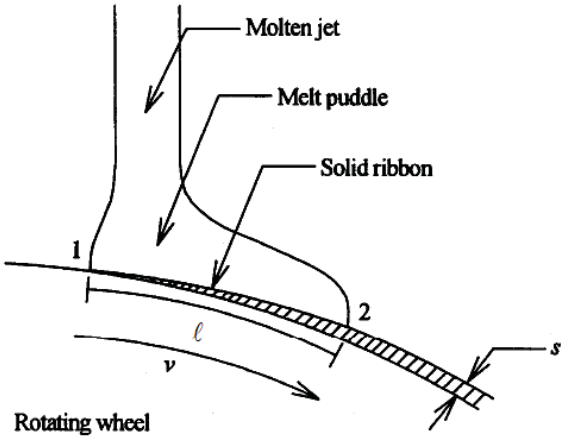

Fig. 3-4: Schematic drawing of the melt puddle and ribbon formation during melt-spinning [3.10].

Wheel: The melt spinning process is dependent upon the rapid removal of heat from the molten material by an appropriate heat sink, i.e. the wheel. The wheel material is therefore important to the process, since different materials have different heat transfer coefficients. The primary goal is to select a wheel material which will transport heat swiftly and continuously away from the ribbon. Common materials used for wheels in the melt spinning process are copper (Cu), copper-beryllium alloy (Cu-Be) and stainless steel. But copper, because of its excellent heat conducting properties and relatively cheap cost compared to silver, is the material most commonly used. Copper molds are not usually water-cooled, but instead made oversized so that the thermal mass of the mold is sufficient to cool the sample. In fact, the high heat conductivity of copper renders additional cooling unnecessary. Also it is possible to use the stainless steel wheel to obtain the lower cooling rates. The wheel of stainless steel has a lower thermal conductivity than the copper wheel, and due to this a lower cooling rate is obtained at the same wheel speed. The surface finish and cleanliness of the wheel greatly influence the quality and form of the cast ribbon, since imperfections on the wheel surface can act as disruptions for the formation of a stable melt puddle on the surface of the wheel. This is important for the production of a uniform ribbon as pointed out by Kavesh [3.14]. The distance of the crucible from the wheel and the angle of impingement of the crucible also affect the formation of a stable "melt puddle". Continuous use of the wheel creates a problem of surface wear. However, this problem may be circumvented by refinishing the wheel following each use.

Wheel Speed: The wheel speed controls the quenching rate and as such is the most important parameter in the melt-spinning technique. Increasing the rotation speed of the wheel decreases the thickness of the ribbon. Other factors that can influence the cooling rate is, the thermal conductivity across the casting/chill-block interface (modified by surface treatment of the chill-block), the thermal conductivity of the material in the chill-block, and the thermal conductivity of the atmospheric gas.

Chamber Atmosphere: Dependent on the physical and chemical properties of the alloy, melt-spinning may be carried out in vacuum or in an atmosphere of air, inert gas, or reactive gas. Alloys susceptible to oxidation are cast in vacuum or in an inert gas atmosphere. Chamber

atmosphere affects the smoothness of the surface and edges of the ribbon. Alloys cast in helium may have smooth, even edges and wheel-side surfaces which mirror the wheel surface. The same alloys cast in argon may have jagged edges and wheel-side surfaces exhibiting indentations [3.13].

Ejection Pressure: Gas pressurization is used to eject the molten alloy from the crucible. Generally, an inert gas is used. Ejection pressures (typical gauge pressures between 5 and 70 kPa [3.13]) are dependent on the desired melt delivery rate. High ejection pressures improve the wetting pattern and, consequently, the thermal contact of the melt with the wheel.

Melt-spinning was performed with a lab built melt-spinner and also two melt-spinner types manufactured by Edmund Bühler in Germany. A schematic of the melt-spinning apparatus is shown in Figure 3-5. The apparatus consists of an induction coil, Cu wheel, and a crucible all of which are contained within a chamber, as can be seen in the Figure. According to the melting point of the sample different crucibles were used. Quartz crucibles resist temperatures up to 1400 °C, boron-nitride up to 1600 °C and graphite up to 1900 °C. Crucibles had nozzle diameters between 0.9 and 1.5 mm and were placed inside a sealed chamber and positioned between 0.6 to 20 mm (mostly 2 mm) above a polished copper wheel (200-250 mm diameter) which was refinished with fine sandpaper and cleaned with alcohol following each use. The distance between crucible and wheel was obtained empirically and is mostly related to the viscosity of the melt. It is worth noting that in contrast of the quartz crucible which does not expand upon heating, when BN or graphite crucibles were used then the thermal expansion occurred, and so a larger initial distance between the wheel and the nozzle had to be set.

The alloys were placed in either a ceramic crucible such as graphite, BN and Al_2O_3 crucible or a quartz crucible coated internally with different coatings such as Y_2O_3, ZrO_2 (sprayed and liquid coated). Y_2O_3 was chosen as it has one of the highest affinities for oxygen of any element at temperatures below 1600 °C, making Y_2O_3 the most stable oxide in this temperature range. The graphite and boron-nitride crucibles were used when the melting point is above 1400 °C and the melt was held for longer time, to prevent Si from the quartz crucibles diffusing into the alloys. These conditions were used to reduce the possibility of oxidation of the ribbons and reactions with the solidifying melt and other gaseous elements or foreign particles.

A combination of rotary and turbo/diffusion pumps provide a high vacuum down to 1×10^{-5} mbar. Before melting the ingot, the chamber is refilled with helium to 200 mbar. Helium is the most suitable gas due to its high heat transfer at low pressures and low kinematic viscosity which gives good gas flow stability. The water-cooled radio frequency induction coil was powered by a medium-frequency generator of 5 to 25 kW, depending on model. The high voltage of the RF field facilitated stirring. The reduced He atmosphere and low ionization in the coil reduced the risk of spark.

Ingots (~7 g) were heated to their melting points, determined from phase diagrams, and an additional super heat of 50-250 °C applied to reduce viscosity thereby reducing problems associated with ejection. The molten alloys were ejected using a pure argon gas overpressure of ~90 to 200 mbar within the crucible onto the cold rotating Cu wheel having a wheel speed of 5 to 45 ms^{-1} to form the ribbon. This resulted in rapid quenching with cooling rates of 10^3

to 10^5 Ks^{-1} being achieved. The cast ribbon was guided towards a collecting box placed near the melt spinner in the direction in which the copper wheel is rotating. When the wheel speed is too slow, no ribbons with a rectangular cross-section were produced, but the material was shaped more like a rope. The distances between the nozzle and the wheel surface were 0.6 to 20 mm. Figure 3-6 shows the transformation of the arc-melted ingots to melt-spun ribbons via the melt spinning processing. It was observed that the quartz crucible reacts with the materials at temperatures above 1400 °C even after coating with Y_2O_3. As can be seen in Figure 3-7, the color of ribbons changed from yellow to violet and to blue. For high temperature melt-spinning, the best results were achieved using a graphite crucible. Table 3-1 gives a description of the specimens and melt-spinning parameters.

The temperature was monitored by an external infra-red pyrometer from the upper surface of the molten alloy through a quartz window. Overheating of the molten metal is one of the major factors and most sensitive parameters affecting the quality of the ribbons and their subsequent mechanical behavior. It is possibly due to the variation of viscosity fluid in terms of temperature. However, there are numerous other factors that may have greater or minor contribution to the different results. For example, the wheel speed only controls the thickness of the film, while ejection temperature can vary the adhesion and thermal conductivity of the molten material, the distance between the hole and wheel, the dimensions of the hole and the uniformity of the product. In addition, to aid the preparation of TEM foils, it was necessary to produce at least 3 mm wide ribbon. Ribbon width can be increased by decreasing the crucible distance above the wheel, increasing the ejection pressure, increasing the nozzle diameter of the crucible, the ejection temperature or by reducing the wheel speed. It was found that increasing the ejection pressure had the largest effect on increasing the ribbon width.

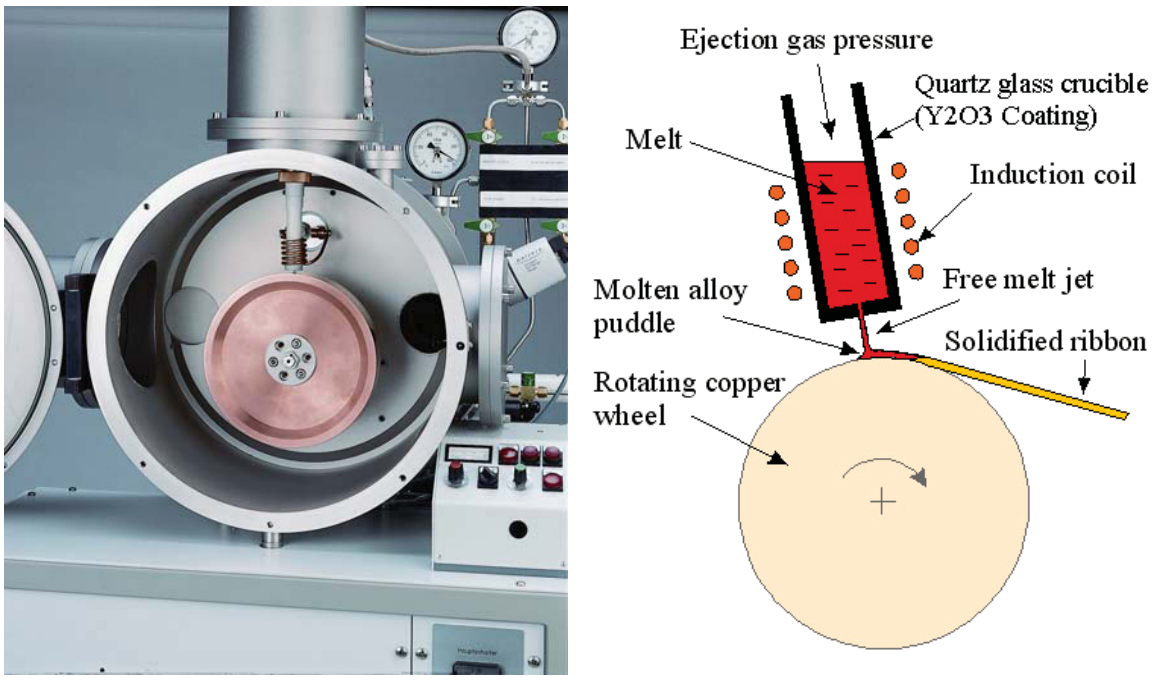

Fig. 3-5: The melt-spinner; (a) photograph of the chamber, (b) schematic illustration of apparatus.

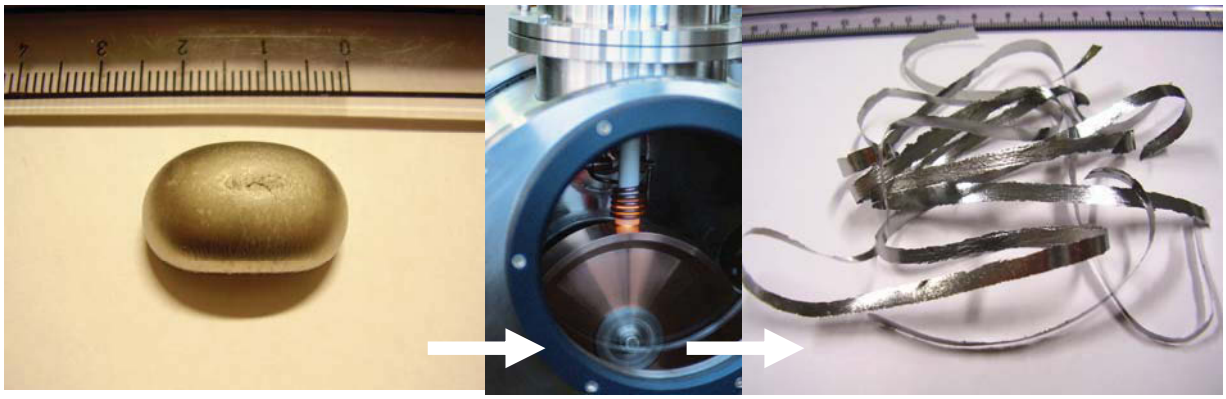

Fig. 3-6: Processing steps of transformation from the arc-melted ingots to melt-spun ribbons.

Fig. 3-7: The brittle melt-spun ribbons occurred after reaction between NiTi alloy and quartz crucible at temperatures above 1400 °C.

Table 3-1: The description of the specimens and melt-spinning parameters.

No.	Composition	Crucible	Crucible/Wheel Distance mm	Nozzle Size mm	Chamber Pressure mbar	Ejection Pressure mbar	Wheel Speed m/s	Melting Temperature °C
1	NiTi	Coated Quartz	0.6, 1, 2, 7, 20	1, slit	800	150	5-30	1350-1400
2	NiTi	BN	0.6, 1, 2	1.5, slit	800	120	15-30	1400-1450
3	NiTi	Graphite	0.6, 2, 4	1.5	800	200	15-30	1450-1500
4	NiTi2W	Graphite	0.6, 2, 4	1.5	800	200	15-30	1550-1600
5	NiTi5Cu	Coated Quartz	0.6, 2	1, 1.5	800	150	15-30	1350-1400
6	NiTi25Cu	Coated Quartz	0.3, 0.6, 2	1, 1.5	800	150	10-50	1300-1350

3.1.3.2 Splat-cooling

Splat-quenchers utilize an electromagnetic levitation coil, which without a container holds and melts the sample. When the current is switched off, the free falling droplet of the melt is pressed into a thin film between two copper pistons that are shot against each other.

In this work, thin sheets (splats) of rapidly solidified shape memory alloy were produced under vacuum of ~1×10^{-5} mbar using a Buehler GmbH twin piston splat-quencher, as can be seen in Figure 3-8. The necessary alloys were prepared from ingots which were cut into cubes of approximately 2×2×2 mm^3 (80-200 mg) and were inductively levitated and molten by compact RF generator in an evacuated chamber (Figure 3-9a). As soon as the power supply of induction heating is switched off, the melt droplet (Figure 3-9b) falls down passing an optical sensor (a laser light barrier) which triggers the rapid closure of a horizontally positioned pair of high-velocity copper pistons system driven by solenoids (Figure 3-9c). The principle of splat-cooling is illustrated in Figure 3-9d. The melt droplet is flattened and quenched rapidly between the piston surfaces which have a high thermal conductivity. The cooling rate during solidification of a molten alloy strongly depends on the sample dimension and the piston material in which the heat is conducted. The resulting disks are shown in Figure 3-10.

Fig. 3-8: Splat-quencher apparatus [3.1].

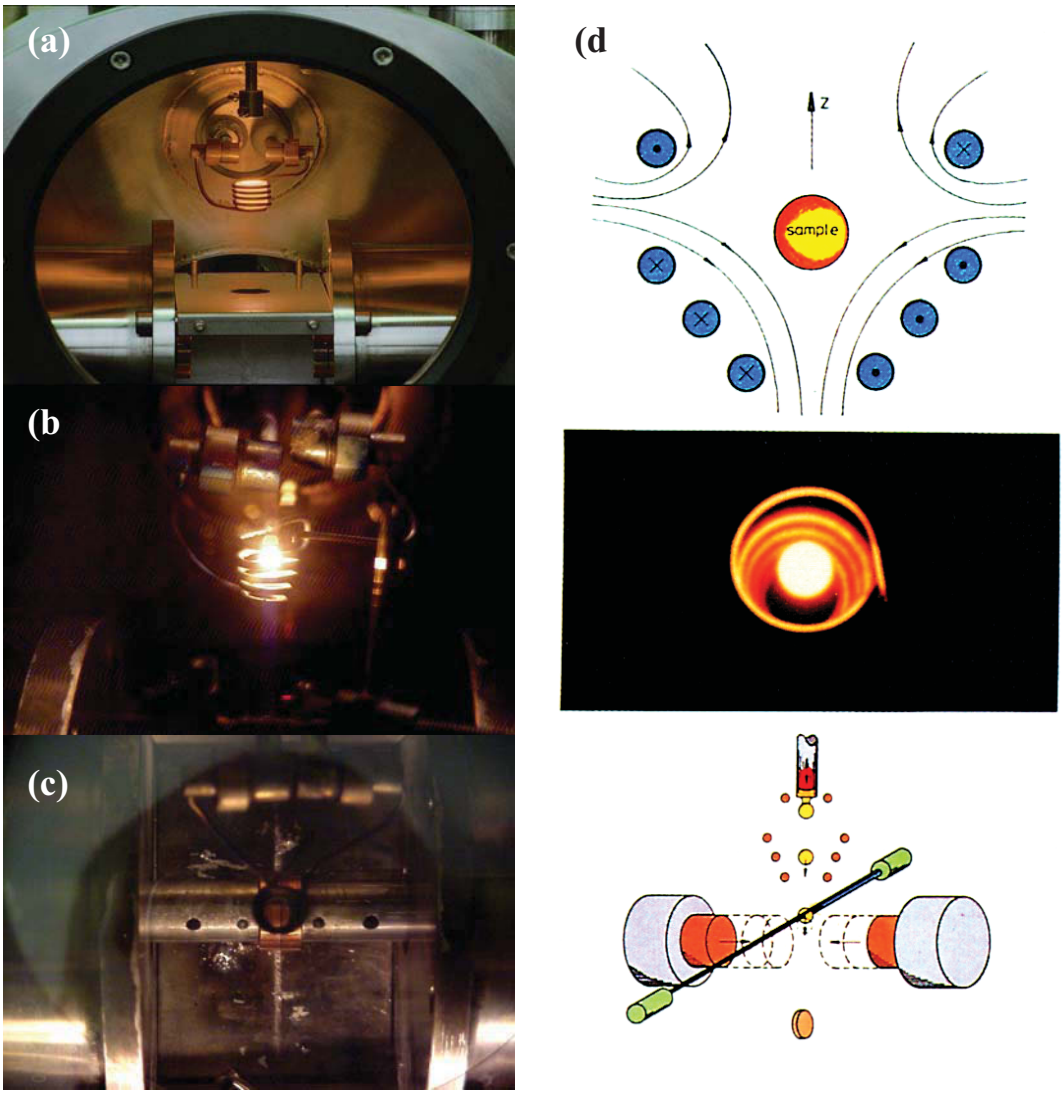

Fig. 3-9: (a) splat-cooling chamber, (b) levitated sample, (c) impacted copper pistons, (d) splat-cooling principle [3.1].

Fig. 3-10: NiTi disk produced by splat-cooling.

3.2 Characterization techniques

A variety of characterization techniques were used in this work. The primary techniques are those of Differential Scanning Calorimetry (DSC), and microstructural characterization. The composition and state of the compounds were characterized by means of X-ray diffraction (XRD) and Energy Dispersive X-ray Microanalysis (EDX) (or energy dispersive spectrometry (EDS)). The sample preparation and operating conditions were standardized as far as possible for parallel comparisons. These techniques are employed to study, both qualitatively and quantitatively, the effects of grain size, alloying elements and training. Brief descriptions of each of these methods are given in the following sections.

3.2.1 Differential scanning calorimetry (DSC)

Phase transformations in the shape memory alloy in the unstressed condition were investigated using differential scanning calorimetry (DSC). The versatility of DSC as an experimental technique is reflected in its ability to obtain data, which can yield valuable information on phase transformations, purity, kinetics, crystallinity and heat capacity [3.15].

There are two types of DSC instruments available: power compensated differential scanning calorimeter and heat flux differential scanning calorimeter. Despite operating differently, the underlying principle behind the function of either type of instrument remains the same. In a differential scanning calorimeter, there are usually two specimens: the sample of interest and a suitable reference material (can be an empty reference crucible). The basic principle of DSC operation is that as a sample undergoes a heating cycle, it may undergo both exothermic and/or endothermic phase transformations. These phase transformations either require or liberate energy (in the form of heat) as they occur. An exothermic reaction is one in which heat is liberated by the sample, and an endothermic reaction is the opposite, heat is required by the sample in order for the reaction to take place. The DSC can quantify this liberation/requirement of heat, which allows one to determine the nature and extent of the reaction taking place. An example of an endothermic and exothermic phase transformation are, respectively, the melting and solidification of a metal.

A power compensation differential scanning calorimeter operates under the principle that the heat flow to both the sample and reference side should be maintained the same (within allowable tolerances). Therefore, any variation in heat flow between the sample and reference side due to a thermal event, is recorded as a temperature difference (ΔT). A heat flux differential scanning calorimeter operates differently than a power compensated differential scanning calorimeter in that the sample and reference side of the instrument should be maintained at the same temperature (within allowable tolerances). As a thermal event occurs, more or less heat is required (depending on the nature of the thermal event) by the sample side to maintain its temperature with the reference. This variation in heat requirement to maintain a

minimal temperature difference between both sample and reference is recorded as heat flow (mW/mg) as a function of sample temperature.

Heat is transferred through the disk to both the sample and reference. The difference in heat flow is monitored by the device. An increase or decrease in temperature of the sample changes the electro-potential, which is converted to a signal and displayed graphically. Figure 3-11 shows schematically the method used to determine the temperatures and the heats. As shown in the Figure, the thermal transformation characteristics of the material measured by DSC are as follows:

M_s: martensite start temperature; A_s: austenite start temperature;
M_p: martensite peak temperature; A_p: austenite peak temperature;
M_f: martensite finish temperature; A_f: austenite finish temperature;
Q_m: heat of martensitic transformation; Q_a: heat of austenitic transformation.

The transformation temperature, for instance, the As temperature, is extrapolated from the intersection between the slope of the curve (line a in Figure 3-11) and the baseline. The transformation heats (the enthalpy of transition) are calculated by integrating the area under the peak obtained in the experimentally-determined heating or cooling curve in the temperature range M_s to M_f or A_s to A_f. The temperatures determined by the extrapolation method are not the exact transformation temperatures according to standard definition. However, the extrapolation method is convenient for practical applications and is therefore widely accepted and used [3.16].

In this work, differential scanning calorimetry (DSC) measurements were used to investigate phase transformations of shape memory alloys. The NiTi-based samples were heated from -40 °C to 200 °C and then cooled to room temperature, in order to resolve the martensite to austenite phase transformation, as well as the reverse phase transformation of austenite to martensite, on the DSC. The experimental work of this research was performed using a heat flux differential scanning calorimeter: Mettler DSC 821e instrument (Mettler Toledo GmbH, Schwerzenbach, CH). Thermograms were recorded under static air from –40 to 180 °C. A circular sample disk was cut with a punch, put in a 20 µl aluminium pan, and sealed with a perforated lid. Reference pans were produced in an identical manner but without the sample.

The samples for the DSC measurements were cut by scissors for ribbons and by a low-speed diamond saw into a nearly cubic or rectangular shape for arc-melted or other samples, followed by chemical etching in a solution consisting of $HF:HNO_3:H_2O=1:4:5$ in order to remove the oxide layer. The weight of the samples varied from 2-3 mg (ribbons) to 8-9 mg (bulks). 10 cycles were run for each sample and the results were usually obtained from the second cycle. The first cycle was used to stabilize the response and to identify any peaks associated with sample preparation. To find the most proper heating/cooling rate for the alloys, the transformations were obtained by measuring the DSC curves at various cooling/heating rates from ±5 to 50 °C/min. From the measured DSC profile, the transformation temperatures and the transformation heats were calculated by the equipment software packages. Finally, the heating or cooling rate was mostly taken to be ±20 °C/min, which is widely used for the investigation of the transformation of SMAs.

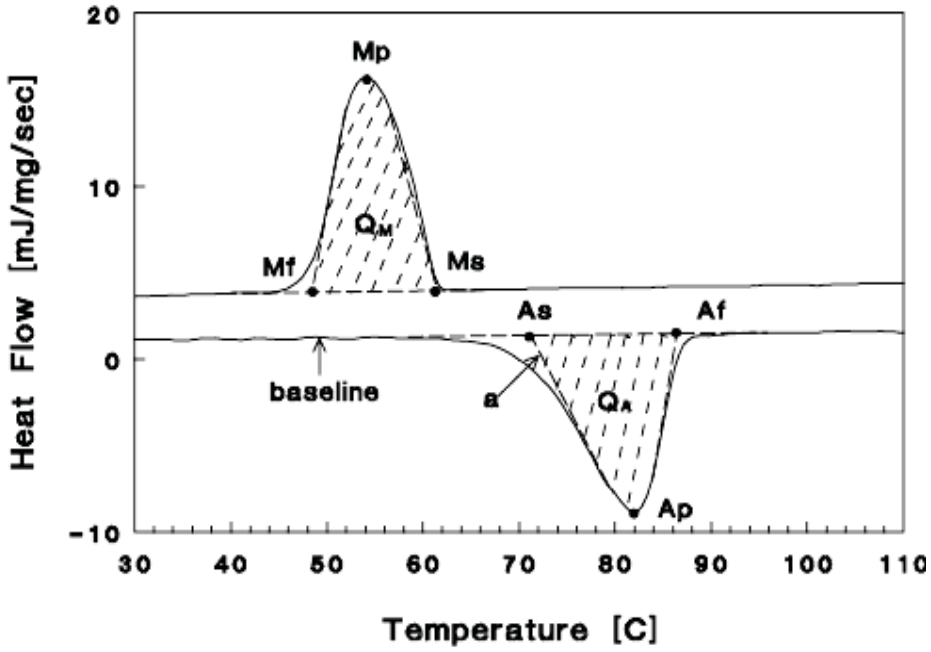

Fig. 3-11: A schematic description of the method for determination of the transformation temperatures and the transformation heats in a DSC profile [3.16].

3.2.2 X-ray diffractometry (XRD)

X-ray diffraction (XRD) was used to identify and analyze atomic structure and the present crystalline phases of the NiTi-based ribbons before and after thermomechanical treatment at room temperature. A Siemens D500 diffractometer in the Bragg-Brentano (θ–2θ) geometry with filtered CuKα radiation was used. The X-ray tube voltage was set at 40 kV, and the current was set at 25 mA with a wavelength (λ) of 0.1542 nm. Angles between 20° and 120° (2θ) were scanned using a step size of 0.02° (2θ) every 1.2 s.

Since it was the aim to measure the XRD-spectra of certain thermomechanical conditions, the specimens could not be pulverized for these investigations. On the other hand, the sections of the ribbons were too small to carry out XRD investigations properly. Consequently, some strips of one ribbon, each one approximately 15 mm in length, were embedded tightly aligned and placed on a flat glass substrate, with either the wheel or free side facing up, as illustrated in Figure 3-12. The ribbons were carefully leveled with the rim of the holder to prevent double diffractions from occurring. A reference using glass and paste was analyzed to determine the shape of the background trace.

Decreasing crystallite sizes are associated with a broadening of Bragg reflections. For use in very thin ribbon analysis the glancing angle (θ) must be small due to the lack of atoms available for scattering. Smaller glancing angles make the sample seem thicker to the XRD system. Additionally, counting times must be large. Also because of the small diffracted intensity, thin films generally require data acquisition as an average of a large area in contrast to bulk materials. A qualitative evaluation of the percentage of crystallinity for each structure can be

obtained through the intensity of the peaks. The larger peaks indicate higher crystallinity. In order to be able to compare between films, relative intensity must be used where the intensity is scaled relative to the major peak.

An amorphous film is indicated by the lack of distinct peaks, while polycrystalline films may produce several peaks. Depending on the crystal structure or orientation of the sample, certain diffraction angles will produce a more intense signal. The position and relative intensity of the resulting peaks can be indexed to provide detailed information about the crystal structure of the material. However, indexing diffraction peaks can be challenging, even for homogeneous ribbons and several factors can shift the location of the peaks relative to 2θ. These include factors such as glancing angles, X-ray type and internal stresses. Any residual stress present in the ribbons can distort the crystal structure and produce a resulting shift in the peaks [3.17].

Crystalline phases were identified by comparing the XRD peaks and intensities with those listed either in the International Centre for Diffraction Data Database files. Diffraction Data Database files and analyzing software were not available for all of the NiTi-based alloys; therefore, the measured spectra were indexed by comparison with corresponding XRD-spectra in published graphs or those listed in the literature.

Fig. 3-12: A melt-spun ribbon fixed on the glass sheet for the XRD investigations.

3.2.3 Microstructure evaluation methods

The shape memory alloys were initially examined with optical microscopy (OM) to study the microstructure. Scanning electron microscope (SEM) and transmission electron microscope (TEM) have been utilized to investigate the microstructures of rapid solidified materials since the grain sizes are quite fine and microstructure can be poorly characterized by OM due to the formation of submicron grains. A picture of the overall microstructural development at a large scale can be obtained also from SEM, and the whole ribbons can be observed instead of just the very thin edges of the samples in the TEM.

One benefit of TEM over other evaluation techniques is its high spatial resolution as a result of a highly focused electron beam. A second advantage is TEM's ability to get both images and diffraction patterns using the same sample. The primary disadvantage of TEM is the time and cost associated with producing TEM samples. Samples that are suited for evaluation must be less than 200nm thick. The two sample preparation techniques that are available for preparation of TEM samples are grinding/ion milling and electro polishing techniques.

3.2.3.1 Optical Microscopy

The fundamental requirement for a good resolution of details, using reflected light microscopy, is an accurate preparation of samples. The used light microscope was of the type Reichert Univar with a magnification of the object between 50× to 2000×, fitted with a CCD color video camera for further picture processing.

Specimens for metallographic investigation were cut from the arc-melted ingots, splat-cooled disks and longitudinal cross-sections of melt-spun ribbons. All mounted OM samples were mechanically ground on SiC grit paper to a final mesh size of 4000 and polished with 3 μm, 1 μm alumina powder and OP-S suspensions sequentially. The samples were etched initially with conventional and wipe-etching in a typical solution of NiTi alloys containing $HF:HNO_3:H_2O$ = 1:4:5 and then compared with various other etching solutions with compositions of 120 ml H_2O, 15 ml HCl, 15 g $Na_2S_2O_5$, 10 g $K_2S_2O_5$, 2g NH_4HF_2 (Fig. 1b) and 100 ml H_2O, 25 ml C_2H_6O, 2g NH_4HF_2 (modification of Weck's reagent). Then the samples were studied by optical microscopy using interference contrast. The etching times were between 2 and 15 seconds.

In many shape memory alloys, the martensite plates are simply viewed through an optical microscope. NiTi however exhibits fine plates that cannot be easily examined through an optical microscope, especially after rapid solidification methods. It is therefore important to prepare samples of NiTi very carefully, since normal grinding and polishing can sometimes disturb the martensitic microstructure. Only after very careful polishing and etching the true microstructure could be revealed.

3.2.3.2 Scanning Electron Microscopy (SEM)

Scanning electron microscopes offer the next level of magnification beyond optical microscopes and are widely used to study the microstructure and the chemical composition of organic and inorganic materials. They have the ability to produce highly magnified images through rastering of focused electrons onto the surface of a material. The electron beam, focused by an electromagnetic lens system, is scanning across the sample's surface, which is located in an evacuated specimen chamber. Due to the interaction between electron beam and sample several signals are generated, which can be measured by various detectors. These signals provide information from the topography, the chemical composition and the microstructure. The capacities of SEM include imaging using secondary electrons, imaging through backscattered electrons or compositional analysis using X-rays. One of the primary advantages of SEM over other imaging systems such as transmission electron microscopes (TEM) is the ease of sample preparation. For use in a SEM system there are few requirements except that the sample must be vacuum compatible and that it must be conductive or covered with a thin conductive layer such as gold.

A Zeiss Evo 50 (Oberkochen, Germany) scanning electron microscope (SEM) was used to study the grain boundaries, martensitic microstructure and fractured surface of ribbons after tensile test. SEM equipped with energy dispersive spectrometer (EDS) and with wavelength dispersive spectrometer (WDS) was used to examine the second phase particles in NiTi-based materials. The rapidly solidified materials were imaged by means of different modes to represent the crystallographic grain structures and the size of particles in the materials: secondary electron (SE) and back scattered electron (BSE) images yielding a phase specific contrast. Throughout the analysis, the acceleration voltage was 30 kV.

The SEM-specimens were mounted in a conductive compound and cross-sectional analyses were carried out on polished and etched samples prepared by conventional metallographic procedures. The same OM sample preparation recipe and etchant solution are used to prepare samples for SEM; however, occasionally they were not etched in order to investigate only the second phase particles without mixing them with the matrix microstructure. The technical specifications of the SEM are as given in Table 3-2:

Table 3-2: Technical specifications of the scanning electron microscope.

Filament type	LaB6 and tungsten
Resolution	2 nm with LaB6, 3nm with W
acceleration voltage	max. 30 kV
Magnification	5 to 100.000 times
Detector	SE and 4 QBSD
max. screen resolution	3072 × 2304 Pixel

3.2.3.3 Transmission Electron Microscopy (TEM)

Transmission Electron Microscopy (TEM) is a microscopy technique where electrons are transmitted through the sample. Images can be obtained through the bright field (BF) and dark field (DF) modes according to the electrons used for imaging. A bright field image is formed from the directly transmitted beam, and a dark field image is formed in an opposite manner through imaging a set of diffracted electrons, which is very useful to study grain orientations or the morphology and distribution of the grains of a particular phase. The TEM has the capacity of collecting structural information in Selected Area Diffraction (SAD) mode from a region as small as ~1 μm in diameter, and further down to about 9 nm when Convergent Beam Electron Diffraction (CBED) is used. TEM is generally equipped with Energy Dispersive Spectroscopy (EDS) and Electron Energy Loss Spectroscopy (EELS) detectors, and based on which, element identification can be easily done. The EDS can only be used to identify elements with atomic number greater than 5, and is suitable for heavy elements and also the only choice if the tested regions are too thick for electrons to penetrate. On the contrary, EELS has better spatial resolution and is more suitable for light elements' identification [3.18]. In the TEM, the specimen holder allows the user to tilt the specimen to certain angles in order to establish the desired diffraction conditions. The resulting image shows diffraction contrast, which highlights faults in the crystal structure clearly.

The submicrostructure of the melt-spun ribbons was investigated on a Philips CM12 TEM microscope operated at an acceleration voltage of 120 kV. Thin disks with a diameter of 3 mm were punched from the ribbons and prepared by mechanically grinding on both surfaces to a thickness of approximately 60 μm using 1200, 2400 and 4000 grade SiC grinding papers before electro-polishing. NiTi-based ribbons were twin jet electro-polished in an electrolyte solution consisting of 20% sulphuric acid and 80% methanol at 273–278 °K at 20 V, according to [3.19]. This results in a mirror-like polished surface. If the voltage is too low etching occurs but if it is too high it results in pitting. This is shown graphically, in terms of current density against voltage, in Figure 3-13 [3.20]. Ion-milling was then performed on the samples for 30 minutes using a dual ion beam miller with Ar atmosphere. The energy of the Ar+ ions was 3.6 keV, the angle to the surface of the specimen was ±4°, and the specimen was kept at a rotation rate of 3 rpm during ion-milling; a rotating stage to ensure uniform thinning.

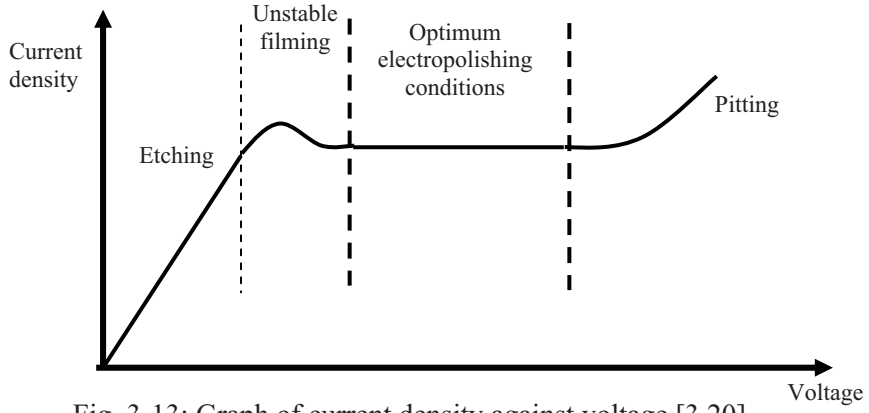

Fig. 3-13: Graph of current density against voltage [3.20].

3.2.4 Mechanical Testing

3.2.4.1 Microhardness

Hardness measurements were used to obtain information about mechanical properties (e.g. elastic modulus, strength) of different phases. Polished longitudinal cross-sections samples were used. The principle of classic microhardness testing can be described as static perpendicular penetration procedure into the samples surface. The method of hardness measurement is forcing slowly (during a defined period of time) a diamond indenter of specific geometry into the pre-polished surface of the samples. After removing the indenter, the Vickers hardness number (HV) is determined by measuring the length of the diagonals of the developed indentation and applied load. The geometry of the indenter is a square based pyramidal diamond with face angles of 136°.

The device used for hardness evaluation of the ribbons and bulk material was a microhardness measuring instrument 3212 from Zwick, fitted with a Vickers indenter. The measurements can be performed which the various force levels of HV5, HV1, HV0.5, HV0.3, HV0.2 and HV0.1. Mean values and standard deviations were determined using average of at least 5 measurements per sample after removing the highest and lowest values. The indents were set in appropriate distances taking into account the impact of the indent deformation zone.

3.2.4.2 Uniaxial Tensile Testing

Tensile tests were performed to obtain basic information on the strength of NiTi-based alloys. Tensile specimens with gauge size of 20–30 mm in length and 2-4 mm in width were cut from the melt-spun ribbons and performed using a miniature tensile device built by Kammrath & Weiss GmbH. Figure 3-14 shows a close-up of the miniature tensile testing apparatus. This static machine was ideal to be sensitive enough to measure the small loads required by the small and thin ribbons. But it is known that test sample size and geometry can affect the mechanical properties in a tension test [3.21]. For instance, in a test on a cylindrical test sample, the elongation to fracture normally increases upon decreasing gauge length. This effect is due to the localization of strain during necking which occurs after maximum load [3.22]. For the present investigation, the change in width and length of the sample might influence the measurement results as well.

Tensile test specimens were subjected to a continually increasing uniaxial load, while simultaneous measurements of the elongation of the specimen were made. From the applied stress and the corresponding strain measurements obtained during the test, a stress-strain curve was plotted. The tensile test samples were loaded at a user specified, constant strain rate.

The first experiment was performed at a temperature below M_f to detwin the martensite. After unloading, the sample is heated to recover austenite and the original shape. Tensile tests were carried out at a constant temperature between 25 °C to 200 °C, to determine the stress-

strain properties of the ribbons. Tensile testing was conducted to the end of the plateau to measure the plateau stress and plateau strain, or until fracture to measure the toughness. The plateau stress was used to determine the constant load for thermal cyclic testing. The tensile testing consisted of: a) straining the specimen up to a load of 0.2 N in order to determine the reference strain (0%); b) heating the ribbon from room temperature to one of the specified temperatures, T, or without heating; c) loading the ribbon with a strain rate of 1 to 5 μm/sec to a specified strain or stress value; d) unloading the specimen back to 0% stress and e) heating to measure the one-way shape memory effect or loading the specimen again until fracture.

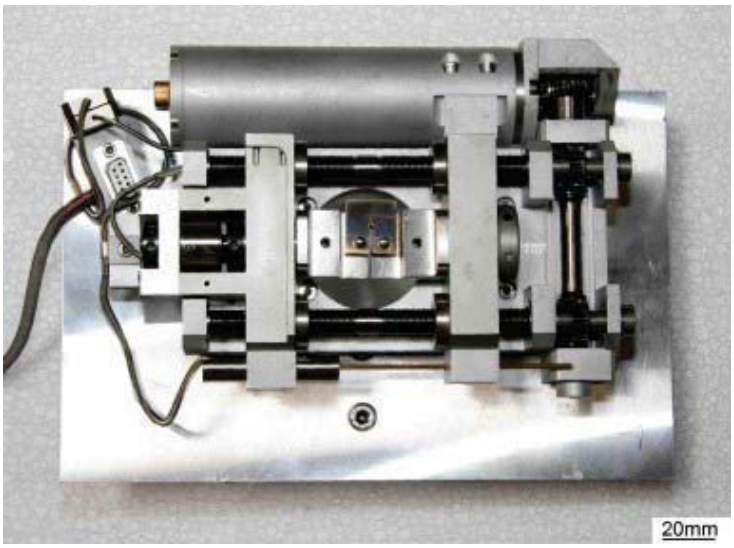

Fig. 3-14: Miniature testing apparatus.

3.2.4.3 Thermomechanical testing

The tensile thermomechanical cycles were performed with the same miniature testing apparatus which was introduced in the last section while bending thermomechanical cycles were conducted using a lab built training and fatigue test facility (Figure 3-15). In bending training the thermal cycling was conducted from room temperature (RT) to 200 °C. Heating and cooling were conducted by a halogen tube lamp and a ventilator, respectively, and the temperature was measured using a thermocouple directly attached to the samples.

The thermomechanical training using bending deformation procedure has been applied mostly as constrained thermal cycling on NiTi-based ribbons. After constrained cycling the ribbons were unloaded and were tested for two-way shape memory effect, and then the stability of this effect was measured by several thousand free thermal cycles.

In training using tensile deformation, cooling-heating cycles under different among of constant strain or constant stress has been investigated to determine the shape memory characteristics such as transformation temperatures, recoverable and irrecoverable strain levels as a function of stress and to find out the critical stress level.

The thermomechanical training using tensile deformation was also performed under different cycling conditions. The cycles were under a constant elongation or a constant load slightly higher than the plateau stress for the sake of experimental determination of the end of the plateau. At the end of the plateau of the stress-strain curve, the volume fraction of the detwinned martensite is maximized. This is the point for the measurement of the transformation strain resulting from the variant growth after thermal cyclic testing.

Thermomechanical trainings have drastic effects on shape memory characteristics of materials. Deformation in austenitic phase (ausforming) and deformation in martensitic phase (marforming) introduce defects to the structure. These defects can raise the critical stress for dislocation slip which can improve SME, TWSME and PE. Also, these defects are possible nucleation sites for martensitic transformations which can lead to a change in transformation temperatures. On the other hand, complex dislocation structures and other internal defects can behave like barriers to martensitic transformations as well. As a result, plastic deformation in SMAs can strengthen the matrix which can result in higher stress for SIM transformation, longer fatigue life by suppressing irreversible dislocation slip and alter transformation temperatures [3.23]. Furthermore, coherent or incoherent precipitates form partly during thermal cycling in appropriate compositions. The precipitates cause an internal stress field around them and this can help or oppose the martensitic transformation depending on the applied stress direction. If there is no applied stress, they increase the M_s temperature due to the internal stress field. Another effect of precipitates is that they change the composition of matrix because precipitates are either Ni-rich or Ti-rich depending on the initial composition [3.24].

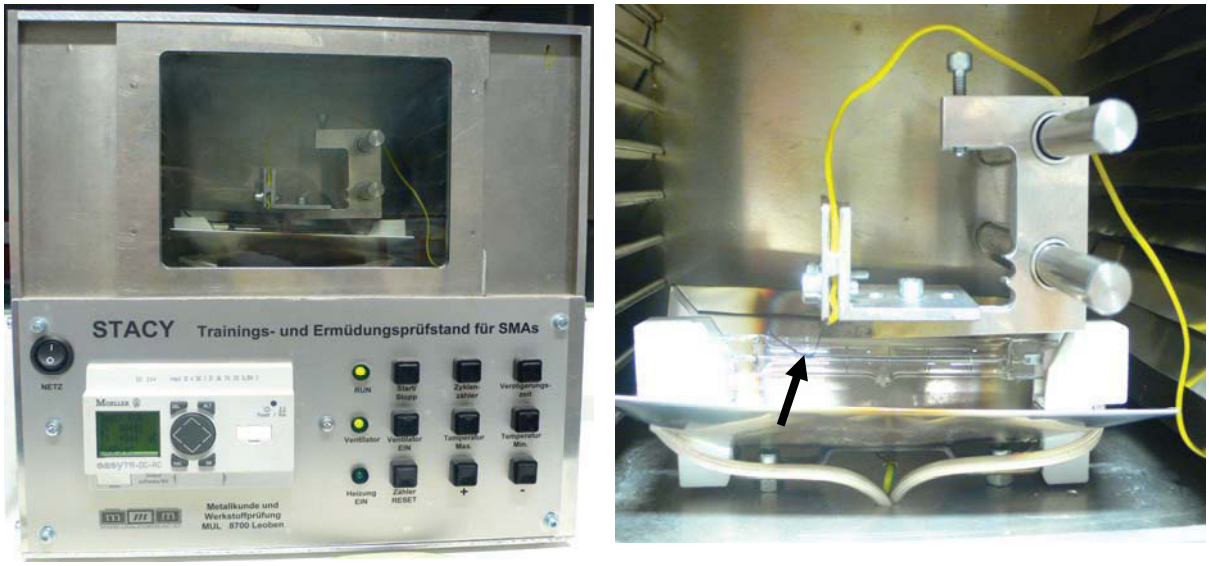

Fig. 3-15: (a) Self-fabricated bending training device (b) close-up of samples holder showing the trained ribbon (arrow).

CHAPTER 4

Results and Discussion

4.1 Specimen production

Three different alloy systems were used for production of rapid solidification specimens: 1) binary NiTi, which represents a standard SMA; 2) ternary NiTiCu (with 5 and 25 at.% Cu); 3) a dual phase alloy consisting of a NiTi matrix containing precipitates of tungsten to investigate the influence of second phase particles.

Some authors (e.g. [4.1–4.3]) consider it necessary that after rapid solidification a heat treatment has to be performed in order to achieve shape memory effects. The reason is that in their work higher cooling rates and therefore partially amorphous structures were obtained which have to be annealed for crystallization. However, the experiments of this work have been performed on three different melt-spinning devices and on a splat-cooling device and always got a fully crystallized microstructure which exhibited shape memory effects immediately after processing. Only in NiTi25Cu at a wheel speed of 45 ms^{-1} amorphous structures were obtained.

In melt-spinning technique by varying the parameters of the device, the ribbons can be produced with different lengths, thicknesses and widths, etc. It was observed that the increase in the wheel speed from 5 to 45 ms^{-1} results in a decrease in the ribbon thickness from ~120 to ~20 µm and from ~4 mm to ~2 mm in width. As the increase in the wheel speed leads to a reduced ribbon thickness, the cooling rate increases and therefore the martensitic substructure gets finer. Figure 4-1 shows the cross-sectional view of ribbons at various wheel speeds. Besides these parameters the result of a melt-spinning experiment is strongly dependent on the sample composition. For NiTi and NiTiW, it is particularly very difficult to obtain ribbons that are perfectly ductile. However, the addition of Cu in NiTi improves evidently ductility, length and surface smoothness. NiTi specimens were also produced by splat-cooling. The resulting disks have a diameter of approximately 20 mm and a thickness of about 50 µm.

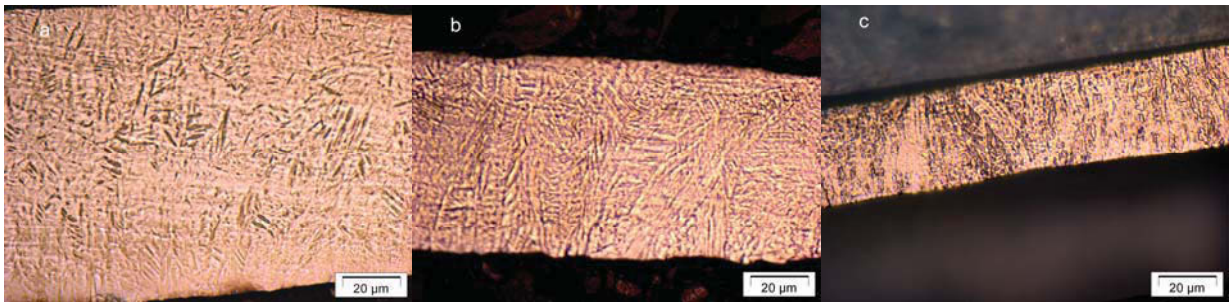

Fig. 4-1: Optical cross-sectional view of NiTi ribbons at various wheel speeds, wipe-etching using interference contrast; (a) 5 m/s, (b) 15 m/s, (c) 30 m/s.

4.2 Microscopic investigations

4.2.1 Microstructure of wires

Polished longitudinal cross-sections of NiTi wires used for melt-spinning were imaged in optical microscopy and SEM, Figure 4-2. As can be seen, Figures 4-2a and 4-2b illustrate only some fine low contrast precipitates in the microstructure. Using backscattered electrons, however, Figure 4-2c enhances the contrast between the Nitinol matrix and different inclusions. Two forms of inclusion morphology were observed: one of elongated row (or stringer) along the cold-drawing direction and the other as isolated particles.

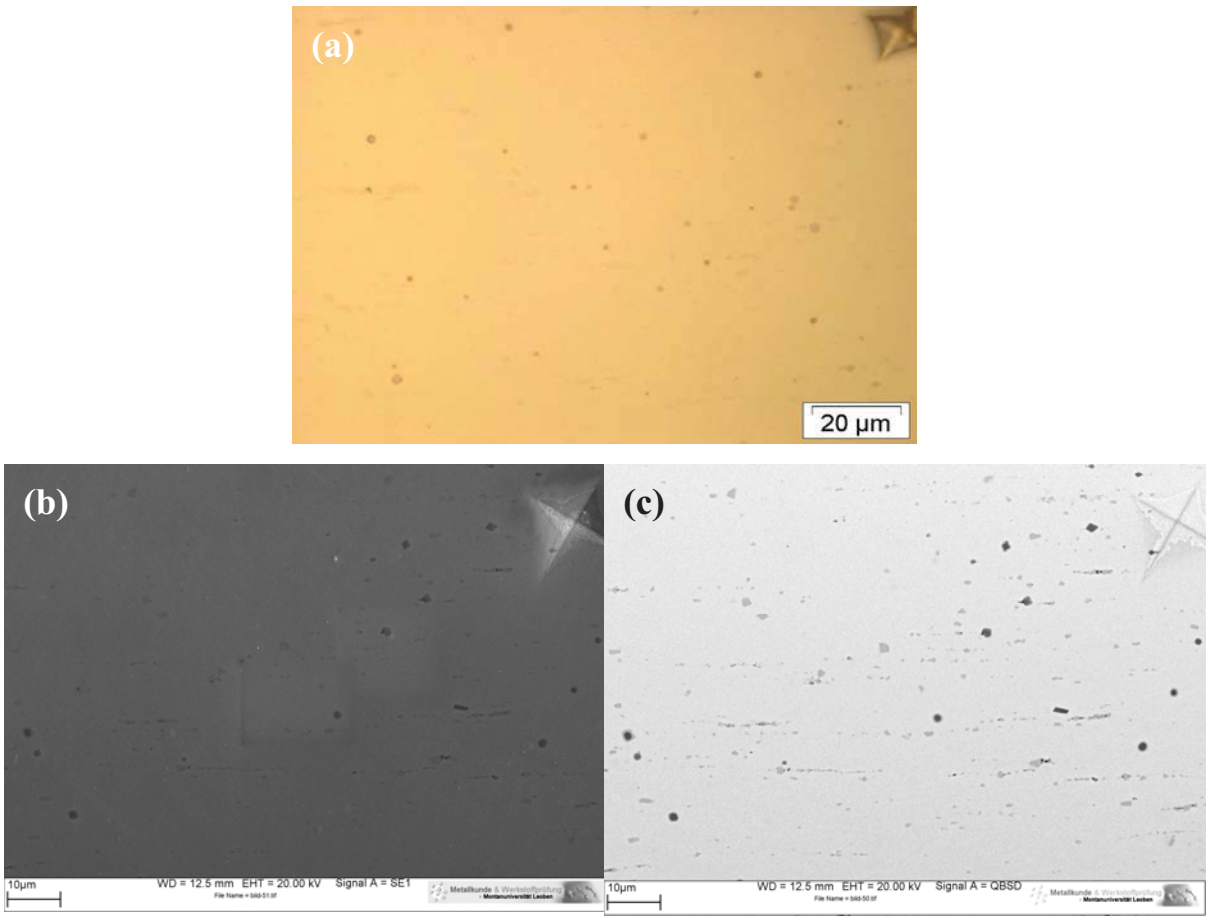

Fig. 4-2: Polished longitudinal cross-sections of NiTi wire; (a) optical microscopy, (b) SEM, secondary electron and (c) back scattered mode.

EDX analysis was used to identify the inclusions in Figure 4-2c which are oxide and carbide particles. The carbides appear darker than the oxide due to the atomic number (Z) contrast and the oxides are darker than the matrix. As can be seen in Table 4-1, carbide and oxide inclusions are probably TiC and Ti_4Ni_2O, respectively. The majority of carbide inclusions remain as round particles during drawing; but the oxides are partly larger than carbides and cracks grow within the oxides.

Table 4-1: EDX results of polished cross-sections of NiTi wire.

All results in atomic%

Spectrum	C	O	Si	Ti	Ni	Cu	W
Grey phase	-	14.17	-	52.41	33.42	-	-
Dark phase	42.79	-	-	56.10	1.11	-	-
Matrix	-	-	-	50.14	49.86	-	-

As shown in Figure 4-3, the cracks are primarily oriented perpendicular to the loading direction, indicating brittle fracture of the precipitates. Larger oxides are fractured but not yet as rows formed, while, usually finer particles arrange in rows. The characteristic of rows is fundamentally the same in all wires consisting of fractured oxide particles that broke up during the cold-drawing process.

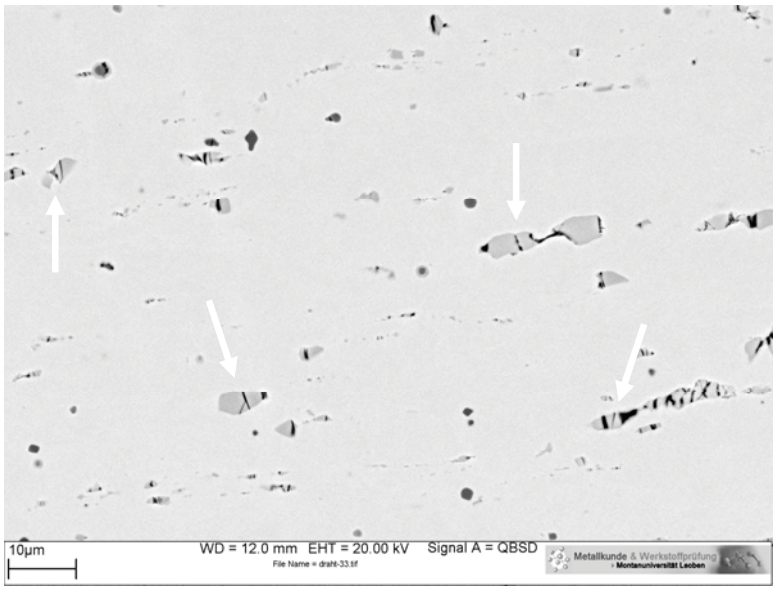

Fig. 4-3: Polished cross-sections of NiTi wire obtained with the back scattered detector, showing a fractured oxide particle (arrows) and encased carbide in oxide inclusion.

After etching, the samples show better contrast between phases and the color contrast presents a good way to differentiate carbides from oxide inclusions in optical metallography as well. As demonstrated in Figure 4-4, it can be observed that Ti_4Ni_2O particles as usual are irregular polyhedral and yellow but the TiC particles are small and round-shaped, almost without any contrast to the matrix. Moreover, some NiTi alloys have been provided from SAES Memry GmbH, Weil am Rhein, Germany to compare with the results of wires which were delivered from the company Fibra, Ostrava, Czech Republic. It was demonstrated that among and size of particles and their compositions are similar. Oxide and carbide impurities in wires cause undesirable increase in hardness and considerable reduction in workability and ductility of the alloy. Therefore, the precursors for the melt-spinning and splat-cooling techniques were prepared by vacuum arc-melting.

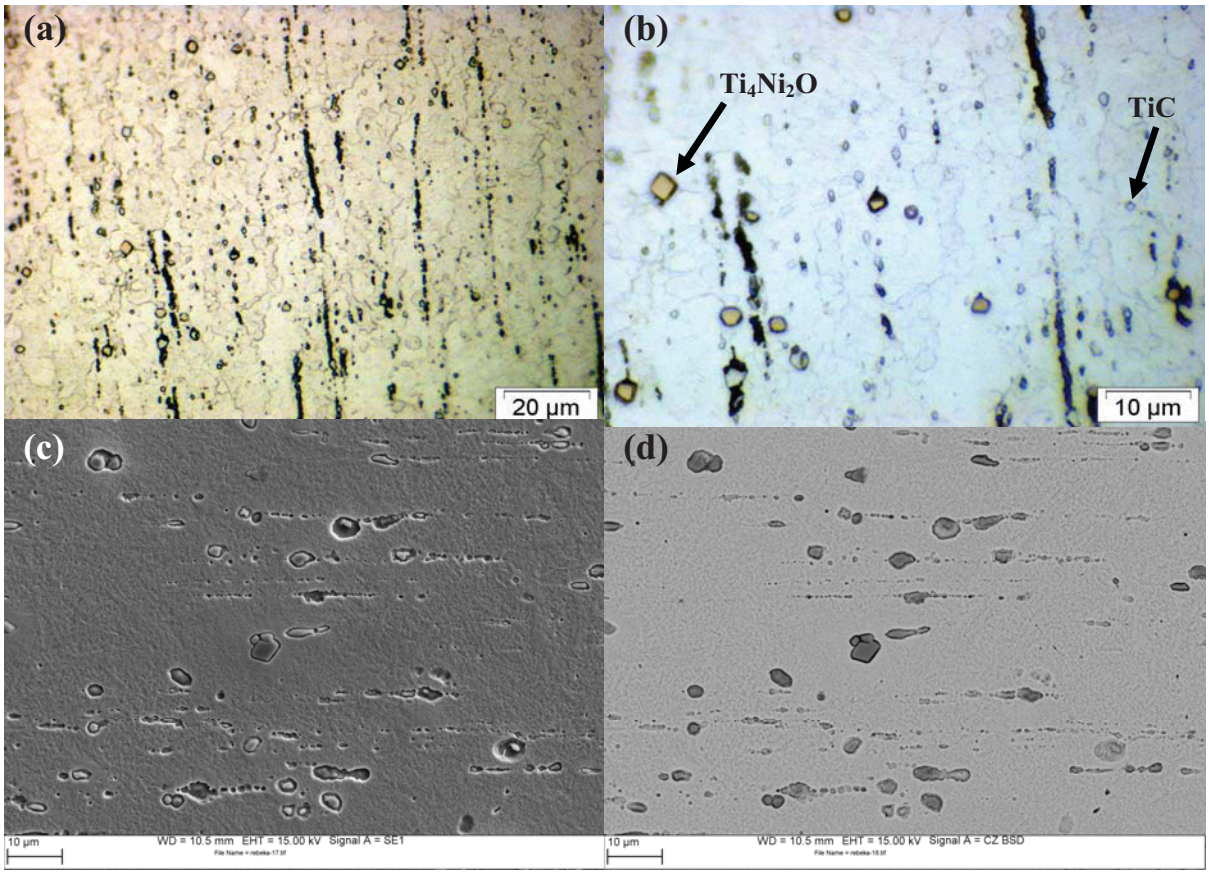

Fig. 4-4: Etched cross-sections of NiTi wire; (a) ×600 and (b) ×1200 magnification, optical microscopy, (c) SEM, secondary electron and (d) back scattered mode.

4.2.2 Microstructure of arc-melted ingots

As revealed in Figure 4-5, the arc-melted ingots have significantly less non-metallic impurities than wires provided from companies. The cross-section microstructures of arc-melted ingots show coarse grains, oriented to the heat outlet from the cooper-hearth during cooling, and a dispersion of second phases. Despite of three times remelting in arc-melting process, inhomogeneity in the alloy composition is inevitable which is not important in this study because of induction melting in the melt-spinning. Local concentration gradients in the as-cast condition generally cause Ti-rich and Ni-rich phases to appear in one sample. For instance, Figure 4-5c represents a Ti-rich part of the NiTi ingot. The precipitations could be identified as Ti_2Ni phase.

A detailed investigation with electron backscatter mode shows that dark dots can be distinguished in the Ti_2Ni phase (Figure 4-5d, arrows). Figure 4-6 shows the spectrum for a small dark particle. Titanium is increased strongly relative to the other phases, therefore this could be remnants of non-molten Ti.

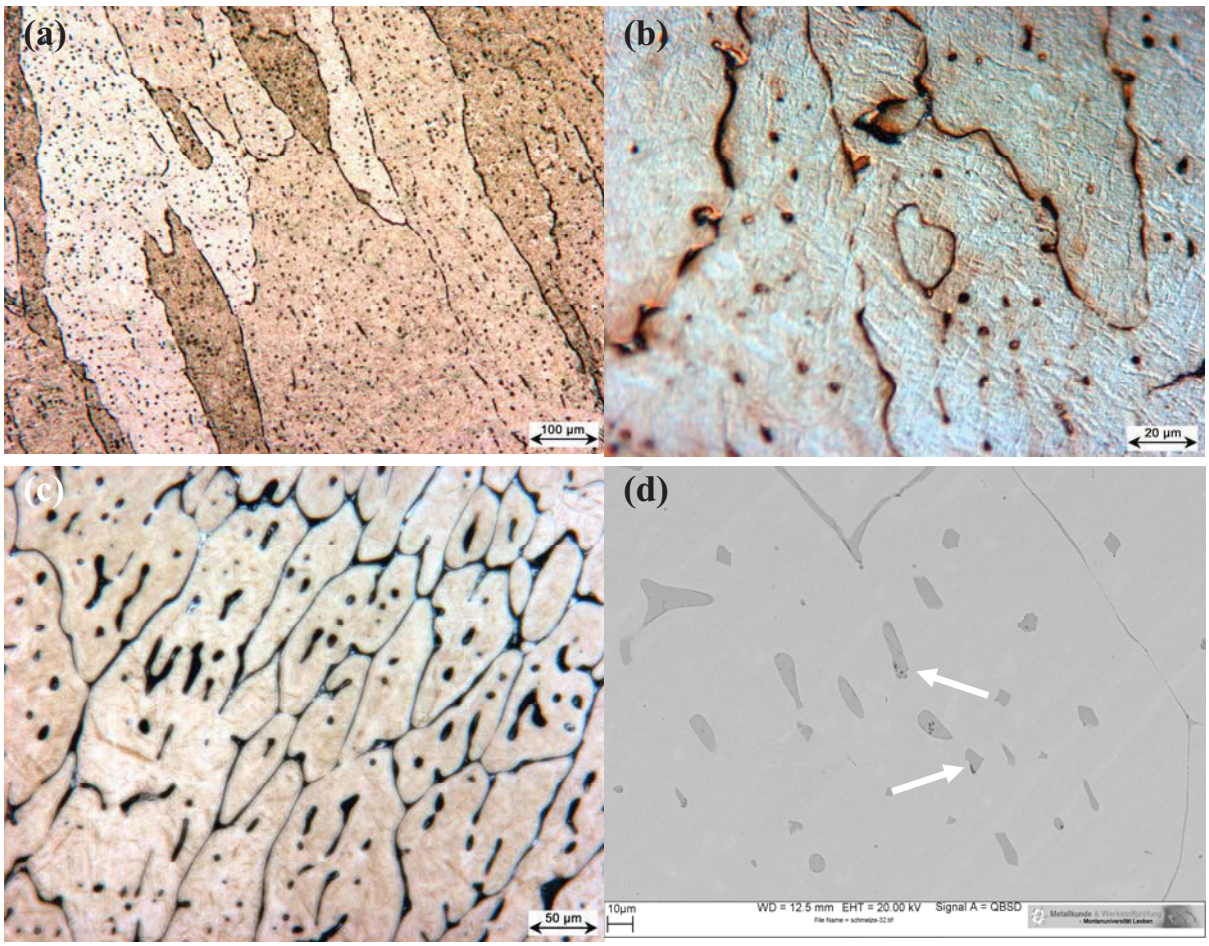

Fig. 4-5: Arc-melted NiTi alloy; (a) ×100 and (b) ×500 magnification, optical microscopy, (c) optical microscopy of Ti-rich part (d) SEM obtained with the back scattered detector.

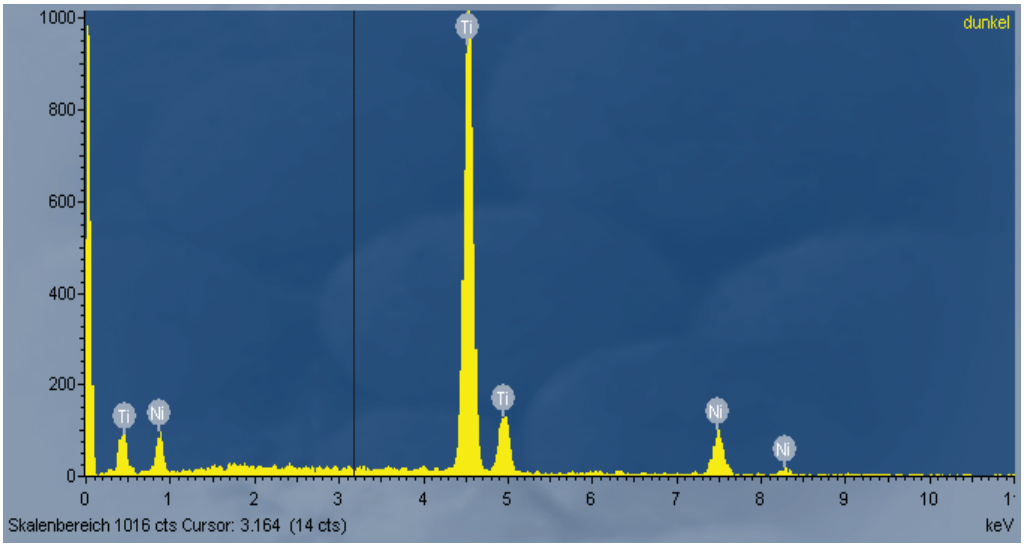

Fig. 4-6: EDS-spectrum for a small dark particle.

Figure 4-7 and Figure 4-8 show the microstructures of arc-melted NiTi5Cu and NiTi25Cu alloys, respectively. Two phases are observed in these arc-melted alloys using back-scattered electrons. According to EDX-analysis, the light grey matrix and the dark grey particles in the Figures 4-7d and 4-8d represent NiTi and $Ti_2(Ni,Cu)$ phases, respectively. No oxides and carbides were revealed in the microscopic investigation. The Ti_2Ni and Ti_2Cu phases look similar, and it is difficult to distinguish between them in the microstructure of ternary NiTiCu alloys.

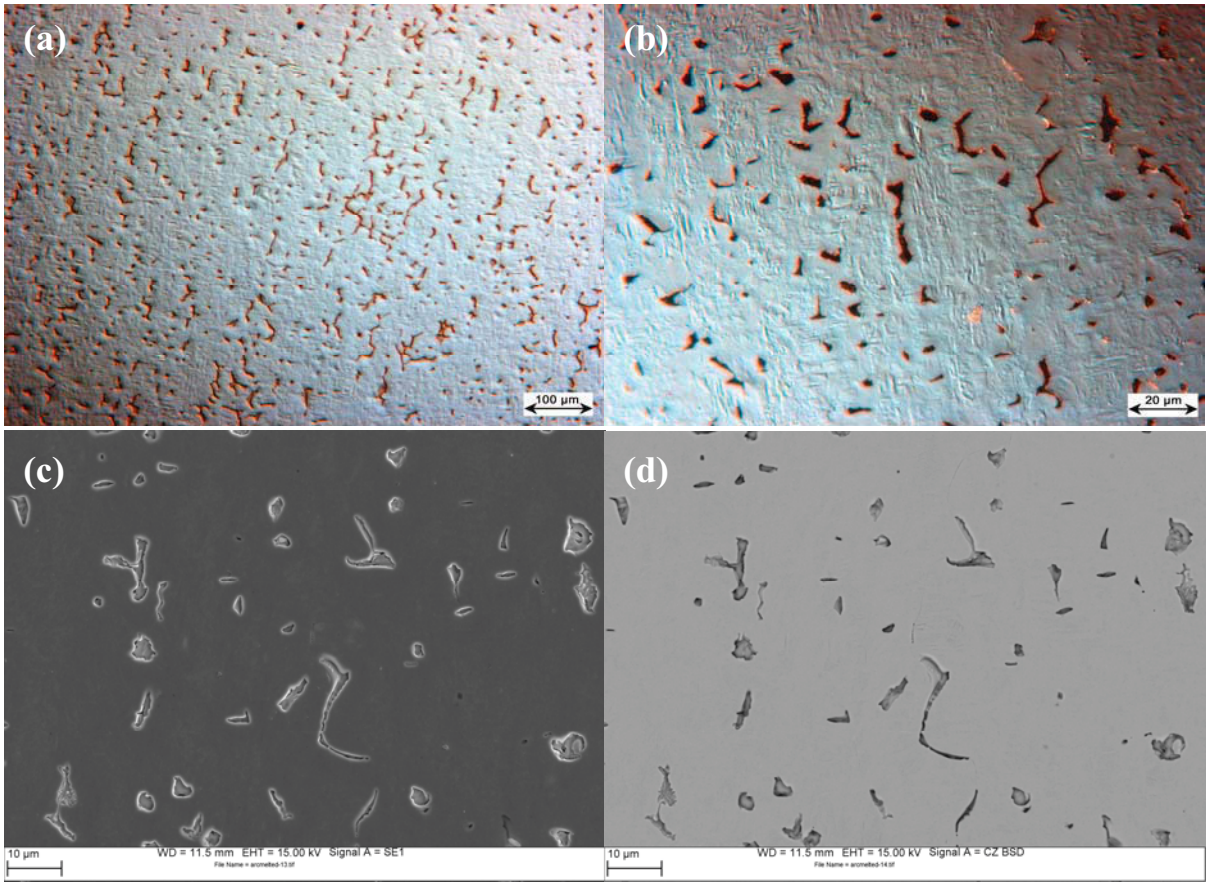

Fig. 4-7: Arc-melted NiTi5Cu alloy; (a) ×100 and (b) ×500 magnification, optical microscopy, (c) SEM, secondary electron and (d) back scattered mode.

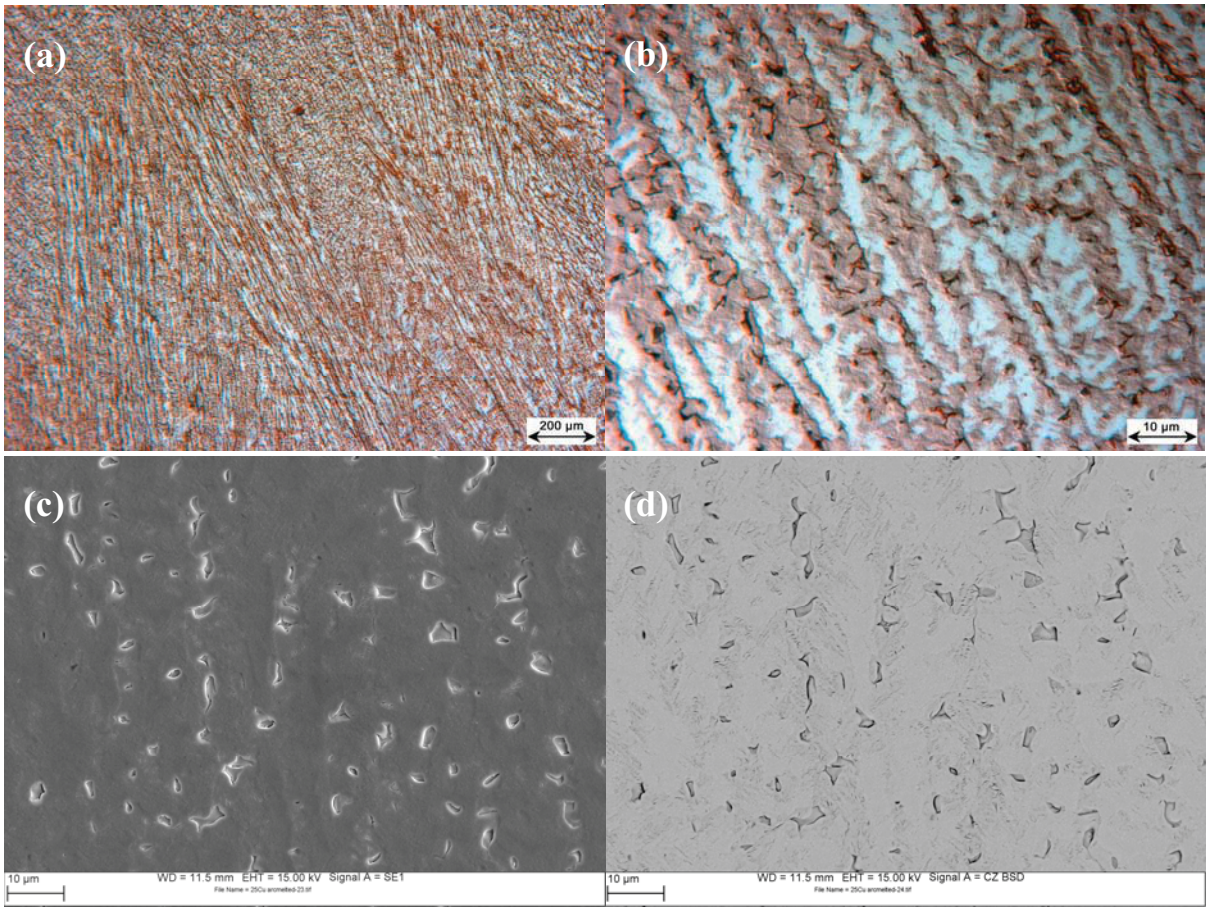

Fig. 4-8: Microstructure of arc-melted NiTi25Cu alloy; (a) ×100 and (b) ×500 magnification, optical microscopy, (c) SEM, secondary electron and (d) back scattered mode.

4.2.3 Microstructure of melt-spun ribbons

4.2.3.1 Experiments with different crucible materials

Non-metallic inclusions have been shown frequently to lead to crack initiation in fatigue specimens and adversely affect the workability and shape memory properties of the ribbons. These inclusions are brittle compounds usually formed during production and processing of the NiTi SMA alloys, especially in the course of their preparation in the crucibles. Questions remain on whether or how the different crucibles or coatings can affect the microstructure and composition of melt-spun ribbons.

In samples which are produced with Al_2O_3 crucible, the micrographs of etched samples reveal that apart from the black dendritic dispersoids, also some light grey coarse phase and very fine round dispersed particles are present in the material. This is due to the factors which govern the reaction between the melt and the crucible. Ti in these alloys is very reactive, thus in contact with Al_2O_3 crucible, despite the greater stability of Aluminum oxide in

comparison with Titanium oxide, some oxide particles can be formed because of impurities. Moreover, oxide formation in NiTi shifts the concentration of individual elements.

Since the stoichiometric and solubility range of NiTi phase is very narrow below 550 °C, NiTi SMAs are very sensitive to the exact chemical composition and homogeneity. A very small deviation of 0.1 at.% from the required composition can change the transformation temperature by 10 K. Moreover, it can cause an undesirable segregation of Ti_2Ni and Ni_3Ti within the NiTi parent phase, enhancing both hardness and strength and reducing the ductility and workability of the NiTi shape memory alloy. It was obtained that the microhardness of ribbons can change from about 500 Vickers to about 950 Vickers.

Figure 4-9 shows the presence of fine grey dispersed particles of TiO_2 (red arrows) after melting in an Al_2O_3 crucible. Furthermore, the dark dendritic precipitates contain about 65 at.% Ti and 35 at.% Ni, which is close to the composition of the intermetallic Ti_2Ni phase (green arrows). Also the bright phase in the NiTi matrix was indicated by EDX analysis as Ni-rich NiTi phase could be Ni_3Ti particles (yellow arrows).

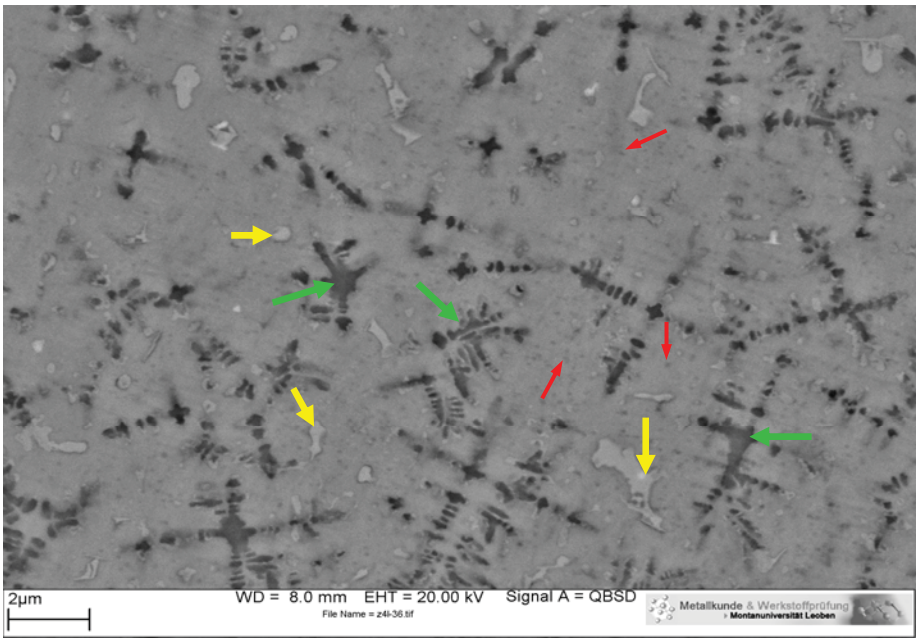

Fig. 4-9: SEM micrograph of NiTi ribbon using Al_2O_3 crucible with backscatter mode.

Figure 4-10 illustrates the microstructures of a ribbon which was produced from NiTi wire using a quartz crucible without coating. It can be seen that this microstructure has also a dendritic appearance similar to that depicted in Figure 4-9. As shown in Figure 4-10c, three kinds of phases can be distinguished, which include grey dendritic phase, small dark phase and matrix. Table 4-2 represents the results of EDX analysis of different phases. The dendritic phase is the intermetallic NiTiSi phase and according to analysis probably with some small Ti_2Ni particles and the small dark phase was identified as TiC. This result is consistent with the Ti-Ni-C ternary phase diagram indicating TiC as the only carbon containing phase present at Ni-50.3 at.% Ti alloy [4.4]. The carbon may come from NiTi wire which was used as feed material. It is also observed that the TiC particles can look partly dendritic.

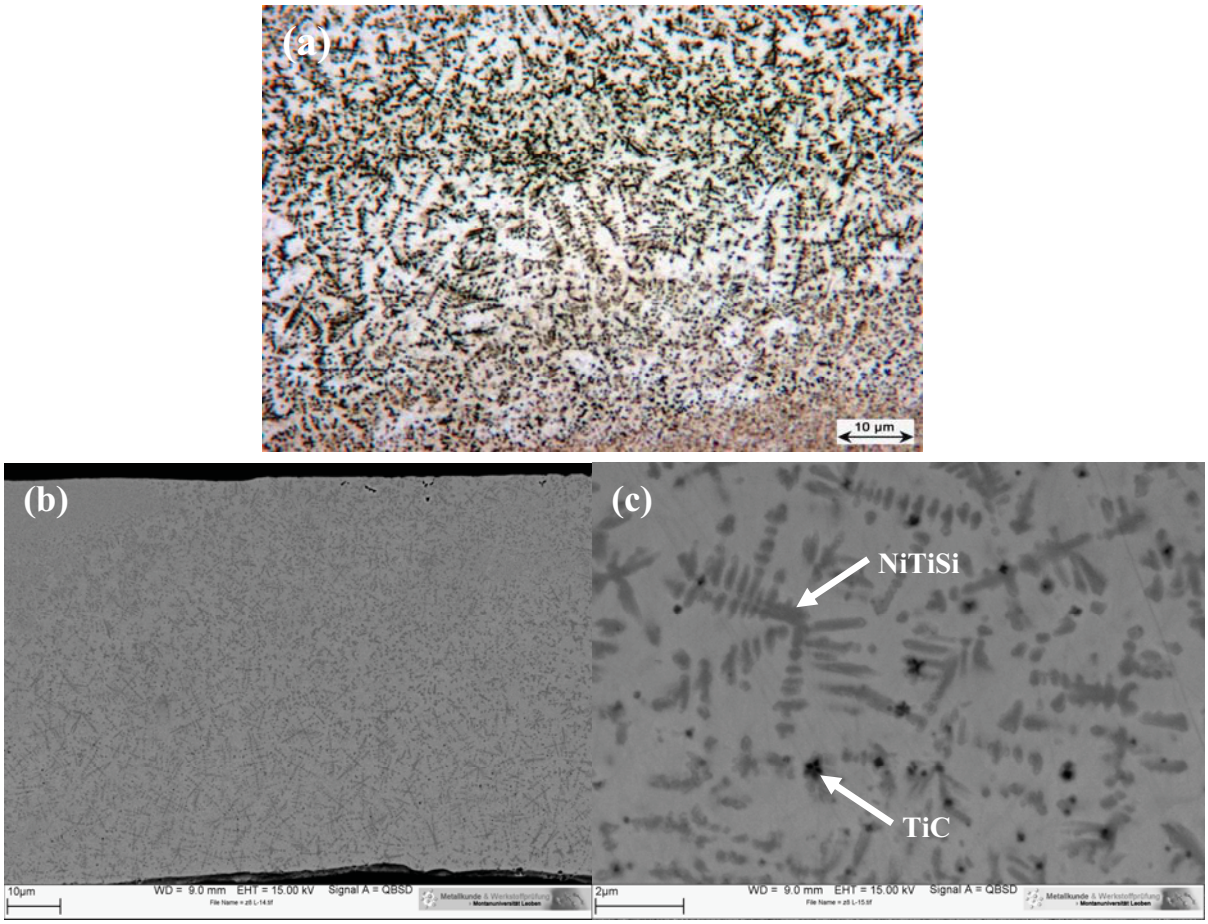

Fig. 4-10: Microstructure of a NiTi melt-spun ribbon with uncoated quartz crucible using wire; (a) optical microscopy of ribbon, (b) and (c) SEM obtained with the back scattered detector.

Table 4-2: EDX results of melt-spun ribbons with uncoated quartz crucible using wire.

All results in atomic%

Spectrum	C	O	Si	Ti	Ni	Cu	W
Dendritic phase	-	-	26.57	48.87	24.55	-	-
Dark phase	45.94	-	-	51.01	3.05	-	-
Matrix	-	-	2.85	47.27	49.86	-	-

The ribbons which produced from arc-melted ingots instead of wire using a quartz crucible without coating, exhibit a cellular microstructure. Optical and SEM micrographs of the precipitated phases are shown in Figure 4-11. The result of EDX analysis indicates that the grey phase at the grain boundaries has almost a Ni:Ti ratio (in at.%) of 1:2, and some fine low contrast dispersoids contain silicon. With consideration of the EDX errors, it can be concluded that the dark grain boundary phase represents Ti_2Ni and the grey small phases are NiTiSi which are located mostly within the grains. The EDX analyses for these particles and NiTi bulk matrix are displayed in Figure 4-12. The spectra related to the dark phase shows that nickel is reduced, and titanium is increased relative to the bulk matrix. In the fine grey particles silicon is increased relative to other phases.

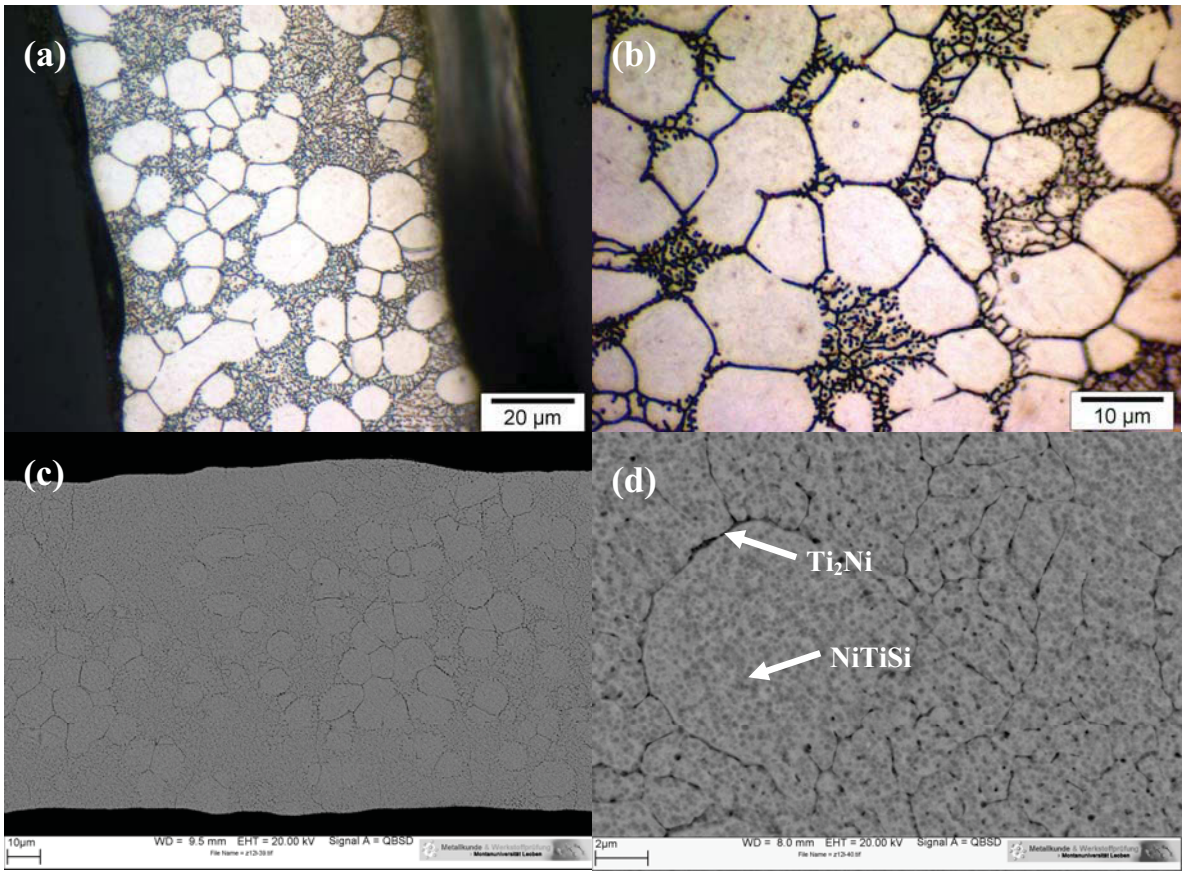

Fig. 4-11: NiTi melt-spun ribbon with uncoated quartz crucible using arc-melted ingots; (a) and (b) optical microscopy of ribbon, (c) and (d) SEM, back scattered mode.

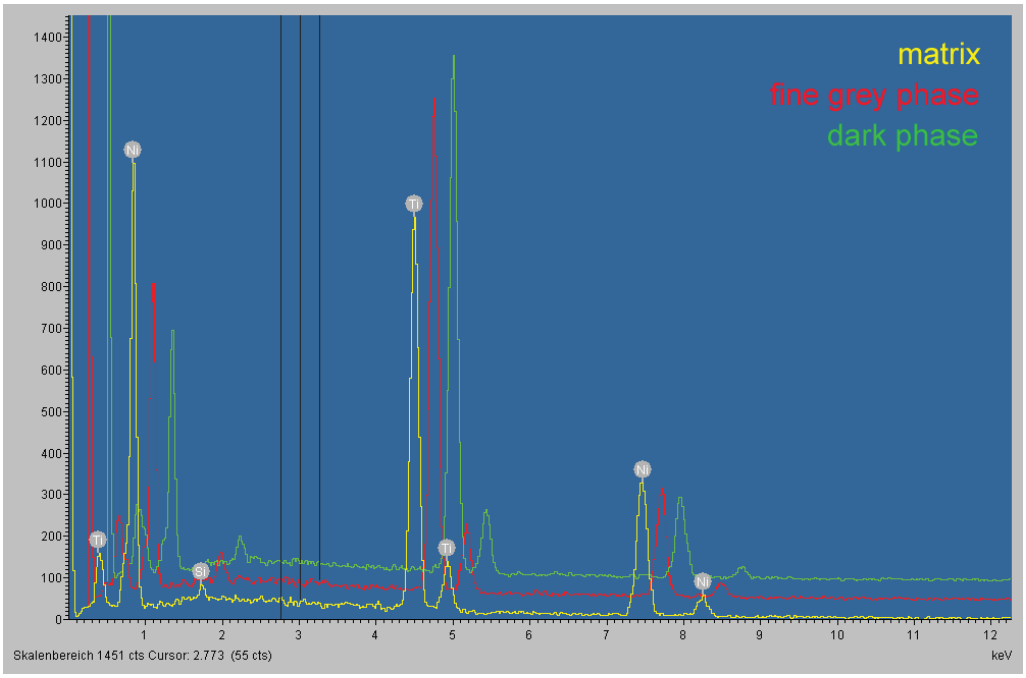

Fig. 4-12: EDX analyses for the precipitated particles in comparison with matrix phase.

The microstructure and XRD analysis on the wheel side of the NiTi ribbons showed that the samples prepared with a quartz crucible with Y_2O_3 coating at injection temperature lower than 1400 °C, consist of single NiTi phase, and thus they are perfectly ductile. This coating was utilized to prevent reaction between quartz crucible and NiTi alloys. At injection temperatures above 1400 °C, however, the coated quartz crucible reacts with the NiTi material and subsequently the color of ribbons changed to violet and blue due to oxidation of the ribbons, and the microstructure of samples consists at least of three phases as illustrated in Figure 4-13. A careful investigation with backscatter electrons shows various types of intermetallic particles, irregular polyhedral dark particles, very small grey dispersoids and bright phases. Table 4-3 shows EDX results. According to the results, the polyhedral particles and small dispersoids contain oxygen (Ti_4Ni_2O) and silicon (NiTiSi), respectively, while the bright ones are Ni-rich NiTi phase (Ni_3Ti).

The atomic structure of the Ti_4Ni_2O phase (fcc, a = 11.3 Å) is quite different from that of both martensite (monoclinic, a = 2.889 Å) and austenite (B2, a = 3.015 Å). The lattice parameter of the oxide phase is in fact much bigger than that of NiTi phases. This causes creation of a incoherency between the oxide phase and NiTi. The specific morphology of the oxide inclusions causes stress concentration at the sharp corners of the polyhedral oxide phase. The hardness number of the oxide phase (about 820 Vickers) is much greater than that of the NiTi matrix (about 500 Vickers).

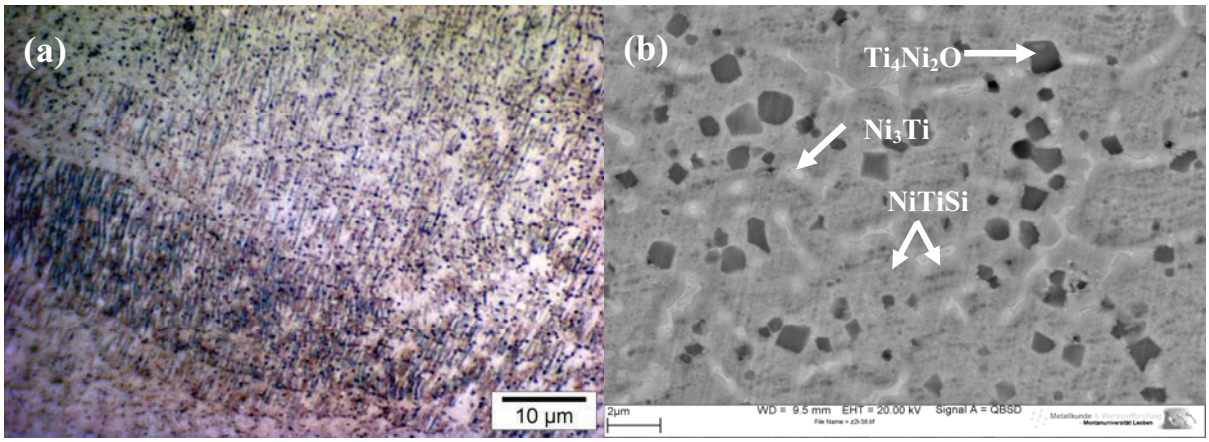

Fig. 4-13: Microstructure of NiTi ribbon with coated quartz crucible at melting temperatures above 1400 °C; (a) ×1000 magnification, optical microscopy, (b) SEM, back scattered mode.

This difference causes the formation of a weak incoherent interface between the oxide inclusions and the matrix. Even applying a small stress can break the weak bonds forming between the two phases and cause the formation of cracks.

Table 4-3: EDX results of melt-spun ribbons with coated quartz crucible at high melting temperature.

All results in atomic%

Spectrum	C	O	Si	Ti	Ni	Cu	W
Polyhedral particles	-	26.54	-	48.87	24.55	-	-
Small dispersoids	-	-	9.68	38.91	51.40	-	-
Matrix	-	-	1.74	28.90	69.35	-	-

Due to utilization of graphite crucibles in melt-spinning process and also in production of the wires, the absorption of carbon and formation of carbon containing phase are studied. It was observed that the NiTi ribbons prepared with graphite crucible apart from very few small particles which could be identified as TiC precipitates consist only of the martensite phase. They are perfectly ductile showing appropriate shape memory effect even at injection temperatures above 1400 °C. To examine the influence of operating time, the melt-spinning procedure was carried out in extreme longer melting time. The microstructure of this ribbon illustrates various intermetallic phases which are highlighted by arrows pointing up in Figure 4-14. Some round small black particles, cross-like dark precipitates and bright phases are present in the inhomogeneous matrix.

EDX analyses of the cross-like particle show 47.32 at.% carbon and 48.1 at.% titanium (Table 4-4), which corresponds to the TiC phase. The round fine particles were identified to have almost double titanium than nickel (Ti_2Ni). The bright phase, on the other hand, is Ni_2Ti.

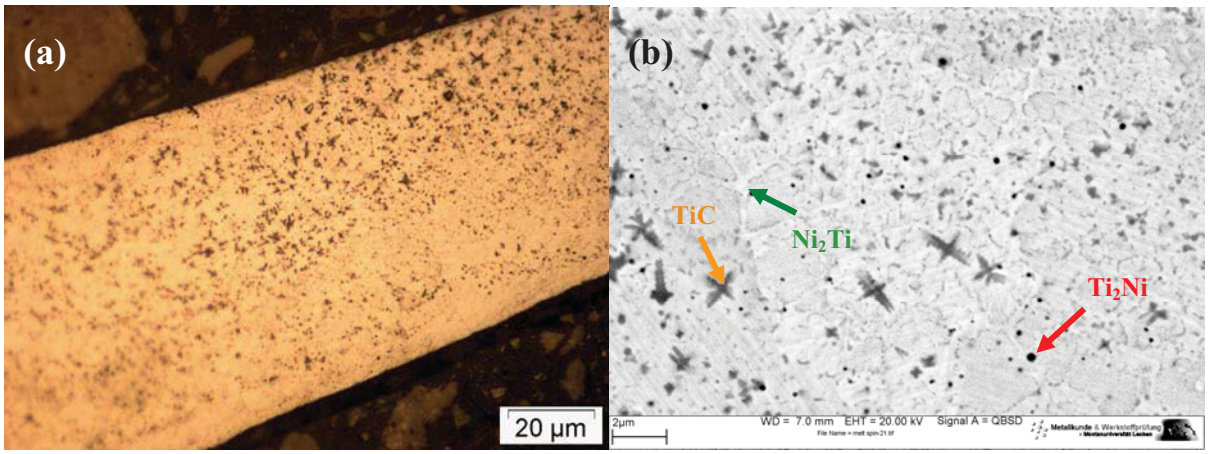

Fig. 4-14: Microstructure of NiTi melt-spun ribbon with graphite crucible at high operating time; (a) optical microscopy, (b) SEM obtained with the back scattered detector.

Table 4-4: EDX results of melt-spun ribbons with graphite crucible at high operating time.

All results in atomic%

Spectrum	C	O	Si	Ti	Ni	Cu	W
Cross-like precipitates	47.32	-	-	48.10	4.57	-	-
Small particles	-	-	-	64.82	35.18	-	-
Bright phase	-	-	-	31.22	68.78	-	-
Matrix	6.20	-	-	49.28	44.51	-	-

Eventually, it was found that the best results of melt-spinning are achieved using quartz crucible coated with Y_2O_3 and graphite crucible, respectively, for injection temperatures below and above 1400 °C. The ribbons are fully ductile showing good SME, therefore, all following ribbons used in this study were prepared from this procedure.

4.2.3.2 Finally used ribbons

In this section different etching solutions and various observation methods were employed to reveal martensite microstructure of finally selected ribbons which were introduced in the last section. For microscopic investigation various etching solutions were initially taken from literatures and then modified to find an appropriate solution for the rapid solidified martensitic microstructures.

During the last few years, various authors have presented micrographs of NiTi-based microstructures showing needle-like structures by using CH_3COOH in the etchant solution that were defined as martensite. In this work as well the ribbons were etched initially with solution of $HF:HNO_3:CH_3COOH=1:4:5$ and then studied by optical microscopy as shown in Figures 4-15a. However, it was observed that these needle-like structures even occurred after etching of an austenitic sample (Figure 4-15b). Therefore, the surface structures observed on NiTi after etching are artifacts and do not represent the martensite microstructure.

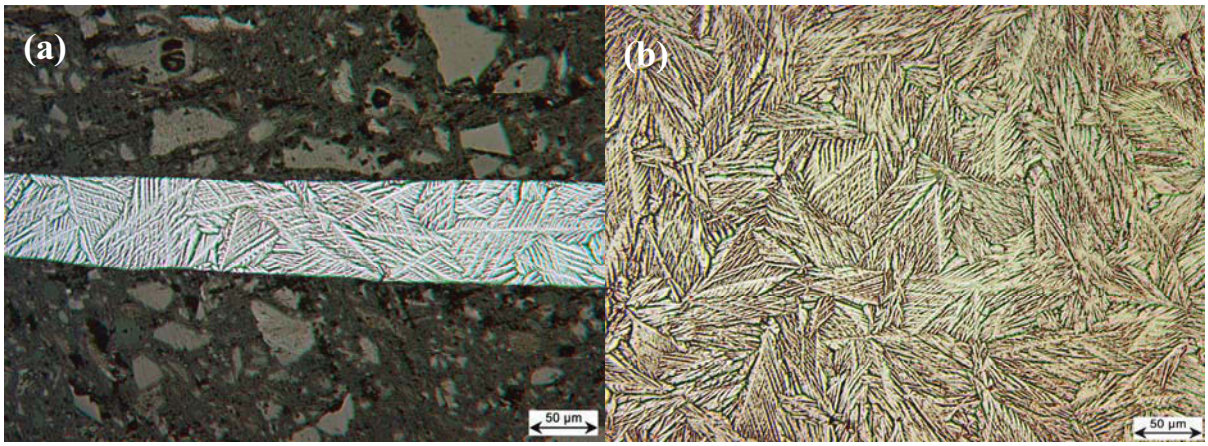

Fig. 4-15: Needle-like structure: (a) NiTi melt-spun ribbon, (b) austenitic NiTi Wire.

In contrast to etching with $HF:HNO_3:CH_3COOH$ =1:4:5, after etching with solution $HF:HNO_3:H_2O=1:4:5$ the distinct grain boundaries are apparent, but no needle-like structures were observed. Stepwise etching of an arc-melted NiTi ingot with solution $HF:HNO_3:H_2O=1:4:5$ and afterwards short-time etching with solution $HF:HNO_3:CH_3COOH$ =1:4:5 (Figure 4-16a) exhibits both the grain structure and the needle-like structure. From Figure 4-16a it is obvious that the needle-like structure cannot originate from martensite, since it extends over the grain boundaries without changing orientation.

In fact, by using CH_3COOH in the etchant composition, an artifacts surface structure could be developed on all the samples, irrespective of the microstructure and the crystallography of the grains that is to be expected for martensite needles. 3D profilometry (Figure 4-16b) reveals that needle thickness can exceed 2.5 µm over the surface of the sample. This fact shows clearly the needle-like structures are surface structures and do not originate from the bulk structure. Apparently the material that is dissolved during etching re-segregates on the surface of the sample immediately.

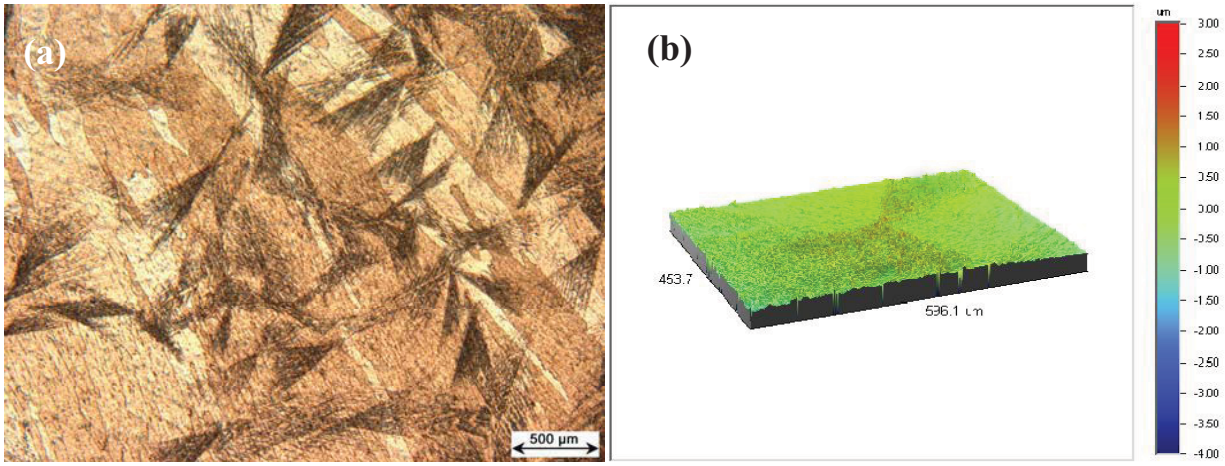

Fig. 4-16: Arc-melted NiTi alloys: (a) Stepwise etching of first by $HF:HNO_3:H_2O$ = 1:4:5 for 10 s and then by $HF:HNO_3:CH_3COOH$ = 2:4:5 for 2 s, (b) 3D profilometry of surface.

To reveal the origin of the needle-like structures, grazing incidence X-ray diffraction (θ=3° with step time of 8 sec.) was applied for analyzing the phases on the surface of an austenitic NiTi sample after the etching process. In addition to the austenitic NiTi peaks, further peaks were detected on the etched sample, exclusively, as can be seen in Figure 4-17. The additional peaks are attributed to different kind of titanium oxide structures of TiO_2, Ti_2O and TiO.

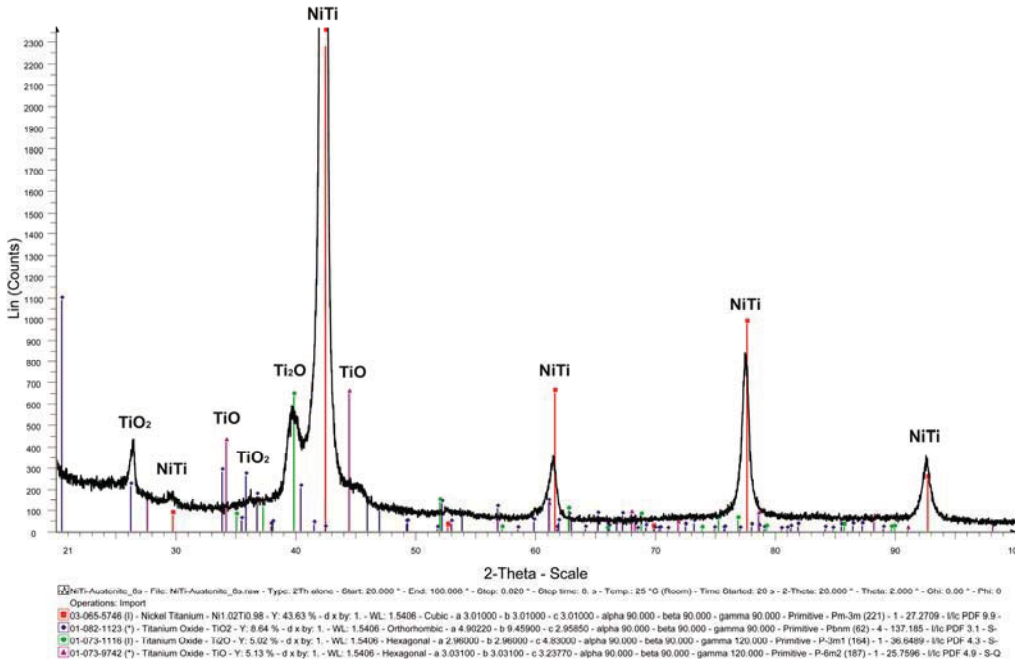

Fig. 4-17: grazing incidence X-ray diffraction of etched austenitic sample.

Figure 4-18a shows microstructures of a ribbon which have been etched in solution of $HF:HNO_3:H_2O=1:4:5$, and by this it is not easy to characterize the martensitic microstructure. Only by using wipe-etching and differential interference contrast (DIC), it was possible to reveal partially the martensitic structure as shown in Figure 4-18b.

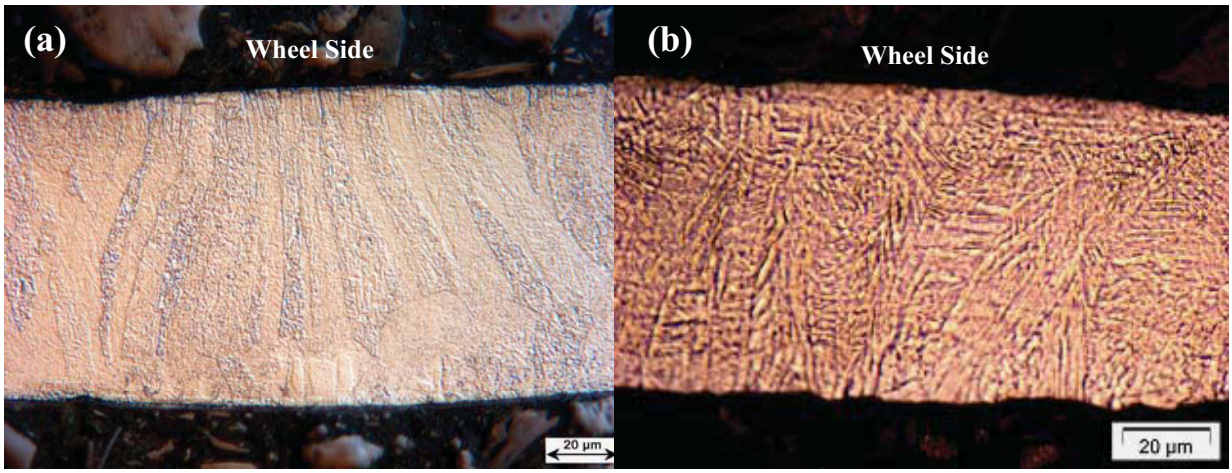

Fig. 4-18: Optical microstructures of melt-spun ribbon: a) conventionally etched surface, b) martensite structure after wipe-etching using interference contrast.

Two other etching solutions with compositions of 120 ml H_2O, 15 ml HCl, 15 g $Na_2S_2O_5$, 10 g $K_2S_2O_5$, 2g NH_4HF_2 and 100 ml H_2O, 25 ml C_2H_6O, 2g NH_4HF_2 (modification of Weck's reagent) were used. The first solution has revealed proper martensite structure in some parts of ribbon after a short etching time of 3-5 seconds (Figure 4-19a). After longer etching time of about 10 seconds, grain boundaries start to reveal, however martensite microstructures disappear slowly as shown in Figure 4-19b. Finally after 15 seconds, grain boundaries could be seen very clearly and detailed (Figures 4-19c and 4-19d). It is shown that the ribbons are composed of columnar grains. Besides, SEM was employed to resolve finer structures and also to inspect the chemical composition for possible impurities. As can be seen in Figure 4-19f, the ribbon is almost single phase. As the crystallization front proceeds through the ribbon, a columnar grain structure is developed. Furthermore, the ribbons revealed smoother surface at the wheel-side than at the free-side (Figure 4-20).

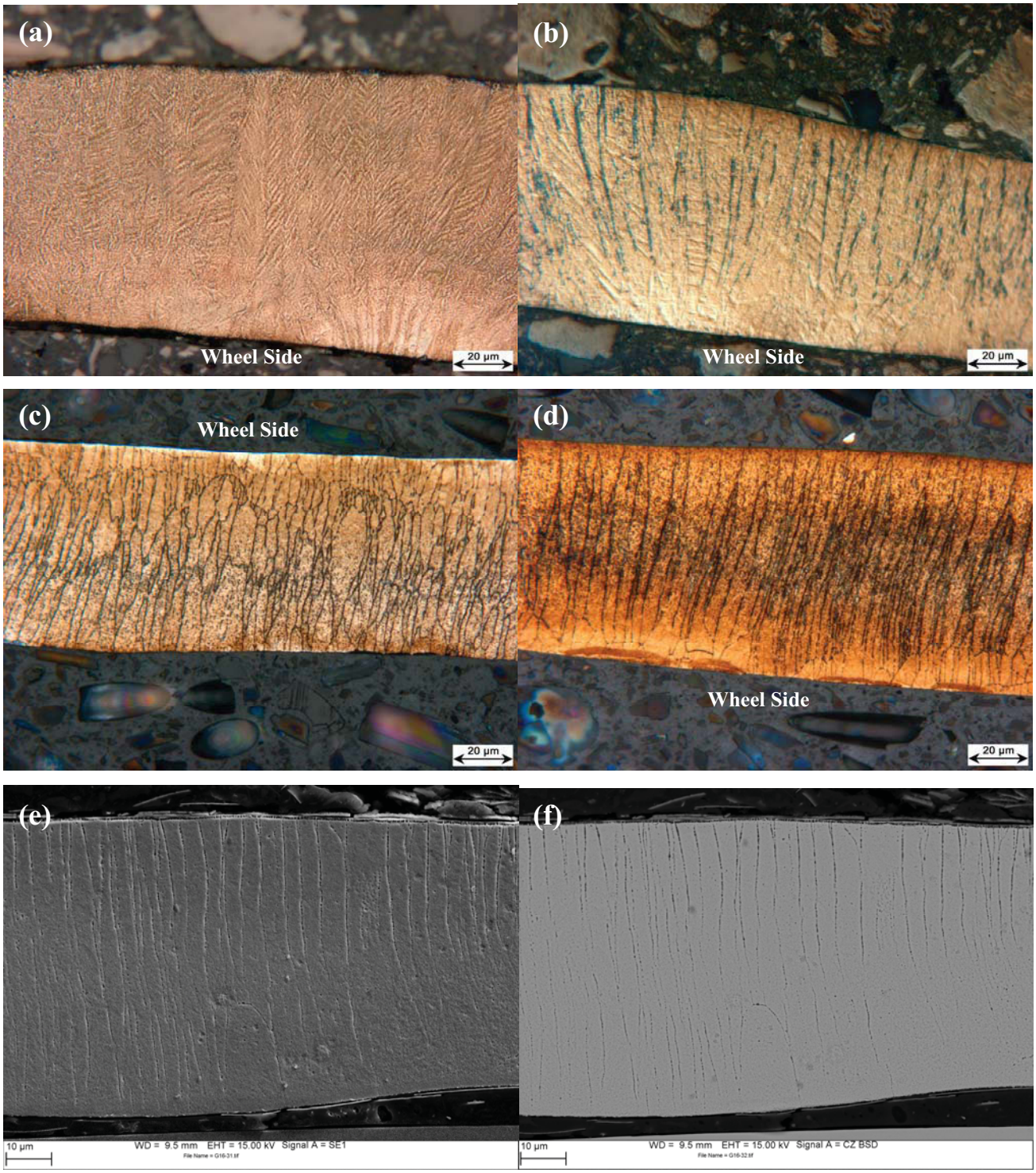

Fig. 4-19: Microstructures of NiTi ribbons etched with 120 ml H_2O, 15 ml HCl, 15 g $Na_2S_2O_5$, 10 g $K_2S_2O_5$, 2g NH_4HF_2; (a) after 3-5 seconds etching, using interference contrast, (b) grain boundaries after 10 seconds etching, (c) and (d) after 15 seconds etching showing columnar grains, (e) SEM, secondary electron (15 seconds etching) and (f) back scattered mode.

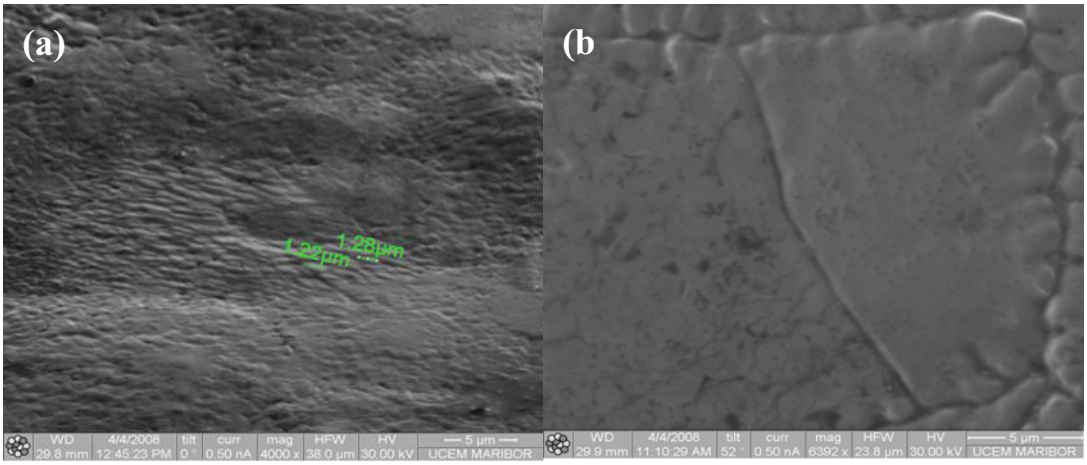

Fig. 4-20: FIB Image of NiTi melt-spun ribbon: (a) free-side and (b) wheel-side.

It was found that by using Weck's reagent, fine reproducible microstructures and grain boundaries over the whole cross-section of the samples could be revealed, which are displayed in Figures 4-21a and 4-21b. Figure 4-21c shows the morphology of the martensite by SEM in the melt-spun ribbon after relief polishing and very short-time (1 second) etching using back scattered electrons mode.

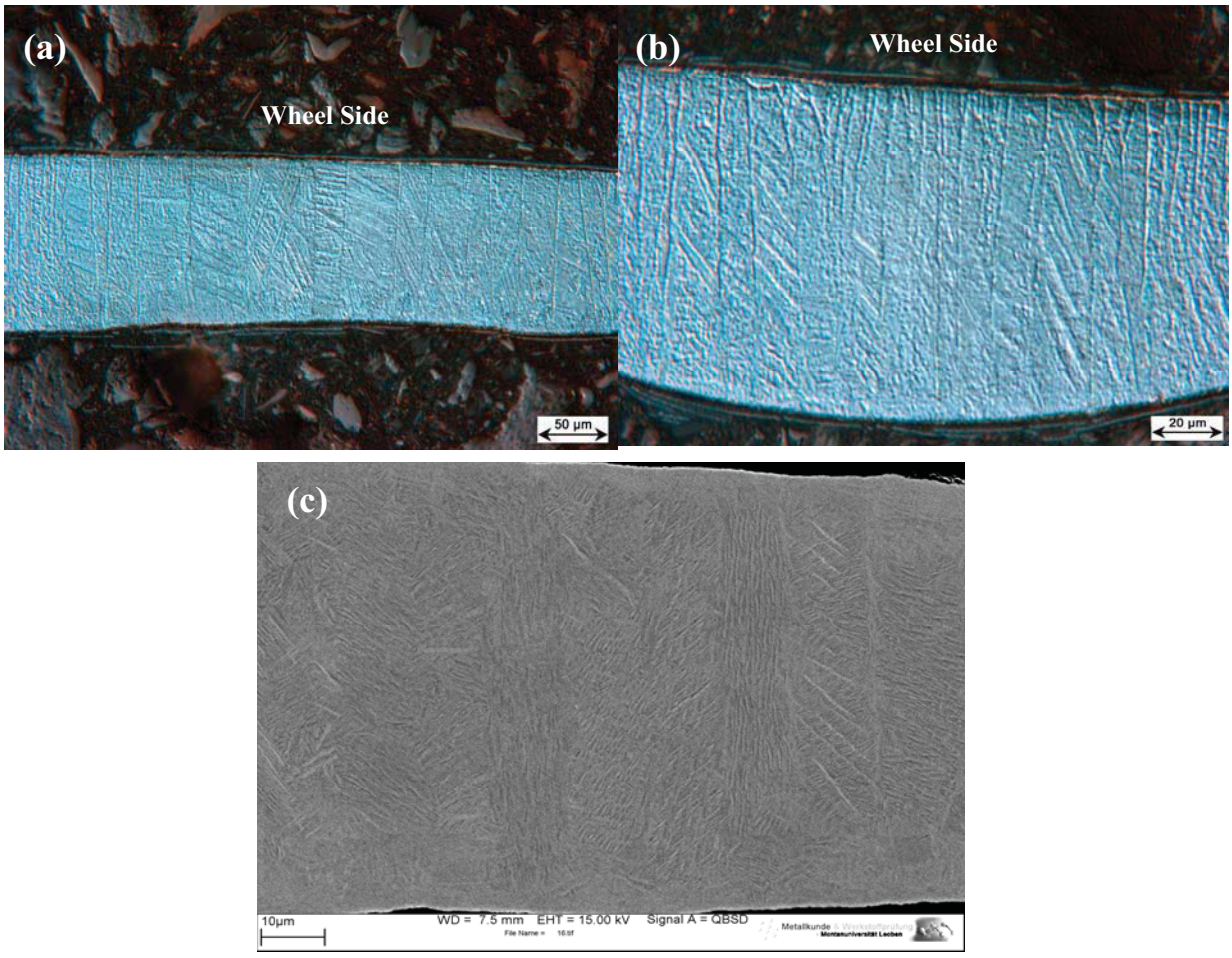

Fig. 4-21: Microstructures of a NiTi ribbon etched with Weck's reagent: (a) optical microstructure ×200, (b) optical microstructure ×500, (c) SEM micrograph using back scattered electrons mode.

Figure 4-22 shows the micrographs of NiTi5Cu and NiTi25Cu ribbons. As shown in Figures 4-22c, 4-22d, even though the Cu content of the alloy exceeds the Cu solubility limit by far, no second phases were observed in our samples, while many second phase particles such as TiCu near grain boundaries have been observed by conventional casting [4.2]. In addition, some regions of NiTi25Cu ribbons clearly consist of twins such as the marked region in Figure 4-22c. The twin-like substructure of the martensite can be seen partially already with the SEM (Figure 4-22d) in the NiTi25Cu sample.

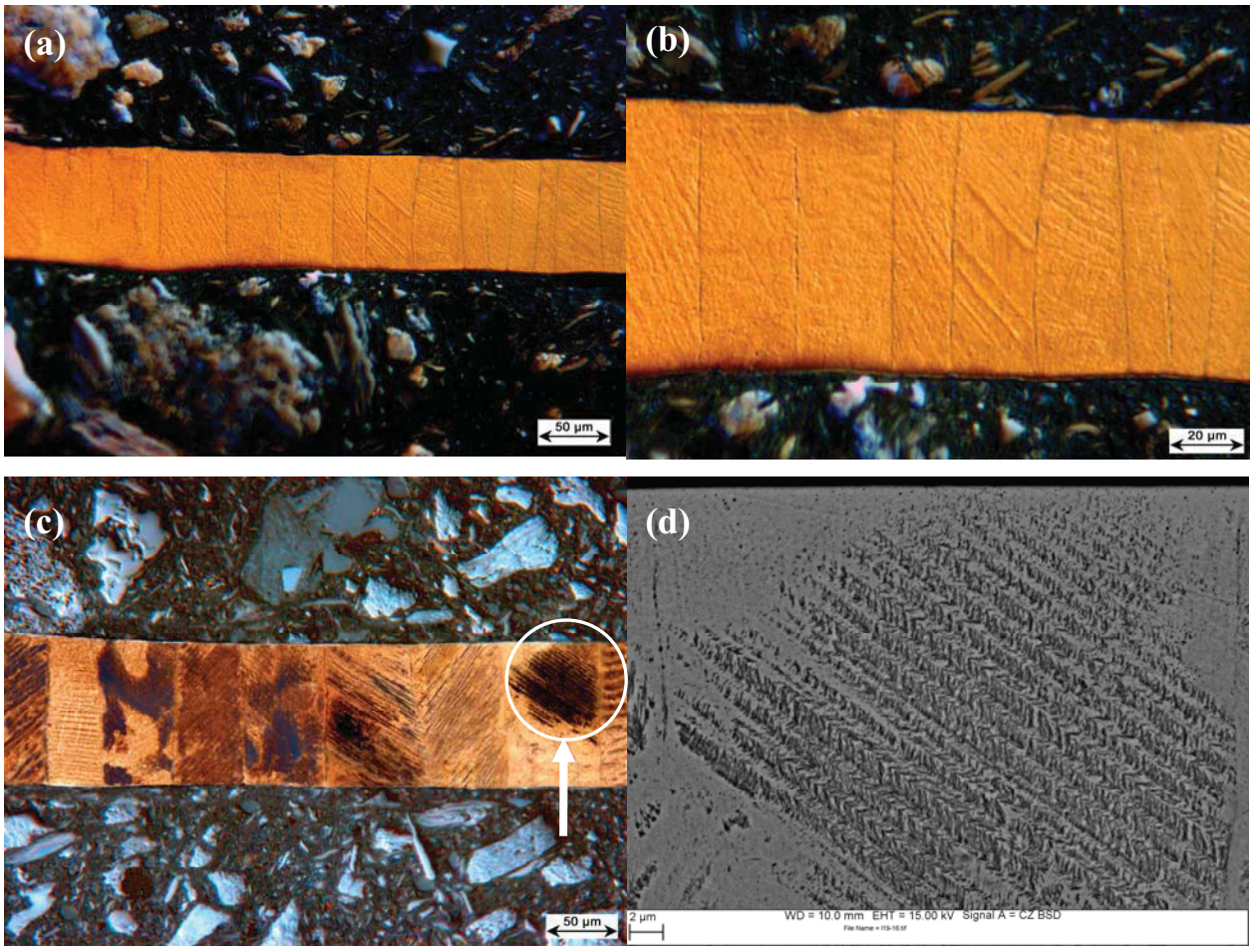

Fig. 4-22: Microstructures of ribbons etched with Weck's reagent: (a) optical microstructure of a NiTi5Cu ribbon ×200, (b) optical microstructure ×500, (c) optical microstructure of a NiTi25Cu ribbon, (d) SEM, back scattered electrons, marked region of Fig. 4-22c.

Figures 4-23a and 4-23b display B19′martensitic structure of NiTi ribbon and B19 martensite structure of NiTi25Cu ribbon, respectively. In NiTi ribbon, the twin-like substructure of the martensite is nano-sized and it has been revealed only using TEM. Therefore, the martensite in NiTi ribbons is much finer than the martensite in NiTi25Cu. TEM was employed to investigate martensitic structures of ribbons, which are too fine to be sufficiently resolved with SEM.

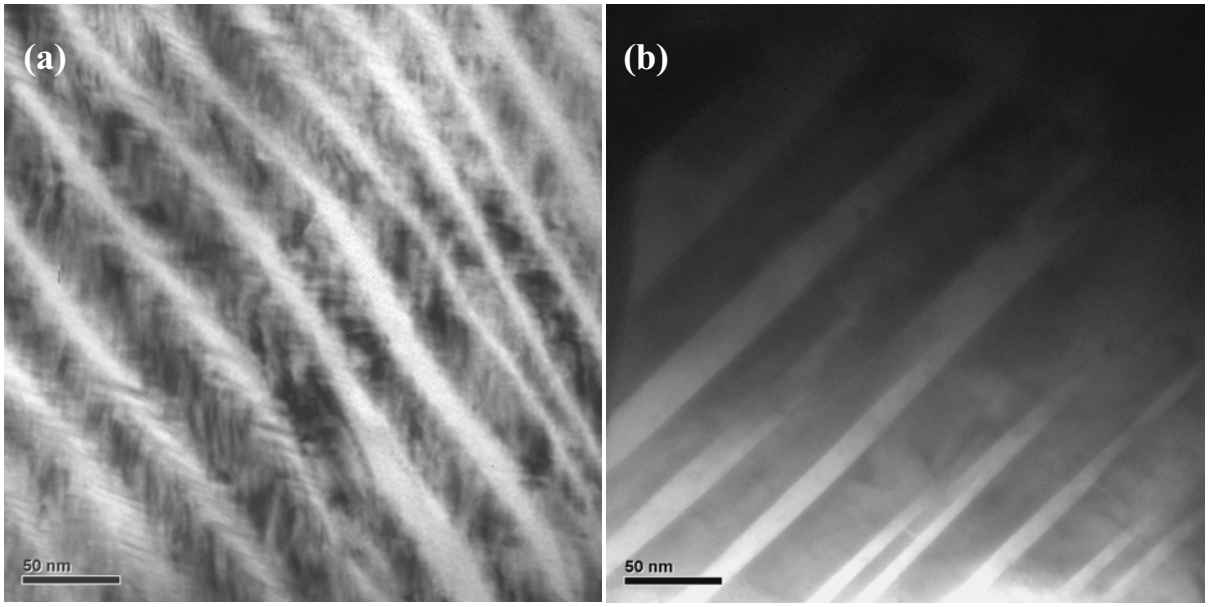

Fig. 23: TEM images of ribbons: (a) B19′ martensite of NiTi, (b) B19 martensite of NiTi25Cu.

From the corresponding binary and ternary phase diagrams [4.5-4.6] it is evident that because of the low solubility of W in NiTi, as little as 2 at.% W (corresponds to 6.6 wt. % W) is enough to obtain W-rich precipitates by super-saturation in the NiTi matrix (Figure 4-24) [4.7]. Alloying with W represents a possibility to introduce a second phase in binary NiTi alloy, with only small influences on the transformation temperature. It was revealed in NiTiW ribbons that the microstructures are not always columnar grain structure. As shown in Figures 4-24c and 4-24d, after relatively long etching time (20 sec. instead of 6 sec.), the W particles can be seen in much more detail for investigation. It was observed that the small particles of tungsten precipitate mostly in grain boundaries.

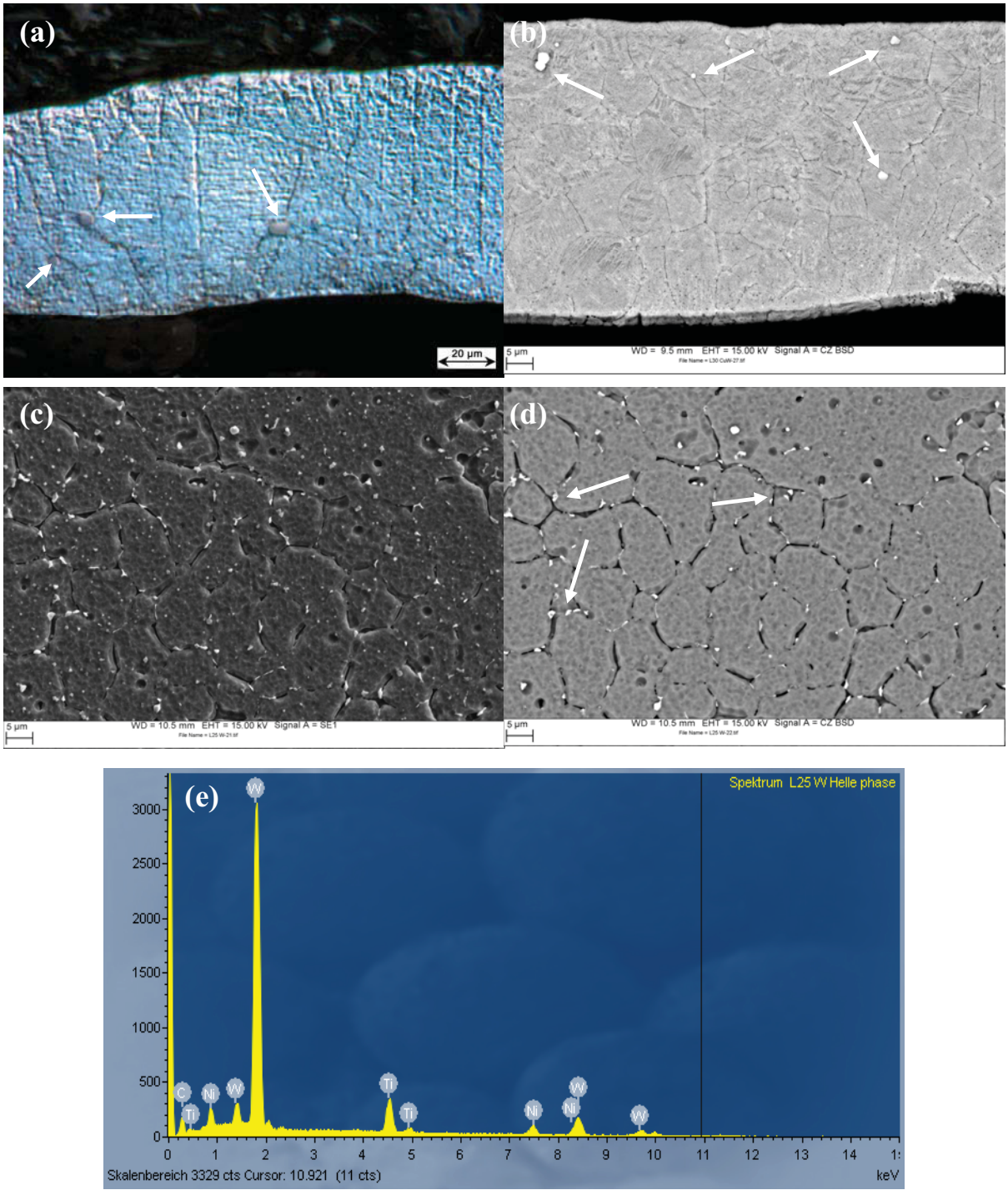

Fig. 4-24: Microstructure of a NiTi2W ribbon, (a) optical microstructure, arrows indicate W precipitates; b) SEM micrograph of NiTiW using back scattered mode and W precipitates (arrows), (c) SEM, secondary electron mode and (d) back scattered electrons mode, (e) EDX analyses corresponding to arrows in Fig. 4-24d.

In this work NiTi-based ribbons are mostly composed of single columnar layer. However, at low cooling rates, the ribbons would consist of several layers of columnar grains. Bhattacharya and Kohn [4.8] named it Eucken–Hirsch texture. Eucken and Hirsch [4.9] have tested single columnar melt-spun ribbons in uniaxial tension applied along the length of the ribbon and found that the class of recoverable strains can be significantly larger in this special microstructure [4.10].

High shear stress concentrations appear because of elastic anisotropy in NiTi SMA [4.11] and consequently incompatible deformations of adjacent grains (Figure 4-25a). Adjacent grains can have different mechanical properties in load direction; consequently, high shear stress concentrations on grain boundaries cause intercrystal fracture at low loads and strains. However, both the single layer structure (Figure 4-25b) as well as the fiber texture contribute to improvement of ductility. In the single layer ribbons, the height of each grain is equal to the ribbon thickness. Therefore, the total surface of grain boundaries parallel to the ribbon's longitudinal axis is much smaller; i.e. no boundaries parallel to the ribbon's surfaces are present. In this way, a single layer structure decreases the number of potential crack-initiation sites. Only boundaries more or less perpendicular to the surfaces still exist. And even at these, the shear stress concentrations remain quite low, if the orientation of the adjacent grains is favorable (Eucken–Hirsch texture). Eucken–Hirsch texture can be achieved by employing metals of high purity and, melting or casting in high vacuum. In this case, mechanical properties of adjacent grains in load direction are quite similar; consequently, shear stress concentrations on grain boundaries decrease and ribbons sustain much higher loads. Maximal strains cannot be achieved if alloying elements such as tungsten obstruct formation of the single layer columnar structure [4.8, 4.10].

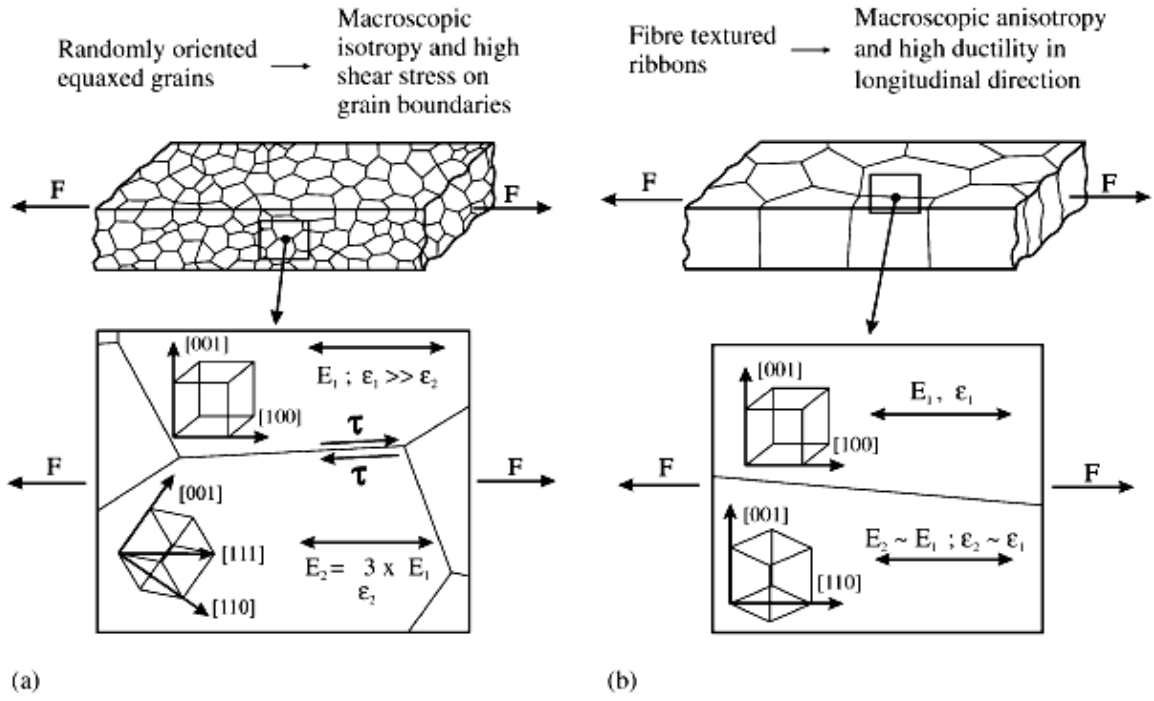

Fig. 4-25: (a) Multi layer equiaxed structure: randomly oriented crystal grains; (b) Single layer columnar fiber textured structure [4.10].

4.2.4 Microstructure of splat-cooled disks

Figure 4-26 presents the cross-section microstructure of a splat-cooled NiTi disk. After pressing of a free falling molten droplet into a thin film between two copper pistons, the thin metal layers solidified on the surface of the piston simultaneously. It can be clearly seen that the solidification front has moved inside from both sides and met in the middle of the sample. The interface on the cross-section remains a straight line separating two symmetrical parts of the disk. The zones, which were in direct contact with the pistons reveal the columnar grains which were extending to the centre of the disk. However, in the case of melt-spinning, the grains run mostly through from the wheel side to the free upper side of the ribbon indicating that the solidification front moved in that direction.

The martensitic microstructures of splat-cooled NiTi samples could be revealed much easier than in arc-melted and melt-spun specimens. Figure 4-26a and 4-26c show the martensitic structure of splat-cooled NiTi with conventional and wipe-etching, respectively. The grain sizes are almost similar in the splat-cooled and the melt-spun samples. The microstructural features and the transformation temperatures of the splat-cooled samples correspond well to the melt-spun ribbons produced with the highest wheel speed, thereby indicating almost a similar range of cooling rates.

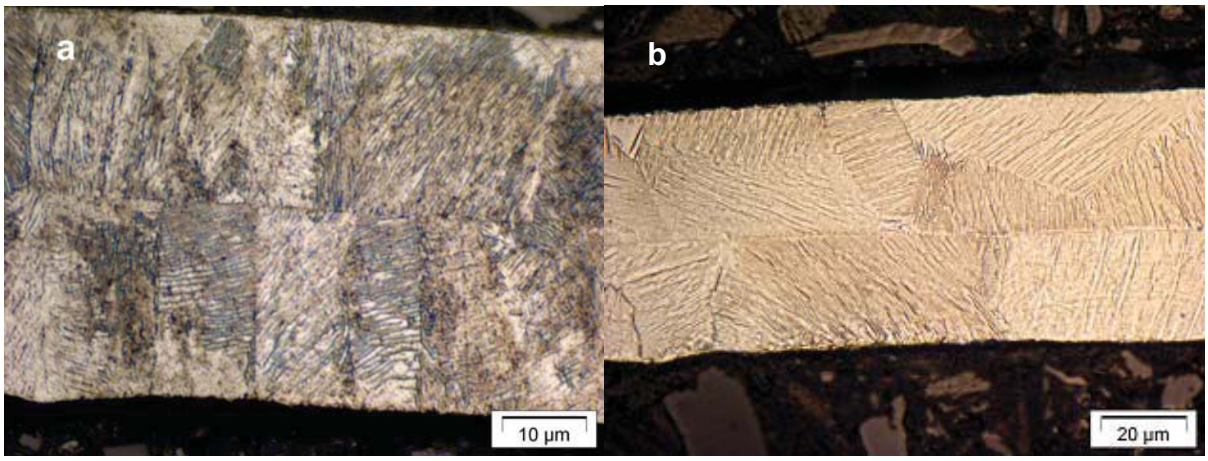

Fig. 4-26: Martensite structure of a splat-cooled sample, (a) conventional etching, (b) wipe-etching.

4.3 Mechanical properties before training

Stress-strain experiments were conducted in order to obtain basic mechanical information about the Ti-rich NiTi-based ribbons used in this investigation. The tensile testing consisted of: a) straining the specimen up to a load of 0.2 N in order to determine the reference strain (0%); b) heating the ribbon from room temperature to one of the specified temperatures, T, or without heating; c) loading the ribbon with a strain rate of 5 μm/sec to a specified strain or stress value; d) unloading the specimen back to 0% strain and e) heating to measure the one-way shape memory effect or loading the specimen again until fracture.

In Figure 4-27, four different NiTi-based ribbons were tested to failure at 25 °C. The stress-strain behaviors of the ribbons are similar and follow typical tensile deformation characteristics in NiTi materials. It can be clearly seen that all the ribbons show martensitic plateau without any subsequent heat treatment. After the stress plateau the curves show a rapid increase of the stress mainly due to the deformation of the detwinned structure. Practically, after the stress plateau, the deformation behavior of the alloy becomes similar to that of traditional structural materials; most of the special properties of the NiTi-based alloys lie in the stress plateau.

The pseudoplastic deformation reaches about 3-4 % strain before plastic deformation occurs, however, for a polycrystalline matrix an exact definition of the different zones is difficult due to the coexistence of the several mechanisms associated with the deformation process. The NiTi-based ribbons fracture at a strain between 6 % and 7 %. The fracture strains of ribbons are limited by a relatively premature fracture in comparison to wires, which is probably caused by irregularities in ribbon dimensions.

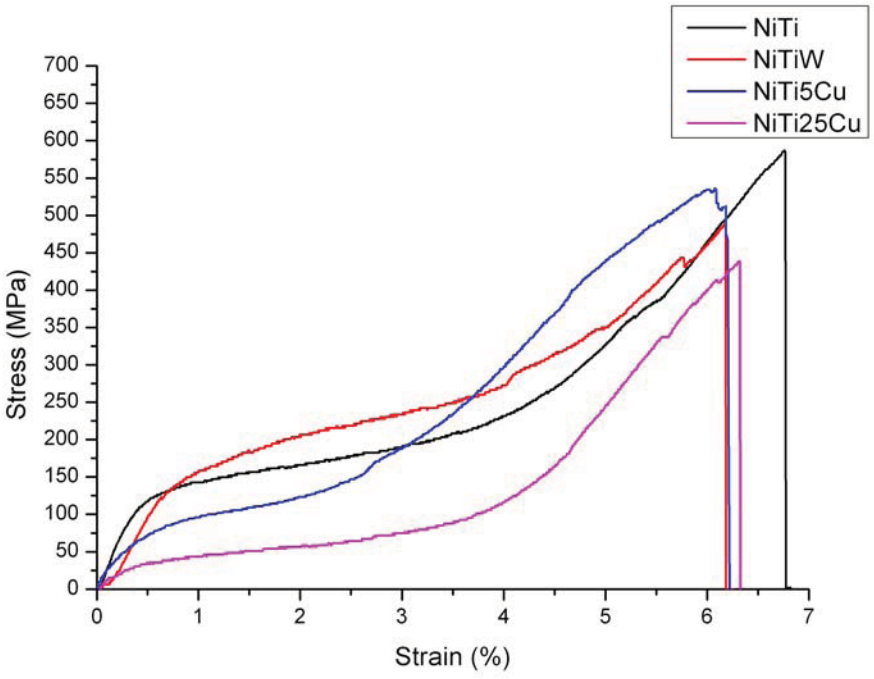

Fig. 4-27: Stress-strain curves of the different alloys. The symbol (x) represents the fracture point.

The different alloys have revealed differences in strength, critical stresses and yielding points. In order to understand the difference in mechanical properties of various NiTi-based ribbons, several factors need to be considered, such as grain size, martensite microstructure, crystal structure and precipitates. For example, the martensite in NiTi, NiTiW and NiTi5Cu has a monoclinic unit cell while that of the NiTi25Cu has an orthorhombic unit cell.

Figure 4-28 shows the mechanical properties of an amorphous NiTi25Cu melt-spun ribbon. Amorphous ribbons without any crystal phases were produced only in NiTi25Cu alloy under high cooling rates at a wheel speed of 45 m/s. The amorphous ribbons exhibit higher tensile fracture strength and Young's modulus than the crystallized ribbons. These properties are caused by the absence of mobile defects and this elastic-type behavior is well known for amorphous alloys [4.12, 4.13]. Several thermal cycles (up to 220 °C) were performed at 2% strain (arrow) to find out if the microstructure changes (i.e. crystallizes), but an unloading-reloading test at 3% showed that evidently there is no change.

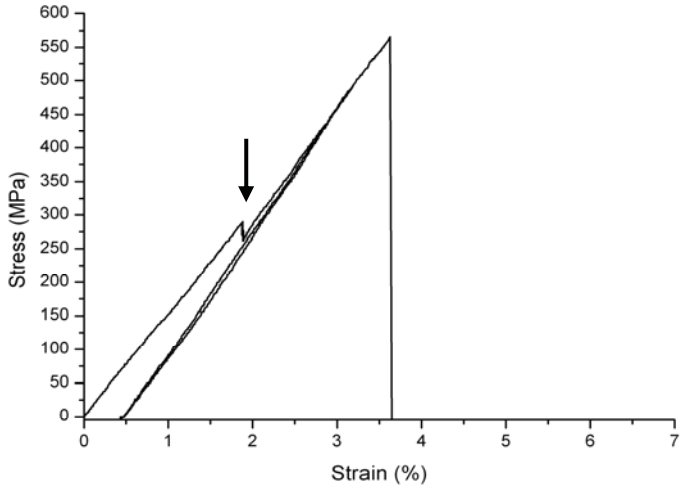

Fig. 4-28: Tensile test result for amorphous NiTi25Cu ribbons at wheel speed of 45 m/s.

A stress-strain curve of NiTi at 140 °C which is above A_f temperature can be seen in Figure 4-29. Also Figure 4-30 shows stress-strain curves of a NiTi25Cu ribbon tested first at 110 °C which is above A_f and then at room temperature. One unloading and reloading was carried out to see whether the ribbon is fully martensitic with pseudoplastic effect or not. It can be seen that the elastic modulus of austenite is higher than that of martensite. At low temperature, the SMA is in its soft martensitic phase; thus, it is easy to deform. But as the temperature increases above A_s, the structure becomes austenitic and stiffer and, therefore, more difficult to deform, requiring a greater stress to obtain the same strain values as in martensitic structure.

Figure 4-31 demonstrates the stress versus strain behavior of the NiTi ribbons at different temperatures above A_f to find the M_d temperature which is the maximum temperature to induce martensite by stress. The ribbons reveal increment in critical stress with increasing test temperature. At temperatures greater than 160 °C and especially at 200 °C, ribbons do not exhibit pseudoelastic effect during unloading-reloading since the temperature of the ribbon is above M_d.

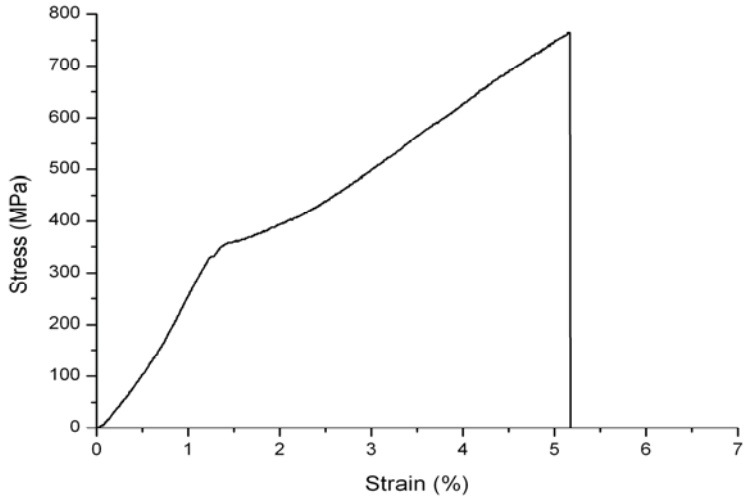

Fig. 4-29: Stress–strain curve of NiTi ribbon at 140 °C.

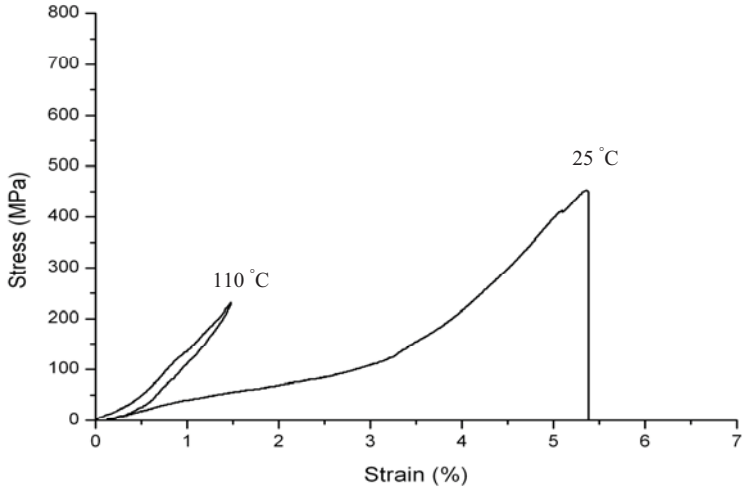

Fig. 4-30: Stress–strain curves of NiTi25Cu ribbon tested at austenitic and martensitic state.

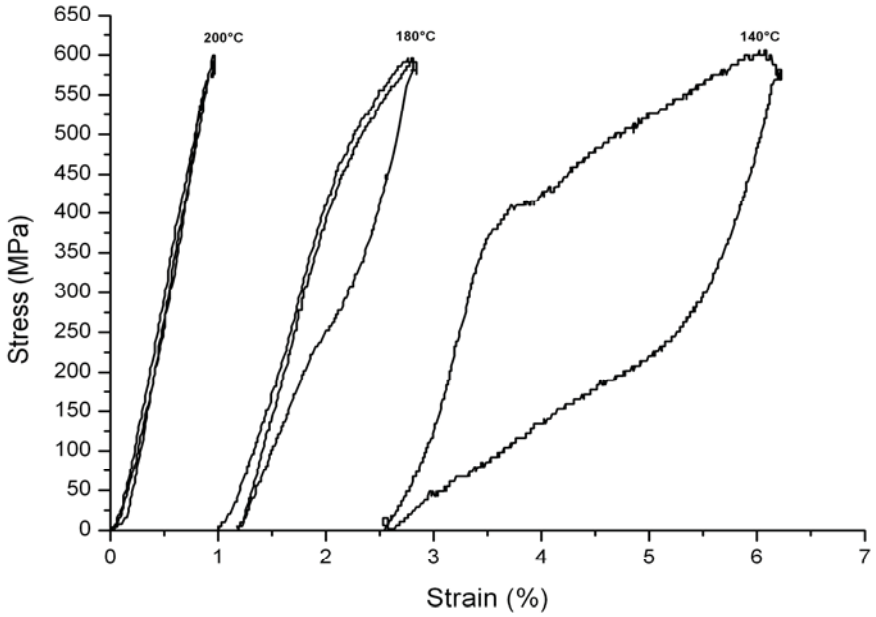

Fig. 4-31: Stress–strain curves of NiTi ribbons at different temperatures.

4.4 One-way shape memory effect

The melt-spun ribbons displayed the shape memory effect, which was easily observed by bending a ribbon and watching it return to its original shape upon heating. This SME also has been evaluated by room temperature tensile test.

Figure 4-32 shows the stress–strain curves of three NiTi ribbons which were loaded to stresses of 200, 250 and 450 MPa at room temperature, well below the A_s temperature of 72 °C. After unloading, 28%, 18% and 15% of the imparted strain was recovered elastically. The pseudoplastic deformation reaches about 4 % strain before plastic deformation occurs. The curves at loading higher than critical stress (150 MPa) unload to a non-zero strain; however, these strains are recoverable on heating. The arrows indicate the recovery strains.

The total strain of the first ribbon is 2.4% with a recovery rate of 100%. The total strain of the second ribbon is much higher, which is 4.5%, and the SME is incomplete with recovery strain of 4.1%, i.e. 91% recovery. The third ribbon was deformed to a total strain of 5.5% without fracture; however, the SME is lower with recovery strain of 3.7%, which is 67% recovery.

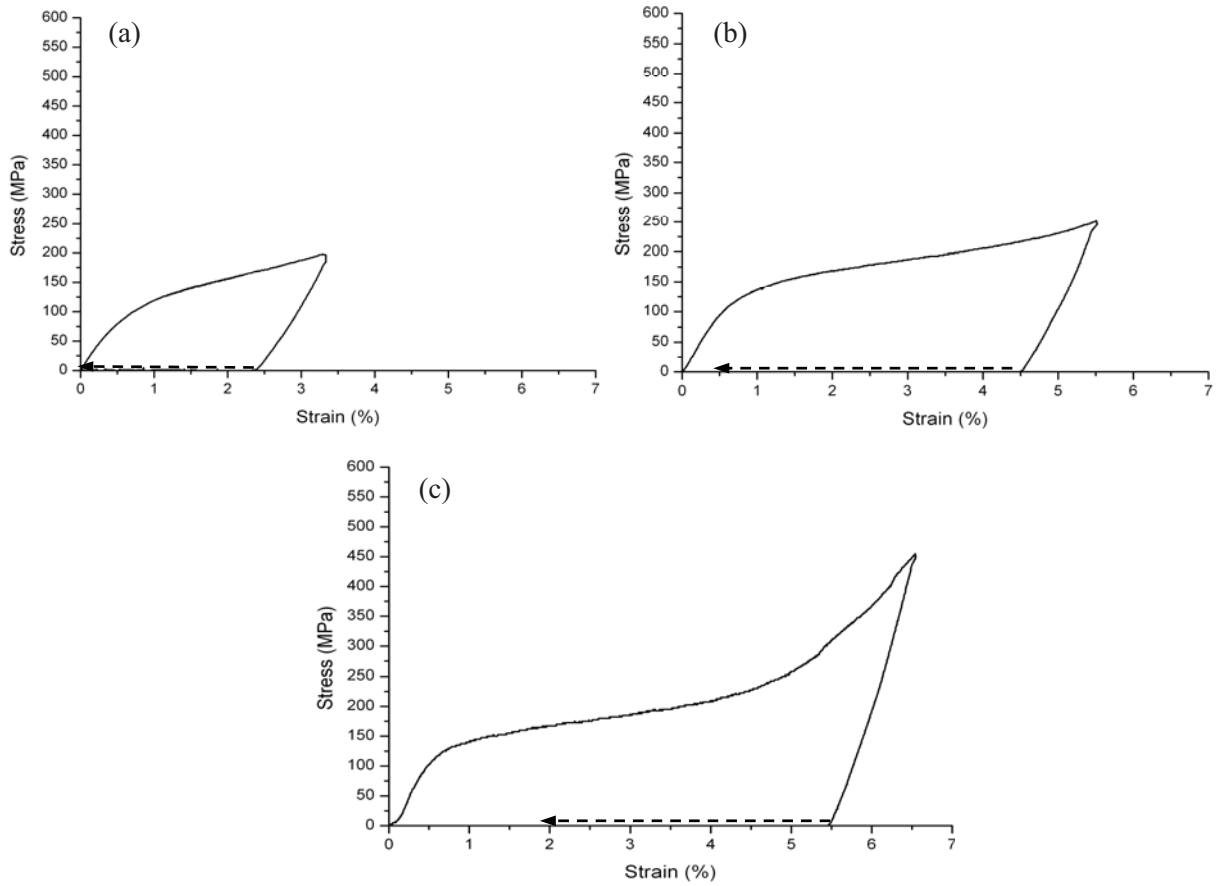

Fig. 4-32: Stress–strain curves of NiTi ribbons loading to maximum stresses of (a) 200 MPa, (b) 250 MPa and (c) 450 MPa at room temperature, indicating different recovery strains after heating. Dashed lines represent the recovered strain upon heating to 180 °C.

As shown in Figure 4-33, two NiTi25Cu ribbons were loaded at room temperature to a strain of 3.4% and 6.2% at about 100 MPa and 250 MPa, respectively. After heating, the reverse martensitic transformation occurs, and the ribbon recovers its extension. The first ribbon was fully recovered and the second one recovered only partially (with recovery strain of 3.3%), as shown by arrow. The lower recovered strain obtained in this alloy is due to the formation of B19 martensite, which has a lower intrinsic transformation strain.

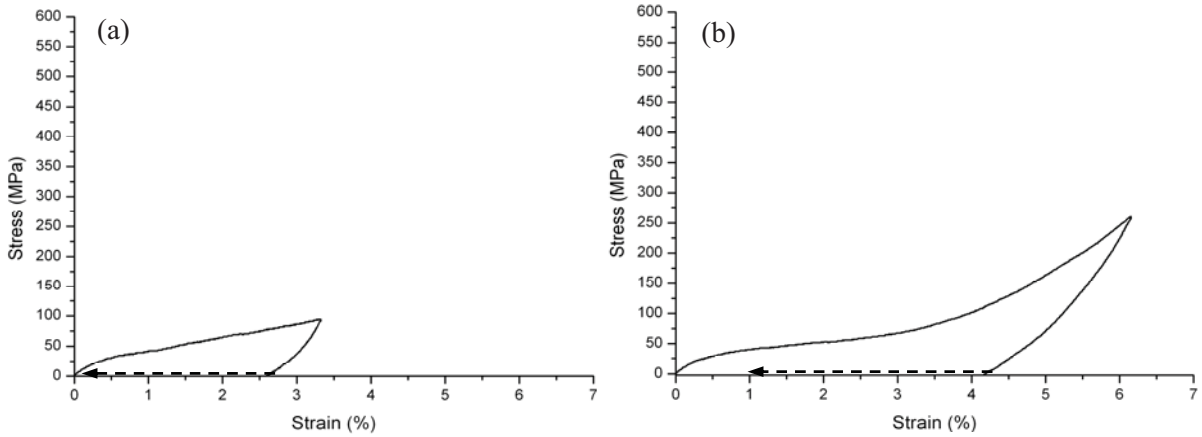

Fig. 4-33: Stress–strain curves of NiTi25Cu ribbons loading to maximum stresses of (a) 100 MPa and (b) 250 MPa at room temperature, indicating the one-way effect after heating.

Figure 4-34 shows representative stress-strain curves for NiTiW and NiTi5Cu ribbons at room temperature. After heating, 4.2 % and 4% strain were recovered, respectively, which are similar to NiTi ribbons. At certain strains the samples was deloaded and reloaded several times to determine if the material was fully pseudoplastic or not. The result reveals that there is no austenite phase and pseudoelastic effect at all.

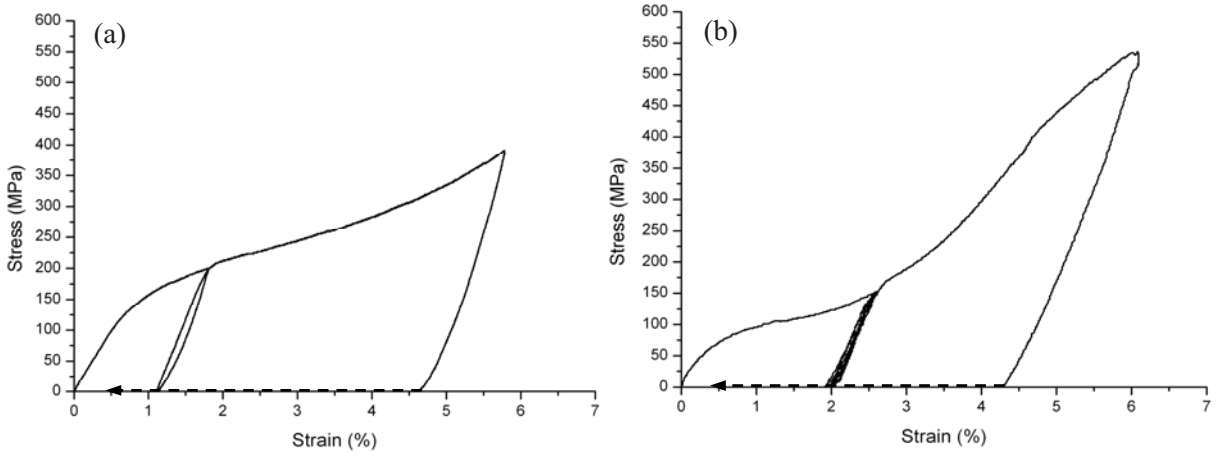

Fig. 4-34: Stress-strain curves of (a) NiTiW and (b) NiTi5Cu ribbons.

4.5 Tensile training and TWSME

4.5.1 Training procedure under constant strain

In order to induce a two-way shape memory effect, a tensile training procedure was carried out, which consists of thermal cycles under mechanical load. To date, more than 20 different training procedures have been investigated and published in efforts to develop a TWSME of both high magnitude and stability which have the common feature that external applied stress should be used, such as tension, compression, torsion or bending. The most common ones are thermal cycling under constant stress or strain using tensile deformation.

The procedure was as follows: (a) Initially the specimen was heated, to a temperature of 180 °C, in order to establish the 0% strain level. (b) The ribbon was then cooled to room temperature and a strain was applied to the ribbon. (c) The ribbon was heated at constant strain to 160 °C and 120 °C for NiTi and NiTi25Cu, respectively, and then allowed to cool to 30 °C. (d) This cycle was repeated 5 times. Information that were obtained from these tests include a comparison of the stress versus temperature behavior between different ribbons as well as between different strains.

Figure 4-35 shows the thermomechanical behavior of a NiTi and a NiTi25Cu ribbon at a constant strain of 3.5% and thermally cycled 4 times (segments 1 to 8). It can be seen that NiTi25Cu ribbons exhibit better repeatability and stability during thermal cycles than NiTi ribbons which show irreversible stresses. As shown in Figure 4-36, NiTi ribbons show an enhancement in irreversible stresses (σ_{ir}) with increasing training strain. Especially at the highest training strain one can see that the maximum stress is reduced after each training cycle. The reason is that there is more and more plastic deformation.

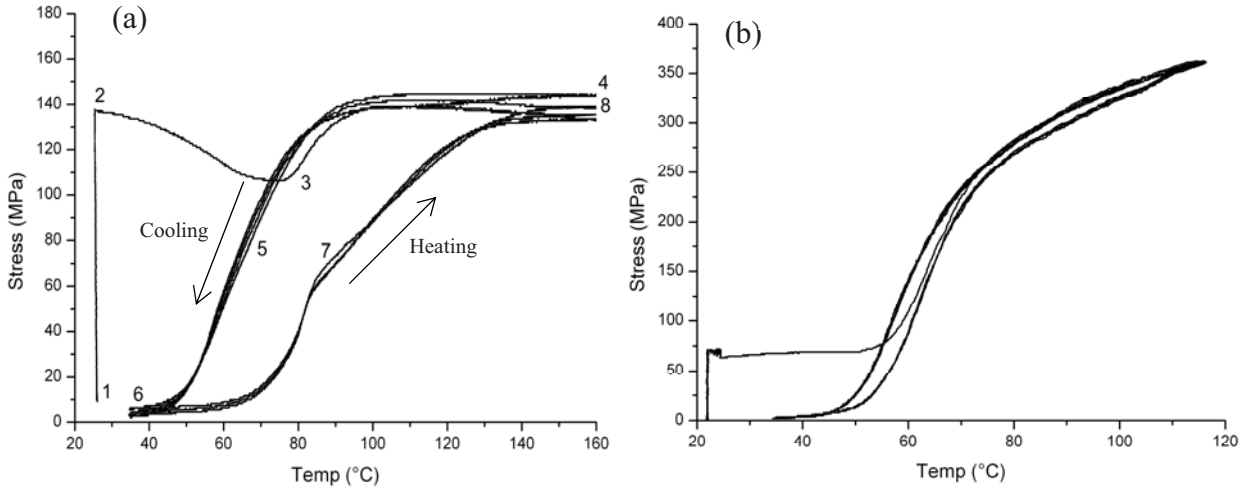

Fig. 4-35: Thermomechanical behavior at a constant strain of 3.5% after 5 thermal cycles (a) NiTi ribbon and (b) NiTi25Cu ribbon.

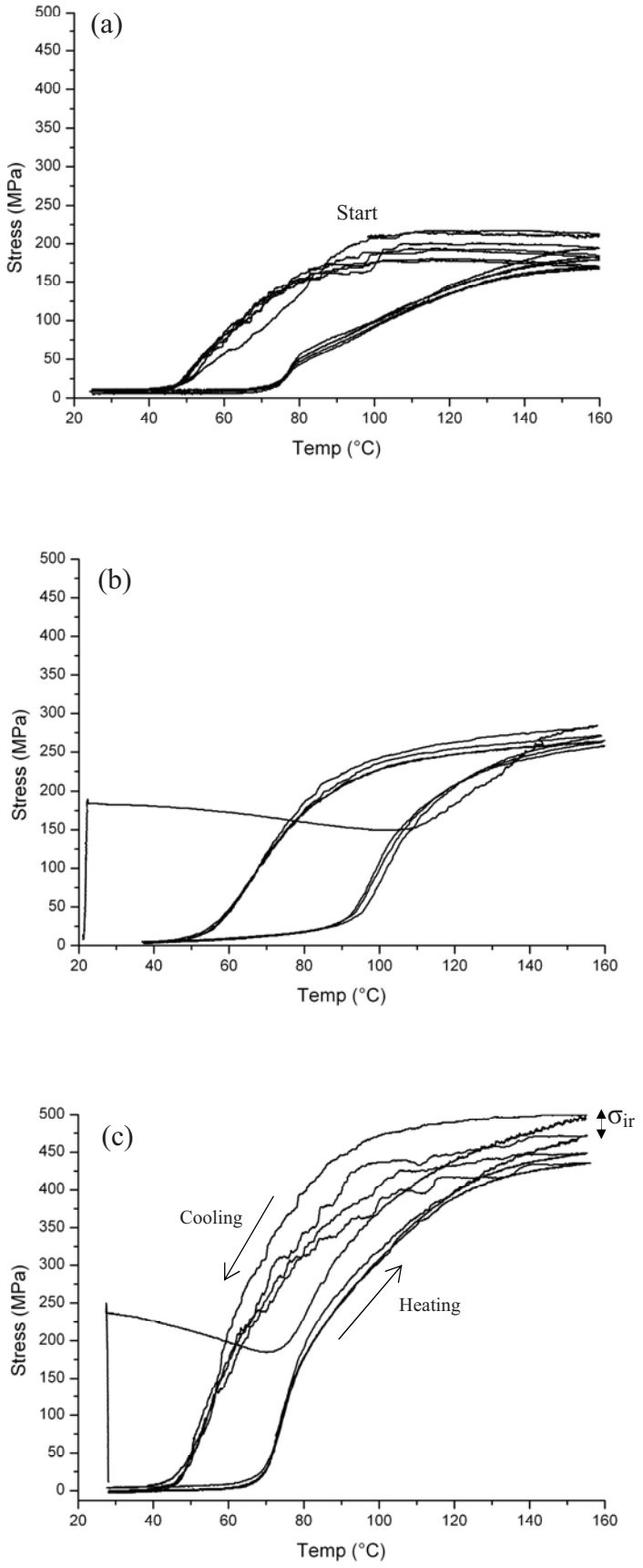

Fig. 4-36: Thermomechanical behavior of NiTi at (a) 4.5%, (b) 5.5% and (c) 6.5% constant strain.

Figure 4-37 shows typical stress versus temperature response for various deformations during second thermal cycle for NiTi and NiTi25Cu. The ribbons are strained to 3.5%, 4.5%, 5.5% and 6.5% for NiTi and 3%, 3.5%, 4.5% and 5.5% for NiTi25Cu, respectively, in order to observe the difference in the recovery stress generation. From the Figures it can be observed that the maximum reversible stress increases with rising of constant strain and can cause higher TWSME due to more required defects for oriented martensite. It has been also illustrated that thermal cycling caused a hysteresis loop during training. It can be attributed to friction associated with the movement of the martensite-parent interfaces.

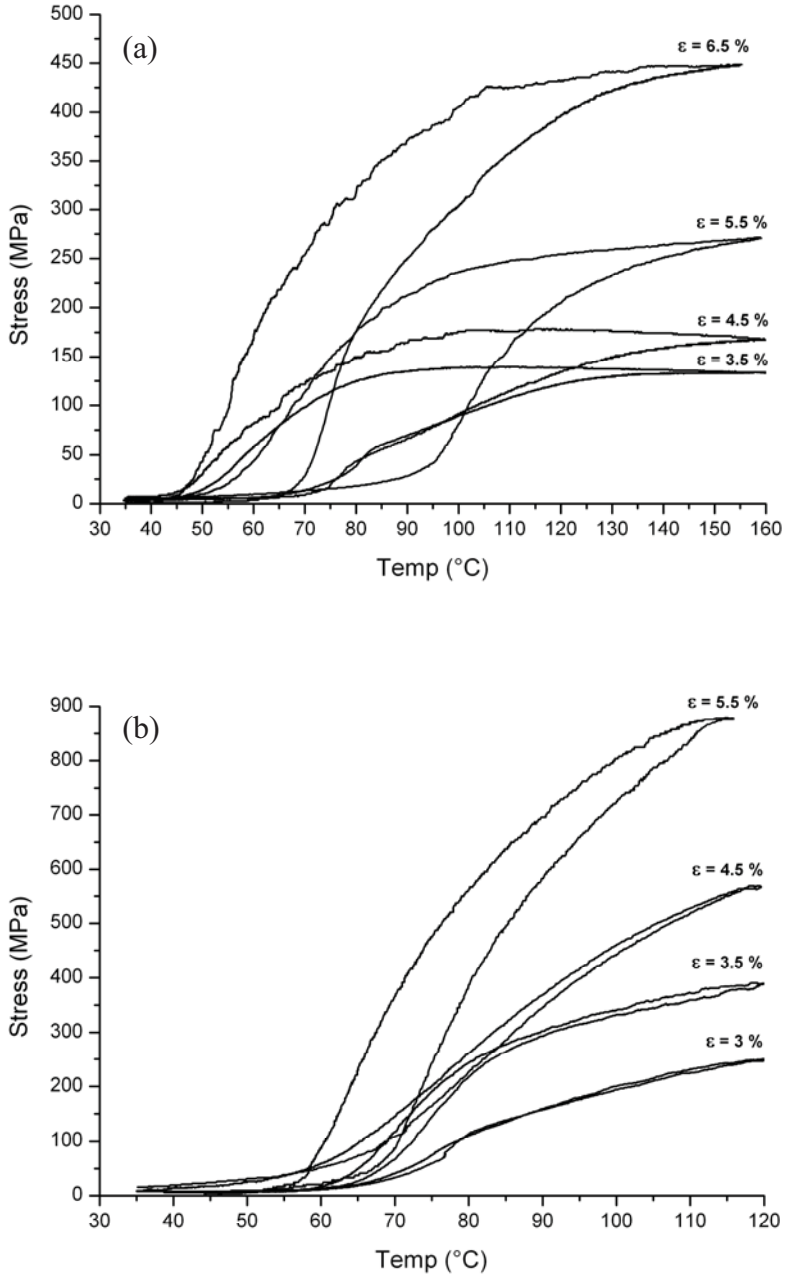

Fig. 4-37: Thermomechanical training with various constant strains during second thermal cycle for (a) NiTi and (b) NiTi25Cu.

After training, thermal cycling of fixed sample without any external stress also caused a hysteresis loop. This spontaneous deformation during a thermal cycle indicates the two-way shape memory effect in ribbons. Figure 4-38 displays the hysteresis loop of a NiTi ribbon which is trained with 4.5% constant strain.

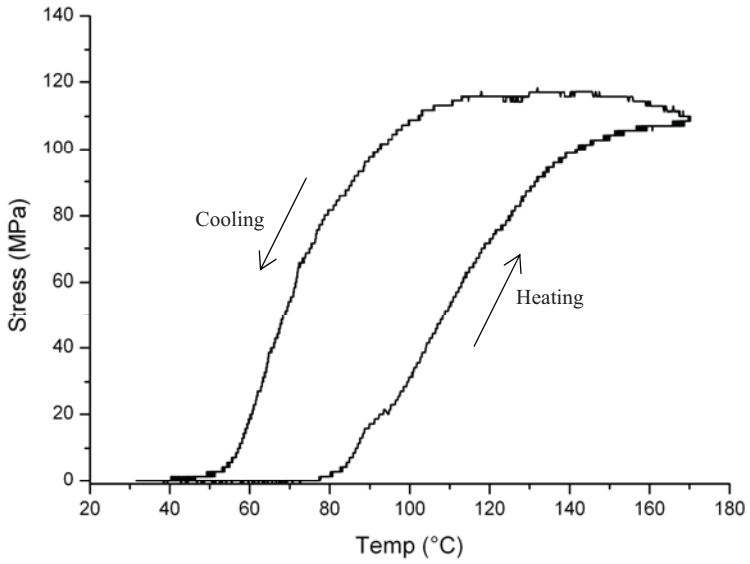

Fig. 4-38: Hysteresis loop of NiTi fixed trained ribbon without external stress.

4.5.2 Two-way shape memory effect

In the previous section, training cycles were performed under constant strain. In this section the two-way shape memory strain (ε_{2W}) was measured during thermal cycles without stress. Figures 4-39 and 4-40 show the measured hysteresis loops, i.e. two-way strains versus temperature, of NiTi and NiTi25Cu trained ribbons, whereas the shape change during the first heating indicates the size of the one-way shape memory strain (ε_{1W}). The NiTi25Cu ribbons (Figure 4-41) illustrate better stability in TWSME than NiTi ribbons but the TWSME is much smaller. In NiTi ribbon during each cycle, less plastic strain was observed than the previous one, and after several cycles the plastic strain become insignificant. It means that the internal stress fields reached a saturated state at higher cycles.

Figure 39c also shows a degradation of TWSME from about 2.9% to 2.4 % after one thermal cycle (arrow). It seems that the rate of degradation is high in the early cycles and then it becomes stable with further cycles, probably due to rearrangement of the internal stresses.

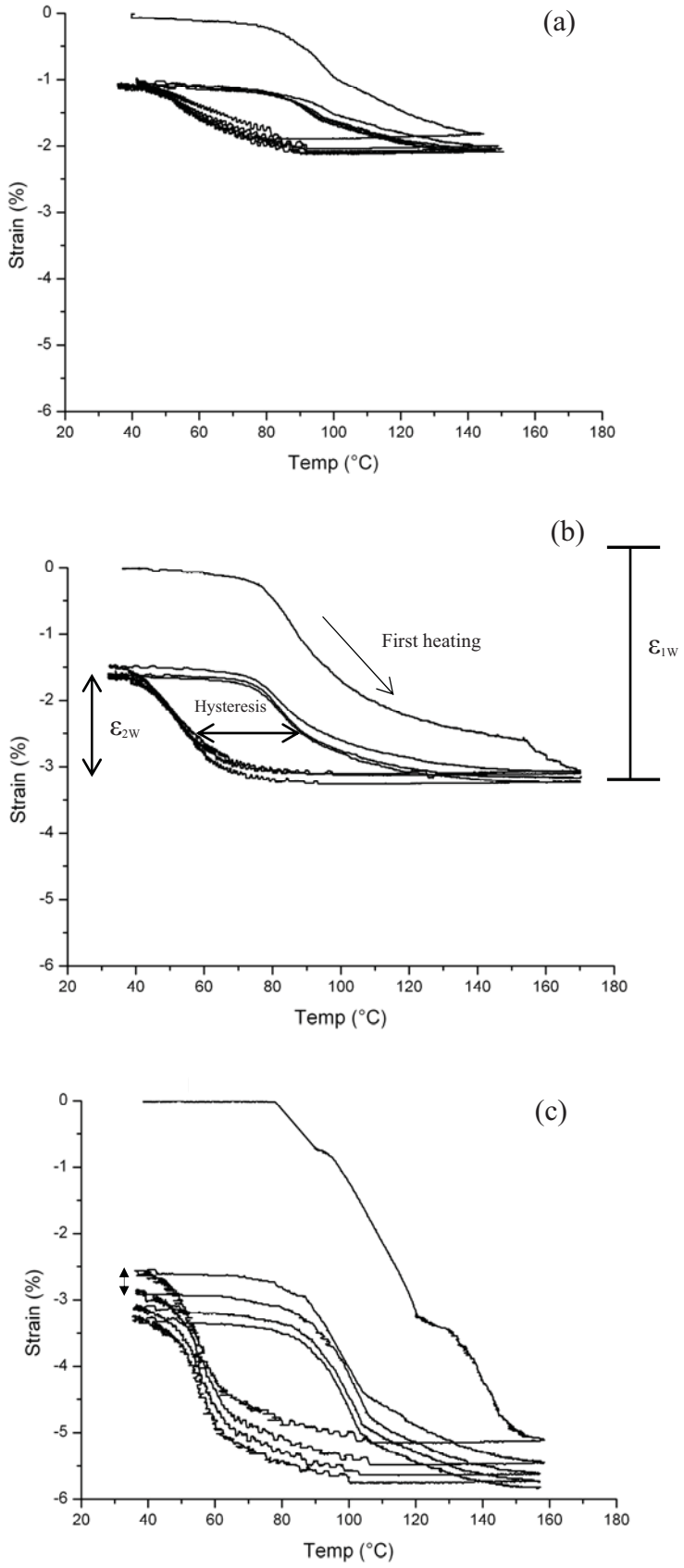

Fig. 4-39: Hysteresis loops of NiTi trained ribbons after four times thermal cycling with: (a) 3.5% strain, (b) 4.5% strain, (c) 6.5% strain.

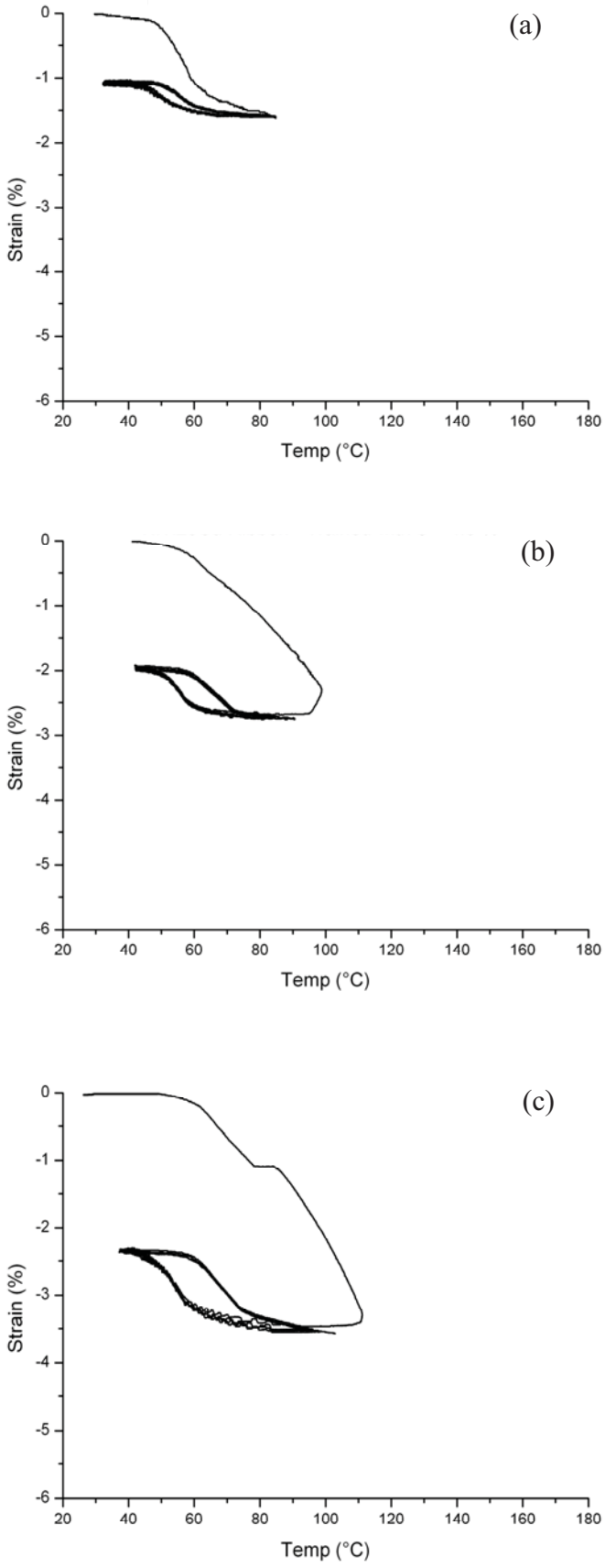

Fig. 4-40: Hysteresis loops of NiTi25Cu trained ribbons after four times thermal cycling with: (a) 3.5% strain, (b) 4.5% strain and (c) 5.5% strain.

The Figure 4-41 shows the measured hysteresis loop of NiTi and NiTi25Cu ribbons in the case of stress free condition trained with various constant strains. As clearly shown with increasing of the constant strain during training, two-way strain increases from about 1% to 2.7% and from about 0.4% to 1.3% for NiTi and NiTi25Cu ribbons, respectively.

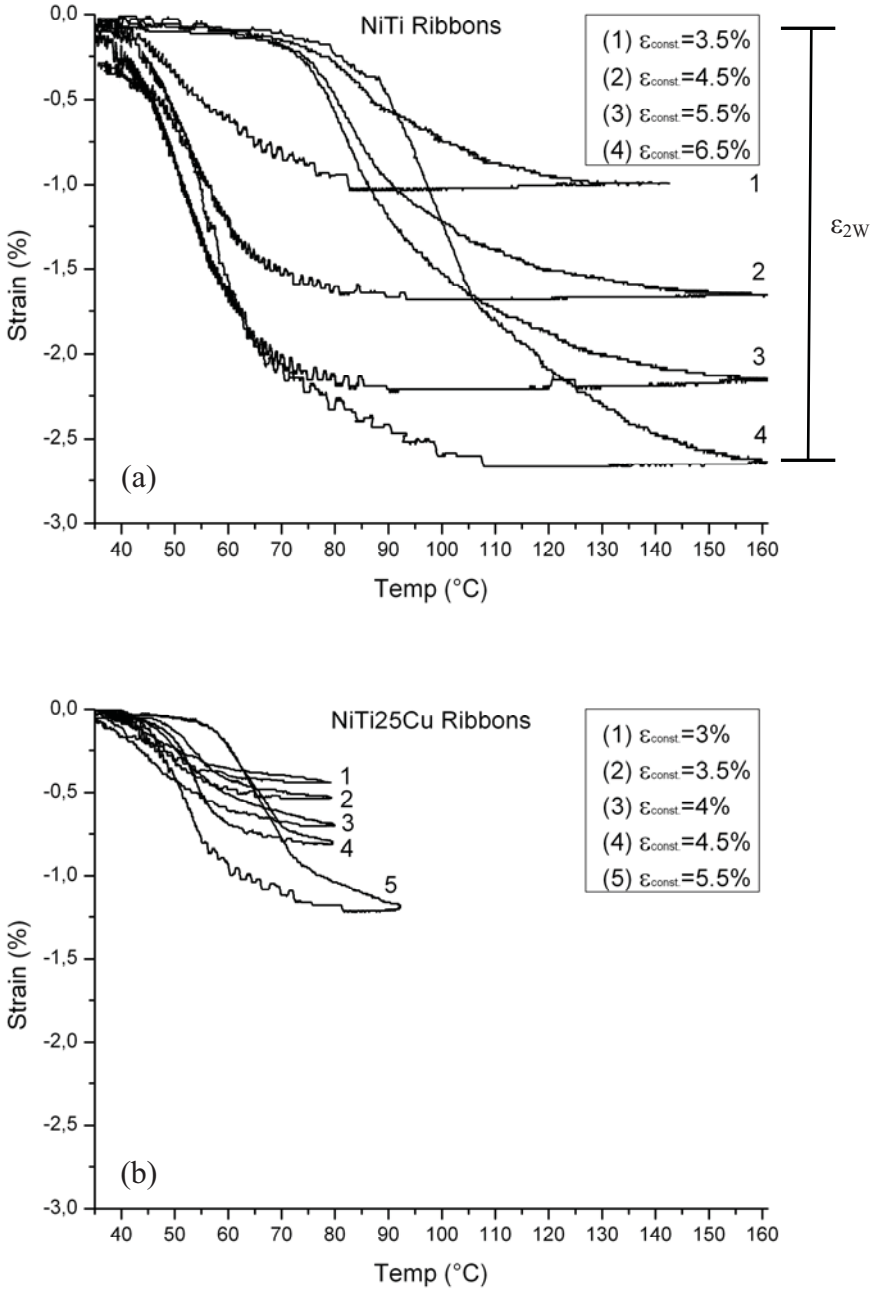

Fig. 4-41: Hysteresis loops at different constant strains, (a) NiTi ribbons and (b) NiTi25Cu ribbons.

The transformation temperatures of the trained ribbons were identified from the hysteresis loops using a slope line extension method, as schematically shown in Figure 4-42.

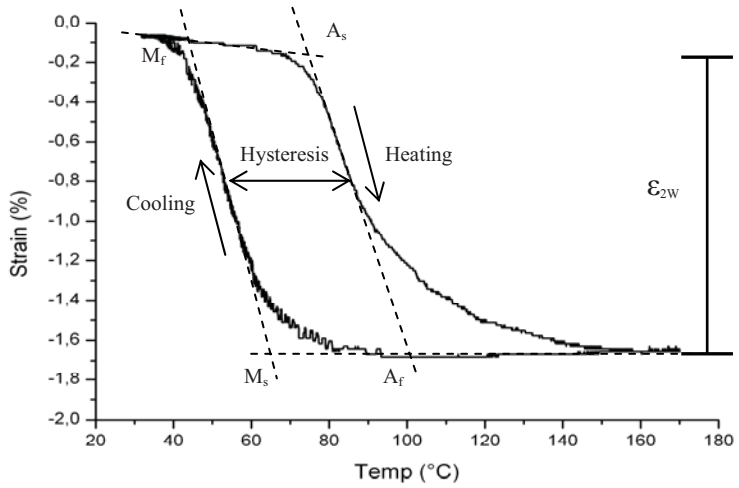

Fig. 4-42: Hysteresis loop of the trained ribbon after free thermal cycling.

To compare the memory effects response of NiTi and NiTi25Cu ribbons, the one-way and two-way shape memory strains and also change in transformation temperatures and thermal hysteresis (A_f - M_s) have been analyzed as a function of the constant strain during training. The following Figures were constructed using the data presented in Figures 4-39, 4-40 and 4-41. Figure 4-43 shows that the NiTi ribbons have higher shape memory strains than NiTi25Cu ribbons and this shape memory strain increases with increasing the training strain, i.e. from 2% one-way effect and 1% two-way effect after training with 3.5% constant strain to 5% one-way effect and 2.7% two-way effect in NiTi ribbon trained with 6.5% constant strain. The memory strains are lower in all the NiTi25Cu ribbons, ranging from 1.4% one-way effect and 0.44% two-way effect with 3% constant strain to 3.4% one-way effect and 1.2% two-way effect after training with 5.5% constant strain.

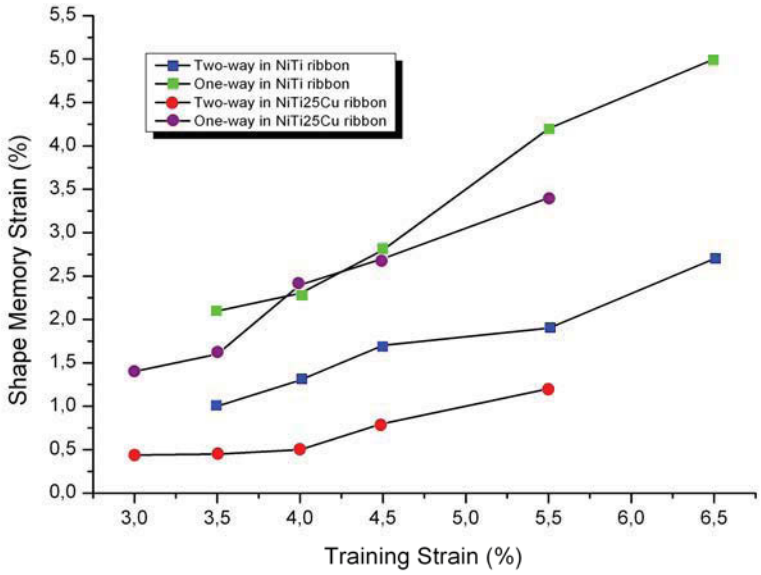

Fig. 4-43: Shape memory strains as a function of the training strain in NiTi and NiTi25Cu ribbons.

Figure 4-44 shows the change in transformation temperatures and thermal hysteresis (A_f - M_s) at different training strains. The main observation in these plots is the increasing of all transformation temperatures with rising of strain or stress level in both the NiTi and the NiTi25Cu ribbons. Among the transformation temperatures, particular attention is paid to the change of M_s temperature to estimate the development of internal stress, as well as to understand the mechanism of dislocations in association with the plastic strain.

The hysteresis increases with increasing stress level in shape memory materials, due to more defect generation which increases the dissipation energy and decreases elastically stored energy, thus the need for additional thermal energy for recovery. In other words, more and more thermal energy is required (for the motion of interface) to compensate the elastic energy dissipation and to overcome the barrier against austenite-martensite interface motion [4.14]. This additional energy is provided by undercooling during forward transformation and overheating during reverse transformation. Also, it was observed that the NiTi25Cu ribbons have a smaller hysteresis than the NiTi ribbons. A small temperature hysteresis provides better control over the recovery stresses and the temperature range in which they can be activated.

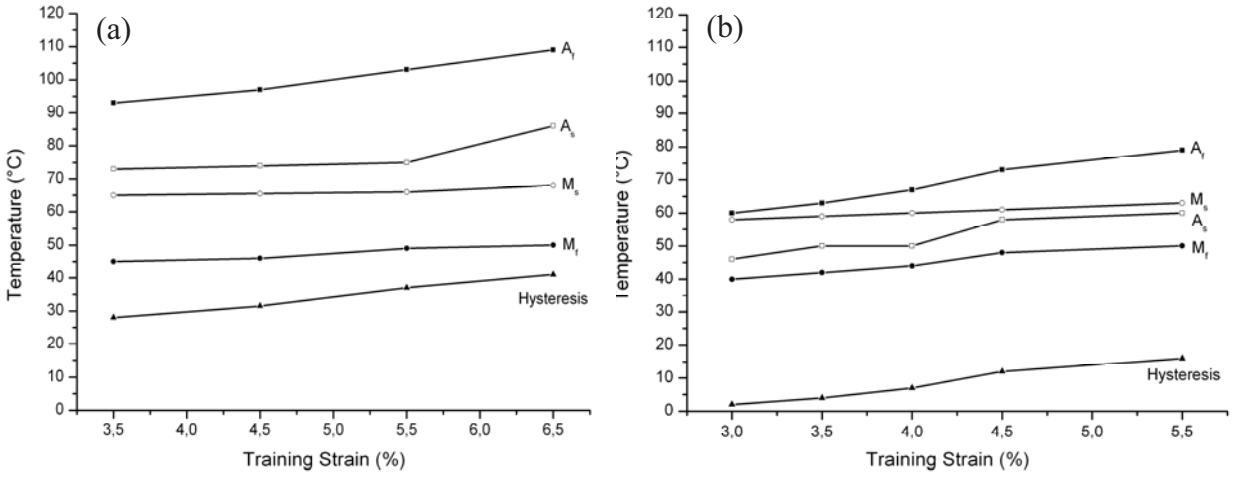

Fig. 4-44: Change in transformation temperatures and thermal hysteresis in: (a) NiTi and (b) NiTi25Cu ribbons.

Furthermore, Figure 4-45 displays two-way shape memory effect, plastic strains and thermal hysteresis as function of the number of free thermal cycles after training with 6.5% strain. A significant observation is that there is a decrease in two-way strain and hysteresis. This can be attributed to decrease of stress level and plastic strain which is less after each thermal cycle.

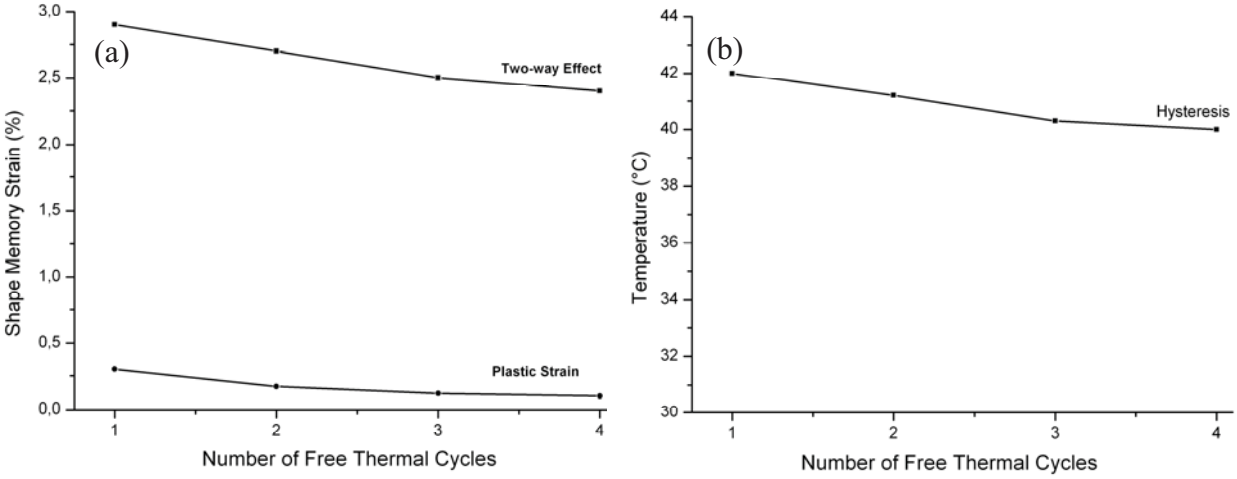

Fig. 4-45: Effect of thermal cycling on (a) two-way shape memory effect and plastic strain and (b) thermal hysteresis of NiTi ribbon trained with 6.5% constant strain.

4.5.3 Stress-assisted TWSME

This study investigates the correlation between the stress-assisted TWSME and the TWSME via experimental approach. When martensitic transformation occurs, the martensite variants form a self-accommodating structure such that no external shape change is observed. When an external stress is applied, one or more of the martensite variants have been change to single variant martensite which leads to external shape change. The shape recovery depicted by the thermal cycling during constant stress represents the stress-assisted TWSME (SATWME) and a gap that illustrates the plastic strain. In other words, it is as part of training procedure, in which martensitic transformation would be assisted by the external stress. Plastic strain exists upon heating, due to generation of dislocations, makes the shape memory effect (SME) incomplete. However, the microstructural mechanism responsible for this plastic strain induces reversible memory effect during subsequent cooling, evidenced by the spontaneous shape change known as SATWME. In general, it is this cyclic behavior which is of particular interest for applications of shape memory ribbons.

Figure 4-46 explains the definition of SATWM strain, plastic strain, and thermal hysteresis on a typical strain-temperature curve of a shape memory alloy thermally cycled under constant stress. Under higher stress the ribbons have a higher volume fraction of single variant martensite, resulting in higher external strain levels. Also during thermal cycling, more defects are introduced at the austenite-martensite interface, which increases the dissipation energy thus causes increasing of the thermal hysteresis.

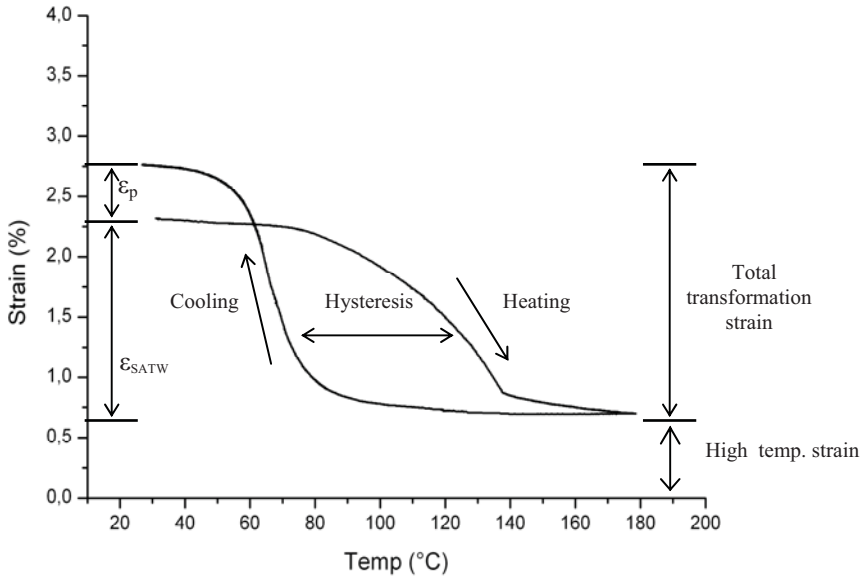

Fig. 4-46: Schematic of the temperature-strain response of an SMA having plastic strains per thermal cycling under stress.

Figure 4-47 shows the effect of thermal cycling on the strain-temperature behavior of the NiTi ribbons (segments 1 to 6) with different loads of 235 MPa and 125 MPa. Incomplete hysteresis loop is seen for both cases, as evidenced by the gap indicated in the Figure with ε_p. When the applied stress is increased, transformation temperatures, thermal hysteresis, plastic strain and stress-assisted TWSME of ribbons also increase. In ribbons with higher stress exist more detwinning regions where dislocations are likely to be introduced in the microstructure, hence providing greater driving force for the SATWME. The increment of transformation temperatures are a consequence of the formation of a dislocation structure, which is confirmed by the increase in the plastic strain, i.e. the deformation in austenitic condition. This effect is in agreement with the literature [4.15, 4.16].

Furthermore on the sample with load of 125 MPa, it is observed that SATWME stabilizes after 15 thermal cycles. As the number of cycles increases, the strain of the ribbon at 170 °C also increases starting from 0.3% and reaching a saturation level of 2.2%. The transformation temperatures also increase with increasing thermal cycles as displayed in the Figure 4-48, while the hysteresis remains almost constant around 40 °C. As can be seen in the Figure, the transformation temperatures become stable during thermal cycling. The defects reach a saturation level and it is prevented the formation of dislocations during repeated phase transformation.

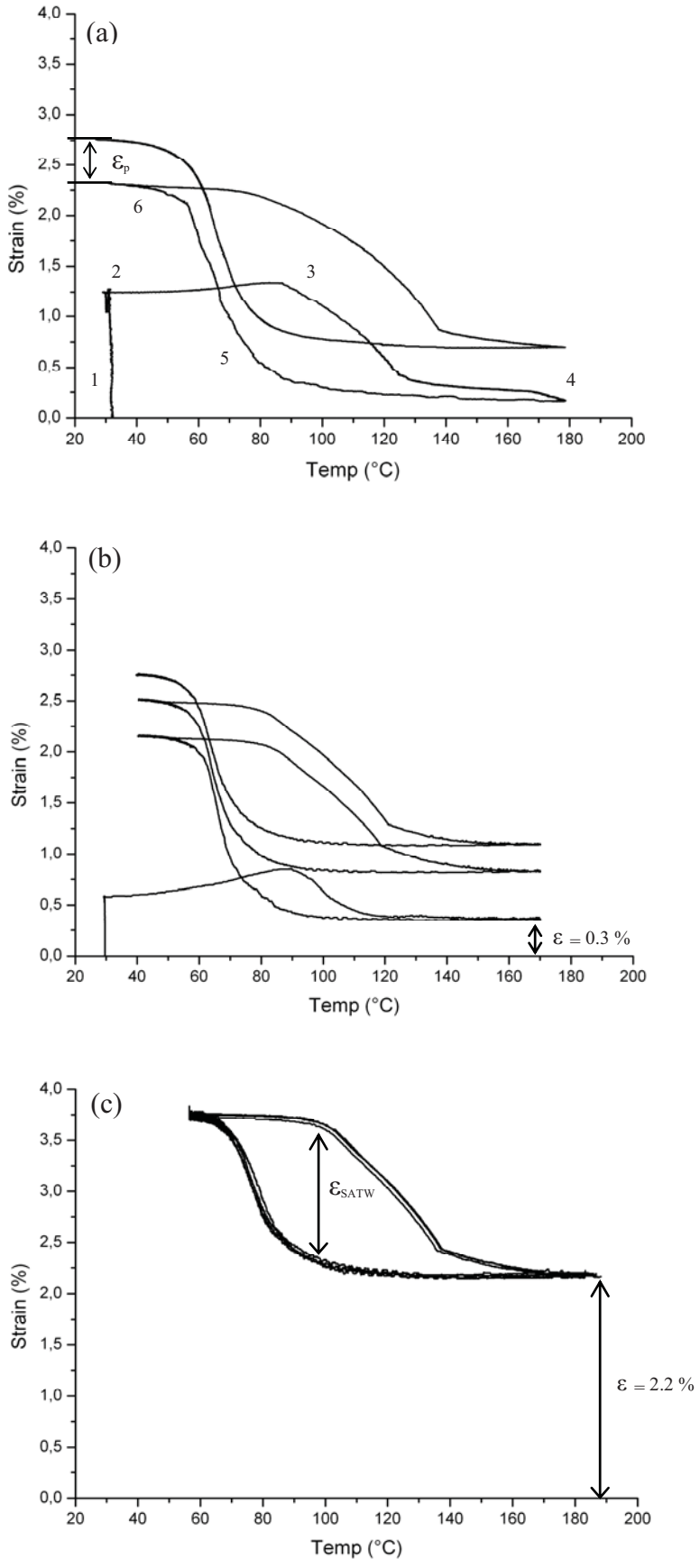

Fig. 4-47: Stress-assisted TWSME of NiTi ribbons; (a) constant stress of 235 MPa, (b) constant stress of 125 MPa and (c) constant stress of 125 MPa after 15 cycles.

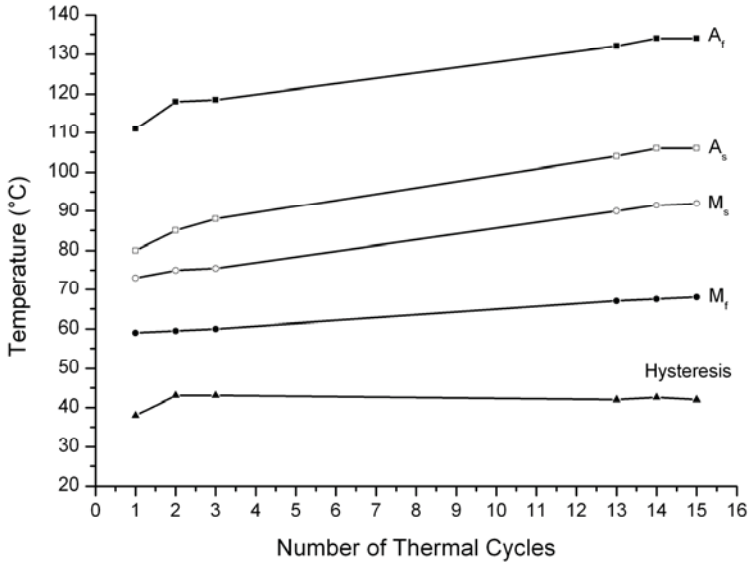

Fig. 4-48: Effect of thermal cycling with constant stress on transformation temperatures.

In Figure 4-49, the total strain (ε_{total}), stress-assisted two-way strain (ε_{SATW}) and plastic strain (ε_p) versus cycle number of a ribbon under constant stress is presented. It is shown that there is a considerably large residual plastic strain after each cycle which contributes to the total plastic transformation strain. In particular, the Figure shows that total strain increases from 2.15%, at the first training cycle, to 3.8% after 15 cycles and plastic strain rises from 0.3 to 2.2%, while a slight drop in stress-assisted TWSME strain is observed in early stages and then remains almost constant during thermal cycling, i.e. good stability of stress-assisted TWSME.

The significant plastic deformation stems from the formation of localized lattice defects, or by stabilization of martensite. The defects are accumulated during subsequent cycles as barriers to reverse transformation, and thus lead to plastic strain. Thermomechanical cycling is a possibility to increase the strength of parent phase and, consequently, cause a proper stability, i.e. to minimize and/or avoid the formation of lattice dislocations during cycling. Therefore, it is suggested that the SATWME stabilizes during thermal cycling as well as the TWSME.

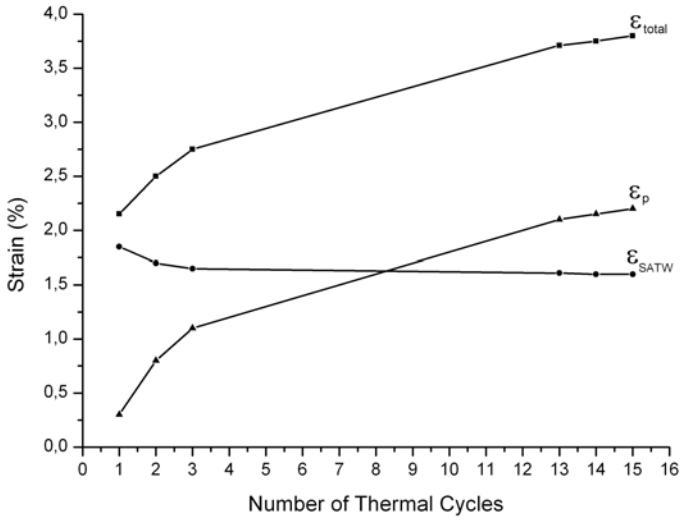

Fig. 4-49: Effect of thermal cycling on total strain, stress-assisted TWSME strain and plastic strain.

4.6 Bending training and TWSME

4.6.1 Bending training procedure

For inducing a two-way shape memory effect, as explained earlier in section 2.4.5, there are several training methods. However, two main groups of thermomechanical trainings using bending deformation are:

- Thermal cycling with deformation below M_f (Shape memory cycling)
- Thermal cycling with constant stress or strain (Constrained cycling)

In this section, this two training methods have been applied on NiTi-based ribbons in a self-fabricated device. One is based on bending below M_f and load free heating above A_f and the other one based on several times thermal cycling under constant bending curvature and then load free thermal cycling.

The bending deformation strain (ε_d) of the outer surface of the specimen was calculated as $\varepsilon_d = d/(D+d)$ where d is the ribbon thickness and D is the diameter of the constrained circle. The one-way shape recovery strain (ε_{1w}), two-way shape memory strain (ε_{2w}) and plastic deformation (ε_p) are measured by the values of:

$\varepsilon_{1w} = [(\theta_0 - \theta_1)/\theta_0] \times \varepsilon_d$

$\varepsilon_{2w} = [(\theta_2 - \theta_1)/\theta_0] \times \varepsilon_d$

$\varepsilon_p = \theta_1/\theta_0$

where the angle $\theta_0 = 180°$ and the deformation angles θ_1 and θ_2 are indicated in Figure 4-50. The value of spontaneous shape change during heating and cooling was recorded by photographing. During the constrained training and subsequent free thermal cycling, temperature was changed from room temperature (RT) to 200 °C. The TWSME was executed several thousand times and the changes in the deformation behavior and the stability of the effect were continuously observed. As example in Figure 4-51, a NiTi ribbon is shown that displays reversible shape change during heating and cooling after 500 free thermal cycles.

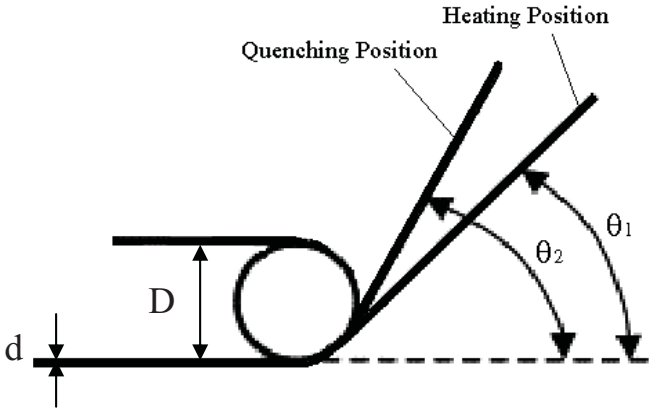

Fig. 4-50: Schematic illustration for bending examination of TWSME.

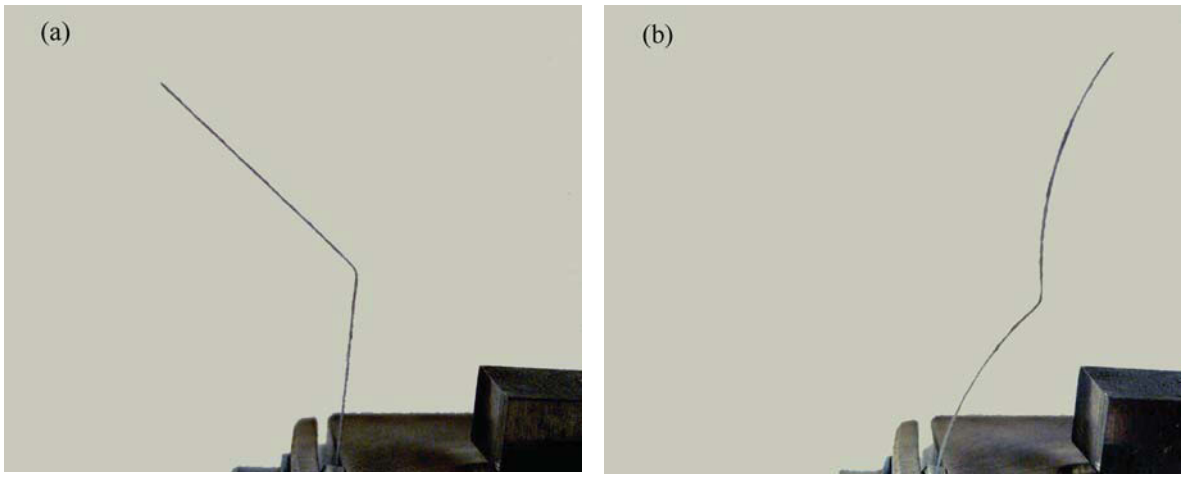

Fig. 4-51: Two-way effect of a trained ribbon: (a) after cooling (T<Mf) and (b) after heating (T>Af).

4.6.2 TWSME using bending deformation

In this study pieces of NiTi-based ribbons (~ 40 mm long, 2 mm wide and 80 μm thick) were bent to different small radiuses from 4 mm to 0.7 mm. The corresponding bending strain are 2.6 %, 4%, 6.5%, 8 % and 9.8%. Figure 4-52 shows the effect of bending strain on the TWSME of NiTi ribbon after 3 training cycles. With increasing strain, TWSME increased to a maximum of 0.58% at 8% strain and then decreased after a deformation to 9.8% due to plastic deformation. Since it was found that 8% bending strain (with bending radius of 0.9 mm) leads to the highest TWSME, the further experiments were performed with that bending strain.

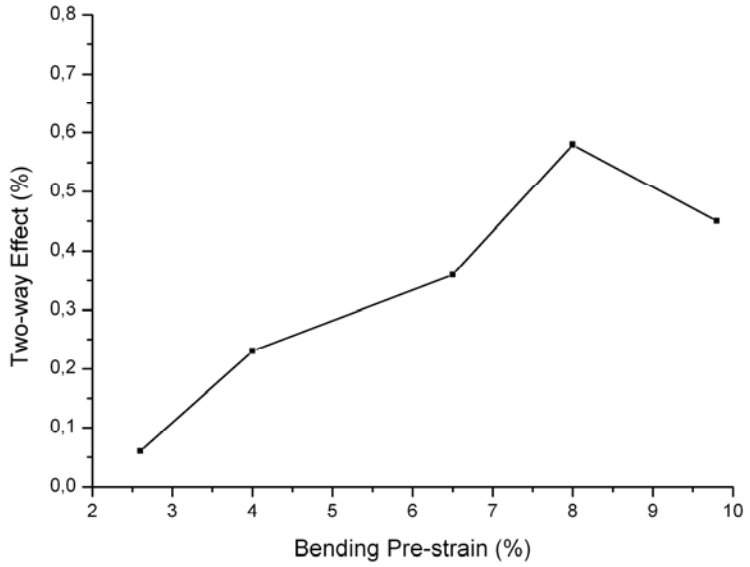

Fig. 4-52: Effect of the bending pre-strain on the TWSME.

Figure 4-53 illustrates comparison of TWSME results from both bending training methods. As can be seen, in the first method (shape memory cycling) the TWSME increased with the number of training cycles. It can be seen that after one training cycle only one-way SME exists, while after several cycles a TWSME can be found. The results of this training method are also exhibited in Table 4-5.

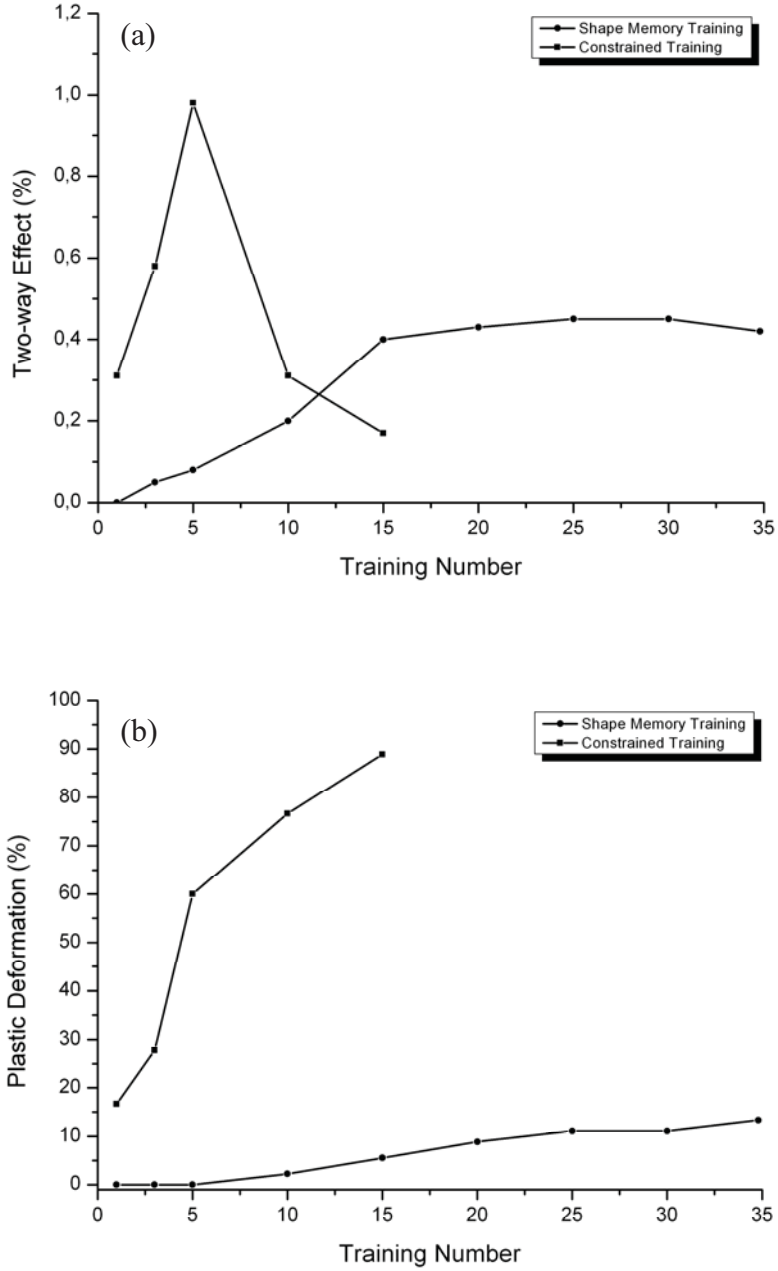

Fig. 4-53: Effect of different training methods on: (a) TWSME and (b) Plastic deformation.

Table 4-5: One-way and two-way memory effects after shape memory cycling method.

Training number	One-way effect, ε_{1w} (%)	Two-way effect, ε_{2w} (%)	Plastic deformation, ε_p (%)
1	2.60	0	0
5	2.60	0.08	0
10	2.54	0.20	2.22
15	2.75	0.40	5.55
20	2.37	0.43	8.88
25	2.31	0.45	11.11
30	2.31	0.45	11.11
35	2.25	0.42	13.33

As shown in Figure 4-53 at constrained training, the TWSME increases during the first few training cycles much higher than during shape memory training method but afterwards decreases because the plastic deformation increases strongly. The largest TWSME is achieved after 5 training cycles. The results of constrained training method are shown in Table 4-6. The experimental results make it clear that during training, the strain energy of bending strain will provide driving force for the preferential orientation of martensite variants. But with the increase of training cycles, plastic deformation accumulates in the crystal grains with the result of unrecoverable strain. Therefore, one-way and two-way shape memory effect of ribbons will decrease with the increase of training number. In other words, this fact suggests that an appropriate density of slip defects is effective for the improvement of the TWSME while an excessive density of defects and plastic deformation reduce the TWSME.

Table 4-6: One-way and two-way shape memory effects after constrained cycling method.

Training number	One-way effect, ε_{1w} (%)	Two-way effect, ε_{2w} (%)	Plastic deformation, ε_p (%)
1	6.66	0.31	16.66
3	5.78	0.58	27.77
5	3.20	0.98	60
10	1.86	0.31	76.66
15	0.88	0.17	88.88

4.6.3 Stability of the TWSME

The opposite effect has been found for two-way shape memory effect during the free thermal cycles. In most cases, after enough constrained training and then several hundred free thermal cycles, the TWSME became larger with higher shape recovery and finally stabilized. As represented in the Figure 4-54, the TWSME of NiTi ribbon trained with 5 constrained cycles was about 1% and after 400 free thermal cycles increased to about 2%, but shows poor stability during the subsequent thermal cycling. When the training procedure is extended to 15

cycles, despite a smaller initial TWSME, the sample shows relatively high stability during 3000 thermal cycles.

Similar to NiTi ribbon, the NiTi25Cu ribbon demonstrated that 5 training cycles were not enough effective to stabilize TWSME and a good stability can be got only after 15 training cycles, however the NiTi2W ribbon after 5 training cycles leads to a TWSME with proper stability. It is due to higher strength of NiTi2W ribbon than other ribbons which causes enough internal stress fields after 5 training cycles. In Figure 4-54, the TWSME and plastic deformation of various ribbons were observed during 3000 thermal cycles. Softer ribbons can be trained easily to higher effect size but the stability is weak. On the other hand, ribbons of higher strength exhibit smaller TWSME values but prove to be relatively stable against functional fatigue. This stability of about 1% TWSME in these ribbons seems very suitable for many applications. The results of TWSME are summarized in Tables 4-7 to 4-10, ε_{1w}, ε_{2w} and ε_p denoting the size of one-way shape memory effect, two-way shape memory effect and plastic deformation, respectively.

The decrease of TWSME and plastic deformation in NiTi ribbons after a high number of thermal cycling may be related to a partially relaxation of the stress field or rearrangement of dislocations formed by the training process and the redistribution of existing defects (dislocations). Also it can be explained that the stabilized martensite nuclei after training now become unstable and again take part in thermoelastic martensitic transformation. With a lowered density of dislocations or stabilized martensite nuclei, the internal stress field is not sufficient to ensure a favored variant to form, but other variants or even other self-accommodation groups form.

Table 4-7: Influence of free thermal cycles on the one-way and two-way shape memory effects of NiTi ribbon after 5 constrained training cycles.

Free thermal cycles	One-way effect, ε_{1w} (%)	Two-way effect, ε_{2w} (%)	Plastic deformation, ε_p (%)
1	3.20	0.98	60
10	4.49	1.11	43.88
100	5.51	1.56	31.11
200	6.18	1.69	22.77
300	6.89	1.78	13.88
400	7.56	1.82	5.55
500	7.73	1.78	3.33
800	7.77	1.33	2.77
1000	7.77	0.93	2.77
1500	7.77	0.35	2.77
2000	7.82	0.13	2.22
3000	7.86	0.08	1.66

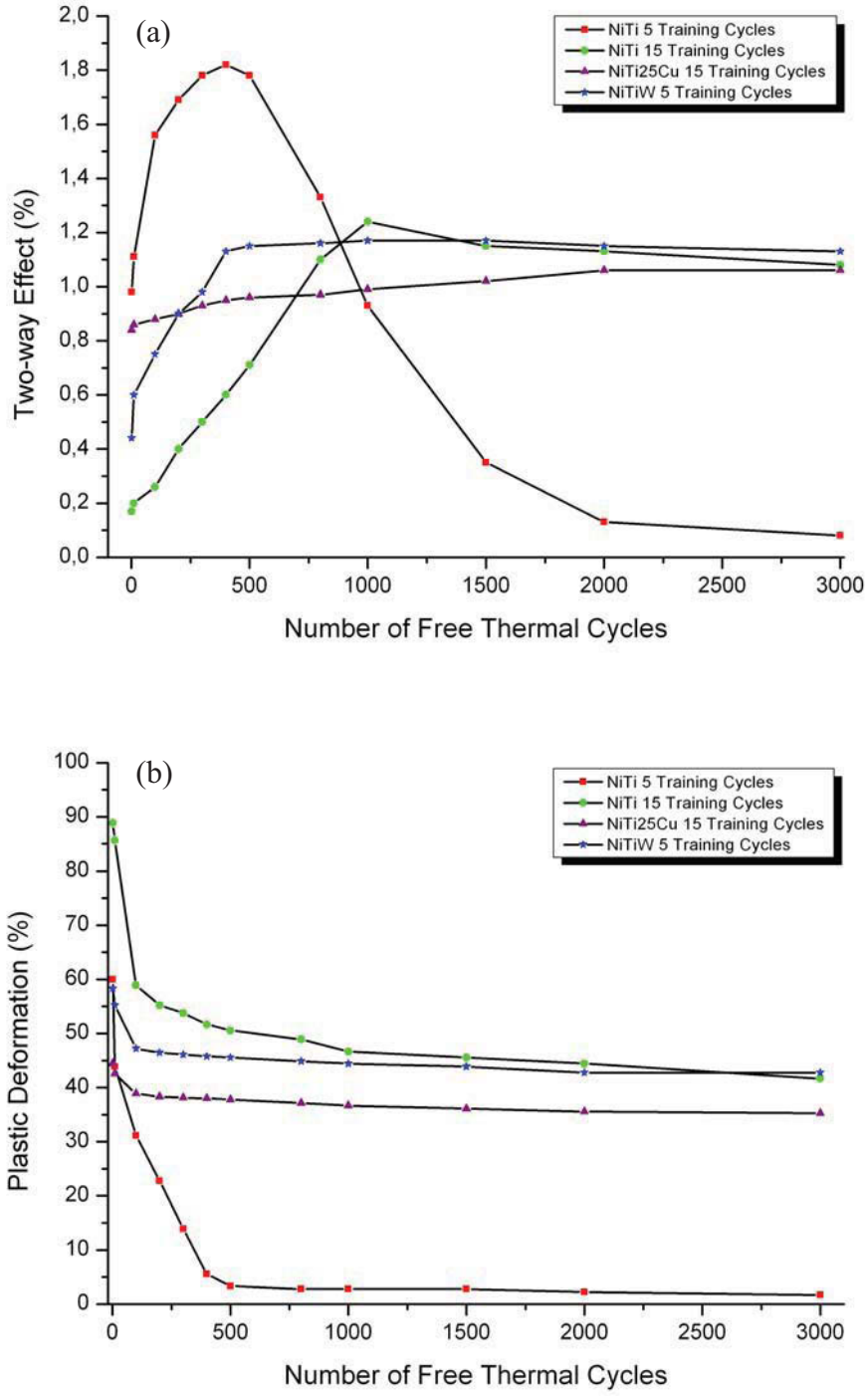

Fig. 4-54: Effect of free thermal cycles in different NiTi-based ribbons on: (a) TWSME and (b) plastic deformation.

Table 4-8: Influence of free thermal cycles on the one-way and two-way shape memory effects of NiTi ribbon after 15 constrained training cycles.

Free thermal cycles	One-way effect, ε_{1w} (%)	Two-way effect, ε_{2w} (%)	Plastic deformation, ε_p (%)
1	0.88	0.17	88.88
100	3.28	0.26	58.88
500	3.95	0.71	50.55
1000	4.26	1.24	46.66
1500	4.35	1.15	45.55
2000	4.44	1.13	44.44
3000	4.66	1.08	41.66

Table 4-9: Influence of free thermal cycles on the one-way and two-way shape memory effects of NiTiW ribbon after 5 constrained training cycles.

Free thermal cycles	One-way effect, ε_{1w} (%)	Two-way effect, ε_{2w} (%)	Plastic deformation, ε_p (%)
1	2.08	0.44	58.33
100	2.63	0.75	47.22
500	2.72	1.15	45.55
1000	2.77	1.17	44.44
1500	2.80	1.17	43.88
2000	2.86	1.15	42.77
3000	2.86	1.13	42.77

Table 4-10: Influence of free thermal cycles on the one-way and two-way shape memory effects of NiTi25Cu after 15 constrained training cycles.

Free thermal cycles	One-way effect, ε_{1w} (%)	Two-way effect, ε_{2w} (%)	Plastic deformation, ε_p (%)
1	2.22	0.84	44.44
100	2.44	0.88	38.88
500	2.48	0.97	37.77
1000	2.53	0.97	36.66
1500	2.55	1.02	36.11
2000	2.57	1.06	35.55
3000	2.60	1.06	35.27

4.7 Transformation behavior

4.7.1 Transformation behavior before training

Figure 4-55 shows the transformation behavior in the NiTi and NiTiCu alloys. To find the most proper heating/cooling rate for the ribbons, the transformations were obtained by measuring the DSC curves at various cooling/heating rates. These rates were ranging from 50 °C/min to 5 °C/min. The results have shown that the heating/cooling rate has strong influence on the transformation temperatures and the absorbed/released heat during transformation.

It is evident that the latent heat of the transformation decreases with decreasing heating/cooling rate. In addition, M_s and A_s are fairly stable at various heating/cooling rates, while A_f increases and M_f decreases with the increase in heating/cooling rate. However, after a critical heating/cooling rate (30 °C/min), M_s increases with increment in heating/cooling rates as well. Therefore with increasing heating/cooling rate, thermal hysteresis increases significantly as well. The dislocations associated with high heating/cooling rates generate an internal stress state which restricts the transformations. Therefore, the absorbed heat during austenitic transformation and the released heat during martensitic transformation increase with the increase in heating/cooling rate in all specimens.

Figure 4-56 shows the starting and finishing temperatures of the transformations and the measurement of transformation hysteresis, defined as A_f - M_s, determined from the DSC curves shown in Figures 4-55. Figure 4-56 shows that thermal hysteresis decreased continuously with decreasing rate. Finally in this work, the heating/cooling rate was taken to be ±20 °C/min for further DSC studies.

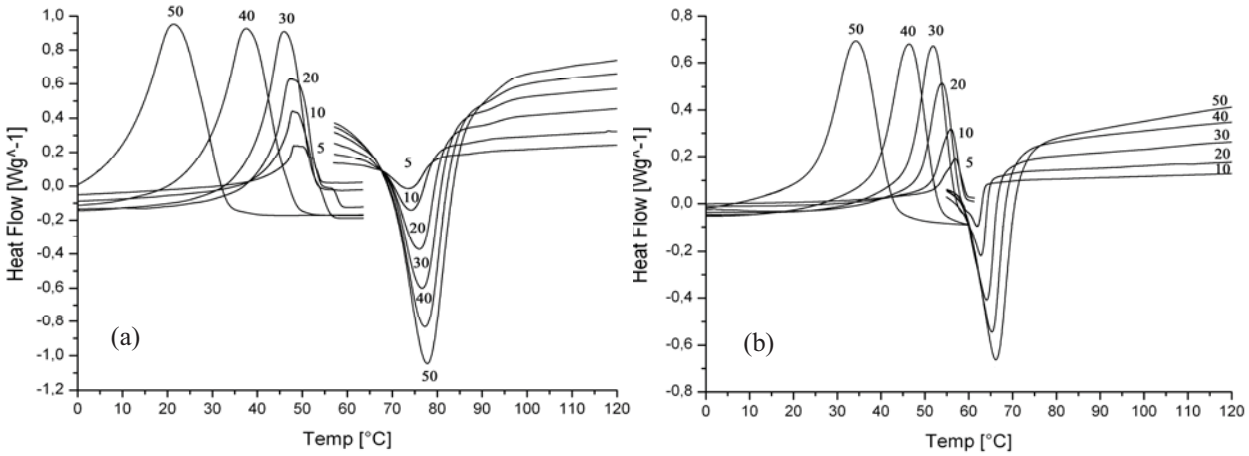

Fig. 4-55: Transformation behavior of ribbons at different heating/cooling rates;
(a) NiTi ribbon and (b) NiTi25Cu ribbon.

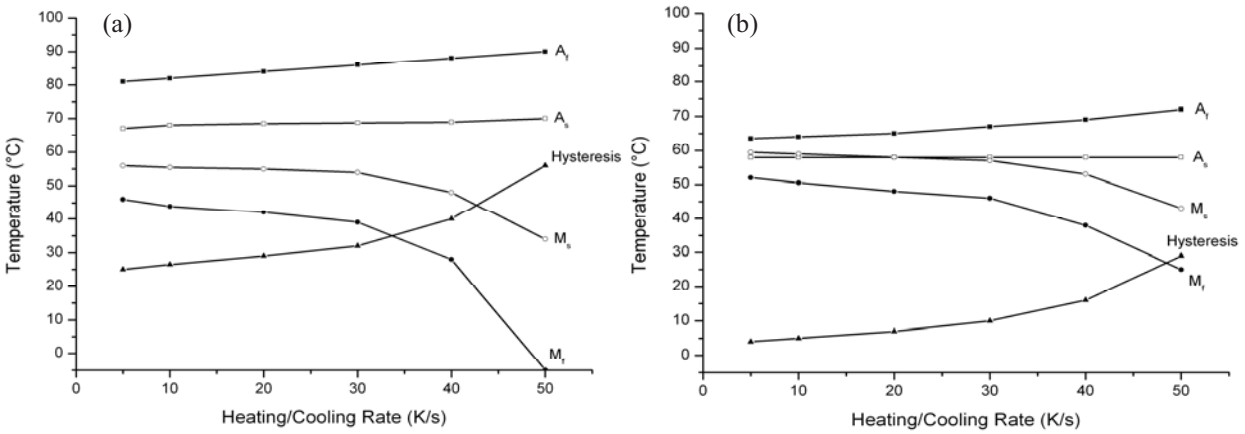

Fig. 4-56: Effect of heating and cooling rates on the thermal hysteresis and transformation temperatures; (a) NiTi ribbon, (b) NiTi25Cu ribbon.

Figures 4-57 displays DSC curves for the NiTi melt-spun ribbons produced at wheel speeds of 5, 15 and 30 ms^{-1}. Figure 4-57a shows the phase transformation for the lowest wheel speed and therefore lowest cooling rate while Figures 4-57b and 4-57c represent the higher wheel speeds and cooling rates. There is only slight difference in the transformation temperatures but additional peaks were appeared at the lower cooling rates (especially Figure 4-57a). These additional peaks are attributed to the fact that with low wheel speed ribbons are relatively thick and transformation temperatures of the chilled side are different from those of the free side of the ribbons. In addition, the materials exhibit higher segregation at lower cooling rate, causing new peaks in the DSC curve.

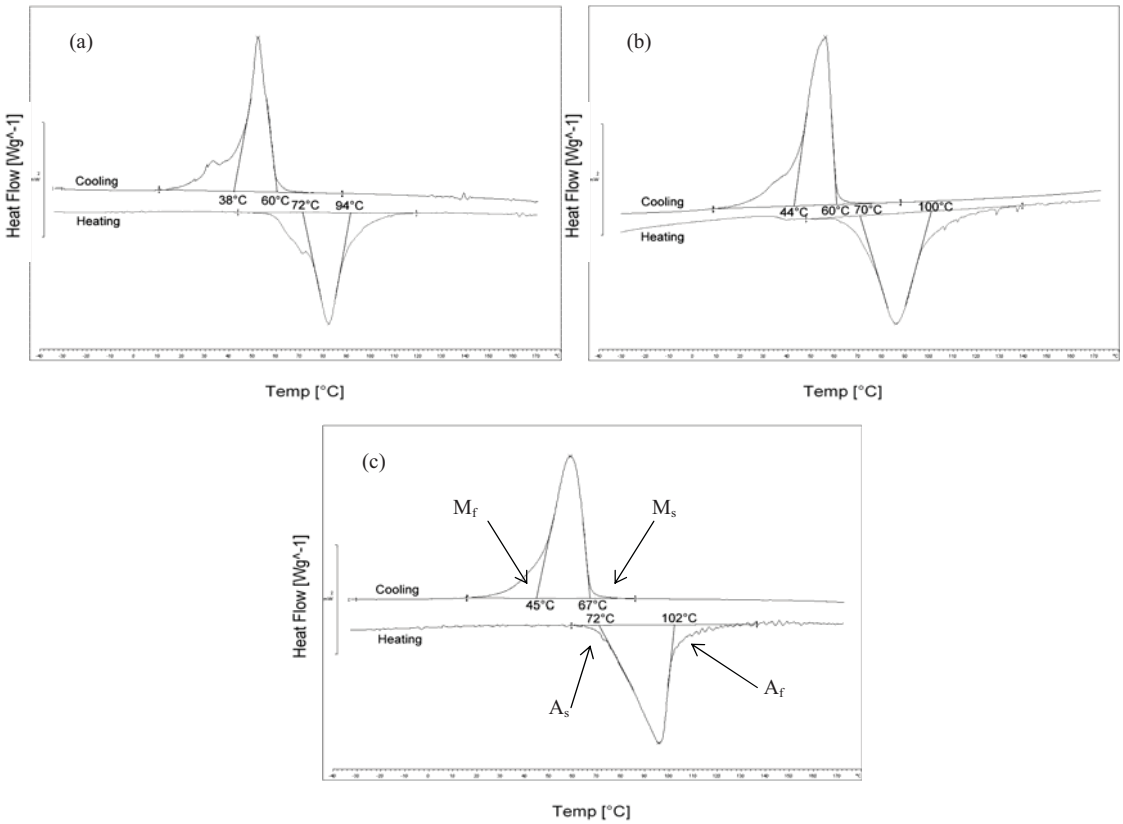

Fig. 4-57: DSC curves of NiTi ribbons at various wheel speeds: (a) 5 m/s, (b) 15 m/s, (c) 30 m/s.

Figure 4-58 shows the transformation of NiTi25Cu ribbons after melt-spinning with various wheel speeds, ranging from 10 to 45 ms^{-1}. The transformation becomes more evident and sharper with lower wheel speeds, i.e. lower cooling rate. The high cooling rate causes high amount of defects and internal stress in ribbons and these defects play an important role in the transformation behavior of the phases. The broad temperature region of the transformation is attributable to the alteration in the local defect distributions. Finally, the ribbons produced with wheel speeds of 40 ms^{-1} and 45 ms^{-1} have partially and fully amorphous structures, respectively.

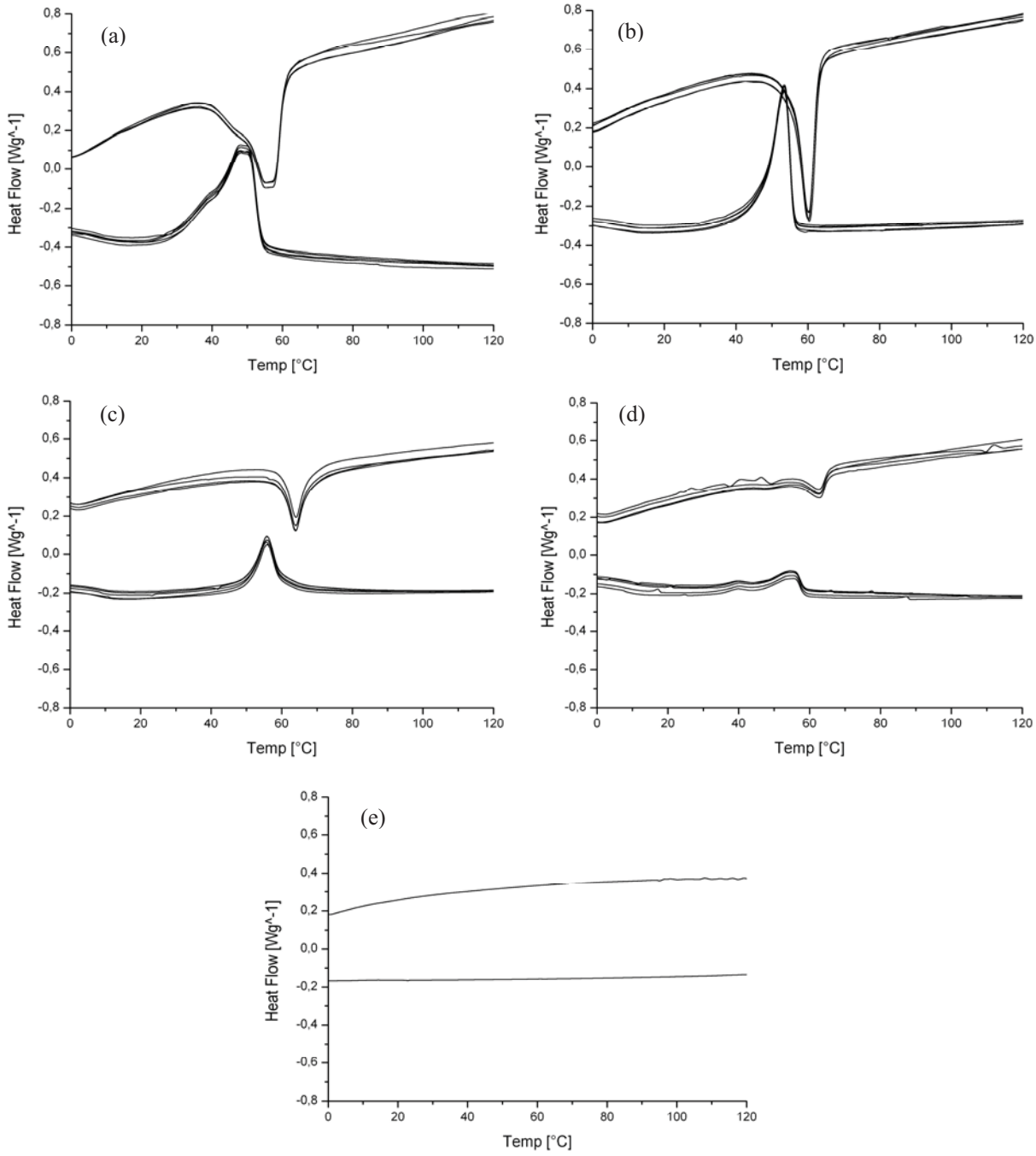

Fig. 4-58: DSC curves (using 20 K/min) of NiTi25Cu ribbons at various wheel speeds; (a) 10 m/s, (b) 20 m/s, (c) 30 m/s, (d) 40 m/s and (e) 45 m/s.

4.7.2 Transformation behavior and properties after training

In many applications the shape memory components experience repeated thermal cycles, either under external load or free of constraint. One critical concern in the development of devices using SME is the functional property stability of the alloys. It is known that the critical temperatures and the internal stresses for the martensitic transformation in NiTi-based alloys are sensitively affected by thermal cycling. Therefore, understanding of the effects of training and subsequent thermal cycling on the transformation behavior has been an important concern for the shape memory alloys.

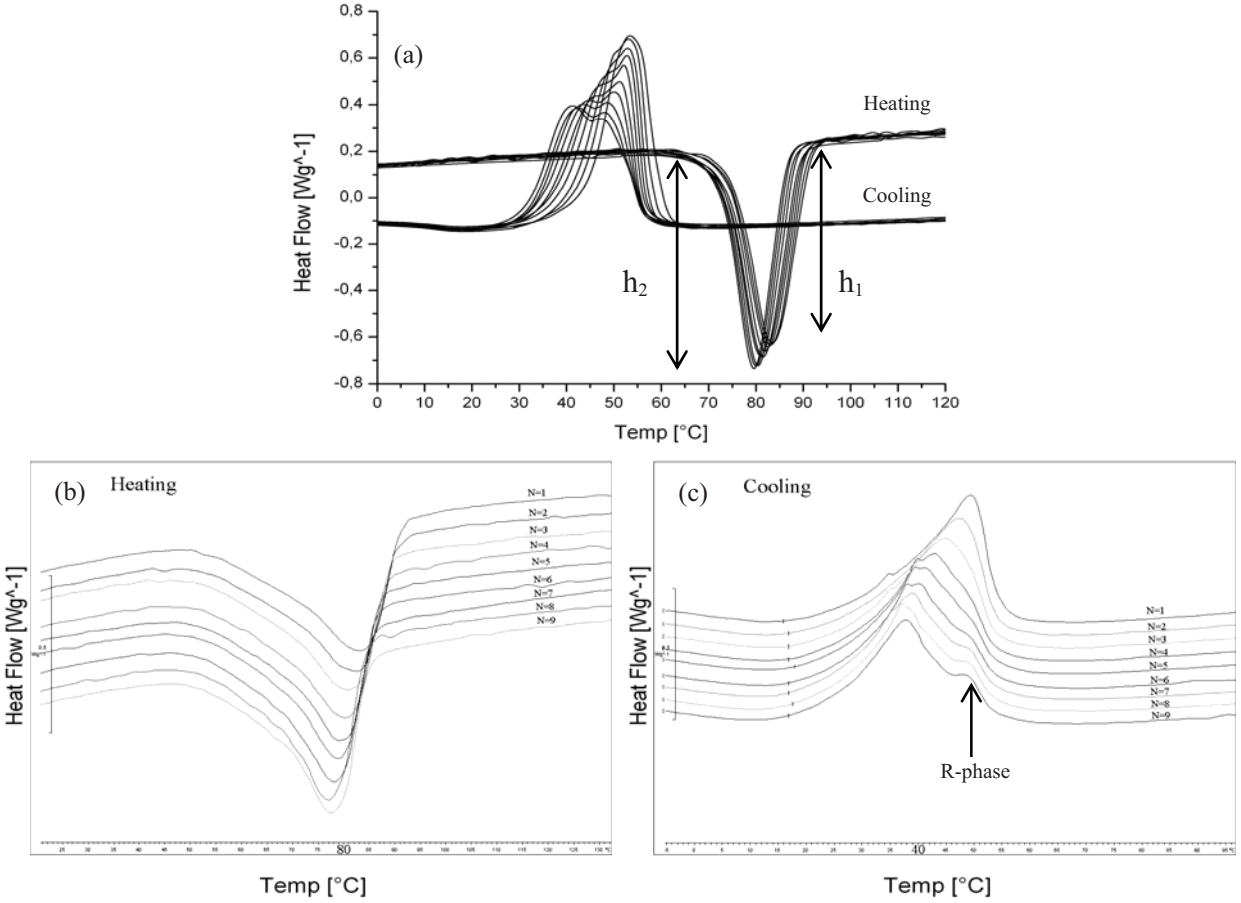

Fig. 4-59: DSC results for NiTi ribbons with different numbers of free thermal cycles after one training cycle: (a) 10 thermal cycles, (b) endothermic behavior and (c) exothermic behavior.

The transformation behavior of a NiTi ribbon with increasing number of free thermal cycles after one constrained training cycle is shown in Figure 4-59. The numbers in the Figure correspond to the number of free thermal cycles. Thermal cycling decreases slightly the transformation temperatures, especially the critical temperatures for both the forward (martensite) and the reverse (austenite) transformations. Moreover as can be seen in Figure 4-59a, the height of the peak of austenitic phase transformation increases mildly during thermal cycling ($h_1<h_2$). The decrease in austenitic transformation temperatures (endothermic

behavior) and the increase in the height of the austenitic peak indicate an easier transformation from martensite to austenite which is generally ascribed to the presence of a dislocation structure that serves as a network of nucleation sites for the austenite phase. It is already established [4.17–4.20] that this drop in transformation temperatures during thermal cycling is due to the defect generation and internal stresses induced during fabrication and subsequent thermomechanical treatment.

The exothermic behavior (during cooling, Figure 4-59c) of the transformation shows that a broad peak with a shoulder on the right side (arrow) appears during thermal cycles, which is very close to the main peak. This phase is R-phase or pre-martensitic transformation. The austenite to martensite transformation temperature gradually decreases with increasing thermal cycles, while the R-phase transformation remains relatively constant. As has been reported also in [4.21-4.24], the appearance of R-phase is common for plastically deformed or thermally cycled near-equiatomic NiTi alloys, since dislocations or precipitates create energy barriers for martensite nucleation, making the R-phase formation a lower energy alternative. Inducing small areas of R-phase can relax the internal stress associated with the dislocations or precipitates. The R phase is probably present ever since the first cycle. Its apparent development is not due to the thermal cycling but to the fact that M_s is shifted to lower temperatures during thermal cycles. For the NiTi ribbon, as exhibited in the Figure 4-59, it is found that the transformation temperatures are not stable in early stages and each cycle of DSC leads to lower transition temperatures (~ 1 °C/cycle), at least for the first 10 cycles.

However in Figure 4-60, DSC curves of the trained NiTi25Cu ribbon with 15 constrained cycles show that the effect of cycling processes decreases and the transformations are much more stable than NiTi ribbon. The decrease in M_s temperature due to DSC cycling is less than 0.2 °C/cycle. Also comparison of the NiTi25Cu ribbons before and after training revealed that the transformation picks of trained ribbon become smaller and wider. It may explain by the increase of the number of nucleation sites and dislocations, i.e. through the training the applied stress causes a decreasing of free energy in one or in a group of variants.

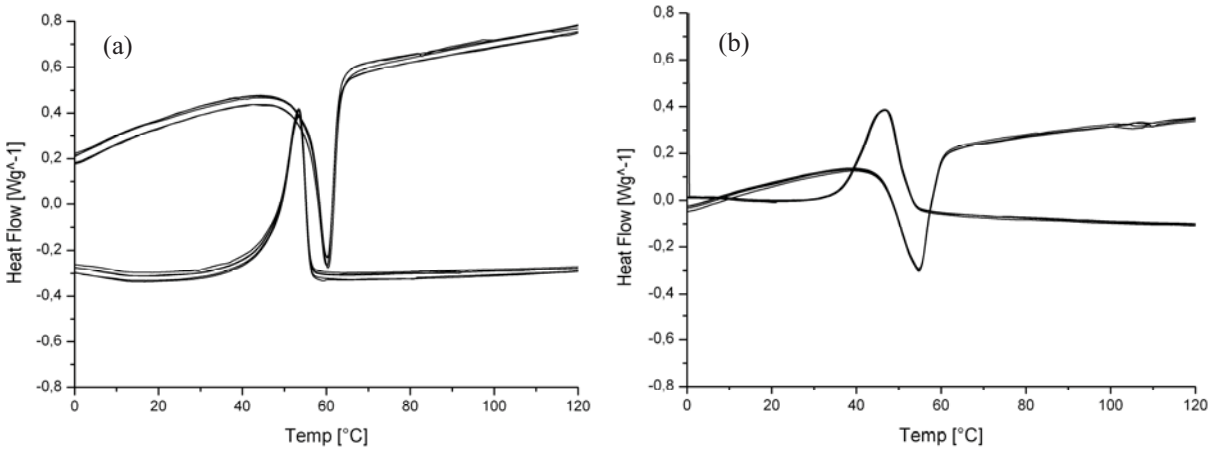

Fig. 4-60: Identification of transformation temperatures by DSC for NiTi25Cu ribbons during thermal cycles; (a) before training, (b) after training.

In addition, DSC curves of NiTi ribbon after 500 and 3000 free training cycles are shown in Figure 4-61. After training cycles, a multiple-stage martensitic transformation by thermal cycling occurred. This is probably associated with R-phase formation and martensitic transformation performed with several steps due to the strain fields around coherent precipitates. Also occasionally some precipitates form and grow during the thermomechanical training, which generates large-scale heterogeneity in microstructure and chemical composition. Therefore some regions undergo a B2-R-B19' two-stage transformation, while the other regions, being free of precipitates, undergo a direct B2-B19' transformation.

Furthermore as exhibited in Figure 4-61b, after sufficient free thermal cycling, when the defects are stabilized, the amount of the shift lessens and a significant stability in the transformation temperature could be seen. This is attributed to the strengthening of the matrix and introduction of precipitates in the matrix.

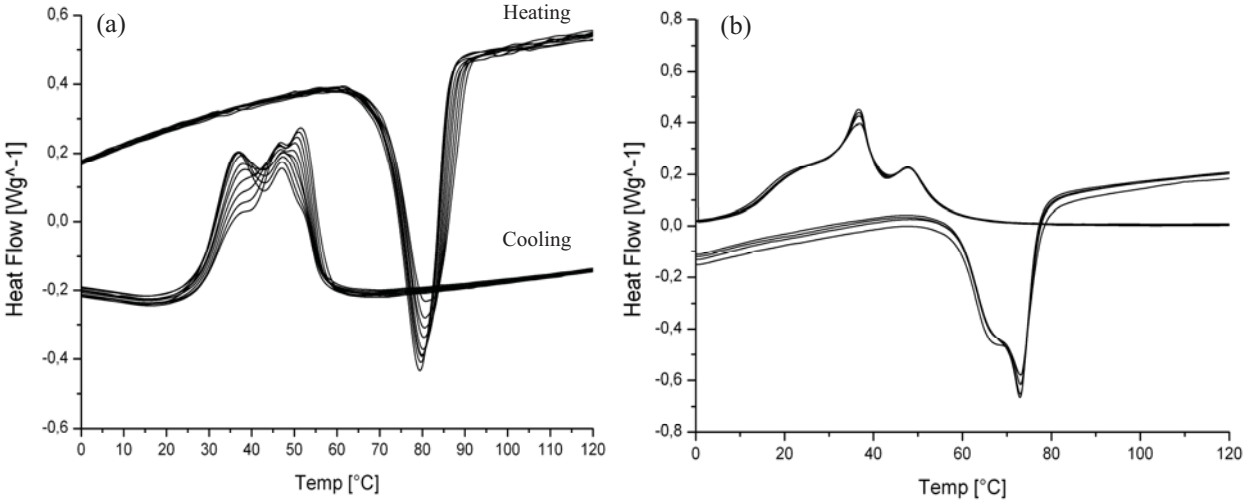

Fig. 4-61: Identification of transformation temperatures by DSC for NiTi ribbons during thermal cycles after: (a) 500 cycles, (b) 3000 cycles.

Results from XRD pattern from the melt-spun ribbons before and after thermomechanical training indicate that the formed precipitates are Ti_2Ni (Figure 4-62). All peaks in the pattern before training belong to the B19′ martensite, while after 500 training cycles Ti_2Ni precipitates are present. It is thought that the accumulation of lattice defects introduced by training and thermal cycles leads to the stabilization of the Ti_2Ni phase.

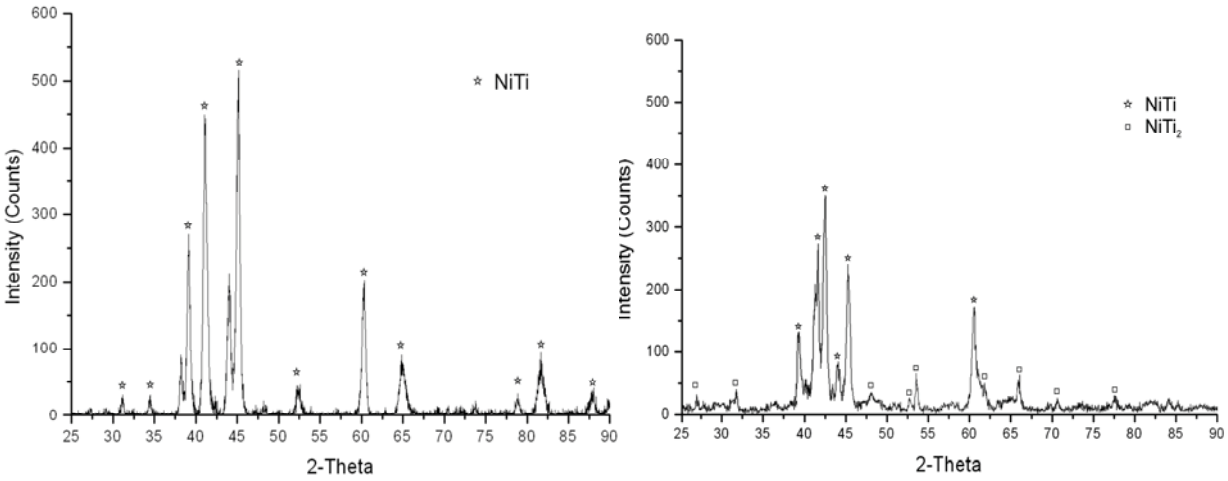

Fig. 4-62: XRD pattern of a NiTi ribbon, B19′ phase: (a) before training, (b) after training.

Furthermore, TEM was employed to investigate the substructures of NiTi ribbons before and after training procedure. Figure 4-63 displays a fine martensitic structure (B19′ phase) with nano-sized twin boundaries in the NiTi ribbons. The corresponding TEM micrograph after 5 training cycles and 500 free thermal cycles shows that, after thermal cycles, many fine spherical particles were precipitated inside the martensite grains. By selected area diffraction and by EDX analysis these particles (indicated by arrows) could be identified as Ti_2Ni. The size of the precipitates was estimated to be in the order of several hundred nanometres.

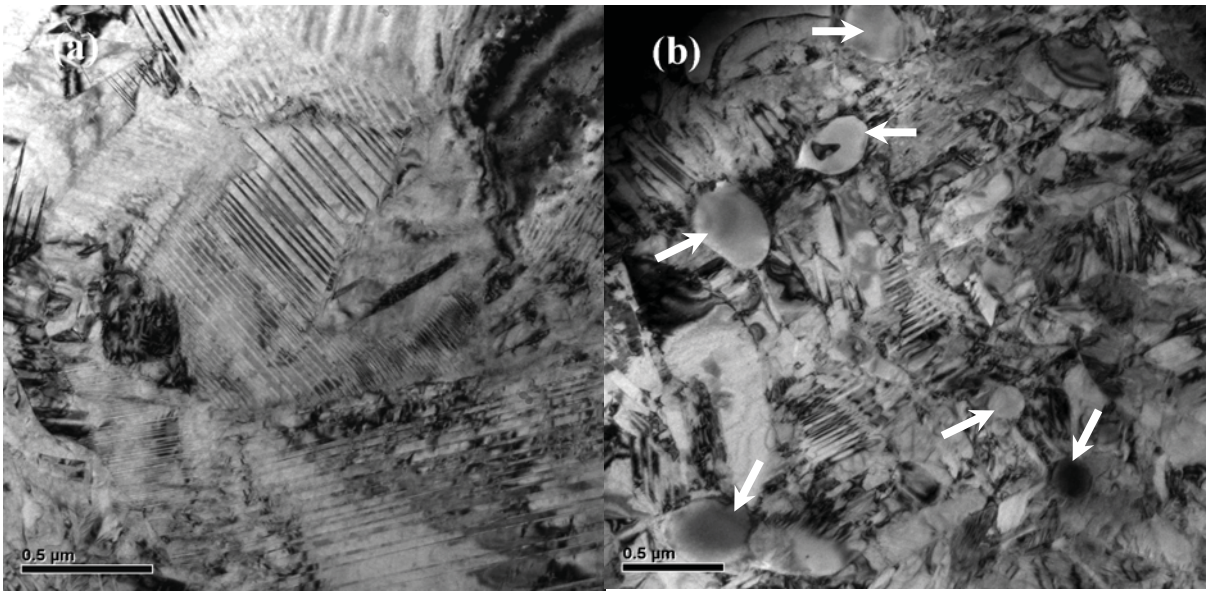

Fig. 4-63: TEM micrograph of the B19′ martensite microstructure in a melt-spun NiTi ribbon: (a) before training, (b) after training showing Ti_2Ni particles.

To examine the effect of training on the mechanical properties of NiTi ribbons, the tensile test was performed before and after training procedure. The results of the tensile test are shown in Figure 4-64. It clearly shows a higher strength than the ribbons without training. The increase in stiffness is caused probably by the Ti_2Ni precipitates and a higher dislocation density. Moreover, unloading-reloading tests have been performed 5 times for trained ribbon. The deviation between the unloading path and reloading path is very small. This experimental result reveals that the deformation of the specimen is fully pseudoplastic and that there is no austenite phase and pseudoelastic effect at all.

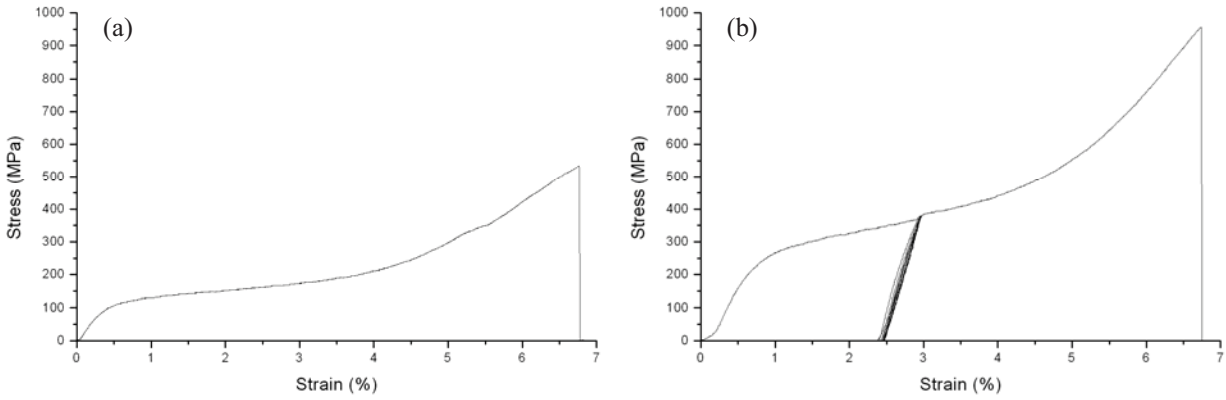

Fig. 4-64: Stress-strain curve from the melt-spun ribbon: (a) before training, (b) after training.

5. Summary

Shape memory alloys are unique metallic materials which have applications in the biomedical, aerospace, and commercial industries because of their ability to undergo large deformations while reverting back to their original undeformed shape through either the application of heat (shape memory effect) or the removal of the load (superelastic effect). NiTi shape memory alloys have been the focus of extensive research; however, there is a lack of past knowledge with regard to the two-way behavior of rapid solidification NiTi-based SMA, which has many advantages and can lead to small-dimensioned samples. The small-dimensioned samples were fabricated by different rapid solidification techniques.

The main objective of this study has been to characterize and optimize the two-way effect in melt-spun Ni- 50.3 at.% Ti SMAs and also to investigate the influence of copper (5-25 at.% Cu) and tungsten (2 at.% W) on the microstructure and the functional and mechanical behavior. In particular, the stress-strain-temperature behavior during training was investigated and the influence of training methods on the two-way shape memory effect (TWSME) of ribbons (magnitude and stability) was analyzed. Moreover, the TWSME and stress-assisted TWSME were studied in the hysteresis and transformation behavior.

The results confirm that the deformation mechanisms involved in the shape memory effect are related to the development of plastic strain in the ribbons structure during thermomechanical training. During training, due to the development of plastic strain, an internal stress field was created; this stress field which interacts with the phase transformation during the training cycles, will provide driving force for the preferential orientation of martensite variants. These effects benefit the formation of the TWSME in the material that, guided by the internal stresses, remember a low temperature shape. The stability of the TWSME was analyzed through several thousand thermal cycles. The TWSME and its stability are well suited for important applications such as microsensors and microactuators.

According to the results and discussions in the previous chapter, this study can be concluded as follows:

- Since the stoichiometric and solubility range of NiTi phase is very narrow, NiTi SMAs are very sensitive to the exact chemical composition and homogeneity, and small deviations of the required composition lead to formation of various inclusions. Formation of inclusions is mainly attributed to the influence of silicon, oxygen and carbon, because of complications during production or not proper crucible or coating. NiTiSi, Ti_4Ni_2O, TiO_2, TiC and Ti_2Ni are brittle compounds usually formed during production and processing of the NiTi SMA alloys. These compounds adversely affect the workability, ductility and shape memory properties of the alloy.

- It was found that the best results of melt-spinning are achieved using quartz crucible coated with Y_2O_3 for injection temperatures below 1400 °C and graphite crucible above 1400 °C.

- Thin ribbons and disks were produced successfully by rapid solidification techniques (melt-spinning and splat-cooling) by using arc-melted ingots and proper crucibles. XRD and DSC investigations show that all samples exhibited fully martensitic structure and shape memory effects immediately after processing without subsequent heat treatment. Amorphous ribbons without any crystal phases were produced only in the NiTi25Cu alloy under high cooling rates during melt-spinning process at a wheel speed of 45 m/s.

- With increasing cooling rates, the martensite transformation temperatures are slightly raised, probably due to higher internal stresses. The splat-cooled samples show very similar microstructures and transformation temperatures as the ribbons produced by the highest wheel speed indicating similar cooling conditions.

- The higher the wheel speed the lower is the thickness of the resulting ribbon and therefore the higher is the cooling rate. With increasing cooling rate the microstructure gets finer and finer and, therefore, metallographic preparation is not easy at all.

- Using of a new etchant (modification of Weck's reagent) and interference contrast, it is possible to reveal the fine microstructures and grain boundaries. By SEM investigations of NITi25Cu the twin boundaries of the martensitic substructure could be shown. The martensite structure in binary NiTi, however, is much finer, and nano-sized twin boundaries could be reavealed using TEM only.

- Two-way shape memory effects have been successfully introduced by different thermomechanical training methods in NiTi, NiTiCu and NiTiW alloys. The addition of copper was effective to narrow the transformation hysteresis. The W addition has improved the stability of the TWSME.

- The NiTi-based ribbons could be trained using a tensile training method under both constant strain and constant stress. The constant stress training also was effective in developing a stress-assisted TWSME, and the maximum effect was comparable in magnitude with TWSME. Moreover, it was found that the SATWME stabilizes during thermal cycling as well as the TWSME.

- The bending training method is also an effective method to induce a TWSME in the NiTi-based ribbons. The resulting TWSME increases with increasing number of constrained thermal cycles in the early stages and then decreases after reaching a maximum point, the plastic deformation increases strongly and hence the shape recovery ratio reduces. After several hundred free thermal cycles (not constrained)

the two-way effect became larger with higher shape recovery and finally stabilized. Therefore, the ribbons could be trained by a combination of constrained and free thermal cycles.

- The NiTi and NiTi25Cu ribbons demonstrated that 5 training cycles were not effective enough to stabilize the TWSME, and a good stability can be reached only after 15 training cycles, however the NiTi2W ribbons achieve a TWSME with proper stability already after 5 training cycles. This is due to higher strength of NiTi2W ribbons which causes high enough internal stress fields after 5 training cycles. The stability of about 1% TWSME in these ribbons seems very suitable for many technical long-term applications.

- The lower the strength of a ribbon the higher is the TWSME immediately after training. Softer ribbons can be trained easily to higher effect size but the stability is weak. On the other hand, ribbons of higher strength exhibit smaller TWSME values but prove to be relatively stable against functional fatigue.

- For NiTi ribbon, the height of the austenitic peak (endothermic behavior) increases and the transformation temperatures decrease slightly with an increase in the number of cycles. The exothermic behavior of the transformation shows that the R-phase appears during thermal cycles. For NiTi25Cu, however, the effect of cycling processes decreases and the transformations are much more stable than in NiTi ribbons.

- After free thermal cycling of trained NiTi, many fine Ti_2Ni spherical particles were observed by XRD and TEM and therefore, the trained ribbons show higher strength than ribbons without training. These ribbons have good mechanical properties (strength and ductility).

The most important results of this work are:

- Fabrication of different NiTi-based ribbons by an optimized melt-spinning process.

- Assessment of the ribbons microstructures, characterization of properties and optimization of the parameters with respect to training and TWSME.

- Performing different training methods and optimization the training conditions with respect to the size and the long-term stability of the TWSME.

- Obtaining new knowledge on the mutual dependence of the chemical composition, parameters of rapid solidification, microstructure, mechanical treatments, training and thermal cycling parameters, mechanical and functional properties.

- The results are very suitable for future microactuator and microsensor applications.

6. References

Chapter 1

[1.1] Z.G. Wei, R. Sandström, J Intelligent Mater Struc 33 (1998) 3743.

[1.2] H. Scherngell, A.C. Kneissl, Scripta Mater 39 (2) (1998) 205-212.

[1.3] H. Scherngell, A.C. Kneissl, Acta Mater 50 (2002) 327-341.

[1.4] K. Kutschej, X. Wu, P. Mayrhofer, A.C. Kneissl, Sonderband der Prakt. Metallogr. 33 (2002) 261-268.

[1.5] X. Wu, K. Kutschej, A.C. Kneissl, Inter J Mater Res (Z. Metallkd.) 94 (2003) 122-126.

[1.6] X. Wu, K. Kutschej, A.C. Kneissl, Mater-wiss u Werkstofftech 34 (2003) 484-489.

[1.7] A.C. Kneissl, K. Kutschej, X. Wu, J de Phys IV 112 (2003) 571-574.

Chapter 2

[2.1] A. Ölander, J. Amer Soc 54 (1932) 3819.

[2.2] A.B. Greninger, V.G. Mooradian, Trans AIME 128 (1938) 337-368.

[2.3] G.V. Kurdjumov, L.G. Khandros, Dokl Akad Nauk SSSR 66 (1949) 211-213.

[2.4] L.C. Chang, T.A. Read, Trans AIME 191 (1951) 47-52.

[2.5] W.M. Wayman, J.D. Harrison, JOM-J Min Met Mater 41 (1989) 26.

[2.6] L.M. Schetky, Shape Memory Alloys, Scientific American 241 (5) (1979) 74-82.

[2.7] A.V. Srinivasan, M.D. McFarland, Smart structures – analysis and design, Cambridge university press (2001) 26-69.

[2.8] G.B. Kauffman, I. Mayo, The Chemical Educator 2 (2) (1996) 1-20.

[2.9] L.S. Castleman, S.M. Motzkin, F.P. Alicandri, V.L. Bonawit, J Biomed Mater Res 10 (1976) 695-731.

[2.10] D.E. Cutright, S.N. Bhaskar, B. Perez, R.M. Johnson, G.S.J. Cowan, Oral Surg Oral Med Oral Pathol 35 (1973) 578-584.

[2.11] T. Duerig, A. Pelton, D. Stockel, Mater Sci Eng A. 273 (1999) 149.

[2.12] A.V. Kulkarni, MSc thesis, Texas A&M University, 2004.

[2.13] D.C. Lagoudas, J.G. Tadjbakhsh, Smart Mater Struc 1 (1992) 162-167.

[2.14] F.X. Kayser, J.W. Patterson, J Phase Equilibria 19 (1) (1998) 11-18.

[2.15] C.M. Wayman, T.W. Duerig, Engineering Aspects of SMAs (1990) 3-20.

[2.16] G.J. Ackland, TMS 2005, vol. 2, Warrendale, PA.

[2.17] C. Darjan, Shape memory alloys, seminar task, University of Ljubljana, Slovenia, 2007.

[2.18] X. Huang, K.M. Rabe, G.J. Ackland, Nature Mater. 2 (2003) 307-311.

[2.19] A. Falvo, PhD thesis, University of Calabria (Unical), Rende, Italia, 2004.

[2.20] K. Otsuka, C.M. Wayman, Shape Memory Materials, Cambridge University Press, 1998.

[2.21] X. Ren, K. Otsuka, Nature 6651 (1997) 579.

[2.22] J.R. Davis, shape memory alloys and composite materials, ASM specialty handbook (2001) 121-126.

[2.23] J.A. Shaw, Inter J Solids Struc 39 (2002) 1275-1305.

[2.24] H. Sehitoglu, I. Karaman, R. Anderson, X. Zhang, K. Gall, H.J. Maier, Y. Chumlyakov, Acta Mater 48 (2000) 3311.

[2.25] T.L. Turner, PhD thesis, Virginia Polytechnic Institute and State University, Hampton, Virginia, 2001.

[2.26] J. Van Humbeeck, J de Phys IV 6, (1996) 371-380.

[2.27] D. Ryan Walker, MSc thesis, University of Waterloo, Ontario, Canada, 2008.

[2.28] Sh.P. Mizar, PhD thesis, Worcester Polytechnic Institute, Waltham, MA, 2005.

[2.29] M. Cohen, E.S. Machlin, V.G. Paranjpe, Thermodynamics in Physical Metallurgy, American Society for Metals (1949) 242.

[2.30] S. Saadat, J. Salichs, M. Noori, Z. Hou, H. Davoodi, I. Baron, Y. Suzuki, A. Masuda, Smart Mater Struc 11 (2002) 218-229.

[2.31] O.H. Xie, PhD thesis, Drexel University, Philadelphia, 2007.

[2.32] J. Ryhänen, PhD thesis, Faculty of Medicine, University of Oulu, Oulu, Finland, 1999.

[2.33] N. Morgan, PhD thesis, Cranfield university, UK, 1999.

[2.34] H. Funakubo, Shape Memory Alloys, Gordon and Breach Science Publishers, New York, NY, 1987.

[2.35] C. Liang, C.A. Rogers, J Intelligent Mater Sys Struc 1 (1990) 207-234.

[2.36] A. Subramaniam, MSc thesis, University of Manitoba, Winnipeg. Manitoba, 1998.

[2.37] T. Duerig, K. Melton, J. Proft, Engineering Aspects of Shape Memory Alloys, Butterworth-Heinemann Ltd, London, 1990.

[2.38] M. Ahlers, Inter Conf Mart Trans (ICOMAT), JIM, Sedai, Japan, (1986) 786.

[2.39] D. Schofield, A.P. Miodownjk, Met Tech 7 (1980) 167.

[2.40] W. Huang, Materials and Design 23 (2002) 11-19.

[2.41] F.E. Wang, Inter Conf on Fractures, Sedai, Japan, BII (1965) 103.

[2.42] T. Honma, M. Matsumoto, Y. Shugo, M. Nishida, I. Yamazaki, 4th Inter Conf on Titanium, American Institute of Mining, Warrendale (1980) 1455.

[2.43] J.H. Mulder, PhD thesis, University of Twente, 1995.

[2.44] J. Beyer and J.H. Mulder, Mat Res Soc Symp Proc 360 (1995) 443.

[2.45] Johnson Service Company, US Patent No. 5, 114, 504, 1992.

[2.46] S.M. Tuominen, R.J. Biermann, J of Metals 2 (1988) 32.

[2.47] S.K. Wu and C.M. Wayman, Scripta Metall 21 (1987) 83.

[2.48] V.N. Khachin, V.G. Pushin, V.P. Sivokha, V.V. Kondratyev, S.A. Muslov, V.P. Voronin, Yu.S. Zolotukhin, L.I. Yurchenko, Phys Met Metall 67 (4) (1989)125.

[2.49] O. Mercier, K.N. Melton, Met Trans 10A (1979) 387.

[2.50] Y. Shugo, T. Honma, M. Hasegawa, Bull Res Inst Min Met Thoku Univ 37 (1) (1981) 79.

[2.51] E.A. Baldwin, MSc thesis, North Carolina State University, Raleigh, NC, 2004.

[2.52] L.I. Barbero Bernal, MSc thesis, Georgia Institute of Technology, 2004.

[2.53] K. Otsuka, X. Ren, Intermetallics 7 (1999) 511-528.

[2.54] J. Fuentes, P. Gumpel, J. Strittmatter, Adv Eng Mater 4 (2002) 437.

[2.55] V.I. Kolomytsev, Inter Syrnp on Shape Memory Alloys, Beijing, China, Inter Read Puclishers (1994) 136-142.

[2.56] V.N. Kachin, V.P. Voronin, V.P. Sivokha, V.G. Pushin, ICOMAT 95, France, Journal de Physique, IV 5, (1995) 707-712.

[2.57] F.J. Gil, J.A. Planell, J Biomed Mater Res 48 (1999) 682-688.

[2.58] T. Ranucci, S. Besseghini, G. Airoldi, Mater Sci Forum 327 (2000) 143-146.

[2.59] Ch. Grossmann, J. Frenzel, V. Sampath, T. Depka, G. Eggeler, Metall Mater Trans A 40 (2009) 2530-2544.

[2.60] TH. Nam, T. Saburi, K. Shimizu, Mater Trans JIM 31 (11) (1990) 959-967.

[2.61] F.J.J. Loo, G.F. Bastin, A.J.H. Leenen, J Less Common Met 57 (1978) 111-121.

[2.62] S.W. Kang, Y.M. Lim, Y.H. Lee, H.J. Moon, Y.W. Kim, T.H. Nam, Scripta Mater 62 (2010) 71–74.

[2.63] V.G. Pushin, S.B. Volkova, N.M. Matveeva, L.I. Yurchenko, A.S. Chistyakov, Phys Met Metallogr 84 (1997) 441-448.

[2.64] S.P. Alisova, N.V. Volynskaya, P.B. Budberg, A.N. Kobylkin, , Russ Metall 5 (1986) 207-209, translated from Izv Akad Nauk SSSR, Met 5 (1986) 210-212.

[2.65] B. Kockar, PhD thesis, Texas A&M University, 2007.

[2.66] S.K. Wu, C.M. Wayman, Metallography 20 (1987) 87.

[2.67] S.K. Wu, C.M. Wayman, Scripta Metall 21 (1987) 83.

[2.68] D.R. Angst, P.E. Thoma, M.Y. Kao, J De Phys IV 5 (1995) 747.

[2.69] S. Besseghini, E. Villa, A. Tuissi, Mater Sci Eng A 273-275 (1999) 390.

[2.70] X.L. Meng, Y.F. Zheng, Z. Wang, L.C. Zhao, Scripta Mater 42 (2000) 341.

[2.71] P. Olier, J.C. Brachet, J.L. Bechade, C. Foucher, G. Guenin, J De Phys IV 8 (1995) 741.

[2.72] P.E. Thoma, J.J.Boehm, Mater Sci Eng A 273-275 (1999) 385.

[2.73] X.L. Meng, W. Cai, L.M. Wang, Y.F. Zheng, L.C. Zhao, L.M. Zhou, Scripta Mater 45 (2001) 1177.

[2.74] B. Kockar, I. Karaman, J.I. Kim, Y. Chumlyakov, Scripta Mater 54 (2006) 2208.

[2.75] J.H. Mulder, J.H. Maas, J. Beyer, Inter Conf on Mart Trans (ICOMAT 93), Monterey Institute for Advanced Studies Carmel, CA. 1993.

[2.76] S.K. Wua, S.F. Hsieh, J Alloys and Compounds 297 (2000) 294.

[2.77] K.V. Ramaiah, C.N. Saikrishna, S.K. Bhaumik, Inter Conf Smart Mater Struc Sys (2005) SC141.

[2.78] X.L. Meng, Y.F. Zheng, Z. Wang, L.C. Zhao, Mater Letters 45 (2000) 128.

[2.79] P.G. Lindquist, C.M. Wayman, Engineering Aspects of Shape Memory Alloys, Boston: Butterworth-Heinemann Ltd, 1990.

[2.80] Y. Xu, K. Shimizu, Y. Suzuki, K. Otsuka, T. Ueki, K. Mitose, Acta Mater 45 (1997)1503.

[2.81] B. Lin, K. Gall, H.J. Maier, R. Waldron, Acta Biomater 5 (2009) 257-267.

[2.82] W. Cai, S. Tanaka, K. Otsuka, Mater Sci Forum 327 (2000) 279.

[2.83] K. Otsuka, K. Oda, Y. Ueno, M. Piao, T. Ueki, H. Horikawa, Scripta Metall Mater 29 (1993) 1355.

[2.84] www.AZoM.com

[2.85] R. Gotthardt, P. Scherrer, R. Stalmans, Mater Sci Forum 327 (2000) 83-90.

[2.86] C. Segui, E. Cesari, J. Van Humbeeck, J Mater Trans JIM 31 (1990) 375.

[2.87] H. Pops, T.B. Massalski, Trans AIME 230 (1964) 1662.

[2.88] S.W. Husain, P.C. Clapp, J Mater Sci 22 (1987) 2351.

[2.89] S. Miyazaki, T. Kawai, K. Otsuka, J De Phys IV 43 (1982) 813.

[2.90] K. Oishi, L.C. Brown, Metall Trans 2 (1971) 71.

[2.91] S. Miyazaki, K. Otsuka, H. Sakamoto, K. Shimizu, Trans Jpn Inst Metals 22 (1981) 244.

[2.92] H. Sakamoto, K. Shimizu, Trans Jpn Inst Metals 27 (1986) 601.

[2.93] G.S. Firstov, J. Van Humbeeck, Y.N. Koval, Scripta Mater 50 (2004) 243.

[2.94] G.S. Firstov, Y.N. Koval, J. Van Humbeeck, R. Portier, P. Vermaut, P. Ochin, Mater Sci Eng A 438 (2006) 816.

[2.95] H. Donkersloot, J. Van Vucht, J Less-Common Mater 20 (1970) 83-91.

[2.96] Y. Lo, S. Wu, Scripta Metall Mater 27 (1991) 1097-1102.

[2.97] J. Wu, Q. Tian, Intermetallics 11 (2003) 773-778.

[2.98] Q. Tian, J. Wu, Intermetallics 10 (2002) 675-682.

[2.99] T. Sawaguchi, M. Sato, A. Ishida, Mater Sci Eng A 332 (2002) 47-55.

[2.100] J. Gill, D. Chang, L. Momoda, G. Carman, Sensors and Actuators A 93 (2001) 148-156.

[2.101] K. Oikawa, T. Ota, F. Gejima, T. Ohmori, R. Kainuma, K. Ishida, Mater Trans 42 (2001) 2472.

[2.102] R. Kainuma, M. Ise, C.C. Jia, H. Ohtani, K. Ishida, Intermetallics 4 (1996) 151.

[2.103] Y. Xu, K. Otsuka, E. Furubayashi, K. Mitose, Mater Letters 34 (1998) 14.

[2.104] W. Cai, K. Otsuka, Scripta Mater 41 (1999) 1311.

[2.105] R.W. Fonda, H.N. Jones, R.A. Vandermeer, Scripta Mater 39 (1998) 1031.

[2.106] R.W. Fonda, H.N. Jones, Mater Sci Eng A 273-275 (1999) 275.

[2.107] J. Khalil Allafi, X. Ren, G. Eggeler, Acta mater 50 (2002) 793-803.

[2.108] K. Otasuka, X. Ren, Intermetallics 7 (1999) 511-528.

[2.109] J. Zhang, W. Cai, X. Ren, K. Otsuka, M. Asai, Mater Transaction 40 (1999) 1367.

[2.110] B. Vicentini, G. Rondelli, A. Cigada, G. Turisini, , Shape memory alloy, China Academic Publishers, Beijing, China, 86 (1986) 447.

[2.111] G. Rondelli, B. Vicetini, A. Cigada, MRS Inter Meeting Adv Mat, Tokyo, Japan, 9 (1988) 237-242.

[2.112] W. Schwenk, J. Huber, SAMPE QUART 5 (1974) 17-20.

[2.113] E.K. Eckelmeyer, Scripta Met 10 (1976) 667-674.

[2.114] S. Kotamala, MSc thesis, The University of Toledo, OH, 2004.

[2.115] F. Laves, H.J. Wallbaum, Naturwissenschaften 27 (1939) 674.

[2.116] D.M. Poole, W. Hume Rothery, J Inst Met 83 (1954) 473-480.

[2.117] P. Duwez, J.L. Taylor, Trans AIME 188 (1950) 1173.

[2.118] G.R. Purdy, J.G. Parr, Trans AIME 221 (1961) 636.

[2.119] R.J. Wasilewski, S.R. Butler, J.E. Hanlon, D. Worden, Metall Trans 2 (1971) 229.

[2.120] M. Nishida, C.M. Wayman, T. Honma, Metall Trans 17A (1986) 1505.

[2.121] A. Ishida, M. Sato, A. Takei, S. Miyazaki, Mater Trans JIM 36 (1995) 1349.

[2.122] K. Otsuka, X. Ren, Progress in Materials Science 50 (2005) 511-678.

[2.123] S. Miyazaki, K. Otsuka, Metall Trans 17A (1986) 53.

[2.124] V.N. Khachin, Y.I. Paskal, V.E. Gunter, A.A. Monasevich, V.P. Sivokha, Phys Met Metallogr 46 (1978) 49.

[2.125] M.B. Salamon, M.E. Meichle, C.M. Wayman, Phys Rev B 31 (1985) 7306.

[2.126] S. Miyazaki, Y. Ohmi, K. Otsuka, Y. Suzuki, ICOMAT, J DE Phys IV 43 (1982) 255.

[2.127] S. Miyazaki, K. Otsuka, Philos Mag A 50 (1984) 393.

[2.128] C.M. Hwang, C.M. Wayman, Scripta Metall 17 (1983) 381.

[2.129] T.B. Massalski, H. Okamoto, P.R. Subramanian, L. Kacprzak, Binary alloys phase diagrams, 2nd edition, vol. 3, ASM International, 1990.

[2.130] G. Chattopadhyay, H. Kleykamp, Z Metallkd 74 (1983) 182.

[2.131] R. S. Dennis, MSc thesis, North Carolina State University, Raleigh, NC, 2003.

[2.132] J. Beyer, J De Phys IV 5 (1995) 433-442.

[2.133] G.M. Michal, R. Sinclair, Acta Crystallographica B 37 (1981) 1803-1806.

[2.134] Lie Zhao, PhD thesis, University Twente, Enschede, the Netherlands, 1997.

[2.135] X. Ren, N. Miura, J. Zhang, K. Otsuka, K. Tanaka, M. Koiwa, Mater Sci Eng A 312 (2001) 196.

[2.136] J.V. Humbeeck, Mater Sci Eng A 273-275 (1999) 134.

[2.137] H. Sehitoglu, I. Karaman, R. Anderson, X. Zhang, K. Gall, H.J. Maier, Y. Chumlyakov, Acta Mater 48 (2000) 3311.

[2.138] K. Otsuka, T. Sawamura, K. Shimizu, Phys Stat Sol(a) 5 (1971) 457.

[2.139] Y. Kudoh, M. Tokonami, Acta Metall 33 (11) (1985) 2094.

[2.140] W. Bührer, R. Gotthardt, A. Kulik, O. Mercier, J De Phys Suppl 43 (12) (1982) C4-219.

[2.141] K.M. Knowles, Phil Mag A45 (1982) 357.

[2.142] R.H. Bricknell, K.N. Melton, O. Mercier, Metall Trans A 10 (1979) 693.

[2.143] J.W. Cahn, Acta Metall, 25 (1988) 721.

[2.144] D.B. Chernov, L.A. Monasevich, N.N. Bashanova, Yu. L. Paskal, Phys Met Metall 59 (6) (1985) 173.

[2.145] G. Tan, Y. Liu, Intermetallics 12 (4) (2004) 373-381.

[2.146] L. Tan, W.C. Crone, Scripta Mater 50 (6) (2004) 819-823.

[2.147] K. Otsuka, X. Ren, Mater Sci & Eng A 273 (1999) 89.

[2.148] S. Miyazaki, K. Otsuka, ISIJ International 29 (1989) 389.

[2.149] G. Fan, Y. Zhou, W. Chen, S.Yang, X.Ren, K. Otsuka, Mater Sci Eng A 438–440 (2006) 622–626.

[2.150] T. Saburi, T. Tatsumi, S. Nenno, ICOMAT, J De Phys IV 43 (1982) 261.

[2.151] K. Otsuka, Introduction to the R-Phase Transition, Butterworth-Heinemann Publishers, London (1990) 36-45.

[2.152] Y. Suzuki, H. Tamura, Engineering Aspects of Shape Memory Alloys, Butterworth-Heinemann Publishers, London (1990) 256-266.

[2.153] H. Tobushi, Y. Shimeno, T. Hachisuka, K. Tanaka, Mechanics of Materials 30 (2) (1998) 141-150.

[2.154] L.C. Brinson, I. Schmidt, R. Lammering, J Mech Phys solids 52 (2004) 1549-1571.

[2.155] K. Gall, H. Sehitoglu, R. Anderson, I. Karaman, Y.I. Chumlyakov, I.V. Kireeva, Mater Sci Eng A 317 (1-2) (2001) 85-92.

[2.156] K. Wada, Y. Liu, J Alloys and Compounds 400 (1-2) (2005) 163-170.

[2.157] Y. Liu, Y. Liu, J. Van Humbeeck, Acta Mater 47 (1) (1999) 199.

[2.158] Y. Liu, Y. Liu, J. Van Humbeeck, J Scripta Mater 39 (1998) 1047.

[2.159] K.N. Melton, Engineering Aspects of Shape Memory Alloys, Butterworth-Heinemann Ltd, London, (1990) 21-35.

[2.160] R. DesRoches, J. McCormick, M. Delemont, J Struc Eng 130 (1) (2004) 38-46.

[2.161] T. Saburi, S. Nenno, Inter Conf Solid-Solid Phase trans, Warrendale, PA, 1981.

[2.162] J.P. McCormick, PhD thesis, Georgia Institute of Technology, 2006.

[2.163] T. Tadaki, K. Otsuka, K. Shimizu, Annual Rev Mater Sci 18 (1988) 25-45.

[2.164] H. Scherngell, PhD thesis, University of Leoben, Austria, 2000.

[2.165] E. Hornbogen, New horizon of materials 45 (1995) 111-122.

[2.166] B.C. Muddle, 6th Inter Conf Mart Trans, Sydney, Australia, 1989.

[2.167] F.E. Wang, W.J. Buehler, Appl Phys Letter 21 (1972) 105.

[2.168] T. Saburi, S. Nenno, Scripta Metall 8 (1974) 1363.

[2.169] R. Oshima, E. Naya, J Jpn Inst Met 39, (1975) 175.

[2.170] G.K. Haritos, Smart Structures and Materials, Amer Soc Mech Eng, 1991.

[2.171] M. Zhu, D.Z. Yang, Scripta Metall 22 (1988) 5.

[2.172] T. Honma, Inter Symp on SMAs, China Academic Publisher, Beijing (1986) 83.

[2.173] R. Kainuma, M. Matsumoto, T. Honma, Inter Conf on Mart Trans, JIM, Sedai, Japan (1986) 717.

[2.174] M.W.M. van der Wijst, MSc thesis, TU Eindhoven, Veldhoven, Nederlands, 1992.

[2.175] I. Ahmad, A. Crowson, C.A. Rogers, M. Aizawa, U.S.-Japan workshop on smart/ intelligent materials and systems, Honululu, Hawaii, 1990.

[2.176] H. Ming Wu, L.McD. Schetky, SMST, Pacific Grove, California (2000)171-182.

[2.177] M. Asai, Y. Suzuki, Materials Science Forum 327-328 (2000)17-22.

[2.178] J. Van Humbeeck, J. Cederstrom, SMST, Pacific Grove, California (1994) 1-6.

[2.179] K. Worden, W.A. Bullough, J. Haywood, Smart technologies, World Scientific (2003) 109–135.

[2.180] R. Murray, Radiology 225 (2002) 835-844.

[2.181] NMT Medical, Inc. http://www.nmtmedical.com

[2.182] L.M. Schetky, Shape Memory Alloys, Scientific American 241 (5) (1979) 74–82.

[2.183] Tinel Shape Memory Alloys, Raychem company literature.

[2.184] W. Huang, PhD thesis, University of Cambridge, Peterhouse, 1998.

[2.185] S.E. Hsu, M.T. Yeh, I.C. Hsu, S.K. Chang, Y.C. Dai, J.Y. Wang, Mater Sci Forum 327 (2000) 119-122.

[2.186] S. Takaoka, H. Horikawa, J. Kobayashi, K. Shimizu, Mate Sci Forum 394-395 (2002) 61-68.

[2.187] B.V. Finander, Y. Liu, 1st inter conf on shape memory and superelastic technologies (1994) 151-156.

[2.188] T. Anson, Shape Memory Alloys - Medical Applications, Materials World 7 (12) (1999) 745-747.

[2.189] J. Musialek, P. Filip, J. Nieslanik, J Archives of Orthopaedic and Trauma Surgery 117 (6-7) (1998), 341–344.

[2.190] C.H. Beauchamp, R.H. Nadolink, S.C. Dickinson, L.M. Dean, 1st European Conf on Smart Struc and Mater, 1992.

[2.191] R. Chandra, Smart Materials Structures 10 (2001) 1018-1024.

[2.192] E.J. Graesser, F.A. Cozzarelli, J Eng Mech 117(11) (1991) 2590-2608.

[2.193] M. Dolce, R. Marnetto, Seismic Devices Based on Shape Memory Alloy, Manside Project 2 (1999) 105-134.

[2.194] R. DesRoches, B. Smith, J Earthquake Engineering 8(3) (2004) 415-429.

[2.195] J. R. Santiago Anadon, MSc Thesis, University of Florida, 2002.

Chapter 3

[3.1] www.edmund-buehler.de

[3.2] P. Duwez, ASM Trans Quarterly 60 (1967) 607.

[3.3] P. Pietrowski, Rev Sci Instrum 34 (1963) 445.

[3.4] M. Ohring, A. Haldipur, Rev Sci Instrum 42 (1971) 530.

[3.5] H.S. Chen, C.E. Miller, Rev Sci Instrum 41 (1970) 1237.

[3.6] E.H. Strange, C.A. Pim, US Patent: 90 57 58 (1908).

[3.7] M. Stoica, MSc Thesis, Technical University Dresden, Germany, 2005.

[3.8] E.R. Arata, PhD thesis, ETH ZURICH, 2008.

[3.9] L. XH, PhD thesis, California Institute of Technology, Pasadena 1997.

[3.10] J.V. Wood, Metallurgica 53 (1986) 372-374.

[3.11] H. Jones, Rapid Solidification of Metals and Alloys, Monograph No. 8, The institution of metallurgists, London, UK, 1982.

[3.12] S. Gulbrandsen Dahl, PhD thesis, Norwegian University of Science and Technology (NTNU), Trondheim, Germany, 2002.

[3.13] T.R. Anantharaman, C. Suryanarayana, Rapidly Solidified Metals, Trans Tech Pub, Brookdield, VT, 1987.

[3.14] S. Kavesh, Metallic Glasses, Papers Presented at a Seminar of the Materials Science Division of the ASM, 36, 1978.

[3.15] Differential Scanning Calorimeter, User Manual, TA Instruments, 1995.

[3.16] L. Zhao, STW Project in University Twente, Enschede, The Netherlands, 1997.

[3.17] B. Warren, X-ray Diffraction, Addison Wesley Publishing Company (1969).

[3.18] Ch. Li, MSc thesis, Iowa State University, 1998.

[3.19] L.J. Chiang, C.H. Li, Y.F. Hsu, W.H. Wang, J. Alloys Compd 462 (2008) 47-51.

[3.20] B.J. McKay, PhD thesis, Linacre College, Oxford, UK, 2001.

[3.21] G. Lombardi, For Better Thermal Analysis (2nd edition), International Confederation for Thermal Analysis (ICTA), Rome (1980) 20.

[3.22] C.M. Jackson, H.J. Wagner, R.J. Wasilewski, NASA Report, SP-5110 (1972) 22.

[3.23] H.C. Lin, S.K. Wu, Acta Metall Mater 42 (1994) 1623.

[3.24] K. Gall, H. Sehitoglu, Y.I. Chumlykov, I.V. Kireeva, H.J. Maier, J Eng Mater, ASME 121 (1999) 19.

Chapter 4

[4.1] R.D. Jean, J.C. Tsai, Scripta Metall Mater 30 (1994) 1027.

[4.2] Y. Liu, P.G. McCormick, ICOMAT 92, Monterrey Inst of Adv Studies (1993) 923.

[4.3] Y. Liu, J. Humbeeck, R. Stalmans, L. Delaey, J Alloys Compd 247 (1997) 115.

[4.4] E.R. Stover, J. Wulf, The Ni-Ti-C System, Trans ALME 215 (1959) 127.

[4.5] J.L. Murray, Binary Alloys Phase Diagrams, ASM int. 3 (1990) 3496.

[4.6] P. Villars, A. Prince, H. Okamoto, Handbook of Ternary Alloy Phase Diagrams, ASM int. 10 (1995) 13061.

[4.7] A.C. Kneissl, K. Mehrabi, M. Bruncko, B.J. McKay, D. Uhlenhaut, Inter J Mater Res (Z. Metallkd) 100 (2009) 1038-1045.

[4.8] K. Bhattacharya, R.V. Kohn, Acta Mater 44 (2) (1996) 529-542.

[4.9] S. Eucken, J. Hirsch, Mater Sci Forum 481 (1990) 56-58.

[4.10] G. Lojen, I. Anzel, A. Kneissl, A. Krizman, E. Unterweger, B. Kosec, M. Bizjak, J Mater Proc Tech 162-163 (2005) 220-229.

[4.11] M. Franz, X. Wagner, J Physics: Conference Series 240 (2010) 012004.

[4.12] A. Sezonenko, V. Kolomytsev, M. Babanly, A. Pasko, P. Ochin, R. Potier, P. Vermaut, J Phys IV 112 (2003) 889-892.

[4.13] A. Inoue, Mater Sci Eng A269 (1999) 171-183.

[4.14] A.V. Kulkarni, MSc thesis, Texas A&M University, 2004.

[4.15] C.M. Wayman, T.W. Duerig, Engineering Aspects of Shape Memory Alloys, Butterworth-Heineman Ltd, London (1990) 3-20.

[4.16] K.N. Melton, Engineering Aspects of Shape Memory Alloys, Butterworth-Heinemann Ltd, London (1990) 21-35.

[4.17] K.N. Lin, S.K. Wu, J of Alloys and Compounds 424 (2006) 171-175.

[4.18] B. Strnadel, S. Ohashi, H. Ohtsuka, S. Miyazaki, T. Ishihara, Mater Sci Eng A 203 (1995) 187-196.

[4.19] L. Jordan, M. Masse, J.Y. Collier, G. Bouquet, J Alloys Compd 211 (1994) 204-207.

[4.20] Y. Liu, P.G. McCormick, Acta Metall Mater 38 (1990) 1321-1326.

[4.21] C.P. Frick, A.M. Ortega, J. Tyber, A.E.M. Maksound, H.J. Maier, Y.N. Liu, Mater Sci Eng A 405 (2005) 34.

[4.22] M. Carroll, C. Somsen, G. Eggeler, Scripta Mater 50 (2004) 187.

[4.23] D. Favier, Y. Liu, P.G. McCormick, Scripta Metall Mater 28 (1993) 669.

[4.24] H.C. Lin, S.K. Wu, T.S. Chou, H.P. Kao, Acta Metall Mater 39 (1991) 2069.

[4.25] Z.G. Wang, X.T. Zu, Y. Huo, Thermochim Acta 436 (2005) 153.

7. Symbols and Abbreviations

List of symbols

Å	angstrom
ε	strain
ε_o	transformational strain
ε_{1W}	one-way shape strain or shape recovery strain
ε_{2W}	two-way shape strain
ε_d	bending deformation pre-strain
ε_{const}	constant strain during thermomechanical training
ε_p	plastic deformation
ε_{rec}	recoverable strain
ε_{SATW}	stress-assisted two-way strain
ε_{total}	total strain
σ	applied stress
σ_{ir}	irreversible stress
θ	deformation angle / Bragg angle
λ	wavelength
A	austenite
A_f	austenite finish temperature
A_s	austenite start temperature
A_p	austenite peak temperature
B2	crystallographic notation for parent austenite phase in NiTi
B19	crystallographic notation for orthorhombic martensite in NiTi
B19’	crystallographic notation for monoclinic martensite in NiTi
D	diameter of the constrained circle
d	ribbon thickness
DO_3	crystallographic notation for parent austenite phase in CuAlNi
E	Young’s modulus or elastic modulus
ΔH	enthalpy of phase transformation / transformation latent heat
M	martensite
M_s	martensite start temperature for B19´
$M´_s$	martensite start temperature for B19
M_f	martensite finish temperature
M_d	maximum temperature to induce martensite by stress
M_p	martensite peak temperature

N	number of training cycles
P	Parent phase (Austenite)
Q_a	heat of austenitic transformation
Q_m	heat of martensitic transformation
R	rhombohedral phase
ΔS	transformation entropy
ΔT	temperature difference
T	temperature
t	time
Y_M	stress-induced martensite plateau
Y_R	Initial yielding point

List of Abbreviations

ARSME	all-round shape memory effect
at.%	atomic percentage
bcc	body-centered cubic
DSC	differential scanning calorimetry
EDX	energy dispersive x-ray analysis
fcc	face-centered cubic
FIB	focused ion beam
HV	hardness vickers
LIS	lattice invariant shear
OM	optical microscopy
PE	pseudoelasticity
RF	radio frequency
rpm	revolutions per minute
RT	room temperature
SATWME	stress-assisted two-way memory effect
SEM	scanning electron microscopy
SIM	stress-induced martensite
SME	shape memory effect
SMA(s)	shape memory alloy(s)
TEM	transmission electron microscopy
TWSME	two-way shape memory effect
wt.%	weight percentage
XRD	X-ray diffraction